Melt-Triggered Seismic Response in Hydraulically-Active Polar Ice: Observations and Methods

Joshua D Carmichael

A dissertation
submitted in partial fulfillment of the
requirements for the degree of

Doctor of Philosophy

University of Washington

2013

Reading Committee:

Ian Joughin, Chair

William Wilcock

Steve Malone

Program Authorized to Offer Degree:
Geophysics

University of Washington

Abstract

Melt-Triggered Seismic Response in Hydraulically-Active Polar Ice: Observations and Methods

Joshua D Carmichael

Chair of the Supervisory Committee:
Professor Ian Joughin
Applied Physics Laboratory

Glacier ice responds to environmental forcing through changes in its sliding speed and mass balance. While these changes often occur on daily time scales or longer, they are initiated by brittle deformation events that establish hydrological pathways in hours or seconds and allow meltwater access to englacial or subglacial depths to facilitate ice motion. In this thesis, we (various contributing authors including myself) use seismic monitoring to detect and locate the creation and growth of some of these hydraulic pathways by monitoring their seismic emissions, or icequakes. More specifically, we address (1) what seismic observables, unavailable from other sensing methods, indicate an initial glaciogenic response to meltwater input and (2) if these comprise evidence of feedbacks that may destabilize polar ice under a warming climate. Supplemental to our scientific contributions, we advance statistical processing methods that demonstrably improve the capability of digital detectors at discriminating ice quakes from astationary noise.

We begin by interpreting geophysical observations collected from a dry-based, subfreezing ($-17°$C), polar glacier environment (Taylor Glacier, ANT). By implementing a calibrated surface energy balance model, we estimate the timing and volume of surface meltwater generated during the collection of seismic data from a six-receiver geophone network. This comparison illustrated that any effectively nonzero meltwater triggered large, repeating ice quakes localized near a deep, supraglacial-to-subglacial crack within a melt-

water catchment region. The focal mechanisms of these icequakes are consistent with an expansive growth within the crack. Their occurrence at night suggests that this expansion was accommodated by volumetric straining of confined, re-freezing meltwater. These cracks likely sustained their surface-to-bed hydrological connection, in the absence of melt-assisted basal sliding. Further, this appears to be the first report attributing seismogensis in glacial ice to fracturing induced by phase change.

We proceed by contrasting these response characteristics with geophysical observations following an early (spring) supraglacial lake drainage within the lake-forming ablation zone of the Western Greenland Ice Sheet. The subglacial drainage system present during this time was considered incapable of efficiently draining large fluxes of meltwater input and therefore likely to undergo transient motion. Using measurements from a $\sim$ 5km-aperture geophone network, we find that the anticipated post-drainage icequakes are diurnally responsive, largely surficial in origin, and indicative of tensile fracturing from shallow cracks in the ice. The creation of the lake-drainage moulin appears to coincide with a shift in mean icequake source locations, and an increase in icequake occurrence at night relative to that in the day. Contrary to our expectations, we find that the timing of GPS-derived surface speeds do not clearly indicate this seismic activity on any given day. Rather, these icequakes are best explained by peaks in localized strain gradients that develop at night when decreased subglacial water flux likely increases variability in basal traction. Additionally, our results appear comprise the first detailed seismic observations targeted at an actively draining lake.

Our last study addresses the apparent deficiency in observed basal icequakes detected from Greenland lake site. To explain the lack of deep icequakes, we compute thresholds on the magnitude of detectable basal events within the network and thereby illustrate that surficial icequakes with similar magnitudes and spectral content are more likely to be observed. By restricting our attention to seismic events that produce lower frequency waveforms, we find a population of nearly monochromatic, sub-1Hz, large magnitude ($M_w \leq 3$) seismic events borne from remote glaciogenic sources. In contrast to surficial icequakes, these events occur without significant bias between day and/or night periods and are best

explained as glacial earthquakes generated by sliding episodes or iceberg calving events in the vicinity of Jakobshavn Glacier. These events occur daily and not correlate with the presence of local, surficial seismicity.

We conclude with three general assertions regarding melt-triggered response characteristics of polar ice. First, hydraulic connections established by fracture events do not necessarily result in seismogenic basal stick slip, and therefore cannot necessarily be observed with conventional GPS monitoring. This was demonstrated at Taylor Glacier. Here, meltwater input to a hydraulic pathway led to fracture growth deep within a cold glacier without any change in surface speed. Second, the presence of melt-triggered basal sliding does not necessarily induce a clear seismogenic basal response in the lakes regions. This was demonstrated on the Greenland Ice Sheet. Seismogenesis may instead be more clearly reflected by surficial strain gradients established by variability in basal traction, suggesting these feedbacks are secondary rather than primary. The response is therefore not clearly indicated from day-to-day timing of GPS-observations. Third, the absence of an *observed* local response does not necessarily indicate the absence of a local *physical* response. This was also illustrated in Greenland. Here, deep local icequakes are likely muted by noise, waveform-attenuating ice, and viscous basal rheology. Magnitude thresholds suggest that ($M_w \leq 2$) for consistent recording of local, non-surficial sources. In contrast, remote, low frequency seismic events were clearly observed, and attributed to activity within ice catchments along the western edge of the ice sheet or Jacobshavn glacier.

Finally, we assert that early-indicators of melt-triggered glacial response include components of spatially localized, brittle deformation that is most suitable to seismic observation. Critically-stable regions along mass-balance equilibrium lines constitute potential sites for newly forming surface-to-bed hydraulic connections in a warming climate, and likewise, a potential target for future seismic experiments.

TABLE OF CONTENTS

Page

LIST OF FIGURES

LIST OF TABLES

Table Number Page

GLOSSARY

DETECTOR: A digital detector (or just detector) is a scalar statistic formed from noise-corrupted data samples, in addition to a decision rule for attributing the statistic's value to the presence or absence of a signal.

GLACIAL EARTHQUAKE: An seismic event that results from the interaction of glacier bodies with the the Earth's surface to produce elastic radiation dominated by 1Hz or lower frequencies with moment magnitudes exceeding 2.

ICEQUAKE: An microseismic event resulting from elastic deformation of glacial ice that produces elastic radiation dominated by 1Hz or higher frequencies with moment magnitudes less than 2.

MOMENT TENSOR: A 2^{nd} order tensor representation of the body-force equivalent for a seismic source that is excited in the absence of actual body forces, such as a displacement discontinuity on a fault.

MOULIN: A surface-to englacial (or subglacial) hydrological pathway within a glacier.

MULTIPLET: Distinct, repeating seismic events that produce nearly identical records of ground motion.

SUPRAGLACIAL LAKE: A body of meltwater that forms on the surface of ice sheets within their ablation area and usually exceeds $\frac{1}{2}$km in one dimension of lateral extent.

STRESS INTENSITY FACTOR: A scalar quantity that gives the amplitude the elastic stresses in the immediate neighborhood of a crack tip, and outside the plastic yield zone.

TARGET WAVEFORM: A general term referring to an information-bearing seismic signal that is (likely) corrupted by noise and interference.

TREMOR: An oscillatory response of an elastic body that is triggered by a near-steady, non-oscillatory forcing and is observed as persistent ice or ground vibration.

ACKNOWLEDGMENTS

The author wishes to express sincere appreciation to Ian Joughin, Erin Pettit, Ken Creager, Matt Hoffman, Andrew Fountain, Bernard Hallet, William Wilcock, Steve Malone, James Pitton, Michelle Koutnik, Don Percival, Ben Smith, the Applied Physics Laboratory Staff, and the University of Washington. Documents, computational codes, and figures were prepared with LaTeX, Microsoft Power Point®, and Matlab®.

DEDICATION

To my supportive family, friends, and partner Makenna

Chapter 1

INTRODUCTION: DYNAMIC RESPONSE OF POLAR ICE TO HYDROLOGICAL FORCING

This chapter summarizes research addressing the effect of hydrological forcing of polar ice in Earth's cryosphere. It reviews open questions in glaciology and identifies icequakes as a crucial geophysical observable for answering these questions. It concludes with an assessment of how the research presented in this thesis advances current understanding of interactions between polar ice and it's environment by using seismic measurements.

1.1 Transient Response of Polar Ice to Meltwater: The Need for Research

The stability of glacial ice in Earth's polar regions is dependent upon the timing and magnitude of it's response to meltwater input under changing climactic scenarios. The transient component of this response is in part exhibited by seasonal variability in basal sliding speeds of ice sheets and glaciers. It is important to understand how the physical mechanisms that facilitate this variable sliding are activated, and to include them in predictive models that are used to estimate glacial mass balance and sea level rise. This understanding requires synoptic geophysical monitoring of ablation zones where conduits (moulins) connect the glacial surface and bed, thereby allowing meltwater to access and interact with englacial and subglacial hydraulic systems [32, 81, 69, 23]. It also requires physical modeling of this interaction at transient time scales (e.g.,[147, 40]). These requirements constitute a significant challenge for assessing the sensitivity of polar ice to changes in meltwater supply, and for monitoring these changes in the near future. This challenge, combined with the modern capabilities of seismic and GPS networks, has created new incentives for original scientific and engineering solutions. This thesis documents two experiments that confront tractable aspects of this problem using seismic monitoring methods and includes novel contributions to seismology and glaciology.

Before documenting these experiments, I summarize the observation-based theories that

describe the meltwater-triggered deformation of glacial ice. In section 1.2, I begin with a review the hydrology of glaciers, with a focus on the deformation feedbacks established by fracture-pathways. In section 1.3, I provide a semi-quantitative description of the mechanical conditions that permit seismogenic fracture propagation and produce icequakes. In section 1.4, I discuss contemporary research involving seismic monitoring of hydraulically active ice and provide motivation for my research.

1.2 Meltwater Driven Glacial Deformation: Review of Glacial Hydrological Systems

The high mobility of meltwater in polar environments facilitates its dynamic exchanges with glacial ice. These exchanges involve the dissipation of momentum and heat energy as meltwater is transported through supraglacial (glacial surface), englacial (glacial interior), or subglacial (glacier substrate) environments along its flow path. The addition of latent and dissipative heat enhances ice flow at the granular level; interstitial water facilitates increased grain-boundary sliding within ice crystals above -10^{o}C, where the activation energy for creep increases by more $2\times$ [28] that of colder ice. In motion, a given volume of meltwater thereby has the potential to influence hydraulically activated deformation mechanisms throughout a glacier and produce a transient response in overall bulk glacier motion. Many of the deformation mechanisms that comprise this response are apparently inactive or suppressed in the absence of meltwater [21]. When response is rapid enough to initiate elastic or brittle deformation, it is observable from radiated microseismic energy (Figure 1.1). Such seismic emissions are observed from processes like tidewater calving [10, 121], basal stick-slip motion [187, 2], and ice-fracture [21, 138, 178, 179, 37]. Here I summarize how some of these processes interact within individual glacial environments.

1.2.1 Supraglacial Water

I first consider transient forcing by supraglacial meltwater. Supraglacial streams form in topographical melwater catchments on glacial surfaces and travel down local hydraulic gradients to create incised channels through thermal erosion [45, 76]. These channels are observed in alpine glaciers where ice temperatures are near freezing year-round, as well as

cold, polar glaciers where melt generation is restricted to $\leq 1\,\mathrm{mm\,hr^{-1}}$ melt rates during brief, sub-monthly periods in the summer (Figure 1.2) [71]. Regional topographical depressions can provide larger catchments for supraglacial meltwater streams, and permit liquid water to persist in larger volumes due to it's relatively high heat capacity (~ 4 for water, ~ 2 for $-10\,\mathrm{C}^\circ$ ice). On the Greenland ice sheet, these catchments can fill with water and are conventionally called supraglacial lakes (Figure 1.3). These lakes may extend to several km in lateral extent, with depths of 15m or more. They are important during the creation of surface-to-bed hydrological connections [32]. These connections initiate through hydrofracture events, whereby the high relative density of water in a crack counteracts the lithostatic closure stresses in the ice and allows the crack to propagate to the ice bed. The resulting drainage of the lake enlarges the crack through turbulent heat transfer to the ice walls and establishes moulins, or glacial conduits. The creation and persistence of these conduits allow additional meltwater to enter the subglacial drainage system and may connect with englacial fracture systems, as observed in alpine glaciers [43]. In colder polar glaciers, the same process is capable creating surface-to-englacial conduits [14, 21]. In these environments, water likely refreezes at depth and temporarily restricts additional meltwater access. Additional melt-triggered fracture can be thermally activated when refreezing events release latent heat to warm the ice-water interface. This allows water to penetrate deeper into the ice during successive fracture events by preventing immediate freeze-on when meltwater contacts cold ice walls [14].

1.2.2 Englacial Water

Second, I consider transient forcing from englacial water. Englacial channels may form from deep surface channels, where water flows along the bottom of existing crevasses. These surface channels (water-occupied crevasses) form englacial channels through a process called downcutting [45]. In this process, a surface channel sinks below the ice surface by thermal erosion, and viscous creep within the host ice pinches the top of the channel closed. Conditions for downcutting minimally require that the incision rate of the water-occupied channel exceed surface ablation rates so that the channel deepens faster than the host-ice

surface lowers. Such englacially channels may additionally retain a crack-like geometry if the channel-depth to channel-width ratio is large. This happens because the narrow bottom of such a channel serves as a stress concentrator and is therefore more likely to fracture under extensional strain. When these englacial water paths further intersect englacial fracture networks, they constitute an englacial water *system*. Such systems have been observed to comprise the primary pathway for water flow in temperate glaciers [43], and are important energy sources if englacial meltwater freezes and releases its latent heat [126]. If cavities within this system do retain liquid water long enough for ice flow to pressurize them, subsequent transient elastic deformation of the host ice may even trigger faulting [176, 36]. Such faulting may occur because shear stresses between the glacial crack planes are zero where water has held them open. Alternatively, if the glacier is cold ($< 0\,^{\circ}\mathrm{C}$) rapid re-freezing of the englacial meltwater can pressurize existing critically stable cracks through volumetric expansion and trigger additional fracture propagation [34]. If freezing is slower, water flows in pre-melted interfacial films at the solid-liquid boundary, causing ice accumulation at local temperature depressions, thereby fracturing surrounding ice through "heaving" [33, 132].

1.2.3 Subglacial Water

Last, I consider transient forcing by subglacial water. Subglacial drainage systems often provide a dominant influence over basal sliding compared with driving stresses from basal and surface slopes, or resistive stresses from lateral drag along the glacial margin. However, subglacial systems are largely unobservable. Because of this, a considerable effort has historically been devoted to their physical modeling using prescribed sources of melt input [147, 87, 119].

Subglacial drainage models are often categorized between two end-member types, the "distributed" and "channelized" drainage system. In either case, conservation equations are applied to compute the pressure, water flow area, and possibly the sliding speeds for given melt input. The first of these models I consider is the distributed drainage system [171]. This system is applicable to low storage volume, high water pressure subglacial conditions that are present during winter or spring seasons. These form when subglacial voids,

previously held open by turbulent melting from meltwater flow, are evacuated so that their overlying ice roofs creep closed. This action pressurizes the remaining poorly connected, low volume water pockets. Basal water pressures can rise further when meltwater input, fed from surface-to-bed connections, then overwhelms the systems' ability to drain the new water. If this pressure is sufficiently high, it can trigger propagation of basal crevasses upward into an englacial storage system [59]. Additional subglacial volume is created as the ice slides over basal obstacles and voids are created on the lee sides of these obstacles. If water pressures increase further and approach overburden, the corresponding effective pressures (water pressure less overburden) can decrease to near zero and cause the overlying ice column to locally float [32, 37]. This ice-bed decoupling increases glacial sliding speeds and may further open or enlarge basal cavities created by basal obstacles; increased water discharge can also enlarge cavities purely through turbulent melting [87]. Under both scenarios, drainage efficiency improves as these cavities open and increase the hydraulic conductivity and storage of the bulk subglacial drainage system. Additional storage volume and melt input eventually creates conditions whereby enlarged cavities connect, and form channels capable of quickly routing out further meltwater input [147]. A channelized (second model) drainage system thereby develops. These channels quickly adapt to new meltwater input, and grow in area with increased discharge as turbulent water flow melts away the wetted perimeter of the conduit walls [119, 26]. As water is drained, basal sliding decreases below mean winter values [82] since less of the bed is lubricated. These channels remain the primary drainage mechanism for late summer and early autumn subglacial systems, until energy and force balance under decreased water input favors eventual collapse into distributed drainage systems. Under both system models, basal traction at the ice-bed interface offers the primary resistive force restricting sliding.

In summary, hydrological connections throughout a glacial volume can create feedbacks that drive bulk ice deformation. These hydrological connections often consist of fracture pathways that allow meltwater generated at the ice surface access to englacial and subglacial storage and drainage systems. The initial development and sustained presence of these fractures thereby determine when and where initial meltwater response may be expected.

In the following section, I review how such these fractures are generated by glaciogenic forces.

1.3 Fracture Mechanics in Hydraulically Active Ice: Summary and Further Considerations

Fracture of glacial ice is typically an indicator of high tensile stresses. This is because the compressive strength of ice greatly exceeds it's tensile strength, as evident from extensive crevasse fields common in glaciers undergoing extensional flow, and the relative absence observed in regions of convergent flow. Fracture events can rapidly release stored elastic (strain) energy and are seismogenic processes, meaning that they are observable as icequakes. On glaciers, only certain stress conditions are favorable for melt-triggered fracture. The glaciogenic forces that must balance to maintain a static crack geometry include: the lithostatic stress, flow-induced far-field tensile/compressive stresses, bending ("beam") stresses within an ice column, the weight of (possibly) overlying supraglacial water, and heaving or thermal expansion from refreezing water. I ignore bulk pore pressures for the cold glaciers I consider in this thesis since the only hydraulically permeable portion of such ice is likely within the temperate zone near the air interface [131] and it is therefore unlikely that pore-pressures influence deeper crack propagation.

Contributing forces that tend to close voids and surface cracks are compressive. These are the far field stress from convergent flow, lithostatic stress from ice weight, and additional load stress from supraglacial water weight. Counteractive forces that tend to open cracks are water pressure (that loads crack faces), extensional flow, and (possible) volumetric-expansion of freezing water within the crevasse or crack. Bending stresses may facilitate either opening or closing of cracks, depending on whether ice flexure is concave up (compressive) or concave down (tensile). Previous observations [32, 37] show that ice flexure occurs as lake water is rapidly injected to the glacier bed and buoys the ice surface up. This puts the ice surface in tension relative to it's pre-drainage stress state.

Crack force-balance is quantified through the concept of the stress intensity factor, K_I [7], or SIF. This is a constant that gives the elastic stress amplification near a given crack

tip is given by

$$\sigma_{ij} = \frac{K_I}{\sqrt{2\pi r}} f_{ij}(\theta), \tag{1.1}$$

where σ_{ij} is elastic stress for a force in direction j on acting on a crack plane with local normal direction i, r gives the distance in the elastic medium from the crack tip, and θ gives the positive angle away from the crack plane, ahead of the crack tip. The dimensionless function $f_{ij}(\theta)$ depends on load and crack geometry. Crack-face force-balance is then described using the linear elastic fracture-mechanics approach advocated by van der Veen [169]. This approach consists of finding the tensile (mode-I) stress intensity factors, for each contributing portion of the stress field individually, then using superposition to compute the net stress intensity factor, K_I^{Net}. While other loading modes involving forces applied at oblique angles to the crack-face plane also occur, tensile fracturing is energetically more favorable. In the mode-I case, fracture occurs if K_I^{Net} exceeds a material property of the ice called the fracture toughness, K_{Ic}:

$$K_I^{\text{Net}} > K_{\text{Ic}}. \tag{1.2}$$

K_{Ic} for glacial ice is $\sim 150\sqrt{\text{kPa}}$ [168]. Three of the five stress intensity factors relevant to the ice fracture problems I implicitly[1] consider are carefully tabulated in [169].

An additional SIF is present during refreezing of water filled cracks. There are two different physical mechanisms that can contribute to fracture propagation during re-freezing. The first physical mechanism was briefly described in Section 1.2.2. It occurs when thermomolecular forces drive water in thin films at the ice-water interface toward colder temperatures, where the water then freezes in a thickening ice layer called segregation ice [117, 33]. This forming ice layer may push against a neighboring ice interface (like a crack wall) and trigger fracture by placing the ice near the crack tip in tensile strain [33, 117, 132]. The second physical mechanism results from expanding, refreezing water exerting pressure on the ice-walls of a stress-confined englacial void [34]. Although elevated pressure may be driven by wall-to-wall contact of segregated ice, it is sufficient to examine pressure change through

[1]The fracture modeling I perform to produce the results in this thesis appears in Chapter 2 only, while the remainder is largely qualitative. A full fracture mechanics analyses of lake drainage or thermal bending moments is outside the scope of my work.

the phase transition [2]. In this simpler model, pressure builds when an ice cap forms within a crack or crevasse at the ice-air interface [34]. This presence of this cap confines the water volume within the crevasse, so that during freezing, there is no stress-free surface to relieve accumulating strain; any additional freeze-on to crevasse walls further reduces the volume available for liquid water. I find a stress intensity factor dK_I of a force-couple acting on a crack-face patch of cross section db to be

$$dK_I = \frac{2\sigma}{\sqrt{\pi d}} G\left(b/d, d/H\right) db = \frac{2\left(\lambda + 2\mu\right)}{\sqrt{\pi d)}} \frac{\delta V}{V} G\left(b/d, d/H\right) db, \tag{1.3}$$

using the notation of van der Veen [168] and Aki [4]. In Equation 1.3, σ is the interstitial stress (pressure), λ and μ are Lamé parameters, $\lambda + 2\mu$ is the elastic longitudinal modulus of ice, δV is the strain-confined volumetric increase of water during freezing, V is initial, pre-frozen water volume, d is crack or depth, b depth below ice surface of the pooled water, $G(\cdot, \cdot)$ is a non-dimensional function [168, Equation 12], and H is glacial thickness. The net stress intensity factor K_I is obtained by integrating dK_I over freezing-water depth. Such a force acts to assist crack opening. Experimentally determined confinement stresses range over $\sigma \sim 0.1\text{kPa} - 1\text{MPa}$, including cases where the ice cap is partially extruded [34] . My estimate of dK_I for a 1m long crack using Equation 1.3 gives $K_I \sim 0.4\sqrt{\text{MPa}}$. This exceeds the fracture toughness K_{Ic} and suggests that freezing water can crack uncompressed ice.

Another SIF may be attributed to uplift that occurs during supraglacial lake drainage when water is injected to the subglacial drainage system. This uplift generates localized, out-of-plane plate bending of the ice sheet and has an associated SIF K_I^b [7]:

$$K_I^b = \sqrt{H\lambda} M_B \left[1.99 - 2.47\lambda + 12.97\lambda^2 - 23.17\lambda^2 + O\left(\lambda^4\right)\right]. \tag{1.4}$$

Here H is ice thickness, and λ is the ratio of the crack depth to ice thickness. The bending moment M_B can be determined from the local curvature $\frac{d^2w}{dw^2}$ of the ice free-surface and it's flexural rigidity using $M_B = EI \frac{d^2w}{dw^2}|_{z=\text{surface}}$, where $w\left(z\right)$ is the vertical deflection of the ice

[2] Alan Rempel stated in a personal communication on July 24, 2013: "...with water essentially encapsulated in cold ice, I suspect that the bulk phase behavior is enough to examine the leading order behavior....it's always possible that the pressure may crack the [ice] lid and squirt water out, like often happens in an ice-cube tray. There is likely an important role for thermomolecular forces, etc..., in describing the details of that problem, but I think [the] seismic source ideas probably don't need to go there just yet."

surface from a reference stress state, E is the elastic modulus of ice, and I is the moment of inertia of a plate about it's center (where lake water is injected to the bed). If the ice sheet is also in tension during lake drainage, K_I^b is superimposed with K_I from extensional flow [169, Equation 5], and makes additional surface fracture more favorable. To obtain an order-of-magnitude scale estimate of K_I^b, I assume in Equation 1.5 that a lake drainage has uplifted the ice surface by 1m near a 10m crack, that the ice is 1km thick (e.g., [32, 37]) and that deflection (quadratically) goes to zero at a 1km radius from the injection point:

$$K_I^b \sim 2\sqrt{H\lambda}EI\frac{d^2w}{dw^2}|_{z=\text{surface}} = 3.6 \cdot I\frac{\sqrt{\text{MPa}}}{\text{kg} \cdot \text{m}^2} \tag{1.5}$$

The moment of inertia scales with the uplifted ice sheet mass and the uplifted area squared, but is complicated by unknown support conditions at the bed. Regardless, this estimate demonstrates that virtually any bending on the scale I suggested promotes additional fracture (compare with K_{Ic}), when ice flow is extensional (in tension).

To summarize, there are several mechanisms for fracture in glacial ice. Two of these are not conventionally documented in glaciology literature but are plausible under the physical conditions I consider. In the following section, I discuss how some of these fractures produce icequakes.

1.4 Melt-Triggered Icequakes: Review and Need for Research

Observational evidence of polar glacier response to sub-daily variations in meltwater supply has largely come from the ablation zones of alpine glaciers and the Western Greenland Ice Sheet where moulins form. Several constituent experiments have in these regions have implemented passive seismic monitoring methods to detect, locate, and discriminate sources of melt-triggered brittle deformation (icequakes). In some cases, these icequakes occur without any evident expression in GPS-measured motion [21], and seismic monitoring has provided the primary sensing technology for identifying localized or transient deformation. These experiments have cumulatively identified sources of microseismic-scale seismicity (moment magnitude $M_w < 2$) originating from glaciogenic processes that include: tidewater calving [130, 121, 10, 97], basal stick-slip motion caused by sliding variability [165, 180, 5], basal ice fracturing during dropping subglacial water pressures [177], tensile fracturing during

water-facilitated speedup [157, 138, 20], hydraulic resonance of water-filled crevasses [111], and propagation of water-filled englacial cracks during confined, volumetric expansion [21].

In most cases, the generation of meltwater was a primary forcing mechanism for driving elastic (brittle) deformation. Larger glaciogenic events (moment magnitude $M_w > 3$) generating long-period ($\sim 1-100$ sec) surface waves energy that is detectable on regional or global seismic networks have also been associated with seasonal and climactic forcing [39, 118, 133]. Many of these events are driven by summer speedup of outlet glaciers, whereby downstream ice sliding generates a reaction force at the basal substrate that points upstream [166], as evident from focal mechanisms. I describe these larger events as "glacial earthquakes" to distinguish them from lower magnitude icequakes, consistent with conventional terminology. The broad range in physical scales and consistency in hydrological input underscore the benefits in comparing available meltwater volumes with seismic activity.

It has been generally impractical to compare measured icequake seismicity with available meltwater volume, however. There are several reasons for this. First, the initial conditions at a field site are often unknown because latent subglacial or englacial water may be present prior to seismic observation. Second, melt production from glacial ice is difficult to directly measure, while water storage in englacial or subglacial systems are inherently hidden [71]. Finally, channels and conduits that collect supraglacially-generated meltwater within a study region may output into non-local water catchments and have little influence over local ice dynamics [57, 56].

To address these uncertainties related to melt input, it is useful to consider first simple environments where melt *can* be estimated with confidence, and where the coincident seismic response can be monitored. A representative field site would be absent of englacial and subglacial drainage systems where added uncertainty from meltwater storage is avoided. In such a case, meltwater production and availability may be restricted to supraglacial sources that can be monitored more easily, or described with physics-based models.

Taylor Glacier in the McMurdo Dry Valleys of Antarctica provides a close analog to this idealization. Here, cold ice temperatures ($-17\,\mathrm{C}^\circ$) prevent liquid water from being sustained englacially or subglacially. Further, deposition from snow is effectively absent and surface ablation dominantly occurs through sublimation, thereby removing supraglacial

meltwater sources [70]. Meltwater generated on the ice surface and within the shallow subsurface during brief melt seasons is confidently estimated using a surface energy balance model calibrated from meteorological observables [71]. Seismic sources typical to temperate glacial environments are also absent at Taylor Glacier: basal sliding is restricted to motion by viscous creep [90], and slow ice-flow rates ($\leq 10\,\mathrm{m a^{-1}}$) prevent surface crevasses from forming and sustaining water, or acting as nuisance sources of seismic "clutter". Cumulatively, Taylor Glacier provides a favorable opportunity for determining how water-activated deformation mechanisms in cold, dry ice first respond to hydraulic forcing.

The hydrological system present in the ablation zone of the Western Greenland Ice Sheet provides a counter-example to those present in Dry Valley glaciers. Here, large volumes of meltwater are sustained on the ice sheet surface in supraglacial lakes. These lakes play an important role in establishing conduits for lubricating seasonal melt water to reach the bed of the Greenland Ice Sheet via drainage. Further, they are likely to drain earlier and more frequently as the the lake-forming ablation zone expands further inland [11] in future climate warming scenarios. At present, it is therefore first important to establish how icequake activity evolves over the summer melt season, before and after the establishment of newly formed moulins. It is particularly important to capture the seismic expression from *early*-season lake drainages, since rapid lake-water input is more capable of overwhelming the relatively inefficient subglacial drainage system, and influencing local ice dynamics. Current monitoring strategies within the lake-forming region that have captured some earlier drainages have involved acquisition of GPS or remote sensing (satellite) data. Therefore, virtually any icequake observables collected near these lakes will be novel.

1.5 Summary and Content of Following Chapters

Several meltwater-activated forcing mechanisms (including refreezing and uplift) are capable of fracturing glacial ice. The elastic or transient nature of this fracturing makes seismic monitoring an effective tool for detecting and localizing these events. Processes that drive such seismogenic fracturing are likely inactive in the absence of meltwater. Each process I have considered can occur in cold polar ice, and must be considered when interpreting geophysical (e.g., seismic) data. Identifying these processes is important, as they each

comprise a meltwater response mechanism that potentially enlarges or creates additional meltwater pathways.

The three following chapters proceed by establishing initial icequake response to meltwater from dry initial conditions in Antarctica, to the almost impulsive input from supraglacial lake drainage in Western Greenland. Chapter 2 describes melt-triggered englacial or subglacial fracture events that occur near the terminus of Taylor Glacier. Chapter 3 summarizes coincident surface fracture and extensional flow observed on $\sim$ 1km thick ice, where strong feedbacks between supraglacial and subglacial hydrological environments are complex. Chapter 4 provides a bound on the observability of basal icequakes from Greenland, and explores long-range detection of glacial earthquakes. Chapter 5 discusses how the observations in the preceding chapters cumulatively provide insight into hydrological surface-bed coupling in glaciers, and how this coupling is observed through relative changes in seismicity.

Three appendices treat the technical aspects of data analysis that are frequently referenced within Chapters 2 - 4. Appendices A- B include quantitative descriptions of the statistical processing methods I developed to improve seismic detection capability in noisy glacial environments. Appendix C includes a resonance analysis of geophone-installation systems destabilized by melt-out in ablation zones.

Figure 1.4 provides a brief summary of the prevalent thesis contents using a word cloud.

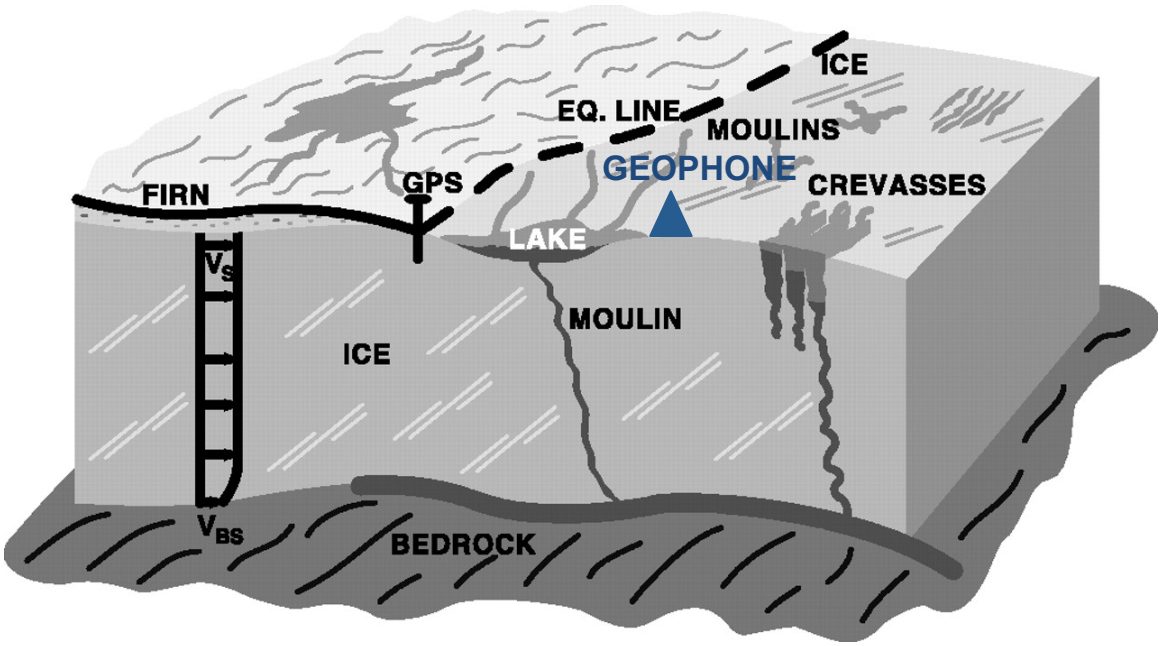

Figure 1.1: A cartoon illustrating a typical ice sheet hydrological system, including GPS and geophone instrumentation (*modified from Zwally, H.J., Abdalati, W., Herring, T., Larson, K., Saba, J. and Steffen, K. (2002). Surface melt-induced acceleration of Greenland Ice Sheet flow. Science, 297, 218-221*).

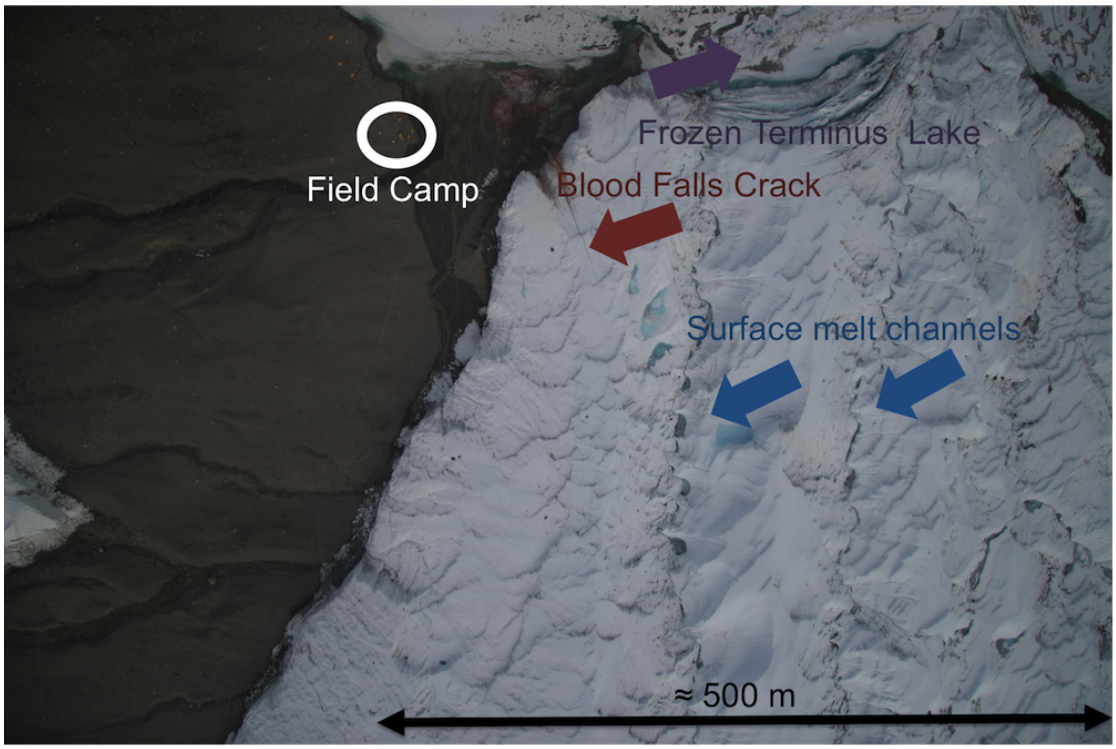

Figure 1.2: Taylor Glacier is a dry-based, polar glacier in the Taylor Valley, ANT (−77.723°, 162.259°). It terminates at the frozen shore of Lake Bonney. Despite precipitation rates below 10 cm, and cold ice (−17C°) melt channels have formed through thermal erosion along the last 2 km of the terminus and carry surface meltwater to englacial, subglacial, and terminus catchments. Meltwater triggers ice quakes near the Blood Falls crack by hyrdofracture, or cracking through confined, volumetric-expansion upon freezing at depth (*Image courtesy of Jack Holt*).

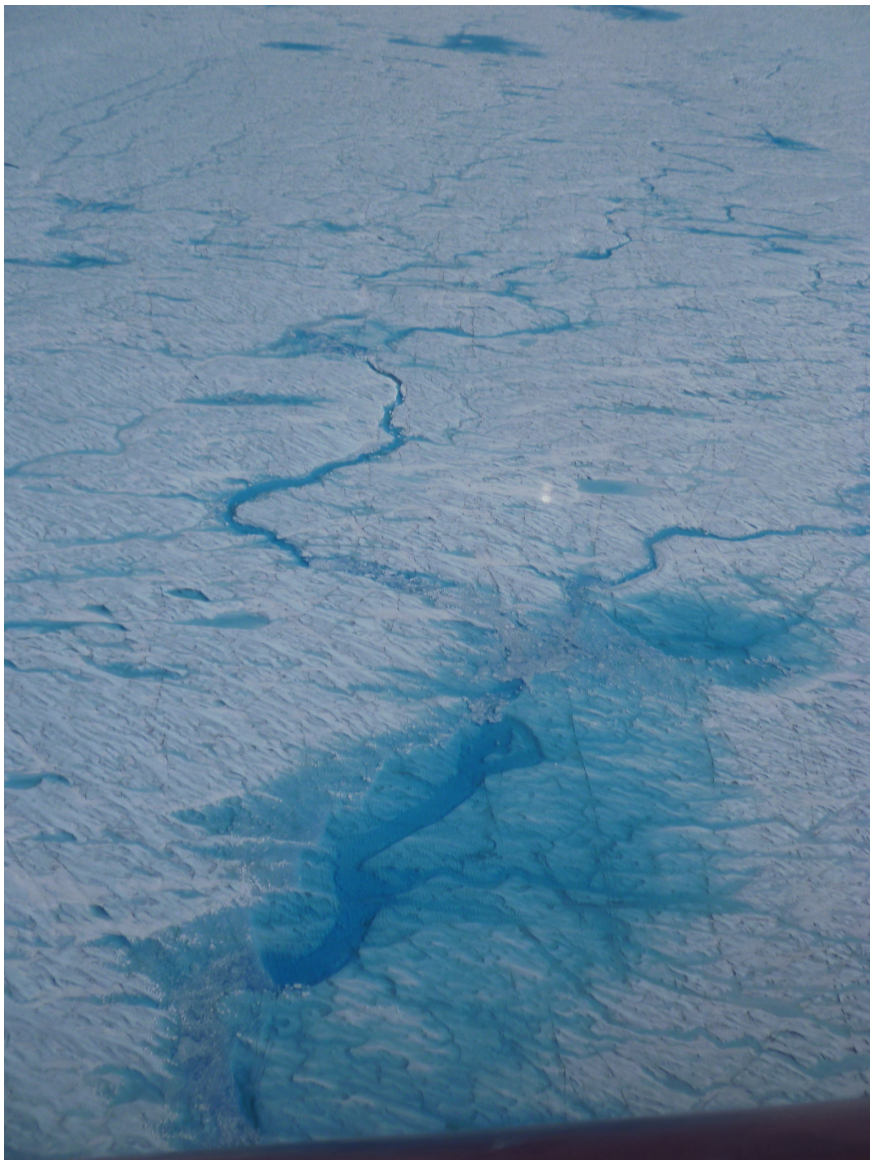

Figure 1.3: A $\sim$ 1 km (lateral extent) supraglacial lake within the ablation zone of the Western Greenland Ice Sheet. A water-filled crevasse is visible on the lake bottom. If the hydrostatic stress from water weight is sufficient to overcome lithostatic weight from the overlying ice plus any compressive stresses present during flow, the crevasse may propagate to the bed and thereby drain the lake water (*Image courtesy of Bjorn Johns.*)

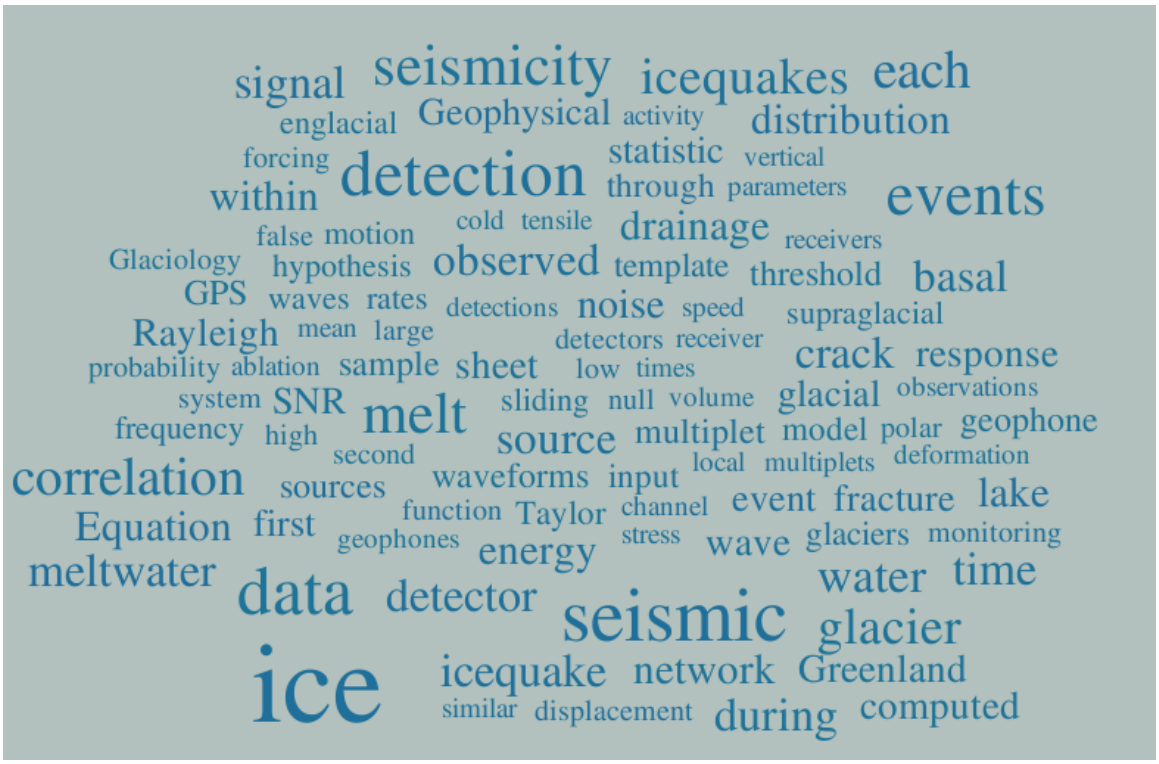

Figure 1.4: A word cloud illustrating the common topics treated in the subsequent chapters. The content was generated by Word it Out, at url: `http://worditout.com/`.

Chapter 2

SEISMIC MULTIPLET RESPONSE TRIGGERED BY MELT, TAYLOR GLACIER, ANTARCTICA

I would like to acknowledge the contributing authors to this chapter of my thesis. They include, in order of contribution: Erin C. Pettit, Matt Hoffman, Andrew G. Fountain, and Bernard Hallet. This chapter was originally published together with Appendix B as Carmichael et al. [2012] [21].

2.1 Abstract

Meltwater input often triggers a seismic response from glaciers and ice sheets. It is difficult, however, to measure melt production on glaciers directly, while subglacial water storage is not directly observable. Therefore, we document temporal changes in seismicity from a dry-based polar glacier (Taylor Glacier, Antarctica) during a melt season using a synthesis of seismic observation and melt modeling. We record icequakes using a dense six-receiver network of three-component geophones and compare this with melt input generated from a calibrated surface energy balance model. In the absence of modeled surface melt, we find that seismicity is well-described by a diurnal signal composed of microseismic events in lake and glacial ice. During melt events, the diurnal signal is suppressed and seismicity is instead characterized by large glacial icequakes. We perform network-based correlation and clustering analyses of seismic record sections and determine that 18% of melt-season icequakes are repetitive (multiplets). The epicentral locations for these multiplets suggest that they are triggered by meltwater produced near a brine seep known as Blood Falls. Our observations of the corresponding p-wave first motions are consistent with volumetric source mechanisms. We suggest that surface melt enables a persistent pathway through this cold ice to an englacial fracture system that is responsible for brine release episodes from the Blood Falls seep. The scalar moments for these events suggest that the volumetric increase at the source region can be explained by melt input.

2.2 Introduction

Seismic monitoring has been successfully applied to the detection and interpretation of melt-triggered icequakes in both glaciers and ice-sheets. This success is largely due to high sample rates that seismic instruments provide for observing brittle ice deformation that cannot be obtained with other instrumentation. In particular, seismic networks provide improved detection thresholds over single seismometers and the necessary spatial coverage for estimating observables such as icequake hypocenters and focal mechanisms. This capability is important for characterizing the response of glacial ice to meltwater. This is because meltwater is observed to trigger glacial faulting [179], basal stick-slip sliding [180], and rapid fracture events [138, 32] from coincident releases of microseismic energy. However, direct comparison between meltwater availability and seismic observations presents challenges, especially at near-freezing or sub-freezing temperatures. These challenges include quantifying water storage in firn [45], observing subsurface melt [105], and discriminating between sublimation and surface melt [71]. We suggest that improving our ability to quantify meltwater production is necessary to bound the influence it has on ice deformation. In this work, we therefore study a glacial regime (Taylor Glacier, ANT) in which no firn is present, meltwater can be confidently modeled, and seismic monitoring is available to estimate icequake activity and characteristics. We present evidence that even very small melt rates on cold glaciers ($\leq 1.2\,\mathrm{mm\,hr^{-1}}$) produce a response that is qualitatively distinct from melt-free conditions, and may trigger relatively large englacial fracture events where liquid water was not expected to exist. Our results follow from a novel network-based processing methodology that we have developed for detecting repeating icequakes and describe here.

2.3 Polar Glacier Background

Cold glaciers and temperate glaciers are distinguished by their temperature profiles. In cold glaciers, interior ice is uniformly below its pressure melting point (PMP), whereas temperate glaciers are composed of ice at or very near the PMP throughout. Cold and temperate glaciers also differ in both the hydrological forcing they receive from their environments and their response to this forcing. In temperate glaciers, englacial and subglacial water

pathways that transmit water are transient in morphology and persistence due to frictional melting from variable water flow. Variable water input can also produce subglacial pressure pulses that accelerate basal sliding and cause rapid creep opening or closure of subglacial cavities that generate icequakes [138, 178, 157]. Comparatively, deformation rates in cold ice are significantly lower. Below -10^{o}C, the activation energy for creep decreases by more than half, and interstitial water that facilitates grain-boundary sliding is less abundant [28]. In cold glaciers, lower water availability and ice flow rates result in suppressed basal sliding and lower crevasse density compared with temperate glaciers [76]. Thus, hydrological forcing may be absent except during brief periods in the melt season when hydrologically-driven ice fracture may permit some surface-to-englacial water input [14].

Consequently, the deformation processes that are triggered by persistent englacial water passage and storage that produce seismic emissions in temperate glaciers may not be present in cold glaciers. Our interest here is to determine which processes *are* observed during the introduction of water to an initially dry, cold glacier by interpreting icequake emissions produced during a brief melt season. We propose that it is necessary to study a setting where meltwater and basal sliding are initially absent, and subsequent surface melt can be adequately estimated. The melt-induced seismic response of the glacier from dry initial conditions will then provide a sensitivity test of exposure to surface melt. This test would address two primary questions: First, "are there initially absent seismic processes that are triggered by melt input?", and second "are these events indicative of significant changes in the glacier's dynamics?"

2.4 Study Area

Glaciers in the McMurdo Dry Valleys are representative of an extreme case of cold, polar glaciers due to the desert environment that they occupy [44]. Among these is Taylor Glacier, which enters Taylor Valley as an outlet from the East Antarctic Ice sheet and terminates at the western lobe of the perennially ice-covered Lake Bonney (Figure 2.1). The mean annual and summer temperatures (respectively -17° C and -3° C) are consistent with a cold environment with limited meltwater input that we require for a study site. Ice thick-

nesses in the terminal 2 km range from ~ 30 m at the terminus ice cliffs, to ~ 200 m along the centerline. Prominent features of the glacier include a pair of meltwater channels that form 7 km upstream and deepen along flow, reaching ~ 25 m near the terminus. During the summer months, micro-climatic conditions within these channels favor melt over sublimation, and cause supraglacial water flow [79]. Observed melt is also produced from calving ice cliffs $20 - 35$ m high at the ablation zone terminus. Basal ice temperatures recorded near the terminus ($-17°$C) suggest that Taylor Glacier is frozen to its substrate, and most of its motion is accommodated by internal creep in the ice and a debris-rich basal ice layer a few meters above the bedrock [183, 141]. A force balance conducted several kilometers up glacier [90] further suggests that no basal motion is required to explain surface speeds. Taylor Glacier is the site of Blood Falls, an anomalous iron-rich seep that flows episodically from the northern end of the terminus. The seep originates from a cyroconcentrated pocket of brine that became isolated during a coupled recession of the Ross Sea Embayment and uplift of Taylor Valley and has probably been trapped since the last major advance of Taylor Glacier into the valley 1.5 My ago [113]. Despite ice flow rates of $3 - 5\,\mathrm{m\,a^{-1}}$ at the terminus, the seep location has remained stationary with respect to bedrock, emerging from a set of long cracks. The primary crack present during December 2006 was surveyed with GPS (Thomas Nylen, personal communication) and measured ~ 80 m in extent, with strike $\cong 45°$ East of North. The maximum crack depth is unknown, but exceeds 15 m at some points. The separation distance between the crack faces increases with distance up ice, with a maximum of 6 m near the crack tip. Other surface cracks upstream of the primary crack run approximately parallel to it and catch summer melt that refreezes as blue ice. The brine emerges near the primary crack as an artesian well, indicating that the brine is pressurized at depth. For our purposes, the seep of Blood Falls is important as a surface-to-englacial pathway for meltwater.

2.5 Data Collection

The data were collected using PASSCAL-supplied geophones, three UNAVCO-supplied GPS receivers, three time-lapsed cameras, and a meteorological station (Figure 2.1). The cameras were mounted on the valley floor and recorded daily images of the northern ice cliffs

from early December 2005 through late March 2006 to document calving events. The meteorological station $(-77.70°, 162.13°)$ recorded 15 min averages of meteorological conditions that provide the data for surface energy-balance modeling [69]. Two continuous GPS stations were deployed on the ice, and a base station was deployed on a nearby benchmark. Data were collected at 30 sec sample rates during the summer for 24 hr per day, which was reduced to 1 hr during winter. The seismic network was deployed at the terminus region of Taylor Glacier from $2004 - 2006$. The data acquisition system (DAS) consisted of six triaxial, 4.5 Hz L-28 geophones equipped with Quanterra Q330 digitizers and solid state data loggers. Three geophones were installed on-glacier in 1 m pits, and the remaining three receivers were coupled to large rocks on the valley floor. Ground velocity was sampled at 200 Hz in continuous recording mode and stored on the data loggers, which were retrieved in November, 2006. For analyses that require displacement records, we deconvolve the cumulative instrument response from these data using a 10^{-12} m water level regularization. Because these DAS time tag data to compensate for linear phase shifts caused by internal filters [75, Appendix C], we found no need to correct for the acausality of the anti-alaising filter as described elsewhere [36].

2.6 Methodology

2.6.1 Quantifying Seismicity

To estimate the emission rate of icequakes (seismicity), we establish a criterion for counting icequakes that is based upon their observability. We first identify seismic events on each station using a standard detection methodology [139] in which we compute the ratio between a short-term average (0.5 sec) front window and long-term average (2.5 sec) back window of the squared-ground velocity (STA/LTA). When this STA/LTA ratio exceeds a threshold of 3.2, we declare a seismic event and retain a 10 second window centered on the pick time to prevent redundant event detections. We chose these picking parameters based upon a training procedure in which we compared the detector-generated picks with manual picks of waveforms from a subset of the data.

To count these events, we define a weighted scoring method that assigns a scalar to each seismic event according to its size, as determined by its detectability at each receiver. A large event should produce observable ground motion at each receiver and closely timed picks, whereas a small event might only be observable by a pair of receivers near the source. If the difference in detector pick times between any pair of receivers is less than or equal to the maximum expected s-wave travel time Δt (0.5 sec), we assign the event a count score $C \leq 1$ that depends upon the square-distance between those receivers. This agrees with empirical relationships between detectability and square-distance observed elsewhere [93]. Quantitatively, we define this count score using:

$$C(\Delta t) = \sum_{k,n=1}^{N} a_{kn} I_{kn} = \frac{\sum_{k,n=1}^{N} ||\mathbf{r}_k - \mathbf{r}_n||^2 I_{kn}}{\sum_{k,n=1}^{N} ||\mathbf{r}_k - \mathbf{r}_n||^2}, \qquad \beta \Delta t \leq ||\mathbf{r}_k - \mathbf{r}_n|| \,. \tag{2.1}$$

Here $\mathbf{r}_j$ is the position of receiver j, β is the s-wave speed in ice, and I_{kn} is the indicator function that is one if receivers k and n both detect an event within Δt, and zero otherwise. The weight function a_{kn} is illustrated with its dependence on network geometry in Figure 2.2. Events observed at every receiver are given a maximum count score of one, and events observed at only one receiver are discarded. For an N receiver network, this scoring provides $2^N - (N+1)$ possible combinations of receivers and event size (bins) that represent a distinct sub-network. Each event is counted only once. We assign each event in the observation period a value $C(\Delta t)$ and average the count scores by hour to obtain a time series of seismicity for each bin. The cumulative seismicity detected by any sub-network is computed by summing over the respective sub-network bins. Figures 2.3 (a, b) illustrate the total seismicity summed over all bins and compared with modeled surface and subsurface melt.

2.6.2 Icequake Hypocentral Inversion

To estimate hypocenters (source locations) for seismic events, we minimize the error between observed seismic wave arrival times and those computed using a geophysical model. We first measure waveform arrival times by manually picking phases for a subset of maximum count-score events ($C(\Delta t) = 1$). Waveforms which we include in our phase-picking procedure are

constrained in two respects. First, the amplitude and energy of the waveform data limit the number of events for which we can pick first arrivals within acceptable certainty above channel noise. Second, we do not pick first arrivals for those events that give sources exterior to the glacial ice, as determined by the relative order that the p-wave arrivals are first observed at the receivers. This quality control removes all but $\cong 150$ events recorded during the melt season between mid December and mid January. From these, we manually select the p-wave and s-wave arrival times, their polarity, and the coda wave duration time for each waveform.

To construct a velocity model of the terminus region of Taylor Glacier, we use a publicly available 2 m resolution DEM (http : //usarc.usgs.gov/lidar_dload.shtml) and manually digitized the terminus outline. Our velocity model uses seismic wave speeds of $3850\,\mathrm{m\,sec^{-1}}$ for p-waves, $1950\,\mathrm{m\,sec^{-1}}$ for s-waves in the glacial ice and $4800\,\mathrm{m\,sec^{-1}}$ for p-waves, $2900\,\mathrm{m\,sec^{-1}}$ for s-waves in the valley substrate, based partially upon a seismic survey conducted in Beacon Valley [151]. Because precise bed topography information is unavailable, the forward model is two dimensional (2-D) and does not include vertical velocity gradients as would be present at the ice-bedrock interface.

To produce each hypocenter estimate, we first perform a 2-D search over an epicentral grid 30 m below the local topography and minimize the error between the predicted p-wave arrival times $\mathbf{T}^P$ and observed p-wave arrival times $\mathbf{t}^{\mathrm{obs}}$ over this grid. We choose 30 m because it is consistent with the depth of the near-terminus ice and used p-wave arrivals because our s-wave pick times are too uncertain to provide adequate constraint for locations. We then use these locations to initialize an inversion for hypocenters $\mathbf{x}_0$ using a centered, scaled version of Newton's method. At each iteration, an update for the hypocenter $\Delta\mathbf{x}_0$ is computed:

$$\mathbf{r} = \mathbf{G}\mathbf{S}^{-1}\Delta\mathbf{x}_0, \tag{2.2}$$

where the centered residual and centered Jacobian matrix components are:

$$r_k = t_k^{\mathrm{obs}} - \left\langle \mathbf{t}^{\mathrm{obs}} \right\rangle - \left(T_k^P - \left\langle \mathbf{T}^P \right\rangle\right), \quad G_{kn} = \frac{\partial T_k^P}{\partial x_{0n}} - \left\langle \frac{\partial T_k^P}{\partial x_{0n}} \right\rangle$$

and the scaling matrix is:

$$\mathbf{S} = \operatorname{diag}\left(\left|\left|\mathbf{G}_1\right|\right|, \left|\left|\mathbf{G}_2\right|\right|, \left|\left|\mathbf{G}_3\right|\right|\right).$$

$\langle \bullet \rangle$ denotes averaging a column vector over its rows, x_{0n} is the n^{th} hypocentral parameter, and $||\mathbf{G}_i||$ is norm of the i^{th} column of Jacobian matrix $\mathbf{G}$. The centering (subtraction of the mean from the linearized equations) removes the source origin time as an inversion parameter, while scaling by $\mathbf{S}^{-1}$ normalizes the columns of the Jacobian matrix, thereby reduces it's rank, and improves the problems' conditioning [55, Section 4.1]. The epicentral locations obtained from the inversion are illustrated in Figure 2.5. To compute the confidence region associated with a particular hypocenter $\mathbf{x}_0$, we perform $\sim 5 \cdot 10^3$ Monte Carlo inversions using 0 sec mean, $(0.01\,\text{sec})^2$ variance Gaussian noise added to the predicted travel time for each receiver. The resulting inversions provide a sequence of misfit vectors. The squared-norm of these misfit vectors form an empirical probability density function for the uncertainty in the squared travel time that we then normalize and integrate to obtain a cumulative density function (Φ) for the squared residual. $\Phi^{-1}(0.95)$ then provides the 95% confidence region $R(\mathbf{x}_0)$ for the hypocenter $\mathbf{x}_0$:

$$R(\mathbf{x}_0) = \left\{ \mathbf{x}_0 + \delta\mathbf{x}_0 : \left|\left| \mathbf{T}^P - \mathbf{t}^{\text{obs}} \right|\right|^2 \leq \Phi^{-1}(0.95) \right\}. \tag{2.3}$$

2.6.3 Multiplet Event Detection and Clustering

Multiplets are distinct, repeating seismic events that produce nearly identical records of ground motion. They provide an observation of repeated stress release from the same source region and from similar source mechanisms [64]. To quantify the similarity between multiplet icequake waveforms, we implement an network-based measure for correlation between events that uses ground motion recorded by all receivers simultaneously. This approach is advantageous for identifying pre-processed multiplet waveforms with small time-bandwidth products (low degrees of freedom) because of the potential for increased detection capability [181]. A sample of ground velocity $\mathbf{v}(t)$ from an N-receiver network is provided by a $3N$ channel record section that we define as:

$$\mathbf{v}(t) = \begin{bmatrix} v_{1e}(t) & v_{1n}(t) & v_{1z}(t) & v_{2e}(t) & v_{2n}(t) & v_{2z}(t) & \dots & v_{Nz}(t) \end{bmatrix} \quad t \in T. \tag{2.4}$$

Here $v_{kl}(t)$ symbolizes the ground velocity for receiver k in geographical direction l, sampled over time window T. In practice these are samples of ground velocity recorded over T seconds, arranged as $3N$ column vectors in a matrix so that $v_{kl}(t)$ symbolizes $\mathrm{col}\,[v_{kl}(t_0), v_{kl}(t_1) \cdots, v_{kl}(T)]$. Inoperable rows (channels) are down-weighted or deleted from the matrix. If $\mathbf{v}(t)$ and $\mathbf{w}(t)$ are each distinct T second record sections observed at the network, we define their normalized cross correlation to be:

$$\rho \triangleq \max_{\tau} \frac{\langle \mathbf{v}(t), \mathbf{w}(t+\tau) \rangle}{||\mathbf{v}(t)||\,||\mathbf{w}(t)||} = \max_{\tau} \frac{\langle \mathbf{v}(t), \mathbf{w}(t+\tau) \rangle_F}{||\mathbf{v}(t)||_F ||\mathbf{w}(t)||_F}, \quad -T \leq 2\tau \leq T. \tag{2.5}$$

Equation A.33 assigns a functional on a product space [156, p. 78], where $\langle \bullet, \bullet \rangle_F$ and $||\bullet||_F$ respectively denote the Frobenius inner product and norm. ρ is bounded by ± 1 and is not equivalent to the mean channel correlation as used by Gibbons [52]. If two sources are separated in distance but are otherwise identical, the differential arrival times between the N receivers cause misalignment between the record sections $\mathbf{v}(t)$ and $\mathbf{w}(t)$ so that $|\rho| < 1$. Thus, ρ near $+1$ requires similar waveforms and source locations, but does not require intra-receiver coherence [52]. An explicit relationship between separation distances of multiplet sources and their displacement field cross-correlation is provided elsewhere [155]. To detect multiplets, we design an unsupervised, partition-based clustering algorithm that groups similar record sections using Equation A.33 with null-weighted horizontal channels. This algorithm operates in two stages. First, it identifies multiplets from an icequake detection catalog (stage 1), and then builds template record sections from these multiplets to search a larger catalog ("database") of record sections for additional events (stage 2). In stage 1, a group of two or more record sections is assigned to a set S (cluster) if the correlation between every possible pair of record sections within S and that group exceeds a threshold of $\rho_0 = 0.65$. This threshold value was found to give negligible false alarm probabilities for waveforms with small time-band-width products [63]. Because high correlation requires similar source mechanisms and hypocenters, the cluster sets S are therefore populated with record sections that come from multiplet events. The record sections within each cluster S are then coherently aligned (to subsample precision) and stacked to form record section templates. In stage 2, each catalog template is correlated with record sections in the database as a match-filtering operation. Additional record sections are then added to the

pre-exising clusters if they correlate above $\rho_0 = 0.65$ with a template. During both stages, ρ is computed in the frequency domain to sub-sample precision using the Fourier shifting-property. Stage 1 of our algorithm differs from typical complete-link clustering methods in that proximity between clusters is computed over all possible pairs. Stage 2 of our method differs from other clustering algorithms in seismology (e.g. [164]) in two important respects. First, we process record sections as the signals rather than the single traces as the signals; second, the templates are built automatically from mutually correlated sets, so no observer bias is introduced through manual template selection. We provide quantitative details of our methodology in the Appendix.

2.6.4 Analysis of Icequake Moment

Seismic moment tensors provide a description of the focal mechanism of icequakes and a measure of their strength. Physical sources like cracks or faults often are modeled as combinations of force-couples using the seismic moment tensor $\mathbf{M}$ which also governs the geometry of the far-field seismic displacement [4, Equation 4.97]. The magnitude is characterized by the scalar moment which is defined by the moment norm, $M_0 = \frac{1}{\sqrt{2}} ||\mathbf{M}||_F$. In practice, M_0 is estimated by contracting the displacement with the p-wave direction $\hat{\mathbf{e}}_P$ at the free-surface and integrating over time [13],

$$\int_0^{t_P} \mathbf{u}\left(\mathbf{x}, t\right) \cdot \hat{\mathbf{e}}_P\left(\mathbf{x}\right) \mathrm{d}t = \int_0^{t_P} \frac{\dot{M}_0\left(t\right) F_C}{4\pi r} \frac{\hat{\mathbf{\Gamma}}^{\mathrm{T}} \hat{\mathbf{M}} \hat{\mathbf{\Gamma}} \left(\hat{\mathbf{e}}_P\left(\mathbf{x}\right) \cdot \hat{\mathbf{e}}_P\left(\mathbf{x}\right)\right)}{\sqrt{\varrho(\mathbf{x})\varrho(\mathbf{x}_0)\alpha(\mathbf{x})\alpha^5(\mathbf{x}_0)}} \mathrm{d}t \tag{2.6}$$

where t_P is the p-wave duration, $\mathbf{u}\left(\mathbf{x}, t\right)$ is the observed displacement at the receiver, $\hat{\mathbf{e}}_P\left(\mathbf{x}\right)$ is the p-wave direction of displacement at the receiver, r is the source-to-receiver distance, F_C is the free-surface amplification, ϱ is medium density (ice or bedrock), $\mathbf{x}_0$ is the source position, $\mathbf{x}$ is the receiver position, α is p-wave speed, $\hat{\mathbf{\Gamma}}$ is the vector pointing from the source to the receiver, and $\hat{\mathbf{M}}$ is the normalized moment tensor. The integrated moment rate $\dot{M}_0$ gives the desired scalar moment M_0:

$$M_0 = \frac{4\pi r\, \Omega}{F_C} \frac{\sqrt{\varrho(\mathbf{x})\varrho(\mathbf{x}_0)\alpha(\mathbf{x})\alpha^5(\mathbf{x}_0)}}{\hat{\mathbf{\Gamma}}^{\mathrm{T}} \hat{\mathbf{M}} \hat{\mathbf{\Gamma}}} \tag{2.7}$$

Here Ω is the area under the attenuation-corrected p-wave seismogram. Physically, M_0 is proportional to either total slip along the crack face or local volume change from crack face

opening. In the case of planar ice crack (fault) faces, $M_0 = \mu \bar{u} A$, where μ is the shear modulus of the faulting ice, $\bar{u}$ is the fault-averaged net slip, and A is the faulted area. If the source is volumetric, the total confined volume change δV at the source region from an icequake is related to the scalar moment of that icequake according to [134, Equation 1]:

$$M_0 = \delta V \left(\lambda + 2\mu\right), \tag{2.8}$$

Elastic parameters for ice are $\lambda \cong 6.5\,\text{GPa}$, $\mu \cong 3.5\,\text{GPa}$, at $-16^\circ\,\text{C}$ [49]. An alternative expression $M_0 = \Delta V \left(\lambda + \frac{2\mu}{3}\right)$ is frequently used in place of Equation 2.8, where $\Delta V \approx 2\delta V$. However, ΔV gives the volume change in stress-free conditions, whereas confinement of buried source prevents the true strain from attaining a stress-free state [4]. We therefore use Equation 2.8 to compute δV. The moment tensor may further be interpreted by decomposing it into a sum of independent tensors that are orthonormal under $\frac{1}{\sqrt{2}} \langle \bullet, \bullet \rangle_F$ and represent different source types. The component of $\mathbf{M}$ attributable to source type "I" (such as tensile opening) with unit moment tensor $\hat{\mathbf{M}}_\text{I}$ then has scalar moment defined by $M_0^{(\text{I})} = \frac{1}{\sqrt{2}} \left\langle \mathbf{M}, \hat{\mathbf{M}}_\text{I} \right\rangle_F$.

2.6.5 Estimating Surface Melt Production

It is difficult to measure surface meltwater production on glaciers directly. Total ablation can be measured over finite time periods, e.g. using ablation stakes, but this method includes contributions from both sublimation and melt. Although melt composes the majority of ablation on temperate glaciers, sublimation is a substantial fraction of ablation on Taylor Glacier [79, 71]. This makes ablation-stake measurements of melt inaccurate. Furthermore, melt can occur below the surface in the upper 50 cm through solar heating of the ice while the ice surface remains frozen, a process which cannot be detected with traditional ablation measurements [69]. Therefore, to estimate meltwater production from the surface of Taylor Glacier, we use a one-dimensional surface energy balance model that has been calibrated against ablation measurements and tested using ice temperature measurements in the upper meter [71, 105]. The surface energy available for melt is computed as the residual from balances between net shortwave radiation, net longwave radiation, the turbulent heat fluxes of sensible and latent heat, and heat conducted into or out of the glacier. This surface energy

balance is coupled with a one-dimensional heat transfer equation that is used to calculate the heat flux through the glacier surface and includes a source term for solar radiation absorbed beneath the surface. The distribution of solar radiation with depth is determined by a spectrally-dependent extinction coefficient which is a function of the solar spectrum, ice surface albedo, ice density, and effective ice grain radius [19, 105]. The model's adjustable parameters include the aerodynamic surface roughness (which affects the magnitude of the turbulent heat fluxes, and therefore sublimation), the effective ice grain radius (which determines the distribution of net solar radiation with depth), and the thickness of the surface layer (which determines the fraction of net radiation included in the surface energy balance).

We apply the model using an hourly time step with meteorological forcings of air temperature, relative humidity, wind speed, incoming solar radiation, surface albedo, incoming longwave radiation, and atmospheric pressure. Model outputs at the surface include ice surface temperature and the ablation components of sublimation and melt, and model outputs for the subsurface ice column include temperature, melt flux, and water fraction. The model is applied at a point (162.237°E, 77.726°S) and calibrated to 14 years of summer ablation measurements averaged from three ablation stakes located within 0.5 km [44]. We consider this location representative of the near horizontal surface of the terminal 2 km of Taylor Glacier, exclusive of the large channels and ice cliffs, which have substantially higher melt rates [79], and Blood Falls, which has substantially lower surface albedo and likely higher melt rates. Local meteorological forcings are obtained by applying the quasi-physically based meteorological distribution model MicroMet [104] from observations at Taylor Glacier and Lake Bonney meteorological stations. The calibration at the Taylor meterological station yielded an aerodynamic surface roughness of 0.2 mm, effective ice grain radius of 0.08 mm, and surface layer thickness of 1 cm, comparable to those at the Taylor Glacier meteorological station, 2 km upglacier [71]. We perform a visual test on surface melt production using the daily images obtained from the time-lapse camera system. During days surface melt occurs in the model, water is visible as a stream around the perimeter of the ice cliffs. Similarly, the stream volume diminishes during days modeled melt is absent. We therefore consider the model qualitatively representative of conditions near the ice cliffs as well. The time

evolution of modeled melt is illustrated in Figure 2.3 (a).

2.7 Observations

2.7.1 Seismicity

Figure 2.3 documents a comparison between modeled melt and an hourly time series of the cumulative seismicity computed from Equation 2.1. Surface melt was confined to brief, sub-daily events in December and January, with peak melt rates $\leq 1.2\,\mathrm{mm\,hr^{-1}}$. Subsurface melt was also present within the ice column at shallow depths ($\leq 50\,\mathrm{cm}$) both December and January, with and without coincident surface melt (Figure 2.3(a)). We estimate that a fraction of the water produced in the subsurface over the season ($\cong 1.8\,\mathrm{cm}$) drained through intergranular veins or subsurface cracks, with drainage rates $\leq 0.5\,\mathrm{mm\,hr^{-1}}$. Comparatively, the surface melt was abrupt in timing and resembles a binary process as represented in Figure 2.3(b). The total seismicity was composed of two qualitatively distinct components that differ with the coincidence of modeled melt. The dominant features of the melt-absent seismicity include a diurnal component in timing and amplitude with minimum emission rates (background rates) that are near zero during the local daytime (Figure 2.4). The dominant features of the melt-coincident seismicity include a non-zero background rate that is superimposed on a reduced diurnal component with a lower overall average count rate (Figure 2.3(b)). We next compare the total seismicity with the seismic events that are sufficiently large to result in a unit-count score (Figure 2.3(c)). The unit-count score events are similar to the melt-coincident seismicity in both timing and localization. We then compare these signals with the subset of seismic events that are observed exclusively on ice-based stations (the ice sub-network) and the subset observed exclusively on land-based stations (the ground sub-network) in Figure 2.3(d). The ice sub-network seismicity exhibits a coincidence with the unit-score seismicity, while the land sub-network seismicity exhibits a coincidence with the melt-absent component of the total seismicity. Thus the seismic events observed exclusively on the ice sub-network are active during the melt season, and the events observed exclusively on the ground sub-network are active from late January through the remainder of the observation period, with little overlap. We observed no change in GPS

speed at any time.

2.7.2 Icequake Locations

We implement the inversion scheme summarized in Section 2.6.2 using travel times from our data set and assemble a catalog of the corresponding icequake hypocenters. The dominant feature present in this catalog is a concentration of epicenters within a "cloud" just west and nearly parallel to the Blood Falls crack (Figure 2.5(a)). The icequake depths are poorly constrained from the tight elevational coverage of the network and we do not interpret them. Using Equation 2.3, we compute the 2D, 95% confidence region for a prescribed hypocenter $\mathbf{x}_0$ coincident with the Blood Falls crack tip 30 m below the surface of the ice (Figure 2.5(b)). Approximately $\sim 75\%$ of all located events are interior to this confidence region. Additional icequakes were located near an actively calving cliff face East of receiver CINDY, and in the topographical depression of the Northern melt channel. In addition to the confidence region, we compute error ellipsoids for each inversion to estimate the individual location uncertainties and illustrate the distribution of the ellipsoid axes lengths in Figure 2.6.

2.7.3 Multiplet Clustering

We identified multiplets from three distinct detection catalogs and database combinations. In the first case, we cluster record sections from the phase pick catalog that we used to locate icequakes. We determine that these events comprise 16 multiplet clusters of varying size containing a total of 85 muliplets. $\geq 81\%$ of these located multiplets are interior to the confidence region and are distinguished by colored epicentral markers in Figures 2.5(a,b). The most populous of these multiplets is composed of 24 events (blue), the second and third most populous clusters are respectively composed of 15 and 9 events (red and green), and the remainder of the multiplet populations are composed of between 7 and 2 events (orange). A residual ~ 30 events had no cluster membership in the phase pick catalog (pale gray). The velocity seismograms for the three most populous clusters are documented with the same color assignment in Figure 2.5(c). Each waveform is < 1 second in total duration, with poor intra-network waveform correlation on average ($\rho \sim 0.5$) relative to the intra-

multiplet record section correlation ($\rho \geq 0.65$). There *is* significant intra-multiplet variance in the network-averaged root-mean-square amplitude of the seismogram displacements that is shown in Figure 2.5(e). We rotate the displacement seismograms for the most populous cluster into a local free-surface and refraction-corrected (non-orthogonal) p, sv, sh wave system and illustrate the p-wave component in Figure 2.5(d). The p-wave first motions for each receiver are upward. Figure 2.7 demonstrates that p and s wave separation on station JAN and GREG is more pronounced relative to the other receivers due to greater receiver-to-source distance, while channel malfunctions on station MARSH lead to an ambiguous rotation.

In the second case, we assemble templates from record section stacks in the phase pick catalog and cluster over all detected unit count-score events from the entire detection database over the observation period. This results in a 3.7-fold gain in the total multiplet population, with a peak multiplet emission rate of ~ 45 events per day (Figure 2.8, top). The largest gain in detected multiplets comes from the the most populous and third most populous cluster templates. We illustrate the detection history of these multiplets in Figure 2.8, (top) where we have maintained the color coding from Figure 2.5.

In the final case, we assemble templates obtained from cluster catalogs that are computed on each separate day. We again cluster over the detection database for the entire observation period. This recovers an additional 936 events from 205 multiplet templates. These multiplets contain 22% of unit-count score detections, 18% of all unit-count score melt season detections, and an additional 5% gain in detections from outside the melt season period (188 new events). The detection history is illustrated in Figure 2.8 (bottom).

2.7.4 Moment Calculations

We compute the scalar moment M_0 for icequakes interior to the 95% confidence interval pictured in Figure 2.5(b). We are confined to use station JAN exclusively to compute moment with Equation 2.7 within the confidence we require, however. Differential arrival

times between p- and s-waves are too small or uncertain, relative to the sample interval, to provide adequate measurements of Ω on other receivers. There are additional sources of uncertainty in our application of Equation 2.7 that are difficult to quantify; for example, the quality factors that we use for attenuation correction ($\sim 10^2$) are not well known, the p-wave pulse may include scattered arrivals that we unintentionally integrate with Ω, and $\hat{\mathbf{\Gamma}}$ and F_C depend on uncertain hypocentral depths. We therefore compute icequake magnitudes using the moment-magnitude scale $M_w = \frac{2}{3}\,(\log_{10} M_0 - 9.1)$ [89] to evaluate the reasonability of our M_0 estimates. We find that $-0.9 \leq M_w \leq +0.3$, comparable to smaller stick-slip events on alpine glaciers [180], and within expectation.

2.8 Interpretations

Figures 2.3(a, b) document a transition in seismicity during melt input that suggests meltwater is the primary trigger for increasing background emission rates, while its absence seems to increase the diurnality of emissions and decrease background rates. We interpret the coincidence of the unit count score (large) seismic events with glacial icequakes in Figures 2.3(c, d) to indicate that the large events without inverted locations are also glacial in origin, and therefore reject the possibility that they are due to a source exterior to the glacier, such as lake ice. From the timing of melt relative to icequake response, we conclude that large icequakes are triggered by meltwater input. Figure 2.3(d) further suggests that there are at least two different mechanisms for triggering smaller seismic events that are detected only on these sub-networks. One set triggers glacial icequakes, and the other drives seismicity exterior to the glacier, such as lake ice.

We next address the possibility that the diurnal signal is borne from noise that would mask waveforms and reduce detections. We estimate the statistics for 10^3, 30 sec noise sequences recorded on each receiver from dates uniformly distributed over the observation period and discard any within 30 sec of a known pick time. From these sequences, we observe that the noise is near-Gaussian and has no statistically significant fluctuation in variance that would reduce the STA of the detector. We conclude that observed seismicity is physical rather than a result of diurnal noise.

We propose that the diurnally responsive icequake sources that are active without melt include fracture of lake ice (and glacial ice to a lesser extent) through generation of thermal bending moments. These occur in thick sea ice [8] when thermal stresses near the surface induce bending moments that store significant strain energy. The release of that strain energy can cause large fracture events and microseismic emissions ($M_w \sim 0.2$) that are recorded as icequakes (Clifford Thurber, personal communication). This is more effective at lengthening large seismogenic cracks in ice compared to thermal diffusion, which is restricted to penetration depths of ~ 20 cm over a daily temperature cycle.

To evaluate this interpretation, we estimate the magnitude of thermally generated moments in the ice as a result of temperature increases, using a sinusoidally heated half-space thermal stress model [167, Equation 4-194]. This model does not include an advection term from interstitial water that may further warm the ice at depth. We compute the thermal bending moment by integrating the product the thermal stress and depth (moment arm) to a reasonable isothermal boundary [8, Equation 4]. Our parameters include a thermal skin depth of 0.17 m and an integration depth of 4 m for either the lake ice lower boundary or an isothermal depth for the glacial ice. The result gives $M_T = 4.25 \cdot 10^6\,\mathrm{Pa} \cdot \mathrm{m}$. We use data from [48] and compute an upper bound on the bending strength for glacial ice of $M_T = 3.0\,\mathrm{kPa} \cdot \mathrm{m}$ at $-5°\mathrm{C}$ for $10^{-5}\,\mathrm{sec}^{-1}$ strain rates. We conclude that thermal bending moments are sufficient for triggering fractures through 4 m of ice.

To determine if seismic energy from these events can couple into the ground, we compute the required size for an event required to be detectable by the land sub-network receivers. We compute an ice-to-water-to-ground net amplitude transmission coefficient and multiply this by the displacement amplitude from the integrand of Equation 2.6, where we use a value for F_C that has been averaged over the focal sphere [15]. We find that a fracture area-crack opening displacement product of $2.2\,\mathrm{m}^3$ will produce peak displacements over a detection threshold of 10^{-9} m for the p-wave that we determine from Figure 2.5(e). These dimensions are consistent with physically abundant fracture features on Lake Bonney. In

summary, we conclude that fracture of lake ice due to thermal bending moments may be observed at the ground based receivers.

Conversely, surface melt apparently triggers seismic events that are not sensitive to diurnal forcing and produces more steady emissions of icequakes. We propose the presence of interstitial melt creates a heat source upon freezing that maintains a more uniform ice temperature, thereby suppressing thermal bending moments and resultant icequakes.

We next evaluate the source of multiplet seismicity. Multiplets often result from repeated stress release within the same source region and produce high intra-multiplet record section correlation [63]. We quantify the prevalence of melt triggered sources for large icequakes as the number of multiplets temporally coincident with modeled surface melt. The epicentral locations for $\geq$ 75% of the multiplets that we identified in Figures 2.5(a,b) are spatially coincident with the confidence region centered on the Blood Falls crack tip. This spatial coincidence suggests that sources near the crack tip likely account for the most populous clusters from the phase pick catalog, with location variability due to typical pick errors. The detection history of multiplets that we obtained from clustering (Figure 2.8) demonstrates that additional icequakes ($\sim$ 230) also belong to these multiplet sequences and therefore likely share the crack tip region. The total number of these multiplets constitute about 7% of all unit count score events observed with the STA/LTA detector.

Waveforms from these multiplet sequences that are documented in Figures 2.5(c,d) and Figure 2.7 have traits common of microseismic events: arrivals are impulsive, intra-receiver coherence is low, and coda waves dominate the latter portion of the wave train. This is consistent with a short duration source-time function and strong scattering environment [122]. The motion of the direct p-wave is up and away from the source location at all receivers, as shown by the record sections in Figures 2.5(d) and 2.7. This uniform p-wave polarity is observed from other sources composed of volumetric or isotropic focal mechanisms [176, 86]. One source consistent with these focal mechanisms that will generate the observed multiplet first motions is the tensile crack.

While pure tensile cracking (mode I cracking) is sufficient for producing compressive p-wave displacements at the receiver locations, it is not necessary. A seismic source composed of a mix of fracture modes can also produce compressive first arrivals at the six receiver locations. To bound the possible modes leading to the observed polarities, we forward model the p-wave surface displacement resulting from a fracture source localized at the Blood Falls crack tip. We first compute motions using a description for whole space [4, Equation 4.97] and a suite of crack face displacement vectors that combine tensile with mode II (slipping) and mode III (tearing) fracture. To estimate the surface motion polarity at each receiver, we then correct for ice-to-ground refraction, surface amplification, and p-wave inclination at the free surface. Some results of this modeling are illustrated in Figures 2.9 and 2.10. Crack face displacements oriented more than 68° from the crack face normal result in insufficient tensile cracking that produces downward first motions at some receivers, inconsistent with observations. The least-isotropic moment tensor consistent with observations has a projection onto a mode-I unit tensor of $0.66 \cdot ||M||_F \approx \frac{1}{\sqrt{2}} \left\langle \mathbf{M}, \hat{\mathbf{M}}_{\mathrm{I}} \right\rangle_F$. This indicates that tensile cracking is the dominant mechanism for these icequakes, regardless of the possibility for other fracture modes. Figure 2.10 suggests that the crack face normal vector and displacement must be within 40° and 60° to match the observed relative seismogram amplitudes.

A second kind of source that is capable of producing the observed first motions is the volumetric expansion of a pressurized source of brine at depth, analogous to what is often observed in volcanic or geothermal systems with inflationary sources [86]. The surface channels of Taylor carry meltwater off-glacier and into Lake Bonney, thereby unloading the glacial substrate. Peak melt rates of $1.2\,\mathrm{mm\,hr^{-1}}$ over the glacier surface produce spatially-averaged peak unloading rates of $\dot{m}\varrho_W g \cong 12\,\mathrm{Pa\,hr^{-1}}$, where $\dot{m}$ is the melt rate in dimensions of length per time per unit area, ϱ_W is water density, and g is gravitational acceleration. [79] report melt rates in the channels to be 4.5 times that of measured melt rates on the flat ice surface, giving an upper bound for the peak unloading rate of $\dot{m}\rho_W g \cong 54\,\mathrm{Pa\,hr^{-1}}$. We compute comparable peak unloading rates of order $10\,\mathrm{Pa\,hr^{-1}}$ from atmospheric tide data supplied by the NSF McMurdo Dry Valley Long-term Ecological Research (LTER),

during December through January. We therefore consider the tensile crack model more likely, because the alternative requires the brine source to respond to changes in overburden comparable to that produced by atmospheric tides. Our estimates do not consider the effect of pressure gradients caused by changes in ice surface topography from melting, because the energy balance model implemented here is one-dimensional.

We therefore propose a physical model for melt triggered seismicity that produces the observed compressive first motions as follows. First, our model initial conditions impose that the Blood Falls crack system is under stress near the brine seep. This is required by the presence of the artesian well at the ice surface and indicates that the brine is under a pressure of at least $\varrho_B g H \geq 290\,\mathrm{kPa}$ to exceed ice overburden, where ϱ_B is brine density (which exceeds water density) and H is the local ice thickness. During the December-January melt season, surface and subsurface melt produced flows down-gradient toward the Blood Falls seep as input into the crack system. Any channel down-cutting that occurs englacially as proposed in temperate glaciers [45] and observed in the high arctic [14] would then increase the stress intensity factor of the crack by lengthening it. Any sustained water catchment within the crack would further increase the stress intensity factor through the additional hydrostatic stress. This, combined with the pressurized brine source, provides conditions favorable for hydrofracture [168]. Melt input would thereby promote hydrologically triggered fracture events that are then observed as icequakes. Once the melt production abates, inflow rates decrease, and englacial water at depth freezes quickly where the ice is cold (-17°C). However, some liquid water may persist at depth on wetted ice or rock surfaces as a thin film. The thermomolecular forces responsible for flow within the films have a net body-force equivalent that is proportional to the film-equivalent ice mass [33]. This proposed process can generate $\sim 2\,\mathrm{MPa}$ stresses in porous bed material and induce fracture [117]. We therefore suggest that the presence of this crack allows a persistent surface pathway for the Blood Falls source by acting as both a catchment for meltwater and site for bed fracture via ice segregation. A more focused seismic study is required to assess post-melt bed fracture as a source of seismicity, however.

Finally, we compare the volume change at the source region with melt input volumes. We first assume the icequakes from the crack region have similar, volumetric source mechanisms so that the moment is proportional to the volumetric increase and sum the cumulative scalar moment with Equations 2.7 and 2.8:

$$(\lambda + 2\mu)\,\Delta V = \sum_{k} M_0^{(k)} \tag{2.9}$$

From Equation 2.9, we compute a source volume change of $\cong 2.3\,\mathrm{m}^3$ at the source region. When we average this volume over the Blood Falls crack face dimensions ($80\,\mathrm{m} \times 15\,\mathrm{m}$), we measure a cumulative crack opening displacement of 2 mm. The melt rates modeled during this time exceed the cumulative water volume required to explain source-volume increase computed from Equation 2.9 (Figure 2.11). The relatively small displacements may explain why no obvious GPS speed-up is observed during the melt season in spite of icequake activity.

2.9 Synthesis

Our goal in conducting this study was to determine the response characteristics of a dry, polar glacier during the transition into a melt season when meltwater influences ice deformation. Our methodology consists of comparing passive seismic data that we process using network-based analyses with meltwater produced form a calibrated surface energy balance model. From our estimate of surface melt and interpretation of the icequake observables, we make three primary conclusions: first, very little meltwater initiates a mode of seismicity distinct from the diurnally responsive, dry, cold mode. The melt-driven mode is composed of comparatively few but large energy icequakes, with diminished response to diurnal forcing. Second, the response time at Taylor Glacier is effectively immediate, with most large icequakes triggered nearby the Blood Falls seep. Third, the first p-wave motions from sources indigenous to the fractured region are consistent with opening cracks. One implication of water triggered fracture in cold ice is that surface melt may reach the sub-freezing bed, and hence allow brief input of heat and mass to the cold basal interface. This does not seem to require the existence of persistent englacial water that exists in temperate ice, and has been observed in the Canadian arctic [14]. The velocities as determined from GPS show

no speedup above measurement noise (Figure 2.12); hence if meltwater does penetrate to the bed, no basal sliding likely takes place. A combination of melt input and a pressurized brine source below the seep may trigger sufficient crack tip propagation to allow persistent hydrological communication to the bed during the melt season. We propose that once the crack formed and enabled brine to escape, it acted as a catchment during melt seasons and induced further fracture through downcutting above pressurized brine, thereby allowing the crack to persist. In wetter conditions, other surface cracks may catch comparable water and create additional pathways to the surface. Thus, the singularity of the release point for the brine may be due to the low melt and deformation rate at Taylor Glacier. Thus, broader impacts of this study may include providing the subglacial-systems community an opportunity to assess the role of surface controls on the brine release episodes.

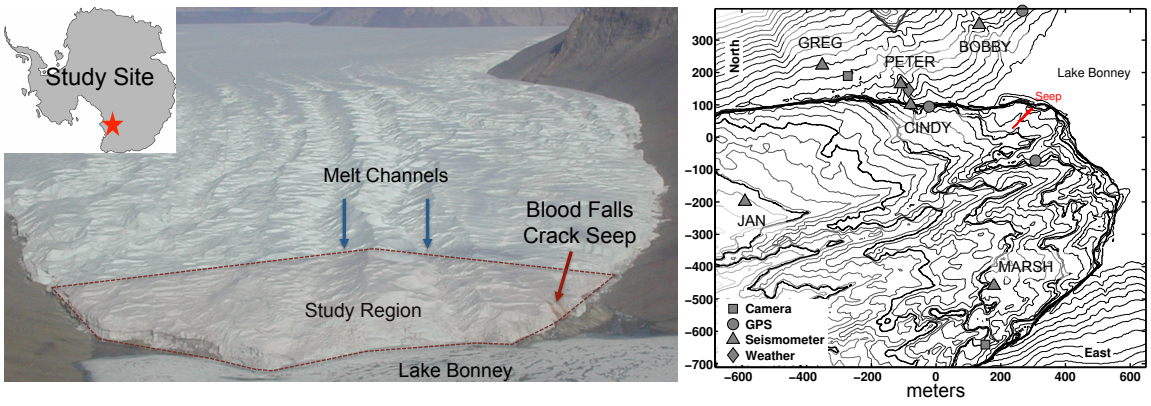

Figure 2.1: Taylor Glacier instrumentation consisted of a 6-receiver, 3-component seismic network, 3 GPS receivers, a weather station, and 3 time-lapsed cameras. The origin of the coordinate system origin is located at the center of the geophone network $(-77.7228°, 162.2589°)$. The network elements are labeled with their respective station codes, and operated continuously from $2004 - 2006$. The primary Blood Falls crack is labeled for reference. Heavy contour spacing on glacial surface is 25 m (dashed lines). Two of the three camera positions are outside the DEM boundaries and are not shown.

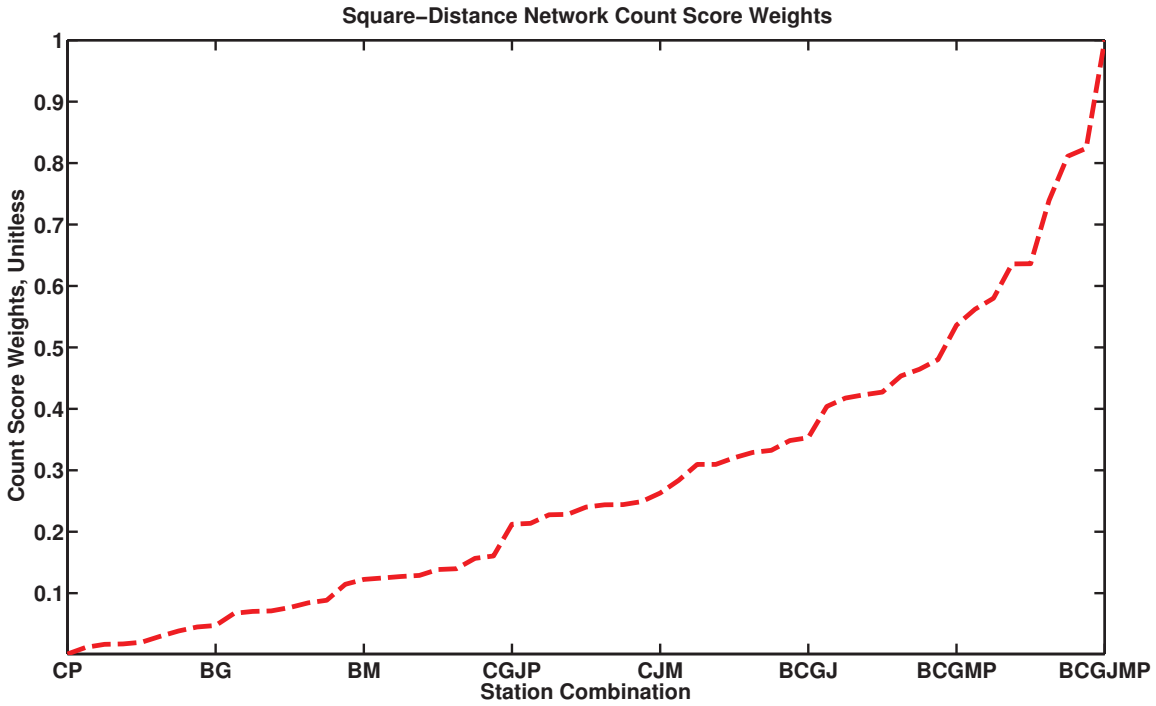

Figure 2.2: The dependence of weight function a_{kn} in Equation 2.1 on receiver combination (sub-network) geometry. The horizontal tick-labels give the first initials of the geophone station codes composing each sub-network; there are 57 sub-network weights in total. For the Blood Falls network, $10^{-3} \leq a_{kn} \leq 1$.

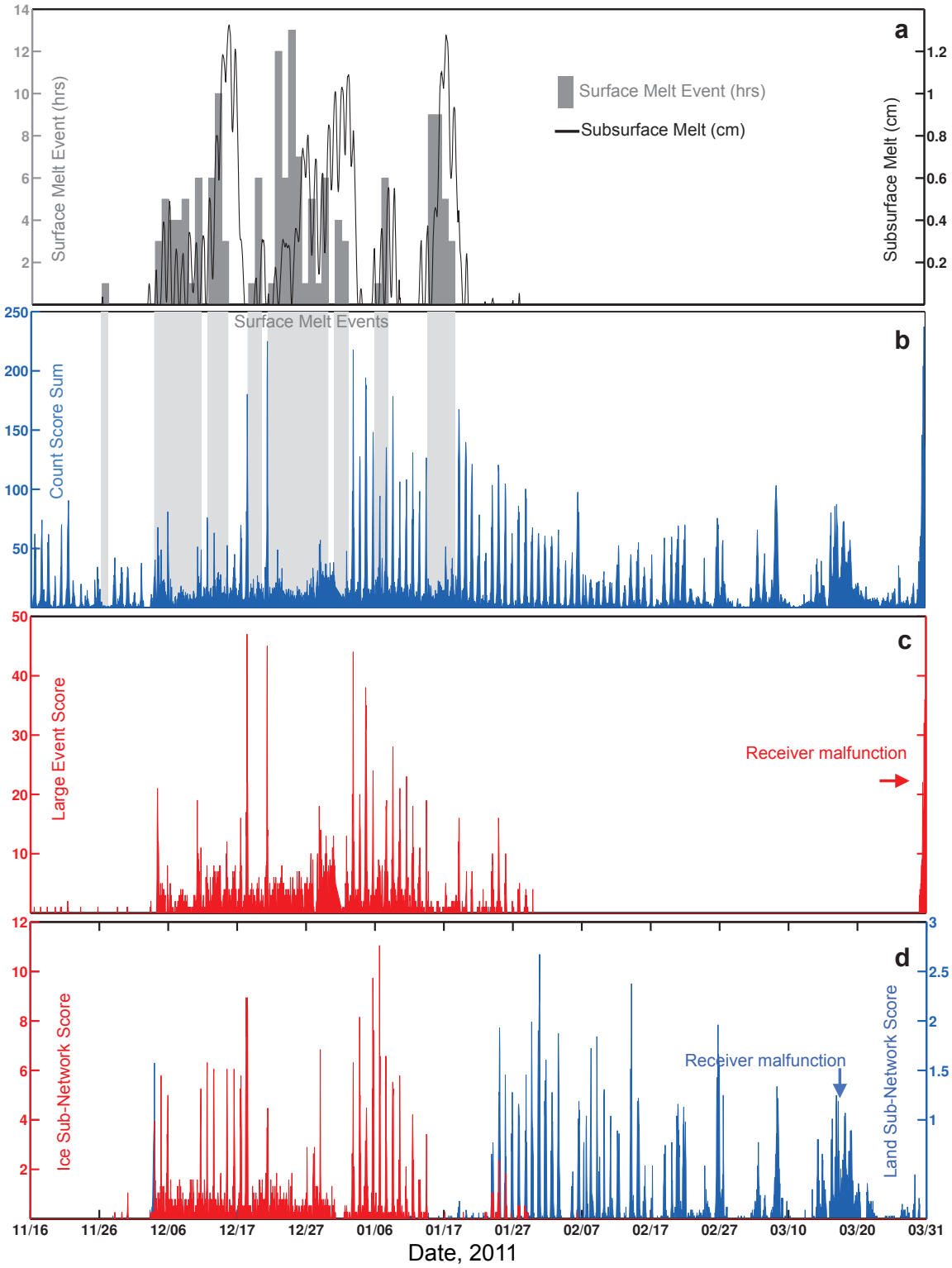
a
Surface Melt Event (hrs)
Subsurface Melt (cm)
Surface Melt Event (hrs)
Subsurface Melt (cm)
b
Surface Melt Events
Count Score Sum
c
Large Event Score
Receiver malfunction
d
Ice Sub-Network Score
Land Sub-Network Score
Receiver malfunction
11/16
11/26
12/06
12/17
12/27
01/06
01/17
01/27
02/07
02/17
02/27
03/10
03/20
03/31
Date, 2011

Figure 2.3: **a**: Surface and subsurface melt computed from the surface energy balance model of [71], for the melt season of 2011. Bar plot illustrates hours of active surface melt production and line graph illustrates the thickness of interstitial melt in the shallow subsurface ($\leq 50\,\mathrm{cm}$) of the ice column. **b**: The seismicity coincident with modeled melt, computed from Equation 2.1 and summed over each hour. Melt-on (gray shading) is accompanied by non-zero background emission rates, while melt-off is accompanied by diurnal seismicity with near-zero background emission rates. **c**: Icequake seismicity of the largest events observed, as defined by their network detectability (unit count score events). These large events are temporally coincident with surface melt. **d**: The seismicity recorded exclusively by the ice network (red) compared to the seismicity recorded exclusively by the land network (blue). The ice-network seismicity is coincident with both large icequakes (c) and melt (a), but distinct from the land network seismicity, suggesting that large icequakes are glaciogenic in origin. Receiver malfunctions due to MARSHA and later PETER give false high emission rates in the post-melt season.

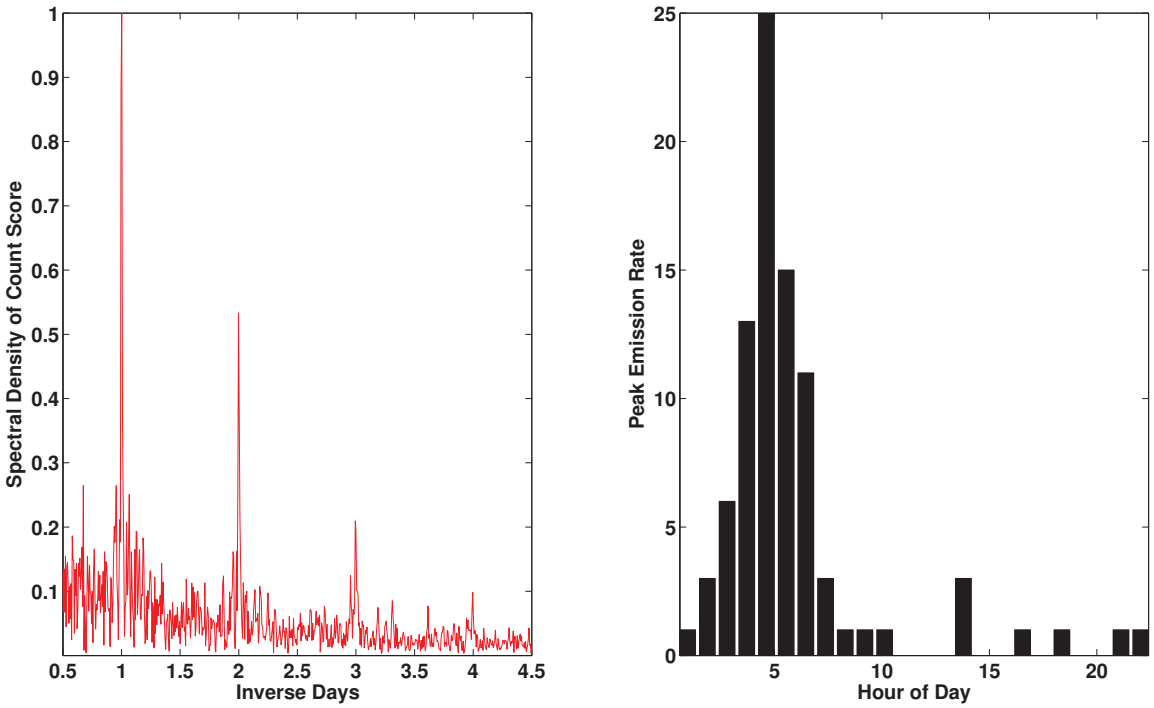

Figure 2.4: **Left**: The power spectral density function for the total seismicity from Figure 2.3(b) illustrates a strong diurnal component and decaying harmonics. **Right**: The histogram for times of peak icequake emission observed during diurnal seismic activity. The highest activity occurs during early morning hours.

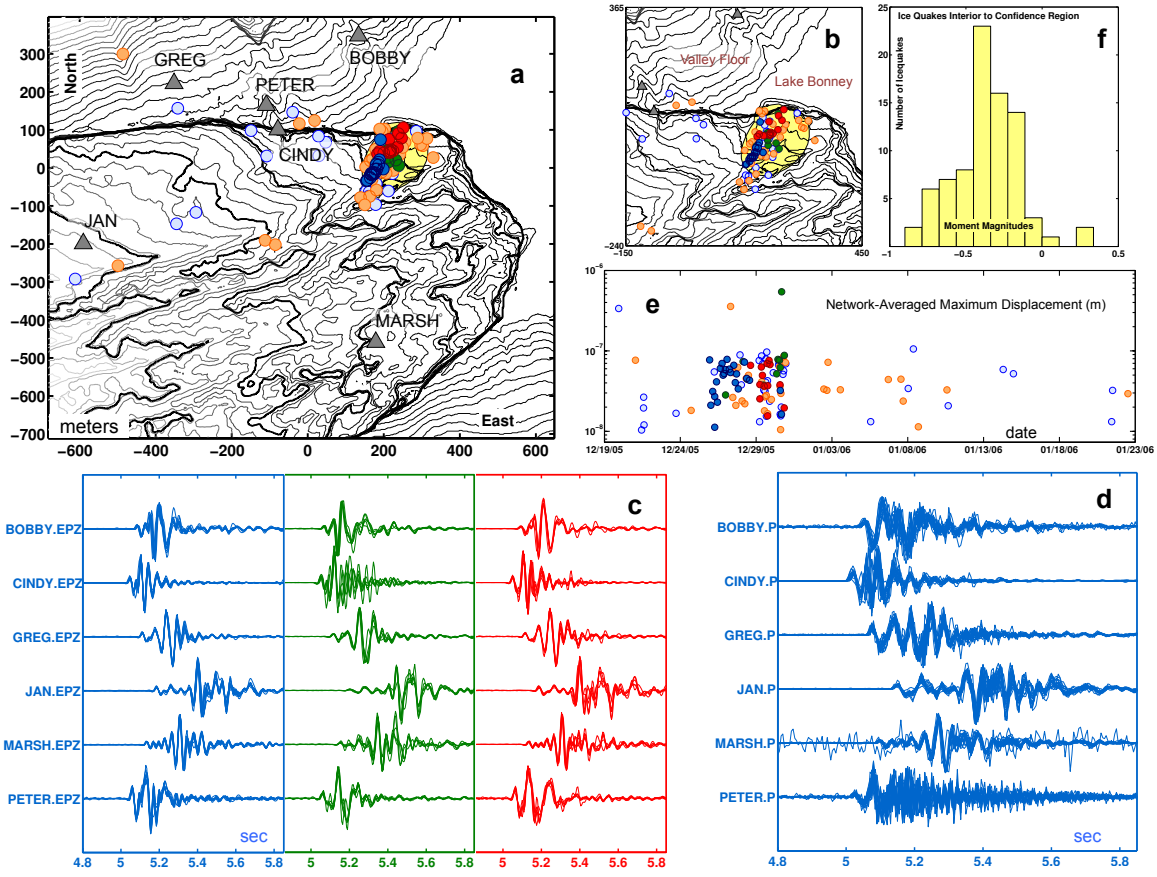
a
North
GREG
BOBBY
PETER
CINDY
JAN
MARSH
meters
East
b
Valley Floor
Lake Bonney
f
Ice Quakes Interior to Confidence Region
Number of Icequakes
Moment Magnitudes
e
Network-Averaged Maximum Displacement (m)
date
c
BOBBY.EPZ
CINDY.EPZ
GREG.EPZ
JAN.EPZ
MARSH.EPZ
PETER.EPZ
sec
d
BOBBY.P
CINDY.P
GREG.P
JAN.P
MARSH.P
PETER.P
sec

Figure 2.5: **a**: Icequake epicenters for all located events. The epicentral marker colors distinguish multiplet membership of the corresponding record sections for each icequake. The blue, red and green markers indicate the three most populous multiplets in descending order of repetition; the orange markers denote the remaining icequakes with some multiplet membership, while the pale blue markers are assigned to remaining non-repeating events. The yellow region illustrates the geometry of the 95% confidence region for a source with a hypocenter at the crack tip, computed using Equation 2.3 with typical phase picking uncertainties. $\sim$ 75% of located events are within this region during the mid-December to January melt season, suggesting that the crack distribution here is responsible for the observed seismicity. All events were located in December or January. Additional locations are coincident with actively calving ice cliffs and the deeper, Northern melt channel. **b**: The confidence region and coincident icequake epicenters in greater detail. **c**: The velocity record sections for each of the multiplet icequakes in **a**. The waveforms are less than a second in total duration, with (non-filtered) dominant frequencies of $\sim 12 - 15$Hz. Surface waves are likely included with scattered energy in the coda. All pairs of record sections within each cluster correlate above $\rho_0 = 0.65$ with their respective stack. **d**: The p-wave portion of the displacement seismograms for the most populous cluster. Each record section has been rotated to a free-surface body-wave coordinate system and the instrument response has been removed. The first motion is up and away from the source. **e**: The magnitude of the vector root-mean-square surface displacements for each located icequake, averaged over the network. Free surface and waveform attenuation effects have been corrected for. **f**: The scalar moment magnitudes computed from Equation 2.7 assuming an opening crack with strike 45°, consistent with the Blood Falls crack geometry.

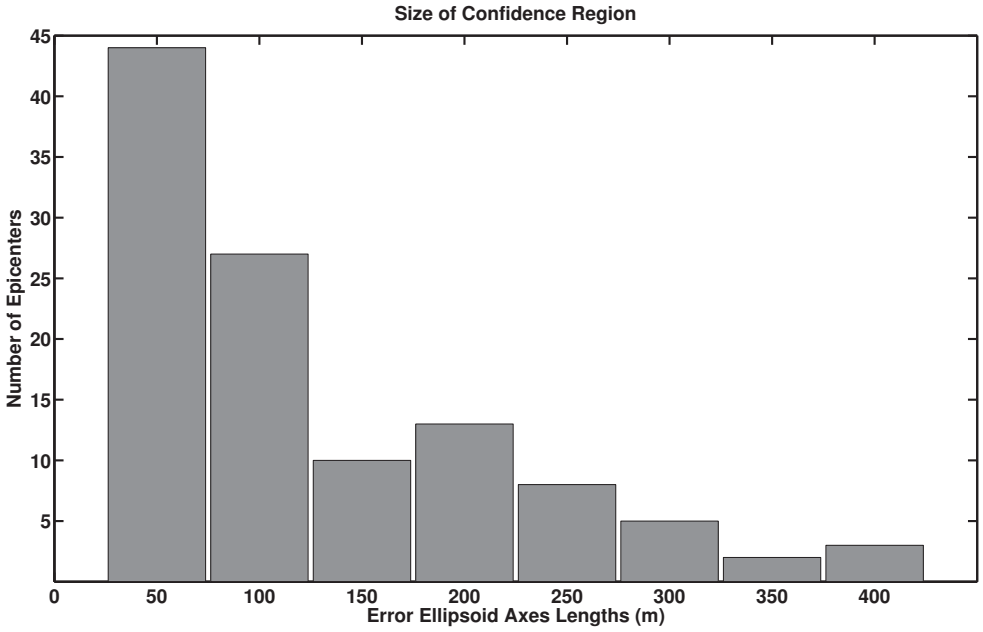

Figure 2.6: The distribution of location uncertainties for epicentral inversions in Figure 2.5. Horizontal axis denotes the axes length in meters of the error ellipsoids at the 95 % confidence level.

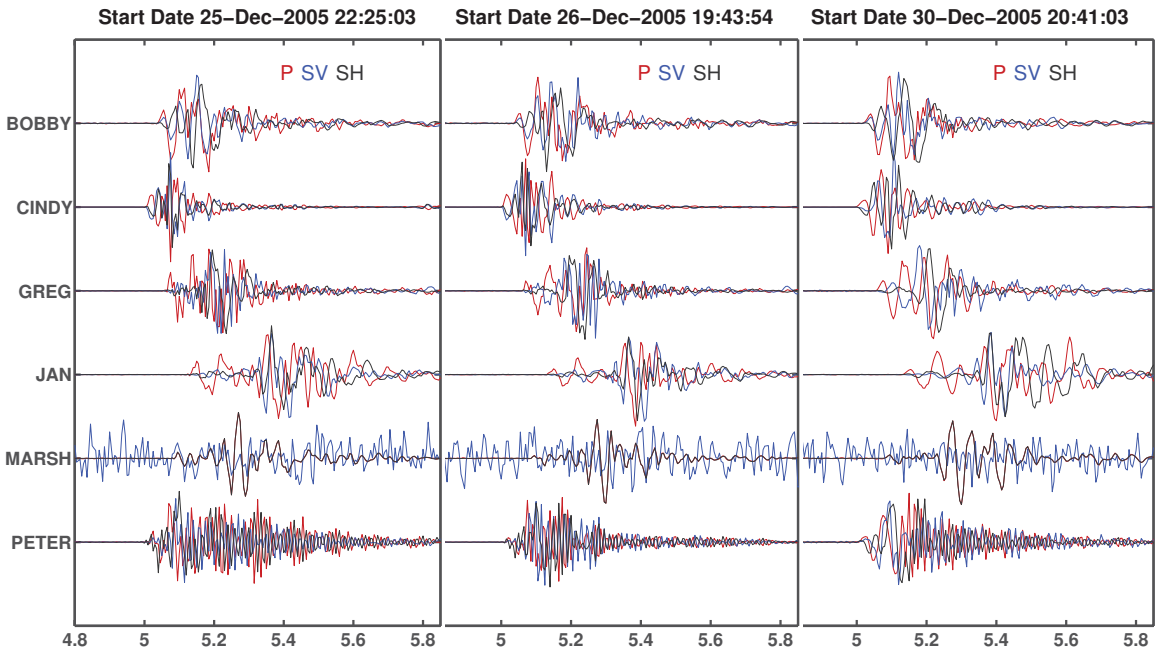

Figure 2.7: Normalized body-wave rotated seismograms from the most populous multiplets in the location database. GREG and JAN illustrate the (upward) p-wave separation most clearly and ambiguous coda after shear wave arrivals. Because of the relatively coarse sample rate (0.005 sec) relative to the small source-to-receiver distances and ice velocity $\left(3900\,\mathrm{m\,sec^{-1}}\right)$, the wave separation is comparatively difficult to distinguish on the other receivers. Only the vertical channel for MARSHA was functional here.

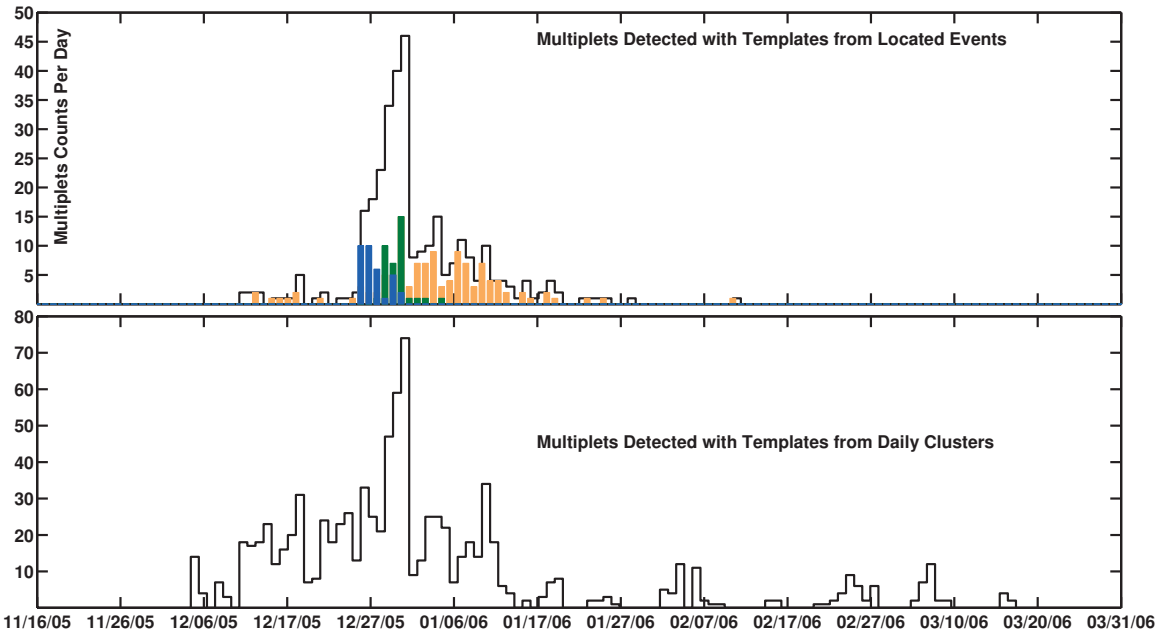

Figure 2.8: **Top**: Multiplets detected over the entire detection database using templates from the phase-pick catalog. A total of 316 multiplets are found in 16 distinct clusters, constituting $\sim 7\%$ of all unit-count score events (largest events). The histogram colors are indicative of the multiplets from Figure 2.5. **Bottom**: Multiplets detected over the entire detection database using the catalog of cluster templates from each day. A total of 936 multiplets are detected from 205 cluster templates that provide 22% of all unit count score events, and 18% of events from the melt season. The most populous multiplet consists of order 30 events. An additional 188 events are found that had been previously undetected.

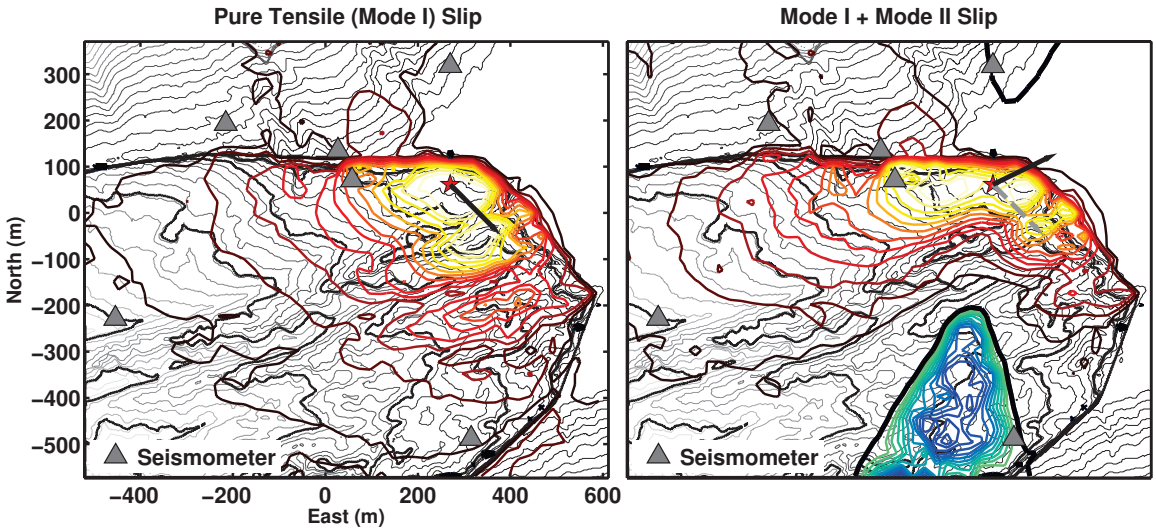

Figure 2.9: The dependence of crack face displacement vector orientation on ground motion polarity. **Left:** Contour lines of ground displacement computed from a model of p-wave motion produced from the impulsive opening of a unit-area mode I crack at the center of Blood Falls. The warm colors (yellow-red) are indicative of positive polarity. **Right:** A model of the p-wave ground displacement produced by a mixed mode crack, when the crack face normal and slip direction are within 71° of each other. The cool (blue) colors are indicative of negative polarity.

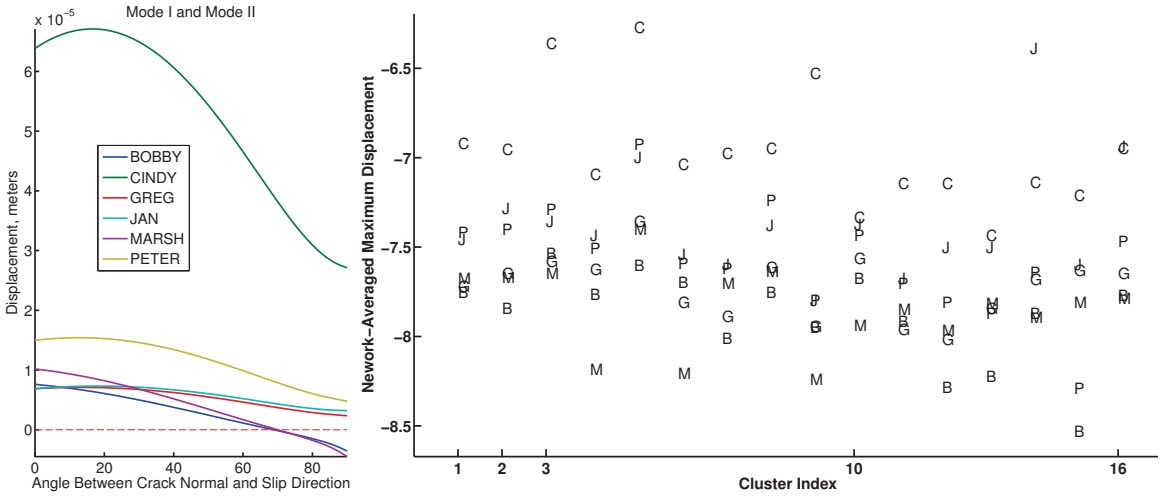

Figure 2.10: **Left**: Modeled p-wave displacement amplitudes computed at the free surface for each receiver using a suite of crack face displacement vectors that combine mode I (tensile) with mode II (slipping) and mode III (tearing) fracture. **Right**: The $\log_{10}$ of the observed displacements are displayed with the first initials of each geophone station code, for each multiplet population, from Figure 2.5. The relative size of observed displacements from located icequakes are most similar to the modeled displacements when the angle between the crack face displacement and crack face normal vector are within 40° to 60°.

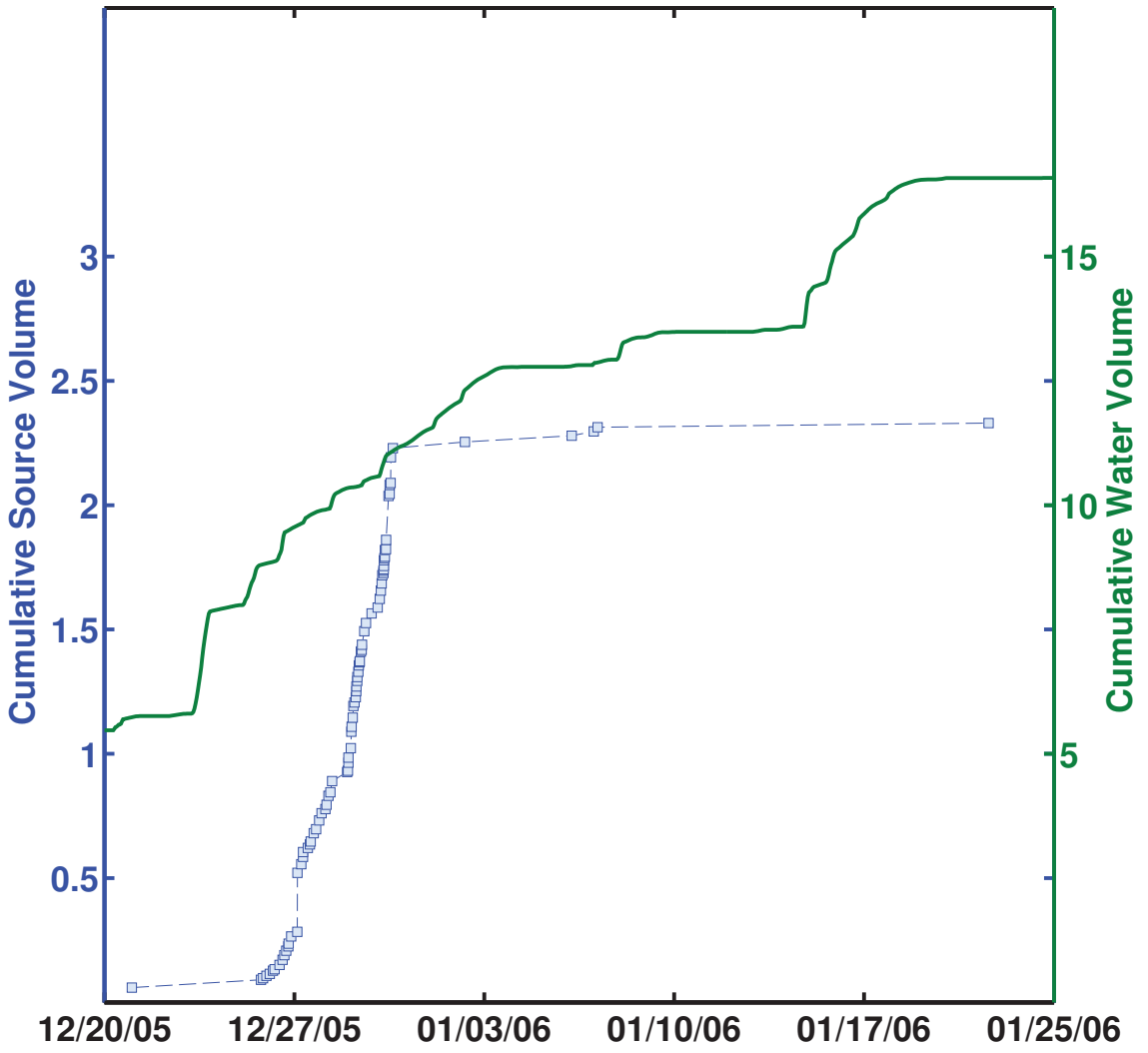

Figure 2.11: The cumulative modeled melt volume over the Blood Falls crack region (top curve) is compared with the volumetric increase at the source region (bottom curve). The modeled melt includes contributions from both the surface and subsurface; because the ice albedo is lower at the seep, it is likely an underestimate of the actual melt volume. The volumetric increase at the source region is computed from Equation 2.9; markers on source-volume plot indicate volume changes for individual ice quakes.

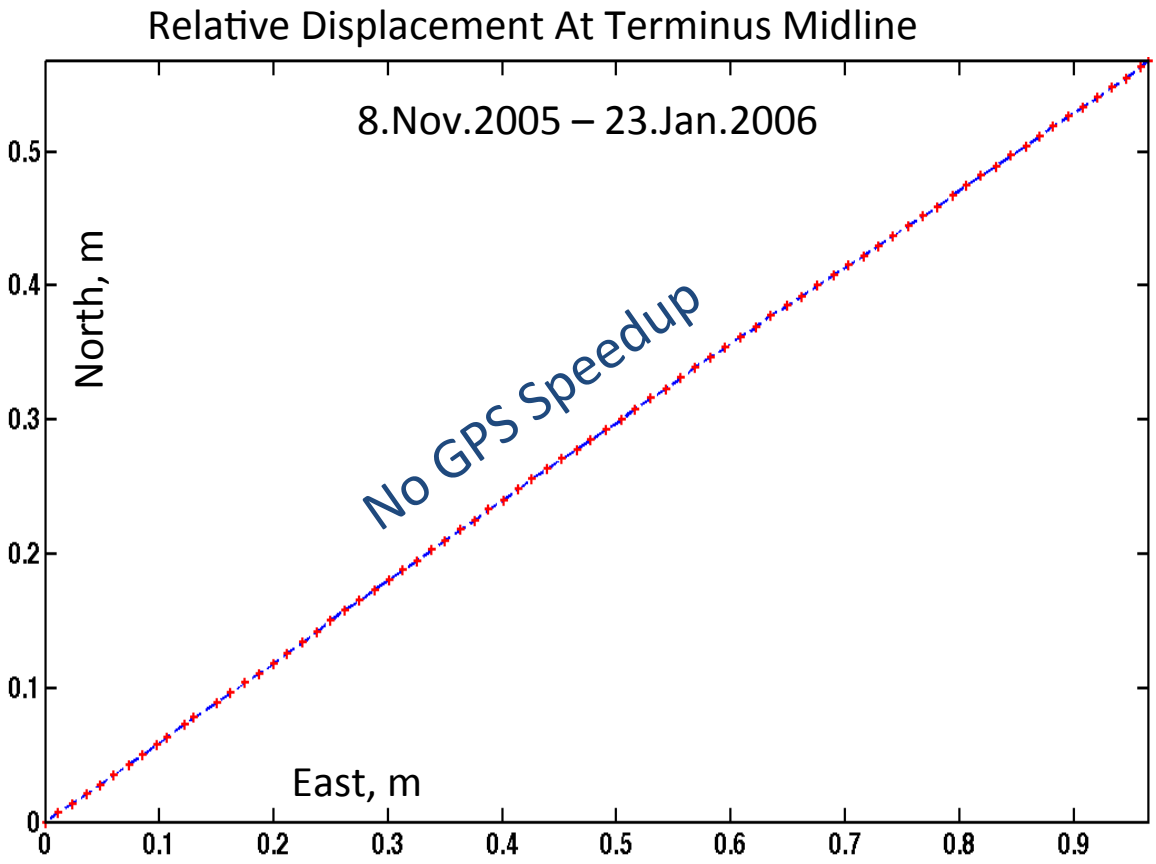

Figure 2.12: Deep englacial or subglacial seismicity in cold ice can occur in the absence of basal sliding. The GPS figure is effectively a straight line through the melt season, indicating no speedup.

Chapter 3

SEISMIC MONITORING OF THE WESTERN GREENLAND ICE SHEET, PART I: RESPONSE TO EARLY LAKE DRAINAGE

I would like to acknowledge the contributing authors to this chapter of my thesis. They include, in order of contribution: Ian Joughin, Mark D. Behn, Matt King, Sarah Das, Laura Stevens, and Dan Lizarralde.

3.1 Abstract

Draining supraglacial lakes exert influence over local flow dynamics of the Greenland Ice Sheet by creating surface-to-bed hydrological connections. To study associated changes in ice deformation, we use geophone and GPS measurements from a period of the 2011 melt season coincident with such a lake drainage. We find icequake activity was largely attributable to Rayleigh waves (95%) excited by shallow-ice fractures. This activity comprised a diurnally variable signal that peaked during early mornings, superimposed with longer-period fluctuations in background seismicity. Epicenters for events leading up to and during lake drainage often co-located with the hydrofracture moulin, but shifted in the general direction of ice flow afterwards. Concurrent flow speeds maintained variable, above-winter values but lacked a clear relation to seismicity. A clearer relation was found with early morning peaks in the spatial range of flow-speeds, and with patterns of InSAR-measured speeds in previous years. To explain this relation, we propose that nightly reductions in surface melt input increased basal traction variability and thereby increased surficial strains. This straining may act in concert with thermally-generated fractures driven by refreezing meltwater to trigger icequakes. We suggest that active moulins enhance spatiotemporal complexity of local ice-flow through surface-to-bed feedbacks in lake-forming regions.

3.2 Introduction

Supraglacial lakes on the western margin of the Greenland Ice Sheet often drain by hydrofracture, thereby establishing pathways (moulins) for surface meltwater to reach the ice-bed interface and influence basal motion [32, 81, 98, 149, 162]. Evidence accumulated to date suggests that subglacial drainage hydrology is qualitatively similar to that of mountain glaciers where sliding is driven by changes in basal water storage and pressure (e.g., [11, 152]). Most documented fast (hours) lake-drainage events in Greenland occur during early-to-mid summer, often between days of year (DOY) 180 and 210 [150]. Earlier or farther inland moulin formation via lake-drainage brought on by a warmer climate could increase meltwater forcing of less well developed, spring drainage systems [72, 103]. The appearance of such surface-to-bed connections earlier in the season could trigger a sustained speedup through prolonged basal decoupling, or alternatively, it could reduce speedup by accelerating development of an efficient drainage network [159, 147]. Evaluating these competing hypotheses requires characterizing the ice-sheet response before and after the early formation of a moulin.

Ice sheet response to meltwater drainage is often monitored using GPS [**?** **?**] or other remote sensing methods (e.g., [82, 81, 123]). Some recent ground-based experiments in western Greenland, where supraglacial lakes are prevalent in summer, also have included seismic networks [32, 37, 80]. In these experiments, elevated seismicity was recorded concurrent with hydrofracture of ice during lake drainage [32] and tectonic faulting of the ice during hydraulic jacking [37].. Unfortunately, the absence of adequate station coverage or capability to associate waveforms on distinct geophones limited the interpretation of their observed icequakes. By contrast, similar experiments that involve alpine and polar glaciers often use seismic network data in a primary role to detect and locate sources of icequakes triggered by meltwater [20, 21, 112, 157, 178]. Some of these icequakes have been associated with basal stick-slip [165] or basal fracturing during subglacial cavity collapse [177]. Other icequakes have been associated with shallow processes like brittle deformation of near-surface ice where high tensile stresses develop during meltwater-activated basal sliding [138].

On the Greenland Ice Sheet, it remains unclear which of these processes produce icequake activity as previously observed [37].]. In particular, the extent to which ice sliding over the bed produces basal seismicity remains unknown. Therefore, it is important to establish (1) when and where icequakes are triggered during a melt season in moulin-forming regions and (2) whether they comprise a strong indicator of ice-sheet response to hydrological or other forcing.

We present seismic observations collected over the 2011 melt season near a previously documented supraglacial lake in western Greenland, which has drained each summer since 2006 [32, 31]. We describe the analysis of these results here and within a following Chapter (Chapter 4). Here, we focus on the analysis of the surficial (Rayleigh wave) seismicity, which comprise 95% of the observed seismic waveforms. In the companion paper, we discuss the potential for seismicity attributable to deeper sources. In contrast to previous work, we focus largely on the period following drainage, rather than on the event itself, in an effort to study the response to subsequent melt input following the creation of the associated moulin. These data comprise the first detailed, passive seismic observations collected from the Greenland Ice Sheet after supraglacial lake drainage.

3.3 Study Region and Instrumentation

The field location illustrated in 3.1 was established in 2006 to study the effects of supraglacial lake drainage on ice deformation and regional flow [32, 82]. Since 2006, geophones, temperature loggers, and GPS receivers and have been redeployed each summer in various configurations around the lake basin. Ablation rates at this elevation ($\sim$1050m) are $\sim 2\text{ma}^{-1}$ and ice thickness is $\sim$ 980 m. Stresses in the lake basin are generally compressive due to flow-convergence over a bedrock depression, and become tensile west and northwest of the lake shoreline where the ice thins by a few hundred meters as it flows over a subglacial ridge. Ice flows west-northwest ($\sim 277^{\circ}$), with mean annual flow rates of $\sim 80\text{ma}^{-1}$ ($\sim 22\text{cmd}^{-1}$).

In mid-June 2011, the lake perimeter was instrumented with six PASSCAL-supplied geophones, eighteen UNAVCO-supplied GPS receivers, and an air-temperature logger. Here

we focus on primarily on analysis of the seismic data. Each geophone site was co-located with a GPS station and included a 3-component, 4.5-Hz, L-28 geophone, and a Quanterra Q330 digitizer sampling at 200Hz, logging to a hard drive. All geophones were mounted on identical pole-platform assemblies that were installed in $\sim$ 2m deep ice pits and back-filled with ice chips. One of these sites, NLBS, was a semi-permanent "base station" that had collected seismic and GPS measurements near the field camp since 2007. Each GPS site consisted of a Trimble NetRS or NetR9 unit sampling at 1-second intervals. Both the GPS and geophone data were recovered in June 2012.

3.4 Methods and Observations

The lake drained on DOY 169 (June 18, 2011) while the instruments were still being deployed so that only a partial network was logging data during the event. Within $\sim$12 hours after drainage, we conducted several aerial surveys by helicopter over the lake basin to document surface features associated with hydrofracture, including moulin and fracture locations. From these surveys we determined that the that the hydrofracture event during drainage opened a crack at least several hundred meters long, which appears to have initiated near a moulin that formed during the previous summer (Figure 3.1). The opening of this crack occurred along a remnant high-angle hydrofracture-formed crack at the lake bottom that is associated with previous drainages described elsewhere [32]. To analyze the pre- and post-drainage seismicity, we analyzed several aspects of the observed seismicity as described in the following subsections.

3.4.1 GPS Data Analysis

The GPS data were processed following the general approach of King and others [95], in which relevant acronyms and software are described. In detail, we analyzed the raw carrier phase and pseudorange GPS data within the GIPSY/OASIS v6.1.2 software using a precise point positioning strategy with uniform observation weighting and a satellite elevation cutoff angle of 10°. We held fixed the high-rate JPL fiducial satellite orbit and clock values and estimated station coordinates every 150 seconds as a white noise process. We also estimated white noise receiver clock terms together with random walk parameters every measurement

epoch associated with residual wet tropospheric zenith delays and tropospheric gradients. For the tropospheric mapping function we adopted the gridded Vienna Mapping Function 1 and a priori tropospheric zenith delays were computed based on ECMWF grids. At the observation level we modeled solid Earth tides and ocean tide loading displacements using SPOTL and based on the TPXO7.2 ocean tide model. Where possible, we fixed carrier phase ambiguities to integer values. To minimize day boundary effects, we processed data in 30 h windows centered on midday and then truncated the time series back to UT days. The final coordinate time series were then rotated into a local North-East-Up coordinate system for further analysis. Remaining outliers, at day boundaries and elsewhere, were visually identified after from detrended data and then discarded. Surface velocities were then computed in each direction by differentiating positions that were pre-smoothed with a 12 hr width, zero-phase Butterworth filter.

3.4.2 Timing and Waveform Characteristics of Icequakes

Icequakes were analyzed for event occurrence rates, waveform attributes, and hypocentral locations as documented in this and subsequent sections. To guide our analysis, we first assembled a visual summary of the seismic records by computing vertical-channel spectrograms for each geophone (Figure 3.2). These spectrograms revealed several coincident periods of elevated seismicity activity measured across the network. We computed network-averaged dominant frequencies of $\sim$15 Hz during these periods, which are somewhat lower than the 25Hz values reported near our site by others [80]. Based on these measurements, we truncated our analysis to frequencies $\leq$ 50Hz, where energy from seismic waveforms was also expected to remain more spatially coherent across the network. These spectrograms also show a strong harmonic signal is visible starting at about DOY 200 and extending through the remainder of the melt season (not shown). An analysis of the resonance modes for the pole used to anchor the geophone suggests that surface melting caused the geophone-pole platforms to melt out, and induced platform resonance (Chapter C). We therefore limit our study to the period from day 165 to 200, when this resonance was absent or minimal.

Following the spectral analysis, we identified individual icequakes using a modified digital energy detector (Chapter A). This detector evaluates a statistic that is computed at each point within a data stream by dividing an estimate of the sample variance within a leading data window by an estimate of the sample variance within a longer, following window (Blandford, 1974). We computed this so-called short-term-average/long-term-average (STA/LTA) statistic using the vertical-channel data from each geophone. To account for correlated background noise (statistically correlated noise samples) that increases false detection rates, we simultaneously estimated the degree-of-freedom (i.e., number of independent samples) parameters of this statistics F-distribution, and updated the detectors parameters hourly (see also [181]). This corrected detection statistic was then evaluated using the Neyman-Pearson decision rule [92, Chapter 7] to achieve a high probability of waveform detection under a false-alarm probability constraint of 10-6. Waveforms detected on different geophones within a time interval less than the expected transit time of a shear wave across the network were identified as the same icequake (i.e., waveform association).

We quantified icequake seismicity by identifying events that were large enough to register detections on three or more geophones, and binning their number each hour. The reliability of this estimate was measured by identifying where the predicted null distribution for the STA/LTA statistic matched its computed histogram within 20% (see Section 3.1). This provided a signal (Figure 3.4) illustrating periods of elevated pre-drainage seismicity (day 166), followed by more energetic signals coincident with lake drainage (day 169). Elevated seismicity associated with lake drainage began at $\sim$ 01:00 hr local time and lasted for $\sim$4 hours. The five days immediately after the lake drainage were characterized by a period of relatively little seismicity, followed by a diurnal signal that is evident network-wide by day 175. This appeared to be further modulated by a $\sim$10 day period signal of elevated background seismicity.

To perform a waveform phase assessment of the detected events, we visually reviewed about two thousand seismic record sections, sampled randomly over the recording period. This analysis revealed consistent differential time lags present between the horizontal and vertical

channels of the dominant waveform phase (Figure 3.3a-b). This is characteristic of Rayleigh waves, originating from shallow or surficial sources [36, 112]. Their dominant features include ∼1-sec signal widths, spectral energy peaks at ∼15 Hz, and displacement-waveform wavelengths of ∼330m. Thus, we conclude that the dominant (95%) source of seismicity is surficial fracturing. By contrast, only a minority of waveforms (∼5%) observed from our sample is characteristic of pure body-wave arrivals. Some of these are attributable to sources external to the lake region based on their relative arrival times within the network. We focus on Rayleigh wave analyses here and the analysis and interpretation of body wave data are included in the companion paper (Carmichael et al., in preparation).

3.4.3 Diurnality of Seismicity

The seismicity in Figure 3.4a shows intervals of both strong diurnal variability and longer-period, elevated background activity. To better assess patterns in this activity over hour-scale or longer periods, we computed a spectrogram of the seismicity using 1 day long windows with 90% overlap (Figure 3.4b). This highlighted $\sim 5 - 10$ day intervals of elevated diurnal and shorter-period variable activity, punctuated by intervals of relative quiescence.We evaluated dependencies in this seismicity on time-of-day by binning icequake counts over hour (Figure 3.4c), and excluding drainage-associated events. The resulting histogram illustrates on average that icequakes are more frequent in early morning hours, with minimum activity occurring near 18:00 local time. The 23:00-hour bin likely underestimated true counts, as seismic data volumes were occasionally truncated before hour 23:30.

To further determine if the pattern of seismicity evident in Figure 3.4b could be produced by a diurnally variable noise source, we estimated the effect of waveform signal-to-noise ratio (SNR) on detection performance. Using the detection statistics F-distribution function and estimates of hourly noise statistics, we computed the threshold SNR required to achieve a 95% detection probability for each hour of each day (see Chapter A). These threshold SNR values were averaged into time-of-day bins for comparison with SNR averages computed from detected waveforms, using an unbiased SNR estimator [99] (Figure 3.4c). These SNR

averages consistently exceeded the threshold SNR by several dB. Thus, we conclude that the diurnal seismicity was produced by geophysical sources, and not caused by changes in noise variance that suppressed or elevated detection rates.

3.4.4 Spatial Icequake Distribution

The relative detection times for many of the seismic waveforms observed across our network suggested they emanated from local sources. We therefore used our geophone network to locate the larger of these icequakes that registered detections on three or more receivers. To obtain these locations, we computed travel time delays from an attenuation compensating cross-correlation analysis that we developed for this study.

In applying this methodology, we first prepared the data by time reversing and re-processing each Rayleigh waveform with the energy detector to compute the signal end-time. The data outside the (original) forward and reverse-detected times were then muted to eliminate noise outside the waveform interval. Next, we applied a frequency-dependent attenuation model [47] in an attempt to correct for the individual propagation-path effects from each waveform to improve our estimate of cross-correlation time delays. These path effects were considered to result from attenuation and dispersion in the near-surface ice [58, 80, 124], and caused a given icequakes waveforms to appear dissimilar on each geophone (Figure3.6a). We therefore processed the waveforms using a causal Futterman filter to model the effects of attenuation and dispersion [129]. This filters coefficients were computed by numerically solving for an attenuation parameter $t^{\star}$ (seismic wave travel time / seismic quality factor) that maximized the intra-receiver cross-correlation coefficient between each icequakes filtered waveforms (Figure 3.6b). If the coefficient solutions gave non-physical (negative or imaginary) values, the waveforms were cross-correlated without further processing.

In both the filtered and unfiltered cases, correlation-derived relative time delays were compared with those computed over a homogenous, 2-m resolution source grid using a Rayleigh wave speed $c = 1670$ msec^{-1} [112]. The grid point minimizing the absolute sum of these

differences was used as the icequake epicentral solution. Solutions exterior to the network, or with misfits exceeding 0.25 sec, were regarded as too uncertain for reliable interpretation and discarded. We applied this location method to a limited subset of large icequakes (435 of $\sim 3.4\dot{1}0^4$ total) that were automatically selected based upon SNR estimates of their waveforms. Seismic quality factors were estimated by dividing the source-to-receiver travel time by the inverted value of $t^\star$, and averaging over the network. The resulting mean values (Q$\sim$35, Figures 3.6b) are within the range of values computed for alpine glacier ice [112], and increase our confidence in the methodology.

The corresponding epicentral solutions for the 435 events shown in Figure 3.5a indicate several prominent features. First, icequake sources active from day 166 to 170 (white markers) are generally concentrated on the western edge of the crack along which drainage took place. The dense cluster of epicenters south of the crack also suggest that these events surround the moulin location from the previous year, which appears to be the site of the crack initiation in the 2011 event and includes visible surface fractures (Figure 3.5b). In contrast, icequake locations for events that follow drainage by 1 day show a mean shift in icequake activity that is roughly in the direction of ice flow (Figure 3.5a, blue markers). These sources are predominantly located farther from the crack, and nearer the zone of extensional strain located in the direction of a subglacial ridge to the northwest (see Figure 3.1). While our locations include only a small fraction of all total events (435 of $\sim 10^4$ in number), they represent the largest observed icequakes (highest SNR) and presumably, the most significant.

3.4.5 Seismic Source Size

To gain additional insight into the mechanism for shallow-ice seismicity, we used relationships between seismic magnitude and source region size to estimate the deformation scale produced at each icequake hypocenter. Based upon visually evidence for surface fractures (Figure 3.5b-c), we assume a crack-like seismic source model. The volumetric change δV

caused by such a seismic source in confined media is given by [4, pg. 62]:

$$\delta V = \frac{M_0}{\lambda + 2\mu}, \tag{3.1}$$

where λ and μ are Lamé parameters, and $\lambda + 2\mu$ is the elastic longitudinal modulus. It is approximately related to the moment magnitude M_0 (dyne-cm) through the surface wave magnitude, M_S [112],

$$\begin{gathered} \log_{10}(M_0) \approx 1.5 \cdot (M_S + 10.7), \text{ where :} \\ M_S \approx 1.5 \cdot \log_{10}\left(\frac{A}{T}\right) + F(R) \end{gathered} \tag{3.2}$$

Here, A/T is the maximum Rayleigh wave amplitude-to-period ratio in microns/sec, $F(R)$ is the amplitude correction for a source-to-receiver distance of R, λ and μ are Lamé parameters, and $\lambda+2\mu$ is the elastic longitudinal modulus. Volume-change estimates similar to Equation 4.3 sometimes include $\lambda + 2/3\mu$, which refers to the stress-free volume change of a planar crack. We prefer Equation 3.1, which gives the ice confined volume change as a combination of the moment required to open a crack and to elastically push the surrounding ice away [116]. This pushing creates a displacement amplitude A_0 at the icequake source that is related to the geophone-recorded amplitude $A(R)$ by:

$$A(R) = \frac{A_0}{\sqrt{R}} \exp\left(-\frac{\pi R}{c\,Q\,T}\right) \tag{3.3}$$

where Q is the dimensionless surface-wave seismic quality factor.

To prepare the data for magnitude estimation, we deconvolved the instrument response of the L-28 from the waveforms to obtain displacement records over $[2.5, 40]$ Hz. Initial waveform amplitudes, A_0, and attenuation factors, $\pi R/c\,Q\,T$, were then simultaneously inverted using a linear regression with the natural logarithm of Equation 3.3. This regression effectively extrapolated measured Rayleigh wave amplitudes to a zero epicentral distance where $F(R) = 0$. Figure 3.7a-c illustrates the resulting estimates of surface wave magnitudes, quality factors and volumetric source increase. We find an average volume change of $+0.85\text{m}^3$ per icequake, and mean quality factor of Q ~ 45, which is consistent with our correlation-based estimate ($Q \sim 32$) as well as values computed from an Alaskan glacier (e.g., $Q = 42$ from [112]).

3.4.6 Seismicity Comparisons with Temperature and GPS Data

To evaluate icequake-concurrent surface motion, we computed 12-hour, causal moving-averages of GPS speeds at receiver locations sharing temporal data coverage with the geophone network. We identified receivers by their latitude relative to site FL03 to determine if North-to-South extensional patterns were present. Additionally, we computed daily-averages of uplift at site NL08, where motion related to lake drainage was most pronounced. Coincident temperature data collected ∼1m above the ice surface was used to identify periods favorable for meltwater production.

Figure 3.8a-c compare the time series of temperature, GPS speeds, GPS uplift and seismicity. The first notable event shown by these figures occurs three days prior to lake drainage (June 15th, day 166), at which time elevated icequake activity accompanies an increase in both uplift and surface speeds. This is followed by several hours of high temperatures on day 168 that should have produced substantial meltwater input to the lake. The second notable event is lake drainage (early June 18th, day 169). This coincides with high icequake activity (up to 220 events/hour), uplift at NL08 (0.6m), and increased sliding speeds (∼1.0 m/day). The day following the drainage includes a decrease in seismicity by an order of magnitude and a return in ice speeds to pre-drainage values. The uplift gradually subsides over the two weeks following drainage, and is punctuated by a brief episode of renewed uplift on day 176, which is accompanied by increased speeds and precedes a several-day period of increased seismicity. Mean temperatures increase to above freezing by day 185, and likely resulted in sustained melt production. Surface speeds then peak again near day 190, after which time icequake activity remains strongly diurnal, and shares no obvious correlation with GPS motion. This activity also shows no clear relation with temperature data, and was occasionally correlated with temperature peaks, while being anti-correlated other times.

Because individual GPS baselines show little clear correspondence with seismicity, we examined whether there was diurnal variation in strain across the network. While it is difficult to measure diurnal patterns in GPS that are comparable to anticipated diurnal noise vari-

ability [95], we can evaluate diurnal changes in strain over the network by assuming that most diurnal noise variation is common to all receivers. To facilitate such a comparison, we computed maximum differential speeds between distinct GPS sites and binned them by time of day as follows. First, the difference between the maximum and minimum GPS speed within the network (i.e., range in speeds) was computed at every time sample. This produced a time series that was then binned by hour of day. The speed differences within each bin were then averaged to compute a mean hourly speed range over the entire observation period. Only the period following day 169 was used in this binning to avoid biasing the data with hours coincident with drainage-induced speedup. This calculation proved insensitive to diurnal noise common to each GPS site, since the speed differencing removed the same trends. Our estimates therefore provided a variance-reduced computation of the mean peak speed gradient as it depends on hour of day. Figure 3.9 shows that these averages are larger during late night/early morning hours, and lowest during mid-day hours, coincident with peak seismic activity. The uncertainty estimate for each bin was computed using a 4ma^{-1} error in the 24-hr filtered speeds that was reduced by $1/\sqrt{30}$ to account for bin averaging. Assuming that the cumulative position error was uniformly distributed among constituent days, these estimates provide a 2 mm day-1 uncertainty ($\sim 15\%$ of the peak-to-peak difference), indicating that higher late evening/early morning speed gradients relative to mid-day are physical.

3.4.7 Radar Measurements of Ice Speed

The above-nominal winter values in surface speed (Figure 3.8b) indicate that surface ice may have been undergoing extensional flow during our observation period. Our sparse GPS network, however, does not provide a good representation of the spatial variation in speed. Although we lack corresponding data from 2011, we can compare our seismic locations with TerraSAR-X data for 2009 and 2010, which provide 11-day average estimates of the spatial variation in speed [81]. These data show substantial spatial variation in speed from one 11-day period to the next and presumably average out greater day-to-day variation. Although these maps of flow enhancement are from different years than the seismic data, they do reveal

similar spatiotemporal patterns in the two years prior to seismic measurement, indicating similar variability is likely to have occurred in 2011. In fact, our epicentral estimates co-locate with the two regions of relatively high ice speed in 2009 and 2010 (Figure 3.10a-b), where extensional strain was likely high due to the comparatively slow upstream ice, and favorable for tensile fracturing that produces icequakes. Furthermore, the data indicate the potential for relatively rapid (days) km-scale transitions between tensile and compressive strain rates. Thus, summer speed enhancement may transiently produce regions of tensile strain within the lake basin where strains are compressive throughout the winter.

3.5 Interpretations and Discussion

Our first and most general result is that seismicity in the lake basin and its immediate vicinity was predominantly (95%) triggered by fracture propagation within near-surface ice. The prevalence of Rayleigh waves before and after drainage indicates that seismogenic deformation was concentrated within a wavelength ($\sim$330m) of the surface. Average icequake magnitudes from these events are more than a magnitude unit greater in size than those measured from Rayleigh waves triggered by surface cracking on an alpine glacier [112], and could be associated with $\sim$1m^3 changes in ice volume. Assuming a crack-source model, these icequake volume changes are equivalent to crack-face opening displacements of $\sim$1mm over a crack-face plane of 10m $\times$ 85m. Such a crack is consistent with thin (mm-width) cracks that extend over tens of meters that often have been observed by members of our field team (Figure 3.5c).

The relatively low occurrence of body wave-dominated seismicity ($\sim$ 5%) attributable to englacial or basal sources either indicates that the geophones pass-band and noise environment make their detection difficult, or that there is relatively low seismogenesis at the ice-bed interface. In the first case, a low seismic quality factor caused by intrinsic attenuation within glacial ice (mean $Q \sim 32 - 45$ for Rayleigh waves) at observed frequencies may disperse and attenuate seismic waveforms originating from the bed so that they are undetectable above the noise floor of the 4.5Hz surface geophones. Alternatively, a relatively low occurrence of basal seismicity would indicate that sliding is largely accommodated by aseis-

mic creep and/or deforming till; this is discussed further in the companion paper (Chapter 4).

Our second general result is that post-drainage seismic activity is diurnally variable. This activity persists throughout most of the record, despite changes in background seismicity. It is most pronounced during the early morning hours and cannot be explained from fluctuations in background noise that reduce icequake detections (Figure 3.4b-3c). These intervals of elevated activity are concurrent with low surface temperatures and meltwater production and may reflect associated cycles in mechanical or thermal influence on ice deformation, as discussed below. Heightened activity during these hours is also consistent with field observations when audible cracking was heard near the NLBS site (Figure 3.1) and newly formed surface cracks were observed during early mornings over a 2-3 day period (Figure 3.5c).

The seismicity also shows a longer-period component of elevated variability that is superimposed with the diurnal signal. This activity appears to comprise 5-day patterns in which daily minimum icequake counts remain relatively steady compared with peak-to-peak amplitudes (Figure (Figure 3.4b-3c)). They indicate a temporal pattern in surficial fracture activity not attributable to changes in noise levels. Rather, these changes are consistent with the temporal complexity documented by Joughin and others [81] in proximity to the same moulins shown in Figure 3.10. This TerraSAR-X imagery shows fluctuations of nearly 100% in surface speeds relative to winter values using $\sim$ 10-day averaged surface velocities. Our seismicity shares this variability, and indicates it may occur over shorter periods.

One source of the surficial seismicity may be local fluctuations in surface strain that produce the surface cracking that our seismic data detect. Decreased meltwater input to the bed during early mornings may increase spatial variability in basal traction as lubricating meltwater declines so that patches of the bed and overlying ice come into contact. This could induce associated spatial variations in surface strain that leads to seismogenic cracking. Although we had difficulty resolving such change with our GPS network, such variation may be occurring at length scales shorter than can be resolved with our GPS network ($\leq$2km, or

2 ice thicknesses). Further, such a link between surface seismicity and basal water input is also consistent with the shift in icequake locations shown in Figure 3.5a. Prior to drainage, it was likely that the bed received most local water input from the active southwest moulin indicated in Figure 3.5b. After drainage, the water input through the lake moulin would have increased total water delivery to the region where seismic activity then increased. The addition of this moulin north of the southwest moulin coincides with the northward shift of the mean pre-drainage and post-drainage epicentral points that are respectfully shown by the white and blue markers in Figure 3.5a. This would suggest that spatial differences in input location, and therefore basal lubrication, drive the high seismogenic strains.

Figure 3.9 illustrates the point-wise range in GPS speeds measured across the network, and averaged in hour-of-day bins. Here, maximum flow differences (on average) peak with increases in average icequake activity during early morning hours. If this timing were unrelated to diurnal modulation (such as from melt input), we would expect no significant hourly differences in peak speed gradients. Additionally, if this diurnal modulation is related to diurnal variation in meltwater input as we have proposed, then decreased melt input drives the measured spatial flow differences. This is again consistent with a model in which increases in spatially variable basal traction induces surface strains that open seismogenic tensile cracks.

Cumulatively, these observations indicate that the temporal relationship between GPS speeds, temperature, and seismicity post-drainage is complex in the lake-forming region. In particular, localized spatial variations in ice deformation, rather than sliding speed, may be provide a better predictor for elevated seismic activity. Since surface speeds were almost uniformly above mean winter values network-wide before drainage (Figure 3.9b), the ice may have undergone significant extensional (tensile) strain at that time, despite flow into the lake basin being generally compressive. The post-drainage events also share spatial coincidence with regions of repeatable, high surface speeds measured during previous years (Figure 3.10), when data was available. The 5-to-10 day period of apparent, elevated background seismicity is additionally consistent with the similar, 11-day variation in the TerraSAR-X data. Therefore, the icequakes triggered by tensile fracturing may reflect

stress modulations relative to an enhanced tensile stress state that differs from the value predicted by average flow characteristics.

Alternatively, thermal effects may trigger some or all of the seismogenic surface fracturing. In one case, this can occur when strong temperature gradients cause elastic contraction in the shallow subsurface that induces tensile fracturing [18]. Alternatively, meltwater produced during warm hours in mid-day may refreeze at night within the cold sub-surface in a process similar to the freeze-thaw cycles that break water-occupied porous rocks through heaving [33, 117]. Such experiments have demonstrated that pressures can greatly exceed the tensile strength of ice. Therefore, it seems plausible that thermal-effects may trigger fracture propagation in the ice. We emphasize that this may also act in parallel with spatial strain gradients to produce our observations.

3.6 Conclusions

In this work, we used a network of geophones and GPS instruments to monitor ice-sheet response before, during, and after the drainage of a km-scale supraglacial lake in Greenlands western ablation zone. We developed and implemented statistically robust detection methods that provided high-confidence estimates of icequake activity for comparison with GPS-measurements of displacement and speed. Post-drainage icequakes exhibited a spatial shift from pre-drainage icequakes as a new moulin opened, but showed an unclear relationship with time histories of GPS-derived surface speeds. These icequakes are roughly co-located with a spatially complex pattern of high strain rates present in previous years, and were most common in early morning hours. We offer two hypotheses to explain the timing of this post-drainage seismic activity. In the first hypothesis, spatially and diurnally varying gradients (Figure 3.8-10) in flow speed produced tensile stresses that peaked (on average) in early morning hours. This model requires ice sheet flow to be modulated by a corresponding diurnal forcing mechanism like meltwater input. In the second model, thermal processes within the shallow ice-subsurface triggered icequakes.

These results are somewhat contrary to our initial assumptions. We expected post-drainage seismicity to dominantly involve basal seismicity once sliding, and presumably basal deformation, increased. Instead, deep seismic events comprised only $\sim 5\%$ of the icequake population at any time, and seismicity was most active at night when peak speed gradients were higher (on average). Our results further demonstrate that the physical mechanisms controlling transient ice-sheet response are spatially and temporally complex, and are still not well understood on scales spanning several ice thicknesses. Seismic networks evidence for associated melt-season surface fracturing at a fine spatial resolution, and may be useful in the study of ice motion following slowly draining lakes or formation of new moulins (e.g., [162])

3.7 Acknowledgements

The authors would like to thank Matt Hoffman for constructive discussions on GPS processing and subglacial hydraulics, Brooke Medley for input regarding exposition, David Shean for photographic data of instrument melt out, and Don Percival and James Pitton for input on detection statistics. Research by J. Carmichael was supported by a NASA NESSF Fellowship Grant, NNX08AU82H and NSF Grant ANT-0424589 . The field work and additional analysis was supported by the National Science Foundations Office of Polar Programs (NSF-OPP) through ARC-1023382 awarded to I. Joughin and ARC-1023364 awarded to S. B. Das and M. D. Behn. Matt King is a recipient of an Australian Research Council Future Fellowship (project number FT110100207).

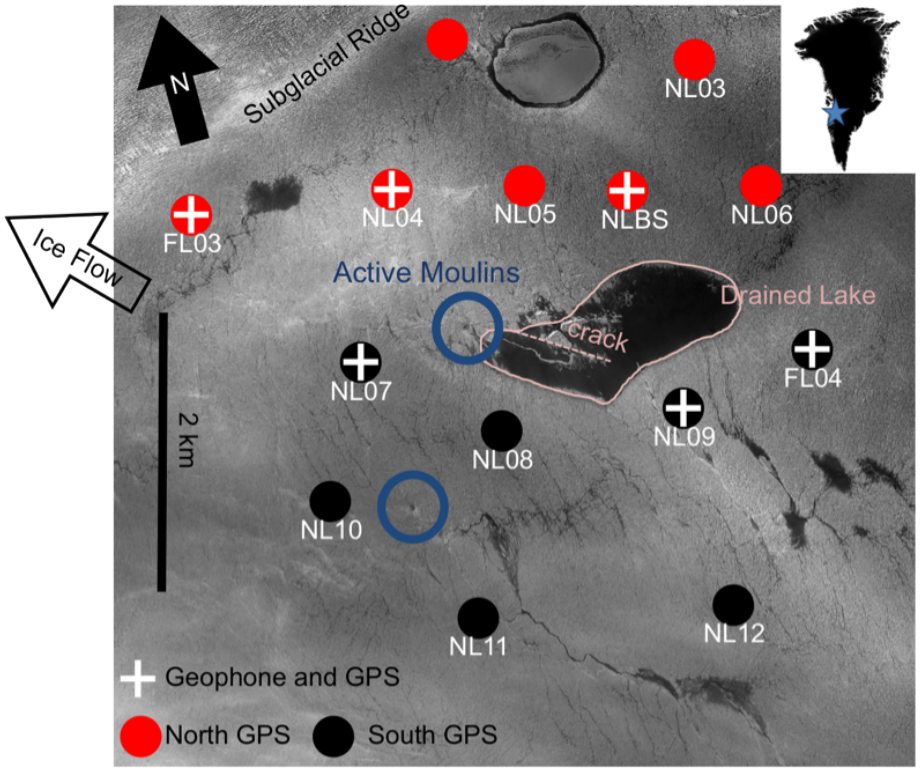

Figure 3.1: The field site location (68.73^{o}N, 49.53^{o}W) in a region where supraglacial lakes form in Greenlands ablation zone. The outlined central dark region in the image center indicates the filled supraglacial lake shortly before drainage along with an older drainage crack. GPS sites where Trimble GPS receivers were deployed in June 2011 are shown by circularly markers. Crosses show locations of the six L-28, 4.5Hz geophones that were paired with GPS stations. Red and black markers respectfully indicate sites North and South of FL03. The moulin that formed following the lake drainage and a second nearby moulin that appears to have been active prior to the lake drainage are also shown (blue circles).

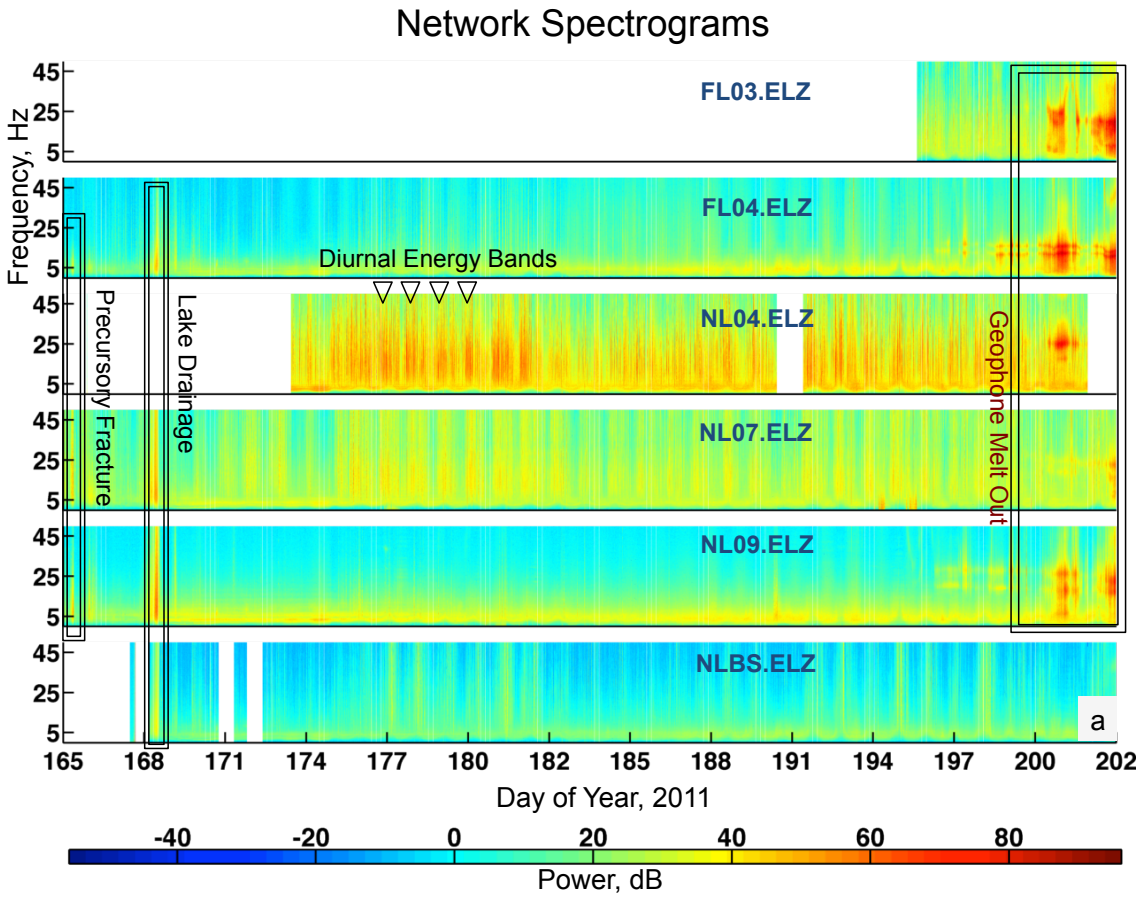

Figure 3.2: Bandlimited spectrograms computed using the vertical component of available geophone data. Color bar indicates range of signal power in decibels (dB). White regions indicate missing data. Features documented on this plot include: elevated seismicity preceding hydrofracture, seismicity coincident with lake drainage, diurnal bands of elevated energy, and spectral curves indicating resonance caused by instrument melt out. All data refer to local time.

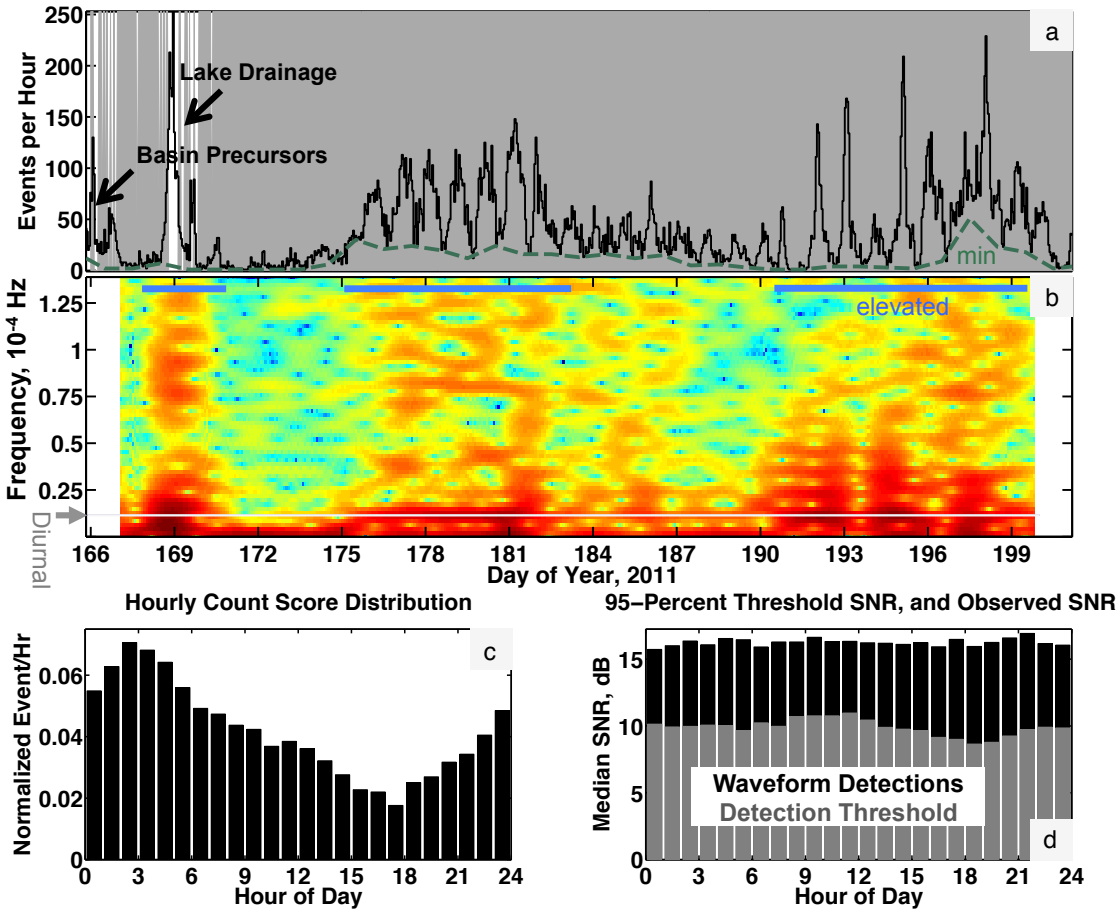
a
Events per Hour
250
200
150
100
50
0
Lake Drainage
Basin Precursors
min
b
Frequency, 10⁻⁴ Hz
1.25
1
0.75
0.5
0.25
Diurnal
elevated
166
169
172
175
178
181
184
187
190
193
196
199
Day of Year, 2011
Hourly Count Score Distribution
c
Normalized Event/Hr
0.06
0.04
0.02
0
0
3
6
9
12
15
18
21
24
Hour of Day
95–Percent Threshold SNR, and Observed SNR
Median SNR, dB
15
10
5
0
Waveform Detections
Detection Threshold
d
0
3
6
9
12
15
18
21
24
Hour of Day

Figure 3.3: A summary of icequake seismicity and corresponding detection statistics. All dates indicate local time. (**a**) Number of icequakes detected per hour (seismicity) on any 3 or more operational geophones within the network. Peaks prior to and during drainage are labeled for reference, and the green dashed line labeled min indicates the minimal count rate in a day. The gray shading indicates bins where the STA/LTA detector statistics predicted null distribution fit the observed distribution with less than 20% error. (b) The spectrogram of the seismicity in (a) with the minimal daily count rate removed. The thin gray line indicates the diurnal frequency component, and blue bars indicate intervals of elevated short-period variability. Blank portions of the spectrogram end-points are due to spectral windowing. (**c**) Seismicity from (a) binned by hour of day. Days preceding drainage were removed from counting. (**d**) Median signal-to-noise ratio (SNR) computed from detected icequake waveforms (black) compared with the median, unbiased SNR threshold required to achieve a 95% detection probability in that hour. This threshold SNR is conditional upon several noise statistics estimated within each detection window.

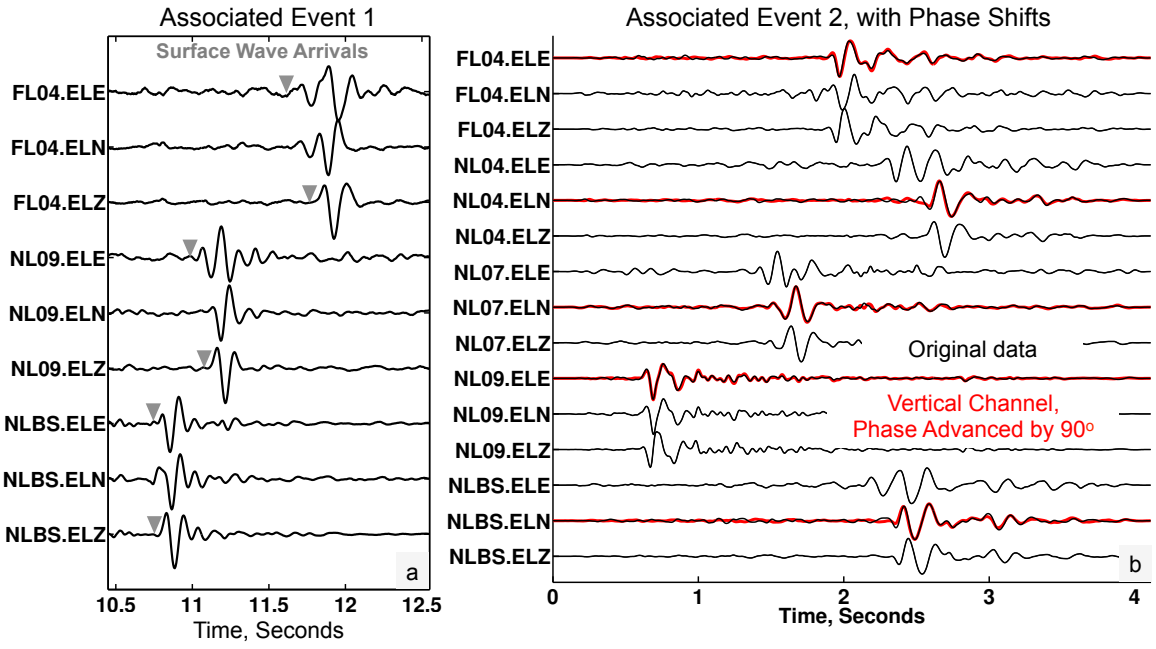

Figure 3.4: (**a**) A typical multi-channel record section illustrating waveforms recorded on 3 of the available 6 geophones for a typical icequake. The gray markers indicate the differential time lags between the vertical relative to the horizontal waveforms. (**a**) A record section for a second event illustrating comparisons between the vertical and horizontal components of motion. Selected horizontal channels for each geophone are superimposed with 90° phase-advanced (Hilbert transformed, shown in red) vertical components to illustrate their strong linear correlation. The phase-similarity between the horizontal and phase-advanced vertical components indicates a Rayleigh wave.

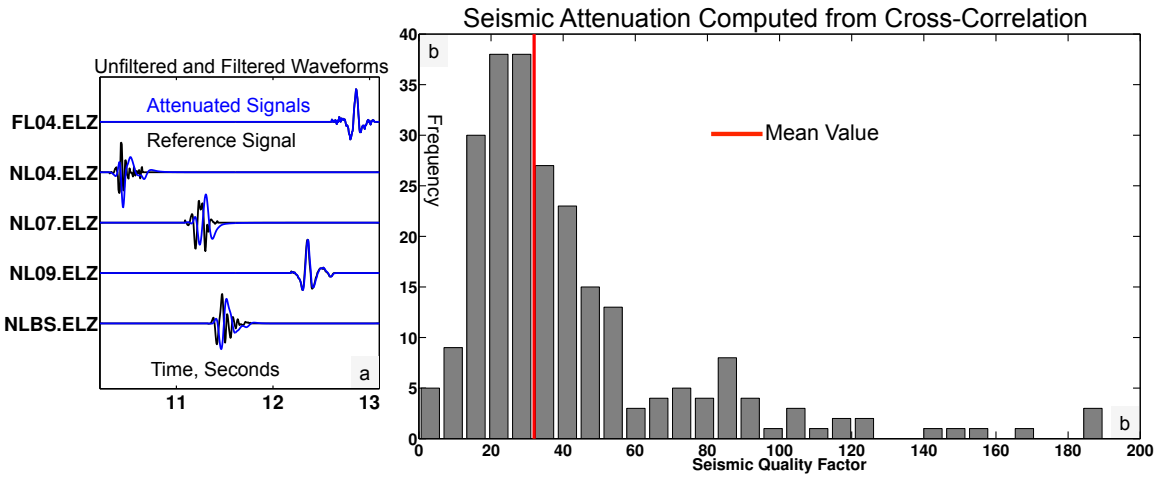

Figure 3.5: (**a**) Pre- and post-processed waveforms used to locate icequakes. Original, recorded waveforms are shown in black. Blue waveforms are causally attenuated to maximally correlate with the latest arriving signals at FL04. (**b**) Seismic quality factors estimated from inverted values of the attenuation parameter $t^{\star}$ that were obtained by maximizing cross-correlation coefficients between waveforms as show in (a). Nonphysical estimates were discarded. These values are in general agreement with attenuation factors computed for two mountain glaciers [58, 112] and the estimates obtained independently in Figure 3.7b

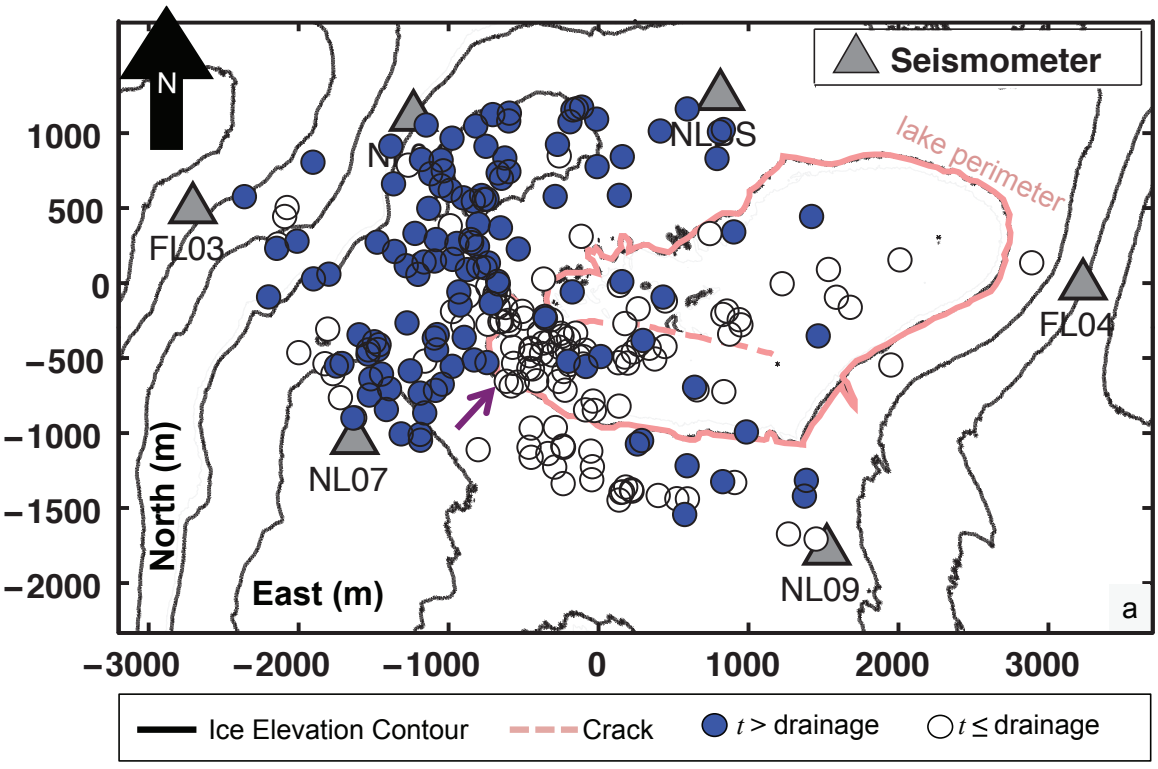
N
Seismometer
NL05
lake perimeter
FL03
FL04
NL07
NL09
1000
500
0
−500
−1000
−1500
−2000
North (m)
East (m)
−3000
−2000
−1000
0
1000
2000
3000
a
Ice Elevation Contour
Crack
t > drainage
t ≤ drainage

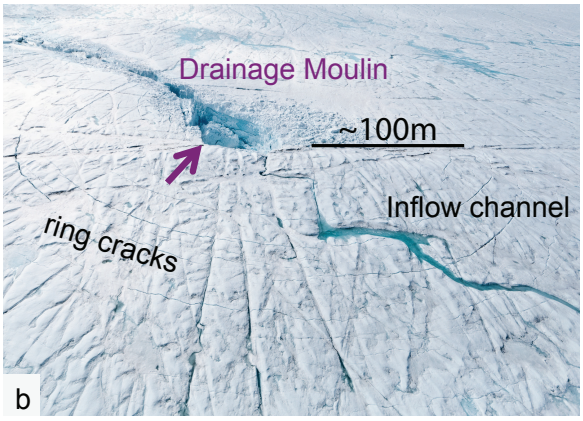
Drainage Moulin
~100m
Inflow channel
ring cracks
b

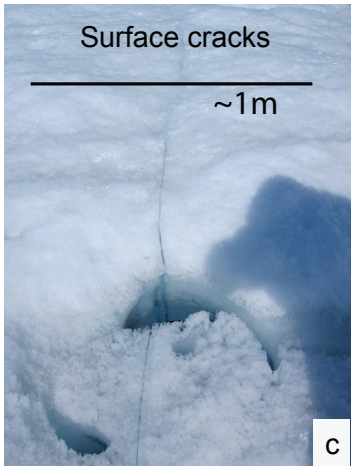
Surface cracks
~1m
c

Figure 3.6: A summary of the icequake locations. (**a**) Epicenters of icequakes over a surface elevation contour map. A total of 435 from $3 \cdot 10^4$ icequakes were selected from the total population of events by selecting high SNR waveforms with pick times available from at least 3 geophones. The local coordinate system origin coincides with the geophone network center. Events detected up to 18 hours after drainage are shown in white. Events detected later are shown in blue. (**b**) The lake-drainage moulin viewed from air. Labeled features in include circularly symmetric "ring cracks" that likely developed from tension induced by the ice-void of the moulin, and a meltwater inflow channel. The purple arrow matches that in (a). (**c**) Visible surface fractures that formed overnight near the NLBS field site and produced audible report and perceived ground motion.

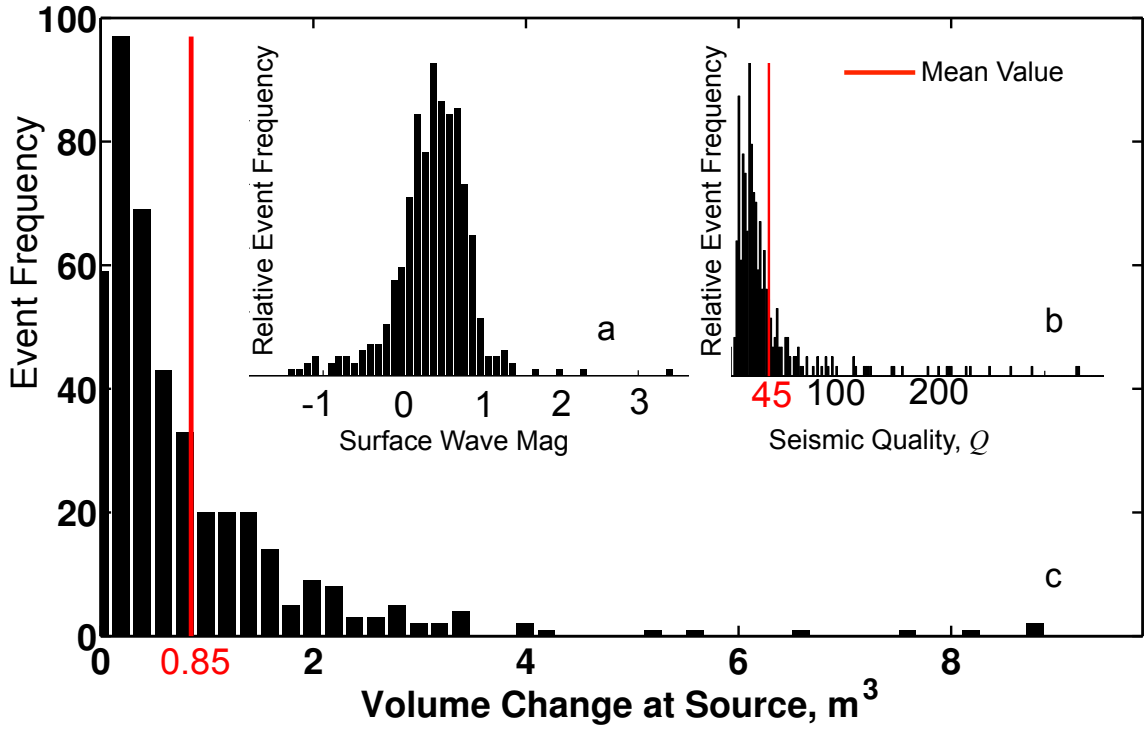

Figure 3.7: Histograms estimated from located icequake waveform amplitudes and epicentral solutions, with red vertical lines denoting mean values. (**a**) The distribution of surface-wave magnitudes, computed from Rayleigh wave peak amplitudes and period. (**b**) The Rayleigh wave seismic quality factor. Values are within range of those reported in glacial ice elsewhere (e.g., [112]) and are consistent with the attenuation factors estimated through correlation (see Figure 3.6b). (**c**) Volumetric growth from icequake sources, assuming tensile fracture-dominated source mechanisms. Values were determined by empirical relationships between surface wave and moment magnitudes scales. The cumulative growth in crack space from the 435 icequakes located here is $\sim$360 m^3.

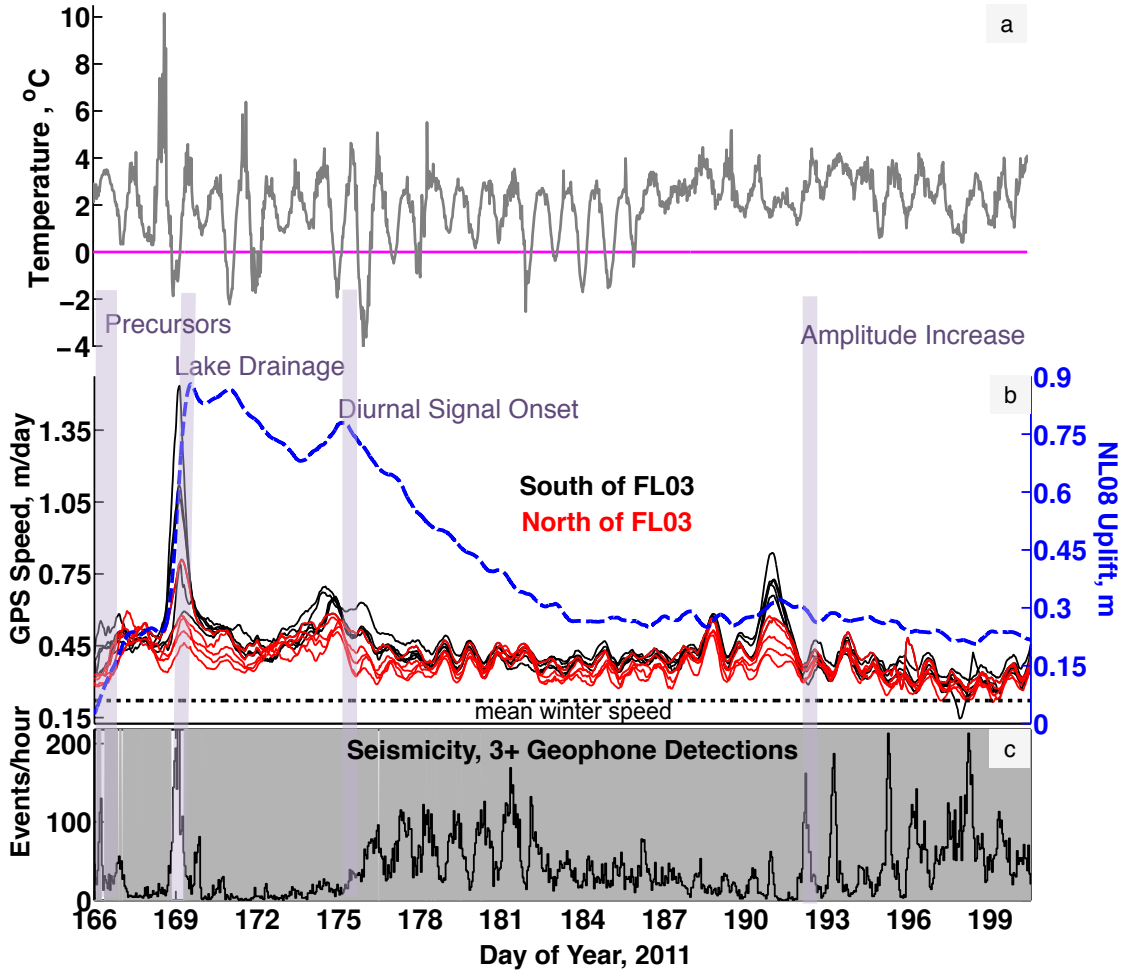
a
Temperature , °C
10
8
6
4
2
0
−2
−4
Precursors
Lake Drainage
Diurnal Signal Onset
Amplitude Increase
b
GPS Speed, m/day
1.35
1.05
0.75
0.45
0.15
South of FL03
North of FL03
mean winter speed
NL08 Uplift, m
0.9
0.75
0.6
0.45
0.3
0.15
0
c
Events/hour
200
100
0
Seismicity, 3+ Geophone Detections
166
169
172
175
178
181
184
187
190
193
196
199
Day of Year, 2011

Figure 3.8: (**a**) Recorded temperatures measured $\sim$ 1m above the ice surface, at the lakeshore. (**b**) Plots of GPS uplift (blue) measured at site NL08 and ice speeds measured at sites with same temporal coverage as the geophones. Colors correspond to Figure 3.1 and indicate sites North (red) or South (black) of FL03, and the dashed, horizontal line indicates the average winter speed. (**b**) Icequake seismicity from Figure 3.4a; the vertical axis was truncated below the signal peak to increase readability of remaining record. Seismicity and temperature in (a) are generally anti-correlated, though phase lags vary. Purple bars across the each plot indicate events interpreted from seismicity.

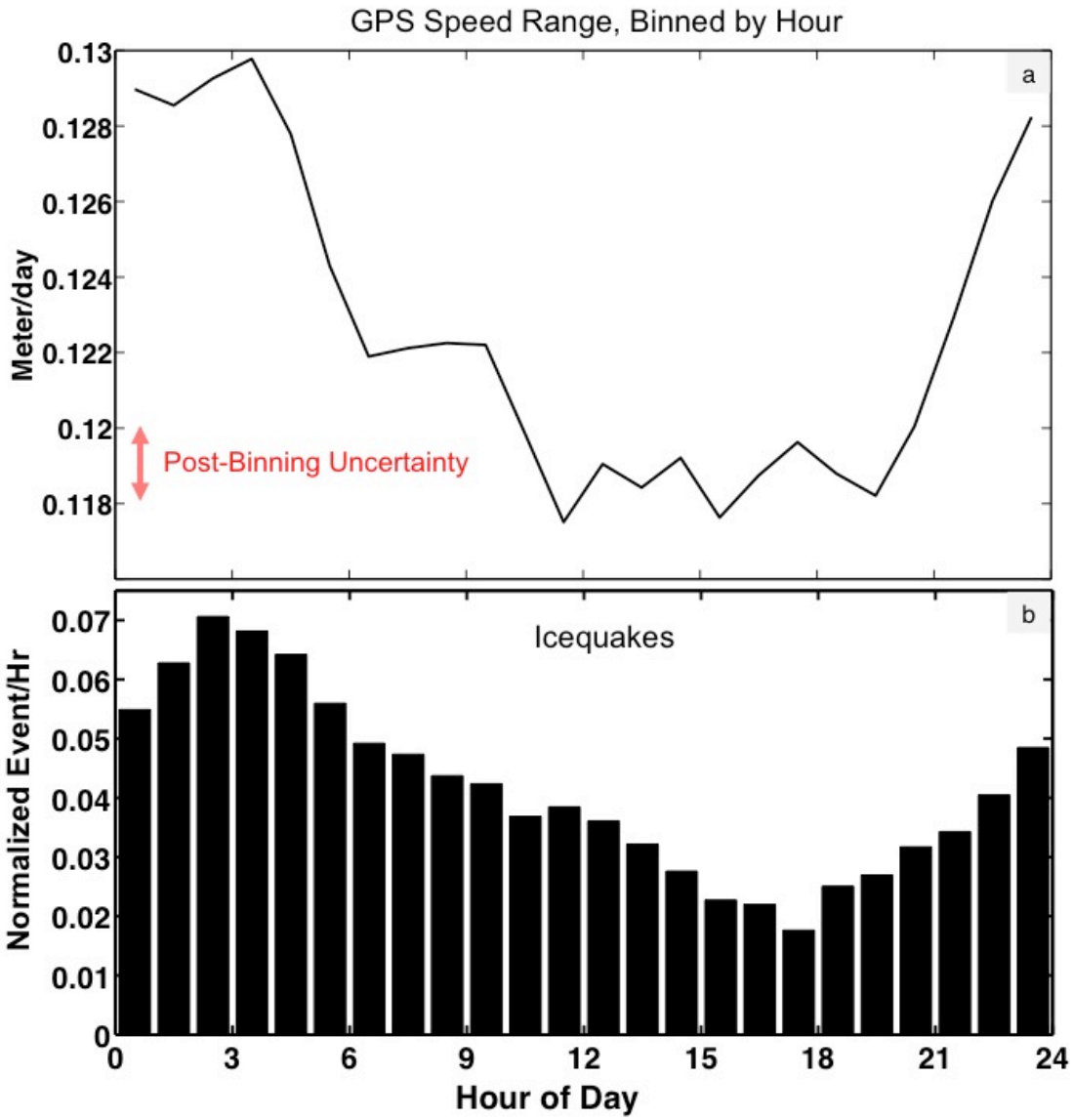

Figure 3.9: A comparison between the range in GPS speeds and icequake seismicity, binned by hour. (**a**) Differences between the maximum and minimum GPS speeds (range) measured across the network, and averaged by hour. Relative extremum indicate that network-wide spatial variability in speed was higher (on average) during early morning hours, and lower during the day. Uncertainty after variance reduction from hourly binning is $\pm 2 \text{mmday}^{-1}$. (**b**) The hourly seismicity from Figure 3.4(b), shown for comparison. Data concurrent with the drainage are excluded from counts in each case.

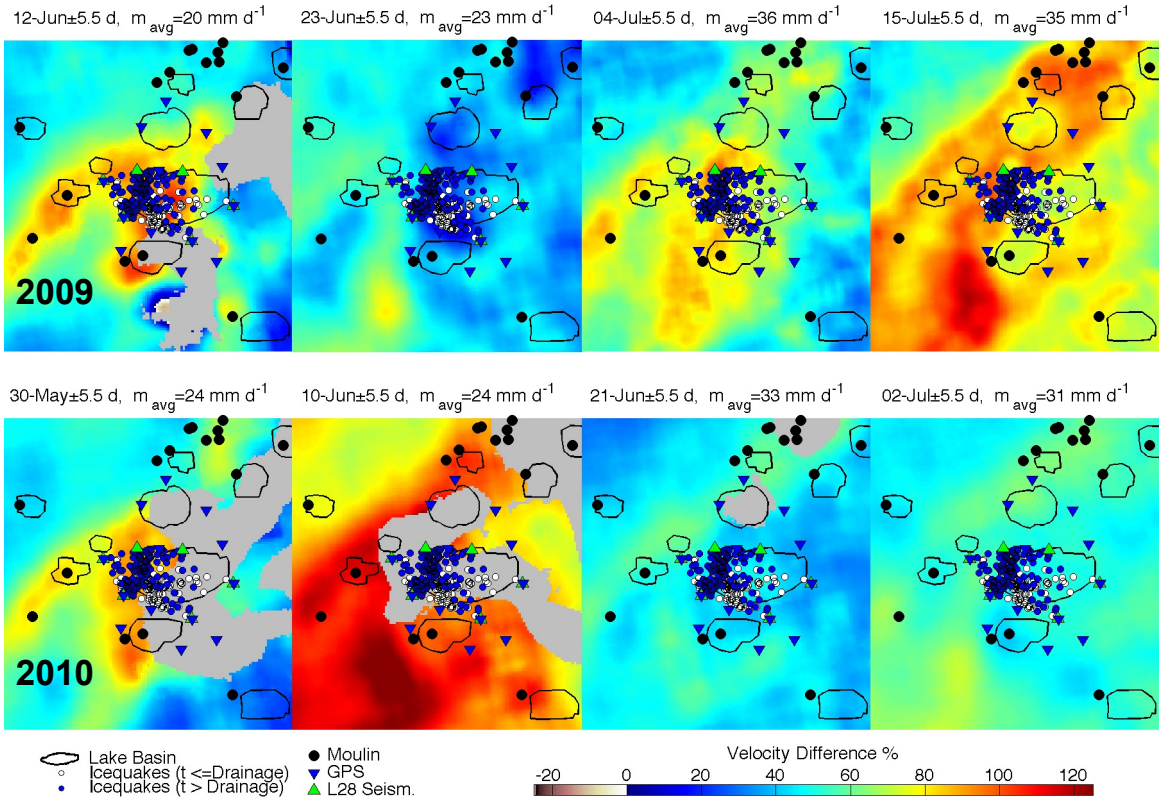

Figure 3.10: A comparison between velocity mosaics from [81] constructed using TerraSAR-X imagery from 2009 and 2010, superimposed with icequake epicenters from 2011; corresponding data from 2011 were unavailable. The left-most panel illustrates a consistent pattern of enhanced velocity between the two years. Icequakes from Figure 3.5a are clustered densely along the regions of enhanced velocity present in the previous two years.

Chapter 4

SEISMIC MONITORING OF THE WESTERN GREENLAND ICE SHEET, PART II: MAGNITUDE THRESHOLD DETECTION OF BASAL SEISMICITY AND LOW-FREQUENCY ICEQUAKES

I would like to acknowledge the contributing authors to this chapter of my thesis. They include, in order of contribution: Ian Joughin, Mark D. Behn, Sarah Das, Laura Stevens, Matt King, and Dan Lizarralde. I would also like to thank Makenna Reeves for digitizing tidal data provided by the Danish Coastal Authority.

4.1 Abstract

Episodes of melt-season speedup on the Greenland Ice Sheet may drive localized surface strains that trigger tensile fracturing that is recorded as Rayleigh waves. To assess the significance of corresponding basal seismicity, we continue our study initiated in Chapter 3 to interpret seismic emissions near active moulins on the Greenland Ice Sheet. Using simple waveform modeling and robust estimation of noise statistics, we find basal icequakes due to sliding below our network must be 1.5 magnitude units larger than surficial events to be equally detectable due to path effects. By targeting lower frequency seismicity, we find identify sub-1Hz, large magnitude seismic events that originate from regional, rather than local sources. Most of these sources are attributable to activity from glaciers 50 km northwestward of the seismic network and have lower-bound body-wave magnitudes of 1-2.8, indicative of small glacial earthquakes. We conclude that lower-frequency body wave seismicity provides a distinct observable that cannot generally be attributed to local icequakes.

4.2 Introduction

The delivery of meltwater to the base of the Greenland Ice Sheet provides seasonal forcing for local and regional speedup in the ablation zone. This water is input through a

spatially distributed set of moulins (∼0.2 per square-km at ∼1 km, [23]) that form during supraglacial lake events each summer. Recent observations show flow speeds of ice in the vicinity of these moulins can be spatially and temporally complex [81], and likely reflect spatially variability in basal lubrication. The surface strains that indicate these flow-speed gradients can be highly localized and therefore under-sampled by even dense GPS networks (Chapter 3). If these strains are sufficiently large to trigger surficial tensile fracturing, they can produce icequakes that may be detected and located. Therefore, seismic monitoring provides a useful compliment to conventional GPS measurements of ice sheet response to meltwater forcing, especially when part of this response includes an elastic component. While such seismic observations are useful, they cannot segregate seismicity triggered by flow-gradients from effects of thermally triggered fractures. Further, they do not provide a direct observable for basal conditions that exert the most control over ice sheet sliding. In these scenarios, response must be retrieved from basal seismicity. Literature documenting the application of seismic monitoring to basal deformation in glaciers is now extensive ([178, 176, 179, 165, 180, 133]) and we avoid re-documenting it's utility to devote more attention to interpreting the records from our site.

Analysis of seismic data from Chapter 3 (hereon called Part I) demonstrated a relative deficiency in detected basal icequakes ($\sim$ 5%) of signals with an SNR exceeding $\sim$ 10dB following episodes of speedup near two active moulins (Figure 4.1). This deficiency was explained by two possible causes: (1) a corresponding deficiency of basal seismogenesis due to plastic basal rheology; or (2) a limited observability due to strong body-wave attenuation and/or the limited range in the frequency response of the geophones that comprised the network. Our objective in this paper is to determine the significance of these infrequent basal events. We address their multiplicity, their relative size compared to surficial seismicity, and their glaciogenic source.

To address these objectives, we have organized the paper as follows. First, we compute the threshold magnitude for basal sources within the network and compare this to surface sources. Second, we identify low frequency seismic events that were not detected previously.

Third, we estimate the arrival direction and seismic slowness for these events to determine their direction of origin. Last, we identify these events and their physical sources.

4.3 Basal Icequake Detectability

Basal icequakes must have sufficiently large magnitudes to generate ground motion detectable by the geophones within a network. Weaker or remote icequakes will produce smaller displacement amplitudes that are statistically more difficult to distinguish from the expected amplitude of background noise. To discriminate an icequake from such noise, an energy detector evaluates a statistic that is computed from a ratio of short-term and long-term averages (STA/LTA) of signal energy [12]. The statistic has two distinct probability distribution functions, one applicable to the case of absent signal (a central F distribution), one applicable to the case of present signal (a non-central F distribution). Deciding an icequake has occurred is equivalent to choosing the distribution function that best explains the measured value of the STA/LTA statistic. The signal-present distribution is parameterized by a so-called non-centrality parameter λ that is proportional to the waveform signal-to-noise ratio (SNR), which is zero for the signal absent case. This parameter is defined by:

$$\lambda = \sum_{k=1}^{S} \frac{w_k}{\sigma}^2 \tag{4.1}$$

where w_k is the waveform amplitude at sample k and σ is the standard deviation of background noise in the short-term window of sample length S. Increasing values of λ results in decreased overlap between the signal-present and signal-absent distribution and makes correctly discriminating between noise and an icequake signal more probable. The statistical tests and parameter estimation involved in icequake detection are described thoroughly in Appendix A. To assess the apparent lack of basal seismicity, we use hourly estimates of noise statistics and distribution parameters at site NL07 4.1 to compute icequake magnitudes providing a 95% detection probability. This seismic signal model includes effects of the source radiation pattern, propagation path, free surface amplification, and instrument

response on a hypothetical recorded waveform. This is summarized through:

$$w_k = M_0 \left(\frac{F R_S}{4\pi r^n \rho_c^3} \right) \cdot \Omega(t_k) \tag{4.2}$$

where M_0 is the seismic moment, F is the free surface amplification factor, R_S is the seismic radiation pattern, r is the source to receiver distance, n is the phase exponent (1 or basal sources, $\frac{1}{2}$ for surface sources), ρ is ice density, c is seismic wave speed, and $\Omega(t_k)$ is the seismic source-time function (a delta function here) at time sample t_k, after undergoing attenuation and convolution with the L-28 geophone instrument response function [122]. The value for λ giving a 95% detection probability was computed hourly from Equation 4.1 using the detection window length S (= 0.8 sec) and false alarm rate (= 10^{-6}) identical to that implemented in Appendix A. Equation 4.2 was then used to invert for M_0 (in dyne per cm) and related to the moment magnitude through:

$$M_w = \frac{2}{3} \left(\log_{10} (M_0) - 9.1 \right) \tag{4.3}$$

[89] Our computations (Figure 4.2) demonstrate that basal icequakes resulting from horizontal sliding are less likely to be detected in the measured noise environment relative to surficial icequakes triggered by fracture opening. On average, a 95% detection probability requires a moment magnitude of $M_w = 1.9$ for basal sources in contrast to $M_w = -0.50$ for surficial sources. The peaks in threshold on day 169 are likely due to unusually high seismic activity concurrent with lake drainage, which increases minimal detection thresholds [135]. This suggests that detection methods with a higher-discrimination capability than the STA/LTA are required for identifying basal icequakes, such as cross-correlation [52, 21, 65].

The results shown in Figure 4.2 are partially conditional upon the duration of the waveform. In these cases, the source function was temporal localized and produced waveforms with high frequency spectral energy ($\leq 20Hz$). Lower frequency (and longer duration) waveforms undergo less attenuation due to the frequency dependence of amplitude, which scales as $\exp\left(-\frac{\pi R \xi}{cQ}\right)$ in the frequency domain [4], where ξ is frequency in Hz. Lower frequency

waveforms are therefore expected to undergo less attenuation and produce more detectable amplitudes within the instrument pass-band.

4.4 Low Frequency Icequakes (LFIs)

To search for icequakes attributable to non-surficial sources, we targeted lower-frequency events that were atypical of Rayleigh waves recorded in Chapter 3. This consisted of visually reviewing vertical-channel spectrograms of each geophone between 0 and 7.5 Hz for each day and manually picking perceived icequakes. This search revealed a consistent population of $\leq$190 nearly monochromatic ($\sim$ 0.75Hz) events consisting of waveforms with $<$ 30 sec duration signals (Figure 4.3) that were observable across the network. These events occurred nearly every day (Figure 4.4), and exhibited no clear hourly bias from day to night (Figure 4.5). Further, they registered well below the 4.5Hz peak frequency response of the L-28 geophone, and indicate that the true amplitude of the recorded ice motion was significantly larger than that for higher-frequency events with the same-recorded amplitude. To determine apparent locations for these events, we used cross-correlation analyses between the waveforms recorded at each receiver to estimate relative time delays of the dominantly low frequency energy. The onset of each signal was generally emergent, however, and made estimating the initial phase and arrival time necessary for computing locations difficult. We visually identified 60 cases in which initial arrivals were both apparent and coherent across the network (Figure 4.6), and inverted for slowness vectors for this subset of events. The inversion revealed a sample of events with abnormally high apparent velocities indicating that their associated seismic wavefronts approached the geophone network from the northwest and at significant vertical incidence (Figure 4.7). To evaluate sources of error in the back-azimuth estimates, we systematically discarded data from each receiver recomputed the slowness from the resulting reduced system of equations. This provided consistent solutions, with estimated back-azimuth directions within 10 degrees between solution sets obtained with different pairs of receivers. Therefore, this high velocity appears physical. We termed these events Low Frequency Icequakes (LFIs), in anticipation of their glaciogenic origin.

4.5 Possible Sources of LFIs

There are three competing hypotheses capable of explaining the origin of the low frequency icequakes, or LFIs. Under the first hypothesis, this seismic energy was not glaciogenic, but generated by overhead aircraft generating air-pressure pulses that were transmitted into the near surface ice where the geophones are buried. This would explain the apparent high velocity of the near vertical wavefronts, but also requires a non-emergent source of energy capable of coherently exciting the 4.5Hz geophones to their observed displacement amplitudes (Figure 4.6). To test this possibility, we computed the transmission coefficient coupling acoustic energy between air and ice ($2.5 \cdot 10^{-4}$ at 0° C) and estimated a minimum an over-pressure of ~ 1 Pa in the air (equivalent in power to loud traffic) [**?**]. It is physically implausible that this occurred at each geophone within a 6km aperture at the same time (coherently), and we reject it.

Under the second hypothesis, the recorded seismic energy was teleseismic in source, rather than glaciogenic. We evaluated this by examining global catalogs for remote earthquakes coincident with the LFI events. In three cases, we found consistency in timing between magnitude $M_w = 5.0 - 7.3$ events originating from the Aleutian region of Southwest Alaska. We removed these events from our database of candidate LFI events, and used them compute station amplitude corrections (e.g., [55]) for later magnitude determination. Teleseismic sources could not be attributed to the remaining LFI events, and we therefore rejected this hypothesis as well.

Under the third hypothesis, the seismic energy was caused by regional glaciogenic events. In this case, we suggest that either rapid basal sliding or calving of glacial ice within an ice catchment northwest of our study site (Figure 4.1) is the most likely source of this energy. This direction coincides with the distribution of 90-120 degree arrival angles for coherent waveforms in Figure 4.6.

4.7, and the dense cluster of slowness values (inverse horizontal velocity) that indicate frequent higher-than-ice velocities. A subset of detected events indicates more remote, but

non-teleseismic sources. In these cases, seismic rays leaving the seismic hypocenters must have refracted deeply into Earth structure to return from depth toward the ice sheet surface at near vertical incidence. This refracting velocity gradient must further dip from West-to-East to return the seismic rays at near vertical toward our network and produce the apparent high velocities (up to 14 km/sec). Again, we propose that these sources are likely to be from rapid ice motion northwest of our network. The remaining event population displayed slowness values consistent with both body waves and surface waves arrivals within ice (Figure 4.7, black ring). Much slower wave speeds outside the expected range for ice may indicate erroneously aligned waveforms from our cross-correlation analysis (Figure 4.6), or dispersed, high order (slower traveling) modes of Rayleigh waves. We additionally note that Jakobshavn Glacier (69.1667° N, 49.8333° W) is the most probable glacial body to generate low frequency, high magnitude seismicity from this direction. Jakobshavn Glacier has in fact produced well-documented longer duration ($\sim$ 45 min) long-period energy at a similar distances ($\sim$ 50 km) and may indicate culminating iceberg calving processes [133]. The waveform durations we observe here are significantly shorter, but still well above the expected duration of a microseismic event.

To determine the size of these events, we estimate body-wave magnitudes using reasoning conventionally applied to interpreting waveforms from teleseismic sources (e.g., [15]). First, we assume the seismic rays leaving the hypocentral focal sphere that arrive at our remote geophone network effectively sample the same region of that focal sphere. This means that the waveform amplitudes recorded at each geophone are roughly scaled by the same radiation pattern coefficient. Therefore, we can average the root-mean-square (RMS) displacement amplitudes over the network to compute the amplitude A used in a body-wave magnitude scale, mb. We use the teleseismic events (gray markers, Figure 4.7) to equalize the ground displacement, and further correct A for instrument response, attenuation, and geometric spreading as done in Chapter 3. These amplitudes are then used to compute magnitudes by implementing $m_b = \log_{10}(\frac{A_0}{T})$ for a period $T = \frac{4}{3}$ sec, where A_0 is the estimated (corrected) source amplitude at zero hypocentral distance. Following others ([133]), we crudely assume the seismic source is 50 km away and use a seismic quality factor of ice

that we estimated in Chapter 3 from Rayleigh wave data; this factor is only appropriate for waveforms with significant propagation path through the ice, and likely results in an underestimate of the magnitudes for events involving seismic ray-paths through geological structure beneath the ice sheet and small slowness. Regardless, we thereby find an average magnitude of $m_b = 1.5$ and greater, with some values near $m_b = 3$ (Figure 4.8). The geophysical source of these LFIs was necessarily large relative to that of the surficial icequakes discussed in Chapter 3 with the same computed magnitude. This follows from the recording limitation of the L-28 geophones used here, which are insensitive to ground motion (velocity) generating energy significantly below 4.5Hz. This means the magnitudes in Figure 4.8 constitute a lower bound on the true magnitudes [55]. By performing the necessary instrument response deconvolution required to compute displacements from velocity, we calculate a reduction in amplitudes of $< 250\times$ at ~ 0.75Hz, relative to that within the pass band. This means that a high-frequency (< 4.5Hz) event with magnitude $m_b - 1$ would be apparently larger than LFI with a magnitude m_b. Further, the spectral localization for some of this narrowband energy is probably controlled by glacial structure for those events slowness values consistent with ice propagation (Figure 4.7). To explain this, we model the ice sheet as an elastic plate overlying a half-space with a relatively high seismic phase velocity. The characteristic eigenfrequenices (resonant modes) of the ice column are thereby estimated from the physical properties of the propagating media and the impedance contrast between them [129]. This calculation is used by others [133], to compute eigenfrequencies near $\sim$1Hz for the first two eigenmodes, which are within range observed in Figure 4.2.

If Jakobshavn Glacier is the source of this large magnitude seismicity, we may further consider that oceanic tidal forcing drives these events. This consideration is motivated by in part by apparent repetition of the monochromatic energy bands that are sometimes spaced throughout the spectrograms in a given day (Figure 4.2). In this case, we consider increasing and decreasing tide heights to provide a potential forcing for episodic basal sliding by triggering both push-back and unloading via water column contact at the ice stream terminus. Analogous forcing has been observed on Antarctic ice streams [2] and has triggered a seismic basal response as far as 85 km upstream [5]. To assess coastal forcing as a possible driver of

seismicity, we use tide table data made available by the Danish Coastal Authority (`http://frv.dk/en/Measurements/Fairway_measurements/Pages/Tide_tables.aspx`) and compare water heights near Disco Bay, Greenland, with network-averaged root-mean-square amplitudes computed from each LFI. This comparison is illustrated in Figure 4.9, with the marker sized scaled by the square-root of the mean amplitude (plus a constant). The LFIs appear at both high and low tides, though a statistical test using binary Bernoulli trials to describe high/low tide coincidence with LFI events (e.g., [92] suggests our sample size is too small to confidently assert or dismiss a causal relationship. We suggest that this deserves additional work.

4.6 Conclusions

An objective of this work was to identify the significance of basal or deep englacial seismicity within the lake forming ablation zone of Western Greenland. We demonstrated that basal seismicity from sliding is simply more difficult to detect relative to surface icequakes. This is due to path effects (geometric spreading, attenuation) and means that basal icequakes must have a ~ 1.5 greater magnitude relative to surficial icequakes in order to match detection rates. This problem is less pronounced at lower frequencies, which spectrally scales as $\exp\left(-\frac{\pi R \xi}{cQ}\right)$. We found that notably energetic bursts of low frequency seismicity was characterized by narrowband sub-1Hz icequakes (LFIs) that were observable network-wide, and that the timing of this seismicity did not have an obvious time-of-day bias as surficial seismicity did. This suggests that these events were not sensitive to locally produced meltwater input. Most of these LFI signals were likely generated by remote glacial earthquakes occurring near the west coast of Greenland, in the vicinity of Jabobshavn Glacier. This suggest that large-scale glacial deformation processes can be observed remotely $\sim$ 50km from their respective forcing mechanism. Finally, we suggest that local surficial seismicity and basal seismicity effectively serve as distinct observables for different processes on the Greenland Ice Sheet. Rayleigh waves from local sources provide an indicator for strain localization that may be undersampled by GPS measurements. Basal seismicity may be most useful for detecting regional deformation processes at very low frequencies that are not as susceptible to high attenuation, and its study would benefit from additional research.

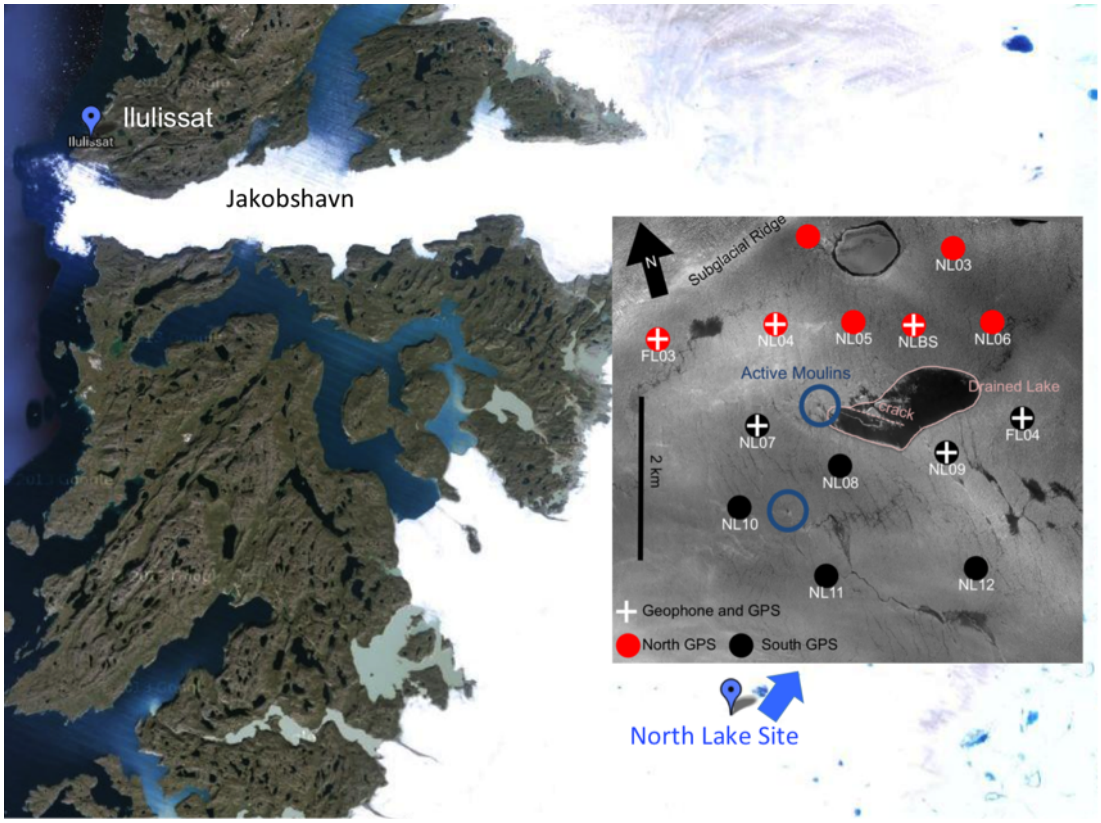

Figure 4.1: The study site (68.73° N, 49.53°W) in Chapter 3 superimposed with a Google Earth image of the larger ablation zone region. The south-most blue marker indicates the lake site. The circular markers indicated by crosses on the digital elevation model inset represent seismometers superimposed with GPS receivers. Jabobshavn Glacier and the city of Ilulissat are labeled for geographical reference.

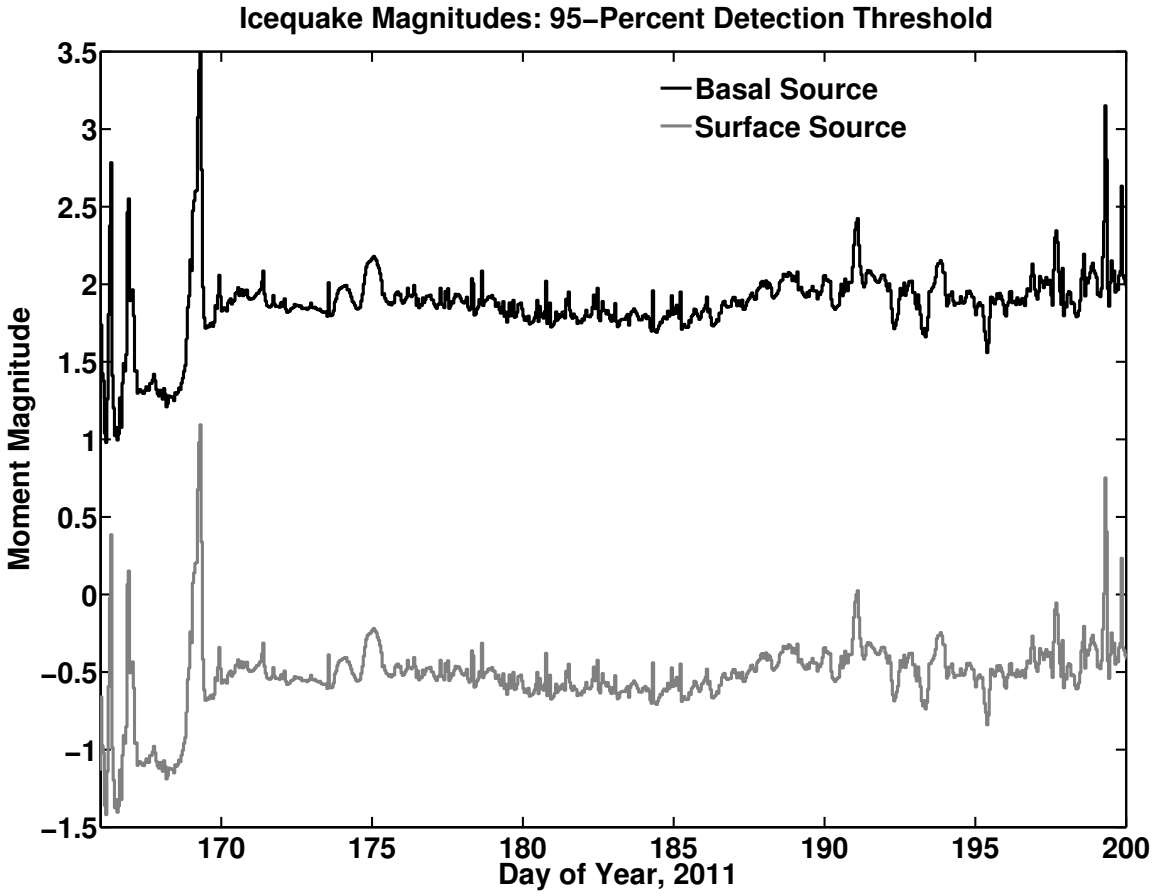
Icequake Magnitudes: 95−Percent Detection Threshold
Basal Source
Surface Source
Moment Magnitude
3.5
3
2.5
2
1.5
1
0.5
0
−0.5
−1
−1.5
170
175
180
185
190
195
200
Day of Year, 2011

Figure 4.2: Icequake threshold magnitudes for surface and basal sources. The black curve illustrates hourly estimates magnitudes for basal-slip icequakes that have a 95% probability of being detected at receiver NL07 when located directly beneath the center of the geophone network in Figure 4.1. The gray curve shows the corresponding detection magnitude for surficial seismicity triggered by opening fractures.

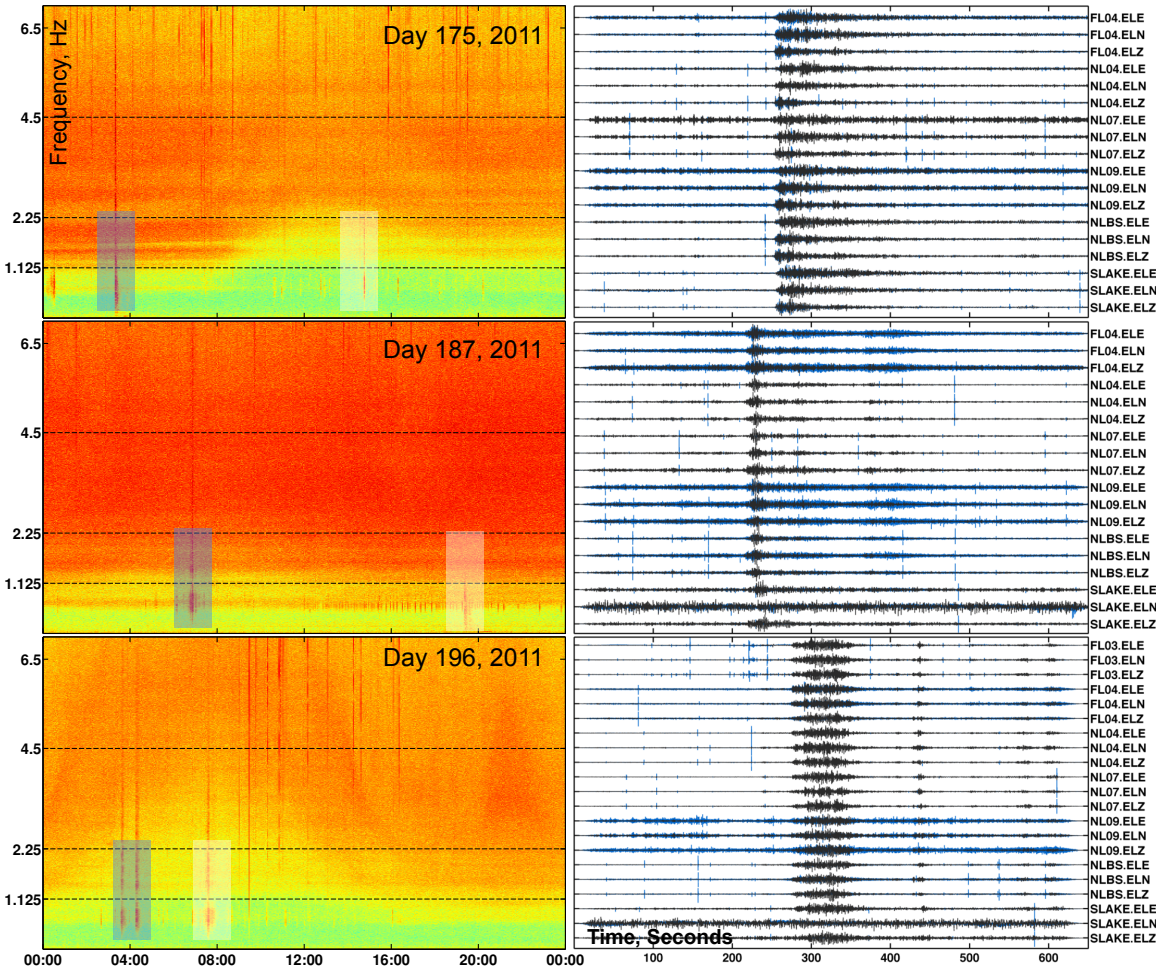
Day 175, 2011
Day 187, 2011
Day 196, 2011
Frequency, Hz
6.5
4.5
2.25
1.125
00:00
04:00
08:00
12:00
16:00
20:00
00:00
Time, Seconds
100
200
300
400
500
600
FL04.ELE
FL04.ELN
FL04.ELZ
NL04.ELE
NL04.ELN
NL04.ELZ
NL07.ELE
NL07.ELN
NL07.ELZ
NL09.ELE
NL09.ELN
NL09.ELZ
NLBS.ELE
NLBS.ELN
NLBS.ELZ
SLAKE.ELE
SLAKE.ELN
SLAKE.ELZ
FL03.ELE
FL03.ELN
FL03.ELZ

Figure 4.3: Daily spectrograms and 650 second seismic record sections illustrating bursts of low frequency energy detected throughout the geophone network in Figure 4.1. Black dashed lines indicate the 4.5Hz peak instrument response, and $\frac{1}{2}$ and $\frac{1}{4}$ peak response frequencies. The blue highlighted region indicates which burst of energy is associated with the record section on the right. The white highlight indicates a subset of additional events. The blue traces data on the right in each record section shows unfiltered data, while the superimposed black traces show data band-pass filtered to [0.2, 2.5] Hz.

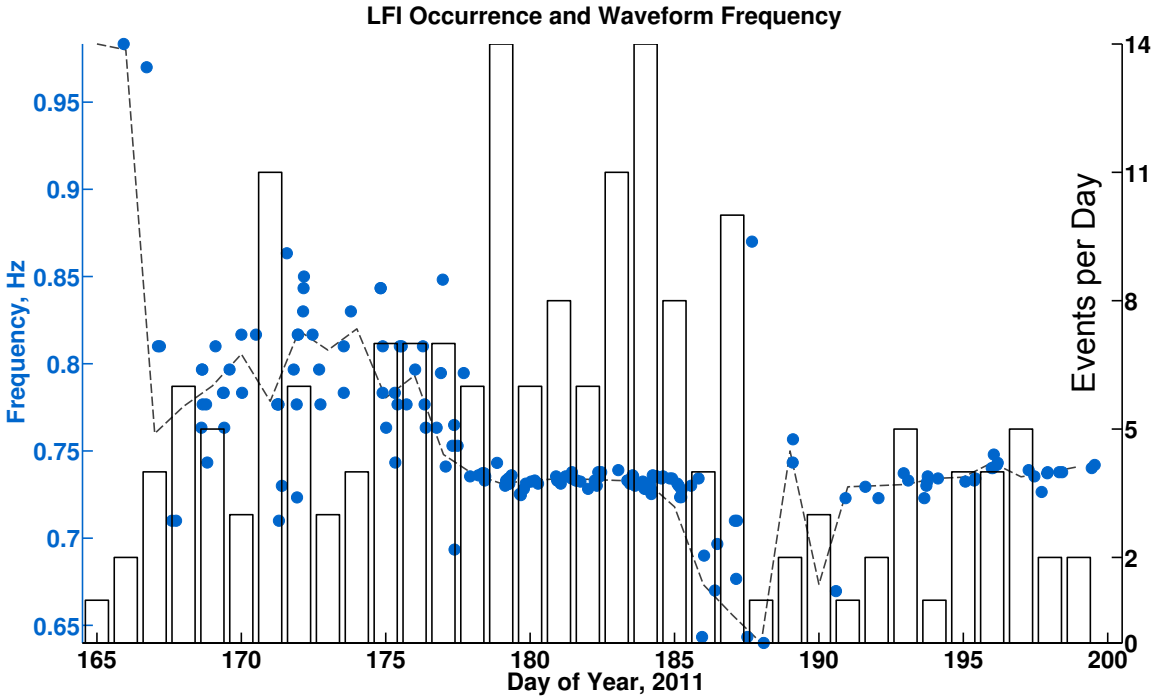

Figure 4.4: Bar plot illustrating occurrence of LFI events, in events per day. Blue markers show the measured dominant frequency of the LFI waveforms. The gray dashed line indicates the dominant frequency, averaged by day.

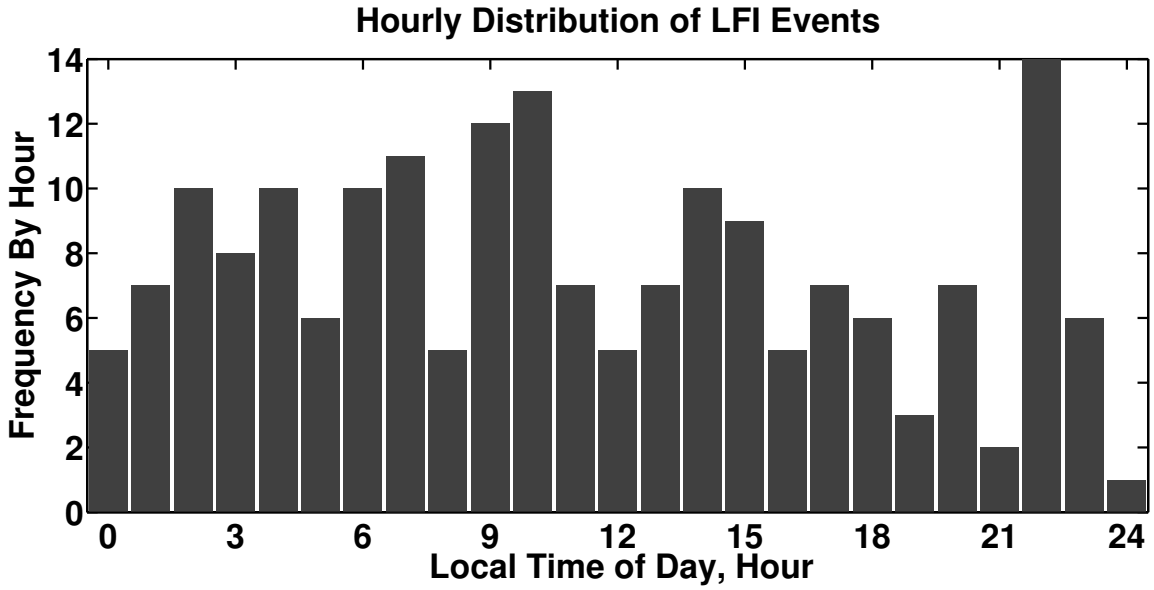

Figure 4.5: A histogram of LFI events binned by hour of day, showing a lack of any day-to-night bias and apparent multi-peaking.

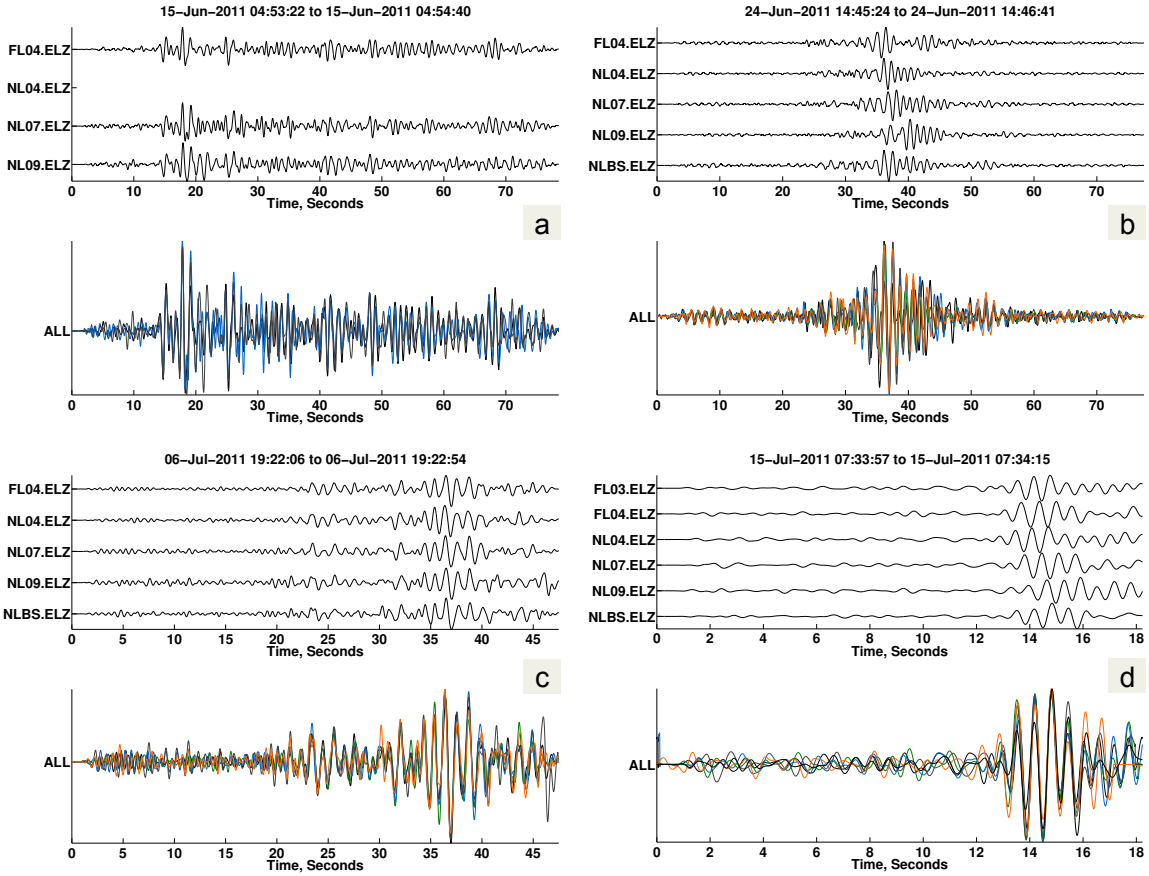

Figure 4.6: A set of vertical-channel seismograms (top, each panel) illustrated with a superposition of the same traces (bottom, each panel), after being temporally aligned to maximize the intra-receiver correlation and demonstrate waveform coherence across the network. Panels (a)-(d) show LFI events observed days 166, 179, 187, and 196

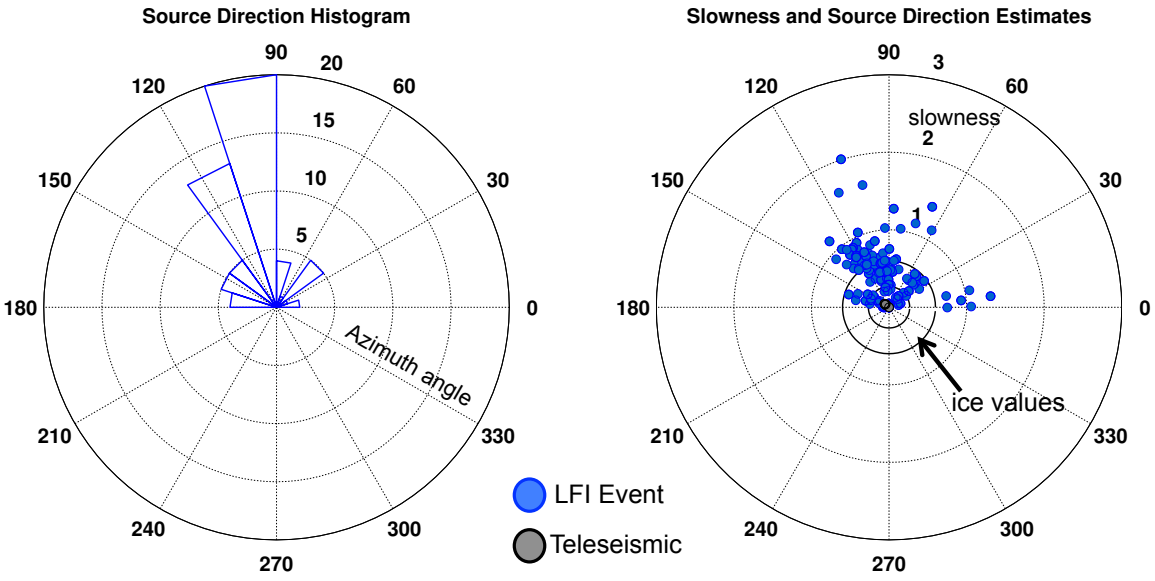
Source Direction Histogram
90
20
60
120
15
30
150
10
0
5
180
Azimuth angle
210
330
240
300
270
LFI Event
Teleseismic
Slowness and Source Direction Estimates
90
3
60
120
slowness
2
30
150
1
0
180
ice values
210
330
240
300
270

Figure 4.7: Left: A polar representation for the source direction angle histogram, computed from back-azimuth estimates for 60 LFI events. Angle 90° indicates North, and 0° indicates East. The lines of constant angle indicate different source direction angles, and the curves of constant radii indicate number of events in a bin. Right: Polar representation of the horizontal slowness and source direction, with the same angular convention as the left plot. The black ring indicates the range of slowness values if single-phase wave propagation was exclusively confined to glacial ice. Slowness values closer to the origin indicate faster-than-ice seismic wave speeds, and values farther from the origin indicate slower speeds. Blue markers indicate values of inverted slowness and azimuthal angles. The gray markers indicate likely teleseismic events, shown for reference.

.

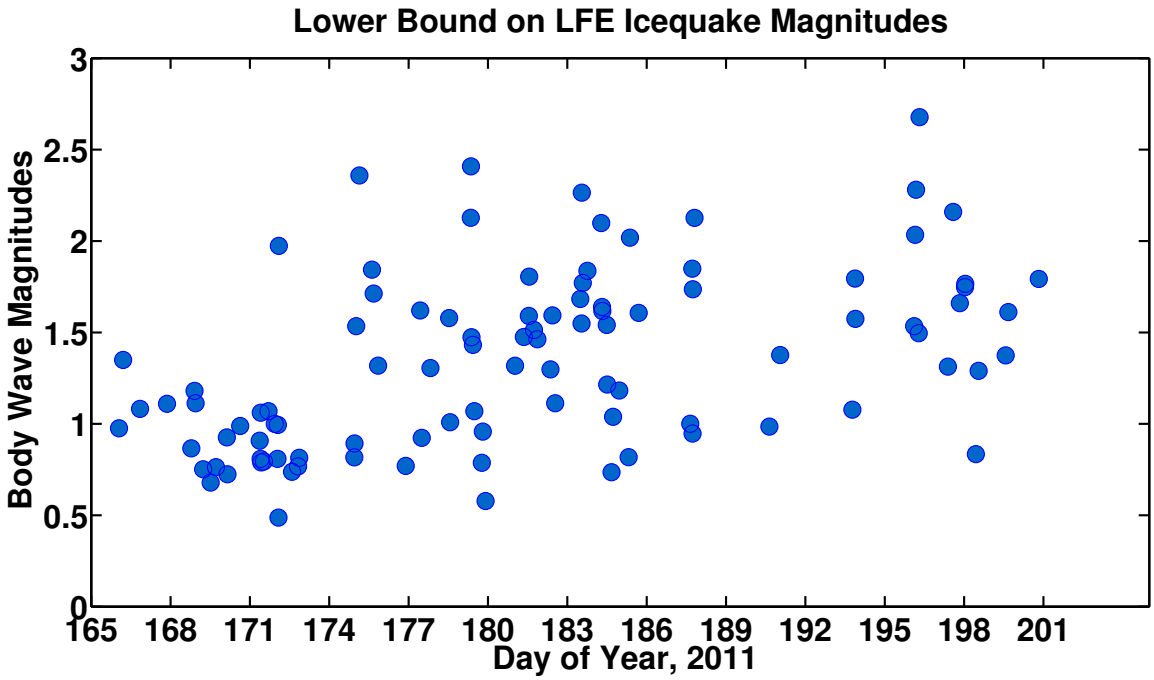
Lower Bound on LFE Icequake Magnitudes
Body Wave Magnitudes
Day of Year, 2011
0
0.5
1
1.5
2
2.5
3
165
168
171
174
177
180
183
186
189
192
195
198
201

Figure 4.8: Body wave magnitudes computed from network-averages of the root-mean-square waveform amplitudes after correcting for station location, attenuation, geometric spreading, and instrument response. These are likely lower bound estimates on the true magnitudes, since the L-28 is insensitive the low frequencies characterizing these events.

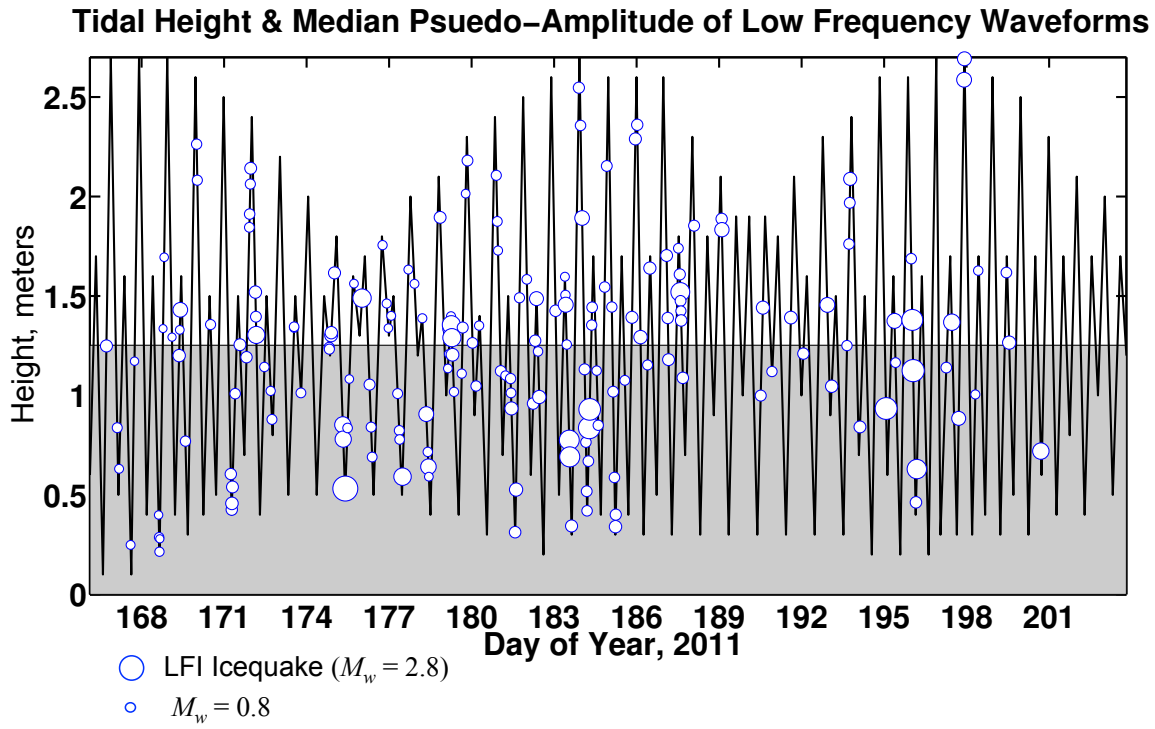

Figure 4.9: Comparisons between tides and coincident LFI magnitudes. The black curve indicates the tidal values near Jacobshavn Glacier. The white markers indicated low frequency events, and marker size scales as the square root of the RMS amplitude of the seismic waveforms, averaged over the network. Larger markers thereby indicate larger icequakes, as shown in the legend. The gray shading shows tidal height values below mean tide.

Chapter 5

CONCLUSIONS REGARDING SEISMICITY IN POLAR ICE

This conclusion is a summary of the work conducted in this thesis and it's anticipated impact on glaciology and seismology. It reviews how seismic observations provide insight into transient forcing of polar ice. I focus on general interpretations from the experiments covered in Chapters 2-4, their consistencies, and their differences. Last, I review the material in Appendices A-C to identify practical issues associated acquiring and processing data from noisy, ablation zone environments.

5.1 Synthesis of Scientific Work and its Impact

I composed this thesis with two primary objectives: (1) to determine how meltwater triggers seismic observables to indicate glaciogenic response and (2) to address evidence of undocumented feedbacks that could destabilize polar ice in the near future. To confront these objectives, I considered two hydrologically dissimilar polar glacial environments. The first of these environments was Taylor Glacier (Chapter 2), which terminates in one of the driest deserts in the world. It consists of sub-freezing ice with low accumulation rates, no firn layer or extensive crevassing, and is apparently absent of a subglacial drainage system that would facilitate sliding. This last feature explains why our terminus-deployed GPS measurements reflected no summer speedup (Figure 2.12). Rather, a single deep crack near the terminus (the Blood Falls crack), initially created by unique brine release episodes from a subsurface pocket, provided the only clear surface-to-subglacial pathway for water. Further, this input did not trigger sliding. The simplicity of this glacial environment allowed us (the contributing authors of Chapter 2) to isolate the response mechanisms starting from pre-melt season initial conditions.

Our experiment at Taylor Glacier was thereby an effort to establish a "baseline" for melt-

season seismic observations in the absence of complicating sources of either water storage or seismogenesis. In this experiment, we found that almost any nonzero melt triggered large co-located microseismic events consisting primarily of body waves. These events were best explained as volumetric expansion of meltwater freezing within deep englacial or subglacial fractures, and this likely sustained the surface-to-bed hydrological connection. More importantly, the absence of sliding or additional crevassing indicated that the cumulative, hypocenter volumetric growth could occur through melt input alone.

These observations had two important implications, one specific to Taylor Glacier, and two to polar glaciers in general. The specific implication is that meltwater input to the Blood Falls crack likely created additional fracture volume that allowed it to persist; whatever the initial mechanism created it, this crack probably remained a brine release point because it provided a catchment for following meltwater input. The related broader implication is that hydraulic pathways in cold ice can remain open through growth of volumetric fracture events triggered by expanding, refreezing water at depth. To our knowledge, this mechanism, similar to frost heaving-induced breaking of rocks ([33, 117], and references therein) has not been documented before as a seismic source. We suggest that experiments should be conducted to determine what physical conditions are required for freezing water to crack ice.

In Chapter 3, we considered a second environment, the lake-forming region within the ablation zone on the Western Greenland Ice Sheet. In contrast to Taylor Glacier, melt-assisted basal sliding is observed year round in Western Greenland, snow layers are deposited each summer, annual ablation rates consistently exceed 1 m, and surface-to-subglacial meltwater input is extensive [82, 69]. Supraglacial lake drainage events [32, 17] can deliver $\sim 10^7\,\mathrm{m}^3$ of water to the bed in hours [37], and provide subsequent surface meltwater input access to the bed. The introduction of this meltwater can pressurize and lubricate the ice-bed interface and thereby trigger episodes of diurnally-modulated speedup. We studied seismic emissions after a lake drainage created such a new moulin early in the melt season to observe the ice sheet response characteristics present with a presumably distributed, inefficient subglacial drainage system.

Our observations were somewhat counterintuitive: we found that the dominant signal following lake drainage was not from basal deformation. Rather, we observed pervasive surficial seismicity indicated by Rayleigh waves, and triggered by tensile fracturing. The source locations for these fracture-events also seemed to depend on the timing of drainage, and shifted after the drainage-created moulin was available to take meltwater input. We further found that complicated, localized spatial gradients in ice flow speedup provided a plausible cause for this forcing mechanism, and that increased seismicity at night could be explained by spatial heterogeneity in basal drag that developed during decreased melt input. Interestingly, GPS speeds were not a clear indicator for timing in seismicity. Rather, we suggest that remote sensing methods for measuring surface speeds (like TerraSar-X [81]) provide better comparison for the localized elastic response we observed near these lakes.

In Chapter 4, we continued our study in Greenland by targeting sources of non-surficial seismicity to determine a physical cause of it's apparent deficiency. We used a Rayleigh wave detector to segregate surficial icequake sources from the remaining detections and identified a small population of potential body-wave seismicity. By restricting our attention further to lower frequency bands ($\leq$ 7Hz), we found repeating, sub-1Hz seismic events of non-local, glaciogenic origin. Their respective waveforms were nearly monochromatic, and roughly 100 sec in total duration. Estimated slowness-vectors consistently pointed West of the network.

Finally, there appear to be significant differences in glacial response to meltwater, depending on the presence or absence of a subglacial drainage system and melt-triggered basal sliding. Meltwater forcing of the sub-freezing ice at Taylor Glacier produced body-wave seismicity from deep englacial or subglacial cracks in the absence of basal sliding. In contrast, melt season seismicity was attributed to surface cracking rather than deeper icequakes in Greenland, where basal sliding was variable and active. Any association of melt-driven seismicity in subfreezing ice within the Greenland Ice Sheet will likely become important in a future warming climate. In such a climate, the current ablation zone is expected to expand into

higher elevations and latitudes [11]. This means that supraglacial lakes could also form and drain to create moulins capable of delivering surface-generated meltwater to the bed where such pathways had previously have been absent. This also means that such surface meltwater forcing may become important at these new locations for this first time. The results I have summarized here may indicate what early indicators of this forcing will look like.

5.2 Impact on Seismic Monitoring Methods and Recommendations

I adapted the statistical signal processing methods that are documented in Appendix A largely to address challenges associated with detecting icequakes on the Greenland Ice Sheet. These challenges were perceived formidable enough elsewhere (e.g., [37]) that geophone data collected from lake sites similar to ours was left largely uninterpreted. The development of these statistically robust detection tools provides a verifiable improvement on their applicability to interpreting icequakes from noisy glacial environments.

One key to improving the capability each of the signal detectors (energy, Rayleigh, multiplet) was to use **objectively**-set thresholds. This required implementing a decision rule known as the Neyman-Pearson criterion. This criterion is generally set by prescribing an acceptable false alarm (false detection) probability when the associated distribution functions in the signal-absent and signal-present case are both known. Such thresholding required accurately describing these distribution functions and was challenged by incomplete knowledge of the effective degrees of freedom within the seismic data (for remote sensing data, see Joughin *et al.*, [85, 84]). I showed in detail how correlated noise or narrowband processing can create an obvious disagreement between the hypothesized (assumed) distribution functions and the observed distribution functions, but that this loss can also be accounted for (Figure A.7). Without re-parameterizing these distribution functions, such detectors generally produce a greater number of false detections. Maintaining detector integrity is particularly important for evaluating whether or not a diurnally variable signal is physically periodic, or a reflection of a diurnally varying detection threshold (e.g., Figure A.11).

BIBLIOGRAPHY

[1] S Aanadakrishnan and CR Bentley. Micro-Earthquakes Beneath Ice Stream-B and Ice Stream-C, West Antarctica-Observations and Implications. *Journal of Glaciology*, 39(133):455–462, 1993.

[2] G. Adalgeirsdottir, A.M. Smith, T. Murray, M.A. King, K. Makinson, K.W. Nicholls, and A.E. Behar. Tidal influence on Rutford Ice Stream, West Antarctica: observations of surface flow and basal processes from closely spaced GPS and pasive seismic stations. *Journal of Glaciology*, 54(187):715–724, 2008.

[3] Keiti Aki and Paul G. Richards. *Quantitative Seismology.* W.H. Freeman and Company, San Francisco, CA, USA, 1980.

[4] Keiti Aki and Paul G. Richards. *Quantitative Seismology.* University Science Books, Sausalito, CA, USA, 2nd edition, 2002.

[5] S Anandakrishnan and RB Alley. Tidal forcing of basal seismicity of ice stream C, West Antarctica, observed far inland. *JOURNAL OF GEOPHYSICAL RESEARCH-SOLID EARTH*, 102(B7):15183–15196, JUL 10 1997.

[6] Kevin K. Anderson. Network detection and association: Statistical assessment of performance. Technical Report DE-AC06-76RLO 1830, Battelle Pacific Northwest Labs, August 1995. ID: 831631045.

[7] Ted L. Anderson. *Fracture mechanics : fundamentals and applications.* Boca Raton, FL: Taylor and Francis, Boca Raton, FL, 2005. ID: UW21342072260001452; Includes bibliographical references and index.

[8] Zdeněk P. Bažant. Large Scale Thermal Bending of Sea Ice Plates. *Journal of Geophysical Research*, 97(C11):17739–17751, 1992.

[9] Alison F. Banwell, Neil S. Arnold, Ian C. Willis, Marco Tedesco, and Andreas P. Ahlstrom. Modeling supraglacial water routing and lake filling on the greenland ice sheet. *Journal of Geophysical Research-Earth Surface*, 117:F04012, OCT 18 2012. PT: J; TC: 0; UT: WOS:000310071400001.

[10] Timothy. C Bartholomaus, Christopher F Larsen, Shad O'Neel, and Michael West. Calving seismicity from iceberg-sea surface interactions. *Journal of Geophysical Research*, pages 1–8, December 2012.

[11] Ian Bartholomew, Peter Nienow, Andrew Sole, Douglas Mair, Thomas Cowton, Steven Palmer, and Jemma Wadham. Supraglacial forcing of subglacial drainage in the ablation zone of the Greenland ice sheet. *GEOPHYSICAL RESEARCH LETTERS*, 38, APR 21 2011.

[12] R. R. Blandford. An automatic event detector at the tonto forest seismic observatory. *GEOPHYSICS GEOPHYSICS*, 39(5):633–643, 1974. ID: 4641584412.

[13] John Boatwright. A Spectral Theory for Circular Sesimic Sources; Simple Estimates of Source Dimension, Dynamic Stress Drop, and Radiated Seismic Energy. *Bulletin of the Seismological Society of America*, 70(1):1–27, 1980.

[14] Sarah Boon and Martin. Sharp. The Role of Hydrologically-Driven Ice Fracture in Drainage System Evolution on an Arctic Glacier. *Geophysical Research Letters*, 30(1916), 2003.

[15] David M. Boore and John Boatwright. Average Body Wave Radiation Coefficients. *Bulletin of the Seismological Society of America*, 74(5):615–621, 1984.

[16] David Bowers and John A. Hudson. Defining the Scalar Moment of a Seismic Source with a General Moment Tensor. *Bulletin of the Seismological Society of America*, 89(5):1390–1394, 1999.

[17] Box, Jason E. and Ski, Kathleen. Remote sounding of Greenland supraglacial melt lakes: implications for subglacial hydraulics. *Journal of Glaciology*, 53(181):257–265, 2007.

[18] Charles C. Bradley. Mendota quake. *American Journal of Science*, 246(6):390, 1948.

[19] Richard E. Brandt and Stephen Warren. Solar-Heating Rates and Temperature Profiles in Antarctic Snow and Ice. *Journal of Glaciology*, 39(131):99–110, 1993.

[20] Pierre Dalban Canassy, Jerome Faillettaz, Fabian Walter, and Matthias Huss. Seismic activity and surface motion of a steep temperate glacier: a study on triftgletscher, switzerland. *Journal of Glaciology*, 58(209):513–528, 2012. PT: J; NR: 45; TC: 0; J9: J GLACIOL; PG: 16; GA: 959KB; UT: WOS:000305310200007.

[21] Joshua D. Carmichael, Erin C. Pettit, Matt Hoffman, Andrew G. Fountain, and Bernard Hallet. Seismic multiplet response triggered by melt at Blood Falls, Taylor Glacier, Antarctica. *Journal of Geophysical Research*, 117, 2012.

[22] G. A. Catania and T. A. Neumann. Persistent englacial drainage features in the Greenland Ice Sheet. *Geophysical Research Letters*, 37, JAN 29 2010.

[23] Ginny A. Catania, Thomas A. Neumann, and Stephen F. Price. Characterizing englacial drainage in the ablation zone of the Greenland ice sheet. *Journal of Glaciology*, 54(187):567–578, 2008.

[24] Eric P. Chael. An automated Rayleigh-wave detection algorithm. *BULLETIN OF THE SEISMOLOGICAL SOCIETY OF AMERICA*, 87(1):157–163, FEB 1997.

[25] X. Chen, P. M. Shearer, F. Walter, and H. A. Fricker. Seventeen antarctic seismic events detected by global surface waves and a possible link to calving events from satellite images. *Journal of Geophysical Research-Solid Earth*, 116:B06311, JUN 30 2011 2011. PT: J; TC: 4; UT: WOS:000292383800002.

[26] GKC Clarke. Subglacial Processes. *Annual Review Of Earth and Planetary Sciences*, 33(128):247–276, 2005.

[27] Kurt Cuffey and W. S. B. Paterson. *The physics of glaciers*. Elsevier, Butterworth-Heinemann, Amsterdam [u.a.], 2011. ID: 785836310.

[28] Kurt M. Cuffy and W.S.B Paterson. *The Physics of Glaciers*. Elsevier, Burlington, MA, USA, 4th edition, 2010.

[29] Gayle L Dana, RE Davis, AG Fountain, and RA Wharton. Satellite-derived indices of stream discharge in Taylor Valley, Antarctica. *Hydrological Processes*, 16, 2002.

[30] Stefania Danesi, Stephen Bannister, and Andrea Morelli. Repeating earthquakes from rupture of an asperity under an antarctic outlet glacier. *Earth and Planetary Science Letters*, 253(1-2):151–158, JAN 15 2007. PT: J; NR: 36; TC: 11; J9: EARTH PLANET SC LETT; PG: 8; GA: 136AK; UT: WOS:000244194800012.

[31] Sarah B. Das, Mark D. Behn, and Ian R. Joughin. Modes of Supraglacial Lake Drainage and Dynamic Ice Sheet Response. In *American Geophysical Union, Fall Meeting 2011*, 2011.

[32] Sarah B. Das, Ian Joughin, Mark D. Behn, Ian M. Howat, Matt A. King, Dan Lizarralde, and Maya P. Bhatia. Fracture Propagation to the Base of the Greenland Ice Sheet During Supraglacial Lake Drainage. *Science*, 320(5877):778–781, May 2008.

[33] J.G. Dash, A.W. Rempel, and J. S. Wettlaufer. The Physics of Premelted Ice and its Geophysical Consequences. *Reviews of Modern Physics*, 78(3):695–741, 2006.

[34] GP DAVIDSON and JF NYE. A PHOTOELASTIC STUDY OF ICE PRESSURE IN ROCK CRACKS. *COLD REGIONS SCIENCE AND TECHNOLOGY*, 11(2):141–153, 1985.

[35] Julia de Juan, Pedro Elosegui, Meredith Nettles, Tine B. Larsen, James L. Davis, Gordon S. Hamilton, Leigh A. Stearns, Morten L. Andersen, Goeran Ekstroem, Andreas P. Ahlstrom, Lars Stenseng, S. Abbas Khan, and Rene Forsberg. Sudden increase in tidal response linked to calving and acceleration at a large greenland outlet glacier. *Geophysical Research Letters*, 37:L12501, JUN 23 2010 2010. PT: J; TC: 6; UT: WOS:000279307700003.

[36] N. Deichmann, J. Ansorge, F. Scherbaum, A. Aschwanden, F. Bernardi, and G.H. Gudmundsson. Evidence for Deep Icequakes in an Alpine Glacier. *Annals of Glaciology*, 31(1):85–90, 2000.

[37] S. H. Doyle, A. L. Hubbard, C. F. Dow, G. A. Jones, A. Fitzpatrick, A. Gusmeroli, B. Kulessa, K. Lindback, R. Pettersson, and J. E. Box. Ice tectonic deformation during the rapid in situ drainage of a supraglacial lake on the Greenland Ice Sheet. *CRYOSPHERE*, 7(1):129–140, 2013.

[38] G. Ekstrom, M. Nettles, and G. A. Abers. Glacial earthquakes. *Science*, 302(5645):622–624, OCT 24 2003 2003. PT: J; TC: 86; UT: WOS:000186119900052.

[39] G. Ekstrom, M. Nettles, and V. C. Tsai. Seasonality and increasing frequency of greenland glacial earthquakes. *Science*, 311(5768):1756–1758, MAR 24 2006 2006. PT: J; TC: 64; UT: WOS:000236204300039.

[40] Mark Fahnestock. *Hydrological Control and Sliding Velocity of Two Alaskan Glaciers: Observations and Theory*. PhD thesis, California Institute of Technology, 1991.

[41] AG Fountain, WB Lyons, MB Burkins, Gayle L Dana, PT Doran, KJ Lewis, DM McKnight, DL Moorhead, AN Parsons, JC Priscu, DH Wall, RA Wharton, and RA Virginia. Physical controls on the Taylor Valley ecosystem, Antarctica. *Bioscience*, 49:961–971, 1999.

[42] Andrew G. Fountain, Matthew J. Hoffman, Frank Granshaw, and Jon Riedel. The 'benchmark glacier' concept - does it work? lessons from the north cascade range, usa. *Annals of Glaciology*, 50(50):163–168, 2009. PT: J; TC: 6; UT: WOS:000279990100024.

[43] Andrew G. Fountain, Robert W. Jacobel, Robert Schlichting, and Peter Jansson. Fractures as Main Pathways of Water Flow in Temperate Glaciers. *Nature*, 433(7026):618–621, 2005.

[44] Andrew G. Fountain, Thomas H. Nylen, Karen Lewis MacClune, and Gayle L. Dana.

Glacier Mass Balances (1993-2001), Taylor Valley, McMurdo Dry Valleys, Antarctica. *Journal of Glaciology*, 52(178):451–462, 2006.

[45] Andrew G Fountain and Joseph S. Walder. Water Flow through Temperate Glaciers. *Reviews of Geophysics*, 36(3):299–328, 1998.

[46] T. J. Fudge, J. T. Harper, N. F. Humphrey, and W. T. Pfeffer. Rapid glacier sliding, reverse ice motion and subglacial water pressure during an autumn rainstorm. *Annals of Glaciology*, 50(52):101–108, 2009. PT: J; NR: 39; TC: 6; J9: ANN GLACIOL; PG: 8; GA: 640FH; UT: WOS:000281033800014.

[47] Walter I. Futterman. Dispersive body waves. *Journal of Geophysical Research*, 67(13):5279–5291, 1962.

[48] R.E. Gagnon and P.H. Gammon. Characterization and Flexural Strength of Iceberg and Glacier Ice. *Journal of Glaciology*, 41(137):103–111, 1995.

[49] P.H. Gammon, H. Kiefte, M.J Clouter, and W.W. Denner. Elastic-Constants of Artificial and Natural Ice Samples by Brillouin Spectroscopy. *Journal of Glaciology*, 29(103):433–460, 1983.

[50] Steven J. Gibbons, Mathilde Bottger Sorensen, David B. Harris, and Frode Ringdal. The detection and location of low magnitude earthquakes in northern norway using multi-channel waveform correlation at regional distances. *Physics of the Earth and Planetary Interiors*, 160(3-4):285–309, MAR 16 2007. PT: J; TC: 14; UT: WOS:000244572200007.

[51] Steven J. Gibbons, Tormod Kvaerna, and Frode Ringdal. Considerations in phase estimation and event location using small-aperture regional seismic arrays. *Pure and Applied Geophysics*, 167(4-5):381–399, MAY 2010. PT: J; TC: 3; UT: WOS:000276260500002.

[52] Steven J. Gibbons and Frode Ringdal. The Detection of Low Magnitude Seismic Events using Array–Based Waveform Correlation. *Geophysical Journal International*, 165(1):149–166, 2006.

[53] Steven J. Gibbons, Frode Ringdal, and Tormod Kvaerna. Ratio-to-moving-average seismograms: a strategy for improving correlation detector performance. *GEOPHYSICAL JOURNAL INTERNATIONAL*, 190(1):511–521, JUL 2012.

[54] Steven J. Gibbons, Frode Ringdal, and Tormod KvErna. Detection and characterization of seismic phases using continuous spectral estimation on incoherent and partially coherent arrays. *Geophysical Journal International*, 172(1):405–421, JAN 2008. PT: J; TC: 4; UT: WOS:000251669800030.

[55] Slawomir Jerzy Gibowicz and Andrzej Kijko. *An Introduction to Mining Seismology.* Academic Press, San Diego, CA, USA, 1994.

[56] J. D. Gulley, D. I. Benn, E. Screaton, and J. Martin. Mechanisms of englacial conduit formation and their implications for subglacial recharge. *QUATERNARY SCIENCE REVIEWS*, 28(19-20):1984–1999, SEP 2009.

[57] J. D. Gulley, M. Grabiec, J. B. Martin, J. Jania, G. Catania, and P. Glowacki. The effect of discrete recharge by moulins and heterogeneity in flow-path efficiency at glacier beds on subglacial hydrology. *Journal of Glaciology*, 58(211):926–940, 2012.

[58] Alessio Gusmeroli, Roger A. Clark, Tavi Murray, Adam D. Booth, Bernd Kulessa, and Brian E. Barrett. Seismic wave attenuation in the uppermost glacier ice of storglaciaren, sweden. *Journal of Glaciology*, 56(196):249–256, 2010. PT: J; NR: 53; TC: 5; J9: J GLACIOL; PG: 8; GA: 630FJ; UT: WOS:000280258200006.

[59] Joel T. Harper, John H. Bradford, Neil F. Humphrey, and Toby W. Meierbachtol. Vertical Extension of the Subglacial Drainage System into Basal Crevasses. *Nature*, 467:579–582, 2010.

[60] D. B. Harris and D. A. Dodge. An autonomous system for grouping events in a developing aftershock sequence. *Bulletin of the Seismological Society of America*, 101(2):763–774, APR 2011. PT: J; NR: 19; TC: 2; J9: B SEISMOL SOC AM; PG: 12; GA: 738NR; UT: WOS:000288647000023.

[61] D. B. Harris and CA Lawrence Livermore National Laboratory (LLNL), Livermore. Covariance modifications to subspace bases. Technical report, Lawrence Livermore National Laboratory, United States, 2008. ID: 15254434135682.

[62] David Harris. Adaptive waveform correlation detectors for arrays algorithms for autonomous calibration. Technical report, Lawrence Livermore National Laboratory. and United States. Department of Energy. and United States. Dept. of Energy. Office of Scientific and Technical Information., 2009. ID: 727282915.

[63] David B. Harris. Characterizing Source Regions with Signal Subspace Methods: Theory and Computational Methods. Technical Report UCID-21848, Lawrence Livermore National Laboratory, December 1989.

[64] David B. Harris. A Waveform Correlation Method for Identifying Quarry Explosions. *Bulletin of the Seismological Society of America*, 81(6):2395–2418, December 1991.

[65] David B. Harris. Subspace Detectors: Theory. Technical Report UCRL-TR-222758, Lawrence Livermore National Laboratory, July 2006. ID: 316300514.

[66] David B. Harris, Steven J. Gibbons, Arthur J. Rodgers, and Michael E. Pasyanos. Nuclear test ban treaty verification improving test ban monitoring with empirical and model-based signal processing. *IEEE Signal Processing Magazine*, 29(3):57–70, MAY 2012. PT: J; NR: 31; TC: 0; J9: IEEE SIGNAL PROC MAG; PG: 14; GA: 924UT; UT: WOS:000302717500009.

[67] David B. Harris and Tormod Kvaerna. Superresolution with seismic arrays using empirical matched field processing. *Geophysical Journal International*, 182(3):1455–1477, SEP 2010. PT: J; TC: 2; UT: WOS:000280997700025.

[68] David B. Harris and Tim Paik. Subspace Detectors: Efficient Implementation. Technical Report UCRL-TR-223177, Lawrence Livermore National Laboratory, July 2006.

[69] M. J. Hoffman, G. A. Catania, T. A. Neumann, L. C. Andrews, and J. A. Rumrill. Links between acceleration, melting, and supraglacial lake drainage of the western

Greenland Ice Sheet. *JOURNAL OF GEOPHYSICAL RESEARCH-EARTH SURFACE*, 116, DEC 28 2011.

[70] Matt J. Hoffman. *Spatial and Temporal Variability of Glacier Melt in the McMurdo Dry Valleys, Antarctica*. PhD thesis, Portland State University, 2011.

[71] Matthew J. Hoffman, Andrew G. Fountain, and Glen E. Liston. Surface energy balance and melt thresholds over 11 years at Taylor Glacier, Antarctica. *Journal of Geophysical Research*, 113, 2008.

[72] I. M. Howat, S. de la Pena, J. H. van Angelen, J. T. M. Lenaerts, and M. R. van den Broeke. "Expansion of meltwater lakes on the Greenland Ice Sheet". *CRYOSPHERE*, 7(1):201–204, 2013.

[73] Alun Hubbard, Wendy Lawson, Brian Anderson, Bryn Hubbard, and Heinz Blatter. Evidence for subglacial ponding across Taylor Glacier, Dry Valleys, Antarctica. *Annals of Glaciology*, 39:79–84, 2004.

[74] J.M Ingram and M.M Marsh. Projections onto Convex Cones in Hilbert Space. *Journal of Approximation Theory*, 64(3):343–350, March 1991.

[75] IRS: Incorporated Research Institutions for Seismology. *Federation of Digital Seismograph Networks: Standard for the Exchange of Earthquake Data, Reference Manual, SEED Format Version 2.4*, 2.4 edition, May 2010. 141–159.

[76] Tristram D. L. Irvine-Fynn, Andrew J. Hodson, Brian J. Moorman, Vatne Geir, and Alun Hubbard. Polythermal Glacier Hydrology: A Review. *Reviews of Geophysics*, 49(RG4002), 2011.

[77] Neal R. Iverson and Ben B. Petersen. A new laboratory device for study of subglacial processes: first results on ice-bed separation during sliding. *Journal of Glaciology*, 57(206):1135–1146, 2011.

[78] A. M. Johansson, P. Jansson, and I. A. Brown. Spatial and temporal variations in

lakes on the greenland ice sheet. *Journal of Hydrology*, 476:314–320, JAN 7 2013. PT: J; TC: 1; UT: WOS:000313861800028.

[79] Robin R. Johnston, Andrew G. Fountain, and Thomas H. Nylen. The origin of channels on lower Taylor Glacier, McMurdo Dry Valleys, Antarctica, and their Implication for Water Runoff. *Annals of Glaciology*, 40:1–7, 2005.

[80] G. A. JONES, B. KULESSA, S. H. DOYLE, C. F. DOW, and A. HUBBARD. An automated approach to the location of icequakes using seismic waveform amplitudes. *AoG Annals of Glaciology*, 54(64):1–9, 2013. ID: 4938050071.

[81] I. Joughin, S. B. Das, G. E. Flowers, M. D. Behn, R. B. Alley, M. A. King, B. E. Smith, J. L. Bamber, M. R. van den Broeke, and J. H. van Angelen. Influence of ice-sheet geometry and supraglacial lakes on seasonal ice-flow variability. *The Cryosphere*, 7(4):1185–1192, 2013.

[82] Ian Joughin, Sarah B. Das, Matt A. King, Ben E. Smith, Ian M. Howat, and Twila Moon. Seasonal speedup along the western flank of the Greenland Ice Sheet. *Science*, 320(5877):781–783, May 9 2008.

[83] Ian Joughin, Ben E. Smith, Ian M. Howat, Dana Floricioiu, Richard B. Alley, Martin Truffer, and Mark Fahnestock. Seasonal to decadal scale variations in the surface velocity of jakobshavn isbrae, greenland: Observation and model-based analysis. *Journal of Geophysical Research-Earth Surface*, 117:F02030, MAY 25 2012. PT: J; NR: 60; TC: 1; J9: J GEOPHYS RES-EARTH; PG: 20; GA: 949CI; UT: WOS:000304553000001.

[84] IR JOUGHIN, DB PERCIVAL, and DP WINEBRENNER. Maximum-likelihood-estimation of k-distribution parameters for sar data. *IEEE Transactions on Geoscience and Remote Sensing*, 31(5):989–999, SEP 1993. PT: J; NR: 28; TC: 85; J9: IEEE T GEOSCI REMOTE; PG: 11; GA: MP174; UT: WOS:A1993MP17400006.

[85] L.R. Joughin and D.P. Winebrenner. Effective number of looks for a multilook interferometric phase distribution. In *Geoscience and Remote Sensing Symposium, 1994.*

IGARSS '94. Surface and Atmospheric Remote Sensing: Technologies, Data Analysis and Interpretation., International, volume 4, pages 2276–2278 vol.4, 1994.

[86] Bruce R. Julian, Gillian R. Foulger, Francis C. Monastero, and Steven Bjornstad. Imaging Hydraulic Fractures in a Geothermal Reservoir. *Geophysical Research Letters*, 37, 2010.

[87] B KAMB. GLACIER SURGE MECHANISM BASED ON LINKED CAVITY CONFIGURATION OF THE BASAL WATER CONDUIT SYSTEM. *JOURNAL OF GEOPHYSICAL RESEARCH-SOLID EARTH AND PLANETS*, 92(B9):9083–9100, AUG 10 1987.

[88] B Kamb, C.F. Raymond, W.D. Harrison, H. Engelhardt, Echelmeyer K.A., N. Humphrey, M.M. Brugman, and T. Pfeffer. Glacier Surge Mechanism-1982-1983 Surge of Variegated Glacier, Alaska. *Science*, 227(4686):469–479, 1985.

[89] Hiroo Kanamori. The Energy Release in Great Earthquakes. *Journal of Geophysical Research*, 82(20):2981–2987, 1977.

[90] J. L. Kavanaugh and K.M. Cuffey. Dynamics and Mass Balance of Taylor Glacier, Antarctica: 2. Force Balance and Longitudinal Coupling. *Journal of Geophysical Research*, 114, 2009.

[91] Steven M. Kay. *Fundamentals of Statistical Signal Processing: Estimation Theory.* Prentice-Hall Inc., Upper Saddle River, New Jersey, USA, 1st edition, 1993.

[92] Steven M. Kay. *Fundamentals of Statistical Signal Processing: Detection Theory.* Prentice-Hall Inc., Upper Saddle River, New Jersey, USA, 1st edition, 1998.

[93] Andrzej Kijko and M. Sciocatti. Optimal Spatial Distribution of Seismic Stations in Mines. *International Journal of Rock Mechanics and Mining Sciences*, 32(6):607–615, September 1995.

[94] Matt A. King and Christopher S. Watson. Long GPS coordinate time series: Mul-

tipath and geometry effects. *JOURNAL OF GEOPHYSICAL RESEARCH-SOLID EARTH*, 115, APR 3 2010.

[95] Matt A. King, Christopher S. Watson, Nigel T. Penna, and Peter J. Clarke. Subdaily signals in GPS observations and their effect at semiannual and annual periods. *GEOPHYSICAL RESEARCH LETTERS*, 35(3), FEB 1 2008.

[96] Matt A. King and Simon D. P. Williams. Apparent stability of GPS monumentation from short-baseline time series. *JOURNAL OF GEOPHYSICAL RESEARCH-SOLID EARTH*, 114, OCT 13 2009.

[97] A. Koehler, A. Chapuis, C. Nuth, J. Kohler, and C. Weidle. Autonomous detection of calving-related seismicity at kronebreen, svalbard. *Cryosphere*, 6(2):393–406, 2012 2012. PT: J; TC: 0; UT: WOS:000304062100012.

[98] M. J. Krawczynski, M. D. Behn, S. B. Das, and I. Joughin. Constraints on the lake volume required for hydro-fracture through ice sheets. *GEOPHYSICAL RESEARCH LETTERS*, 36, MAY 16 2009.

[99] T. Kubokawa, C.P. Robert, and A.K. Md. E Saleh. Estimation of Noncentrality Parameters. *The Canadian Journal of Statistics / La Revue Canadienne de Statistique*, 21(1), March 1993.

[100] Jonathan M. Lees. Multiplet Analysis at Coso Geothermal. *Bulletin of the Seismological Society of America*, 88(5):1127–1143, October 1998.

[101] A. A. Leeson, A. Shepherd, S. Palmer, A. Sundal, and X. Fettweis. Simulating the growth of supraglacial lakes at the western margin of the greenland ice sheet. *Cryosphere*, 6(5):1077–1086, 2012. PT: J; TC: 0; UT: WOS:000310465500011.

[102] Karen J. Lewis, Andrew G. Fountain, and Paul Langevin. Mcmurdo Dry Valleys LTER: The role of terminus cliff melt in streamflow, Taylor Valley, Antarctica. *Antarctic Journal of the United States*, 31:189–190, 1998.

[103] Yu-Li Liang, William Colgan, Qin Lv, Konrad Steffen, Waleed Abdalati, Julienne Stroeve, David Gallaher, and Nicolas Bayou. A decadal investigation of supraglacial lakes in West Greenland using a fully automatic detection and tracking algorithm. *REMOTE SENSING OF ENVIRONMENT*, 123:127–138, AUG 2012.

[104] Glen E. Liston and Kelly Elder. A Distributed Snow-Evolution Modeling System (SnowModel). *Journal of Hydrometeorology*, 7(6):1259–1276, 2006.

[105] Glen E. Liston, Jan-Gunnar Winther, Oddbjrn Bruland, Hallgeir Elvehy, and Knut Sand. Below-Surface Ice Melt on the Coastal Antarctic Ice Sheet. *Journal of Glaciology*, 45(150):273–285, 1999.

[106] DR MacAyeal, TA Scambos, CL Hulbe, and MA Fahnestock. Catastrophic ice-shelf break-up by an ice-shelf-fragment-capsize mechanism. *Journal of Glaciology*, 49(164):22–36, 2003.

[107] Karen Lewis MacClune, Andrew G. Fountain, Jeffrey S. Kargel, and Douglas R. MacAyeal. Glaciers of the McMurdo Dry Valleys: Terrestrial analog for Martian polar sublimation. *Journal of Geophysical Research*, 108(E4), 2003.

[108] D Mair, P Nienow, I Willis, and M Sharp. Spatial patterns of glacier motion during a high-velocity event: Haut Glacier d'Arolla, Switzerland. *Journal of Glaciology*, 47(156):9–20, 2001.

[109] Douglas Mair, Bryn Hubbard, Peter Nienow, Ian Willis, and Urs H. Fischer. Diurnal fluctuations in glacier ice deformation: Haut Glacier d'Arolla, Switzerland. *EARTH SURFACE PROCESSES AND LANDFORMS*, 33(8):1272–1284, JUL 2008.

[110] DWF Mair, MJ Sharp, and IC Willis. Evidence for basal cavity opening from analysis of surface uplift during a high-velocity event: Haut Glacier d'Arolla, Switzerland. *Journal of Glaciology*, 48(161):208–216, 2002.

[111] Jean-Philippe Metaxian, Sebastian Araujo, Mauricio Mora, and Phillippe Lesage. Seismicity related to the glacier of Cotopaxi Volcano, Ecuador. *Geophysical Research Letters*, 30(9):1483–1486, 2003.

[112] T. D. Mikesell, K. van Wijk, M. M. Haney, J. H. Bradford, H. P. Marshall, and J. T. Harper. Monitoring glacier surface seismicity in time and space using rayleigh waves. *Journal of Geophysical Research-Earth Surface*, 117:F02020, MAY 10 2012. PT: J; NR: 43; TC: 0; J9: J GEOPHYS RES-EARTH; PG: 12; GA: 941ZU; UT: WOS:000304009800001.

[113] Jill A. Mikucki, Ann Pearson, David T. Johnston, Alexandra V. Turchyn, James Farquar, Daniel P. Schrag, Ariel D. Anbar, John C. Priscu, and Peter A. Lee. A Contemporary Microbially Maintained Subglacial Ferrous Ocean. *Science*, 324:397–400, 2009.

[114] T. Moon, I. Joughin, B. Smith, and I. Howat. 21st-century evolution of greenland outlet glacier velocities. *Science*, 336(6081):576–578, MAY 4 2012. PT: J; NR: 33; TC: 12; J9: SCIENCE; PG: 3; GA: 935DJ; UT: WOS:000303498800042.

[115] Hirokazu Moriya, Hiroaki Niitsuma, and Roy Baria. Multiplet-Clustering Analysis Reveals Structural Details within the Seismic Cloud at the Soultz Geothermal Field, France. *Bulletin of the Seismological Society of America*, 93(4):1606–1620, 2003.

[116] Gerhard Muller. Volume Changes of Seismic Sources from Moment Tensors. *Bulletin of the Seismological Society of America*, 91(4):880–884, 2001.

[117] Julian B. Murton, Rorik Peterson, and Jean-Claude Ozouf. Bedrock Fracture by Ice Segregation in Cold Regions. *Science*, 314(5802):1127–1129, 2006.

[118] Meredith Nettles and Goeran Ekstroem. Glacial earthquakes in greenland and antarctica. *Annual Review of Earth and Planetary Sciences, Vol 38*, 38:467–491, 2010 2010. PT: S; TC: 11; UT: WOS:000278757100018.

[119] J.F. Nye. Water flow in glaciers: jkulhlaups, tunnels and veins. *Journal of Glaciology*, 17(76):181–207, 1976.

[120] Shad O'Neel, H. P. Marshall, D. E. McNamara, and W. T. Pfeffer. Seismic Detection and Analysis of Icequakes at Columbia Glacier, Alaska. *Journal of Geophysical Research–Earth Surface*, 112, 2007.

[121] Shad O'Neel and W.T. Pfeffer. Source mechanics for monochromatic icequakes produced during iceberg calving at Columbia Glacier, AK. *Geophysical Research Letters*, 34, 2007.

[122] Volker Oye, Hilmar Bungum, and Michael Roth. Source Parameters and Scaling Relations for Mining-Related Seismicity within the Pyhasalmi Ore Mine, Finland. *Bulletin of the Seismological Society of America*, 95(3):1011–1026, 2005.

[123] Steven Palmer, Andrew Shepherd, Peter Nienow, and Ian Joughin. Seasonal speedup of the greenland ice sheet linked to routing of surface water. *Earth and Planetary Science Letters*, 302(3-4):423–428, FEB 1 2011. PT: J; NR: 27; TC: 18; J9: EARTH PLANET SC LETT; PG: 6; GA: 724ZL; UT: WOS:000287614900017.

[124] L. E. Peters, S. Anandakrishnan, R. B. Alley, and D. E. Voigt. Seismic attenuation in glacial ice: A proxy for englacial temperature. *Journal of Geophysical Research: Earth Surface*, 117(F2):– F02008, 2012.

[125] Elizabeth J. Petrie, Matt A. King, Philip Moore, and David A. Lavallee. Higher-order ionospheric effects on the GPS reference frame and velocities. *JOURNAL OF GEOPHYSICAL RESEARCH-SOLID EARTH*, 115, MAR 24 2010.

[126] Thomas Phillips, Harihar Rajaram, and Konrad Steffen. Cryo-hydrologic warming: A potential mechanism for rapid thermal response of ice sheets. *GEOPHYSICAL RESEARCH LETTERS*, 37, OCT 23 2010.

[127] Myrto Pirli, Steven J. Gibbons, and Johannes Schweitzer. Application of array-based waveform cross-correlation techniques to aftershock sequences: the 2003 lefkada island, greece, case. *Journal of Seismology*, 15(3):533–544, JUL 2011. PT: J; CT: 31st ESC General Assembly of the Data Acquisition, Theory and Interpretation, Array Seismology in Europe - Status and Perspectives; CY: SEP, 2008; CL: Hersonissos, GREECE; TC: 1; SI: SI; UT: WOS:000292816500007.

[128] S. F. Price, A. J. Payne, G. A. Catania, and T. A. Neumann. Seasonal accelera-

tion of inland ice via longitudinal coupling to marginal ice. *Journal of Glaciology*, 54(185):213–219, 2008.

[129] Jose Pujol. *Elastic Wave Propagation and Generation in Seismology*. Cambridge University Press, Cambridge, United Kingdom, 2003.

[130] A. QAMAR. Calving icebergs - a source of low-frequency seismic signals from columbia glacier, alaska. *Journal of Geophysical Research-Solid Earth and Planets*, 93(B6):6615–6623, JUN 10 1988. PT: J; NR: 20; TC: 31; J9: J GEOPHYS RES-SOLID; PG: 9; GA: N8005; UT: WOS:A1988N800500044.

[131] C.F. Raymond and W.D. Harrison. Some Observations on the Behavior of the Liquid and Gas Phases in Temperate Glacier Ice. *Journal of Glaciology*, 14(71):213–233, 1975.

[132] Alan W. Rempel. Frost heave. *Journal of Glaciology*, 56(200):1122–1128, 2010. PT: J; SI: SI; UT: WOS:000294750900017.

[133] J. A. Rial, C. Tang, and K. Steffen. Glacial rumblings from jakobshavn ice stream, greenland. *Journal of Glaciology*, 55(191):389–399, 2009. PT: J; NR: 41; TC: 4; J9: J GLACIOL; PG: 11; GA: 483CP; UT: WOS:000268939900001.

[134] Paul G. Richards and Won-Young Kim. Equivalent Volume Sources for Explosions at Depth: Theory and Observations. *Bulletin of the Seismological Society of America*, 95(2):401–407, 2005.

[135] F. RINGDAL. Estimation of seismic detection thresholds. *Bulletin of the Seismological Society of America*, 65(6):1631–1642, 1975. PT: J; NR: 15; TC: 28; J9: B SEISMOL SOC AM; PG: 12; GA: BE659; UT: WOS:A1975BE65900007.

[136] MJ Roberts, AJ Russell, FS Tweed, and Knudsen O. Ice Fracturing during Jokulhlaups: Implications for Englacial Floodwater Routing and Outlet Development. *Earth Surface Processes and Landforms*, 25(13):1429–1446, 2000.

[137] Sebastian Rost and Christine Thomas. Array Seismology: Methods and Applications. *Reviews of Geophysics*, 40(1008), 2002.

[138] P.F. Roux, F. Walter, P. Riesen, S. Sugiyama, and M. Funk. Observation of Surface Seismic Activity Changes of an Alpine Glacier during a Glacier-Dammed Lake Outburst. *Journal of Geophysical Research*, 115, 2010.

[139] Pierre-Francois Roux, David Marsan, Jean-Philippe Metaxian, Gareth O'Brien, and Luc Moreau. Microseismic activity within a serac zone in an alpine glacier (Glacier d'Argentiere, Mont Blanc, France). *Journal of Glaciology*, 54(184):157–168, 2008.

[140] Andrew L. Rukhin. Estimation of the noncentrality parameter of an f-distribution. *Journal of Statistical Planning and Inference*, 35(2):201 – 211, 1993.

[141] D. Svennson Samyn and S. J. Fitzsimons. Dynamic Implications of Discontinuous Recrystallization in Cold Basal Ice: Taylor Glacier, Antarctica. *Journal of Geophysical Research*, 113, 2008.

[142] David P. Schaff. Broad-scale applicability of correlation detectors to china seismicity. *Geophysical Research Letters*, 36:L11301, JUN 3 2009. PT: J; UT: WOS:000266741600003.

[143] David P. Schaff and Paul G. Richards. On finding and using repeating seismic events in and near china. *Journal of Geophysical Research-Solid Earth*, 116:B03309, MAR 23 2011. PT: J; UT: WOS:000288869600003.

[144] DP Schaff, GHR Bokelmann, WL Ellsworth, E. Zanzerkia, F. Waldhauser, and GC Beroza. Optimizing correlation techniques for improved earthquake location. *Bulletin of the Seismological Society of America*, 94(2):705–721, APR 2004. PT: J; UT: WOS:000221200900024.

[145] DP Schaff and F. Waldhauser. Waveform cross-correlation-based differential travel-time measurements at the northern california seismic network. *Bulletin of the Seismological Society of America*, 95(6):2446–2461, DEC 2005. PT: J; UT: WOS:000234412100028.

[146] Louis L. Scharf and Benjamin Friedlander. Matched subspace detectors. *IEEE Transactions on Signal Processing*, 42(8):2146–2156, 1994.

[147] Christian Schoof. Ice-sheet acceleration driven by melt supply variability. *NATURE*, 468(7325):803–806, DEC 9 2010.

[148] J Schweizer and A Iken. The Role of Bed Separation and Friction in Sliding over an Undeformable Bed. *Journal of Glaciology*, 38(128):77–92, 1992.

[149] N. Selmes, T. Murray, and T. D. James. Fast draining lakes on the Greenland Ice Sheet. *GEOPHYSICAL RESEARCH LETTERS*, 38, AUG 10 2011.

[150] N. Selmes, T. Murray, and T. D. James. Fast draining lakes on the Greenland Ice Sheet. *GEOPHYSICAL RESEARCH LETTERS*, 38, AUG 10 2011.

[151] David E. Shean, James W. Head III, and David R. Marchant. Shallow seismic surveys and ice thickness estimates of Mullins Valley debris-covered glacier, McMurdo Dry Valleys, Antarctica. *Antarctic Science*, 19(4):485–496, 2007.

[152] Andrew Shepherd, Alun Hubbard, Peter Nienow, Matt King, Malcolm McMillan, and Ian Joughin. Greenland ice sheet motion coupled with daily melting in late summer. *GEOPHYSICAL RESEARCH LETTERS*, 36, JAN 7 2009.

[153] Danielle J. Sitts, Andrew G. Fountain, and Matthew J. Hoffman. Twentieth century glacier change on mount adams, washington, usa. *Northwest Science*, 84(4):378–385, FAL 2010. PT: J; TC: 3; UT: WOS:000285797800007.

[154] A.M. Smith. Microearthquakes and subglacial conditions. *Geophysical Research Letters*, 33, 2006.

[155] Roel Snieder and Mark Vrijlandt. Constraining the Source Separation with Coda Wave Interferometry: Theory and Application to Earthquake Doublets in the Hayward Fault, California. *Journal of Geophysical Research*, 110, April 2005.

[156] Henry Stark and Yongyi Yang. *Vector Space Projections: A Numerical Approach to Signal and Image Processing, Neural Nets, and Optics.* Wiley John and Sons, Incorporated, New York, NY, 1998.

[157] Graham Stuart, Tavi Murray, Alex Brisbourne, Peter Styles, and Sam Toon. Seismic emissions from a surging glacier: Bakaninbreen, Svalbard. *Annals of Glaciology*, 42:151–157, 2005.

[158] A. V. Sundal, A. Shepherd, P. Nienow, E. Hanna, S. Palmer, and P. Huybrechts. Evolution of supra-glacial lakes across the Greenland Ice Sheet. *REMOTE SENSING OF ENVIRONMENT*, 113(10):2164–2171, OCT 2009.

[159] Aud Venke Sundal, Andrew Shepherd, Peter Nienow, Edward Hanna, Steven Palmer, and Philippe Huybrechts. Melt-induced speed-up of Greenland ice sheet offset by efficient subglacial drainage. *NATURE*, 469(7331):522–U83, JAN 27 2011.

[160] Steven R. Taylor, Stephen J. Arrowsmith, and Dale N. Anderson. Detection of short time transients from spectrograms using scan statistics. *Bulletin of the Seismological Society of America*, 100(5A):1940–1951, OCT 2010. PT: J; NR: 32; TC: 3; J9: B SEISMOL SOC AM; PG: 12; GA: 652KK; UT: WOS:000282005100007.

[161] M. Tedesco, M. Luthje, K. Steffen, N. Steiner, X. Fettweis, I. Willis, N. Bayou, and A. Banwell. Measurement and modeling of ablation of the bottom of supraglacial lakes in western greenland. *Geophysical Research Letters*, 39:L02502, JAN 18 2012. PT: J; TC: 2; UT: WOS:000299393400001.

[162] M. Tedesco, I.C. Willis, M.J. Hoffman, A.F. Banwell, P. Alexander, and N.S. Arnold. Ice Dynamic Response to two Modes of Surface lake Drainage on the Greenland ice Sheet. *Environmental Research Letters*, 8:034007 (9 pp.), Sept. 2013.

[163] TM THARP. Conditions for crack-propagation by frost wedging. *GEOLOGICAL SOCIETY OF AMERICA BULLETIN*, 99(1):94–102, JUL 1987.

[164] Weston Thelen, Mike West, and Sergey Senyukov. Seismic Characterization of the

Fall 2007 Eruptive Sequence at Bezymianny Volcano, Russia. *Journal of Volcanology and Geothermal Research*, 194(4):201–213, 2010.

[165] Weston A. Thelen, Kate Allstadt, Silvio De Angelis, Stephen D. Malone, Seth C. Moran, and John Vidale. Shallow repeating seismic events under an alpine glacier at mount rainier, washington, usa. *Journal of Glaciology*, 59(214):345–356, 2013. PT: J; NR: 49; TC: 0; J9: J GLACIOL; PG: 12; GA: 154ZV; UT: WOS:000319716100012.

[166] Victor C. Tsai and Goran Ekstrom. Analysis of glacial earthquakes. *Journal of Geophysical Research-Earth Surface*, 112(F3):F03S22, APR 14 2007 2007. PT: J; TC: 22; UT: WOS:000245729100001.

[167] Donald Lawson Turcotte and Gerald Schubert. *Geodynamics*. Cambridge University Press, Cambridge, New York, USA, 2nd edition, 2002.

[168] CJ van der Veen. Fracture Mechanics Approach to Penetration of Bottom Crevasses on Glaciers. *Cold Regions Science and Technology*, 27:213–223, 1998.

[169] C.J. van der Veen. Fracture mechanics approach to penetration of surface crevasses on glaciers. *Cold Regions Science and Technology*, 27(1):31 – 47, 1998.

[170] J. Vila, R. Macia, D. Kumar, R. Ortiz, H. Moreno, and AM Correig. Analysis of the unrest of active volcanoes using variations of the base level noise seismic spectrum. *Journal of Volcanology and Geothermal Research*, 153(1-2):11–20, MAY 1 2006. PT: J; NR: 22; TC: 10; J9: J VOLCANOL GEOTH RES; PG: 10; GA: 051PC; UT: WOS:000238172000003.

[171] Joseph S. Walder. Hydraulics of Subglacial Cavities. *The Journal of Glaciology*, 32(112):439–445, 1986.

[172] Felix Waldhauser and William L. Ellsworth. A Double-Difference Earthquake Location Algorithm: Method and Application to the Northern Hayward Fault, California. *Bulletin of the Seismological Society of America*, 90(6):1353–1368, December 2000.

[173] Felix Waldhauser and David Schaff. Regional and teleseismic double-difference earthquake relocation using waveform cross-correlation and global bulletin data. *Journal of Geophysical Research-Solid Earth*, 112(B12):B12301, DEC 5 2007. PT: J; UT: WOS:000251527800002.

[174] Felix Waldhauser and David P. Schaff. Large-scale relocation of two decades of northern california seismicity using cross-correlation and double-difference methods. *Journal of Geophysical Research-Solid Earth*, 113(B8):B08311, AUG 15 2008. PT: J; UT: WOS:000258514400003.

[175] Fabian Walter, Jason M. Amundson, Shad O'Neel, Martin Truffer, Mark Fahnestock, and Helen A. Fricker. Analysis of low-frequency seismic signals generated during a multiple-iceberg calving event at jakobshavn isbrae, greenland. *Journal of Geophysical Research-Earth Surface*, 117:F01036, MAR 27 2012 2012. PT: J; TC: 4; UT: WOS:000302240400001.

[176] Fabian Walter, John F. Clinton, Nicholas Deichmann, Douglas S. Dreger, Sarah E. Minson, and Martin Funk. Moment Tensor Inversions of Icequakes on Gornergletscher, Switzerland. *Bulletin of the Seismological Society of America*, 99(2):852–870, 2009.

[177] Fabian Walter, Pierre Dalban Canassy, Stephan Husen, and John F. Clinton. Deep icequakes: What happens at the base of alpine glaciers? *Journal of Geophysical Research: Earth Surface*, pages n/a–n/a, 2013.

[178] Fabian Walter, Nicholas Deichmann, and Martin Funk. Basal icequakes during changing subglacial water pressures beneath Gornergletscher, Switzerland. *Journal of Glaciology*, 54(186):511–521, 2008.

[179] Fabian Walter, Douglas S. Dreger, John F. Clinton, Nicholas Deichmann, and Martin Funk. Evidence for near-horizontal tensile faulting at the base of Gornergletscher, a Swiss Alpine Glacier. *Bulletin of the Seismological Society of America*, 100(2):458–472, 2010.

[180] C.S. Weaver and S.D. Malone. Seismic Evidence for Discrete Glacier Motion at the Rock-Ice Interface. *Journal of Glaciology*, 23(89):171–184, 1979.

[181] Stephen Weichecki-Vergara, Henry L. Gray, and Wayne A Woodward. Statistical Development in Support of CTBT Monitoring. Technical Report DTRA-TR-00-22, Southern Methodist University, August 2001.

[182] Michael West, Christopher F. Larsen, Martin Truffer, Shad O'Neel, and Lara LeBlanc. Glacier microseismicity. *Geology*, 38(4):319–322, 2010.

[183] Erin. N. Whorton, Erin. C. Pettit, Edward. D. Waddington, Ron. Sletten, and Bernard. Hallet. Debris-rich basal ice layer effects on polar glacier dynamics. In *American Geophysical Union, Fall Meeting 2008*, 2008.

[184] Paul J. Winberry, Sridhar Anandakrishnan, and Richard B. Alley. Seismic observations of transient subglacial water-flow beneath MacAyeal Ice Stream, West Antarctica. *Geophysical Research Letters*, 36, 2009.

[185] Cecily J. Wolfe. On the Mathematics of Using Difference Operators to Relocate Earthquakes. *Bulletin of the Seismological Society of America*, 92(8):2879–2892, December 2002.

[186] Yongyi Yang and Henry Stark. Design of self healing arrays using vector space projections. *IEEE Transactions on Antennas and Propagation*, 49(4):526–534, 2001.

[187] Lucas K. Zoet, Sridhar Anandakrishnan, Richard B Alley, Andrew A. Nyblade, and Douglas A. Wiens. Motion of an Antarctic glacier by repeated tidally modulated earthquakes. *Nature Geoscience*, 5:623–626, August 2012.

[188] HJ Zwally, W Abdalati, T Herring, K Larson, J Saba, and K Steffen. Surface Melt-induced Acceleration of Greenland Ice-Sheet Flow. *SCIENCE*, 297(5579):218–222, JUL 12 2002.

Appendix A

NOVEL CONTRIBUTIONS TO ICEQUAKE DETECTION METHODS

This work summarizes some simple and effective improvements to digital detectors used for seismic monitoring applications described in this thesis. I consider challenges specific to the detection of icequake waveforms. These waveforms are consistently transient, approximately a second in duration, and embedded in temporally correlated noise. Detection problems often arise because erroneous assumptions are made regarding the signal or noise models used to represent data from real geophysical environments. As a consequence, hypotheses tests used in routine detection scenarios are not appropriate for determining the presence of seismic signal. It is therefore necessary to improve parameterizations of the signal and noise probability distribution functions (PDF) included in these hypotheses tests. I demonstrate that these challenges, and their solutions, become increasingly important as the effective data dimension is reduced.

These solutions demonstrably extend the performance of the three primary analysis tools that I use to evaluate icequake data (Figure A.1). They include (1) adaptive energy detectors (Section A.5), (2) Rayleigh wave detectors (Section A.8), and (3) multiplet detectors (Sections A.11 – A.13). I conclude each section with examples of detector implementation, applied to real icequake data.

A.1 Seismic Icequake Monitoring

Icequake monitoring is an observational procedure that uses ground motion data recorded by geophones to identify seismic events that occur within ice. In the past 30 years, it has developed into a conventional technology for sensing brittle deformation processes triggered by meltwater in glaciers and ice sheets [133, 180, 184, 130]. Such processes release microseismic energy and are often active at depths that are inaccessible with

other sensing methods. In some cases, this inaccessibility means that glacial response to environmental forcing must be interpreted from icequake data alone [21]. However, this same environmental forcing can excite unwanted sources of seismic and acoustic noise that degrade the quality of target signals produced from icequakes. This degradation presents practical challenges to the most fundamental task of icequake monitoring: detection.

In icequake detection, band-limited, noisy data are used to evaluate the presence of a seismic waveform through a statistical test. During such a test, geophone data are processed with a digital detector to compute a certain statistic. This statistic is then compared to a prescribed threshold value, and a decision rule is implemented to either accept or reject the hypothesis that a waveform has been observed. Successful waveform detection depends upon both the applicability of this hypothesis test and the decision rule. It is therefore important to account for statistical effects introduced to the threshold value and decision rule by noise and signal processing operations. Consequently, a reliable interpretation of seismicity requires the ability to quantify false and true waveform detection probabilities, despite these effects. If these probabilities can be confidently estimated, they provide the most objective evaluation of the detection performance of an icequake monitoring experiment.

A.2 Seismic Processing Notation

To proceed, it is necessary to first establish notational conventions. I represent the signal acquired from channel i of a geophone data stream $x_i(t)$ at digitization rate Δt as a sequence of N samples arranged into an N-row column vector:

$$\mathbf{x}_i = [\, x_i(0), x_i(\Delta t), \ldots x_i(k\,\Delta t), \ldots, x_i((N-1)\,\Delta t)\,]^{\mathrm{T}}, \tag{A.1}$$

where commas denote distinct columns, and superscript T denotes the matrix transpose. I discard the symbol t to explicitly identify $\mathbf{x}_i$ as a discretized time series and refer to sample k of $\mathbf{x}$ using $\mathbf{x}[k]$. If the channel index is irrelevant, I will also discard the subscript i. I represent contemporaneous multi-channel data samples acquired from an M-channel seismic

network as columns in a matrix of dimension $N \times M$ written as $\mathbf{X} \in \mathbb{R}^{N \times M}$:

$$\mathbf{x} = [\, \mathbf{x}_1,\ \mathbf{x}_2,\ \ldots\, \mathbf{x}_i,\ \ldots\, \mathbf{x}_M \,]^{\mathrm{T}} \tag{A.2}$$

where $\mathbf{x}_j$ $(j = 1, 2, \ldots, i, \ldots M)$ is defined by Equation A.1, and commas separate distinct columns within the matrix. Inoperable or absent rows (channels) are down-weighted or deleted from this vector. Other authors reformat $\mathbf{x}$ into a column vector that is multiplexed by time-sample, of dimension $MN \times 1$ written as $\mathbf{x} \in \mathbb{R}^{MN \times 1}$ (e.g., [65, 63]). Regardless of structure, I refer to these simultaneous multi-channel records of ground motion as "record sections", consistent with seismological terminology

Concerning statistical quantities, the statement $\mathbf{x} \sim \mathcal{D}(\boldsymbol{\theta}_0, \boldsymbol{\theta}_1)$ indicates that data vector $\mathbf{x}$ is distributed as a multivariate random variable with parameters $\boldsymbol{\theta}_0$ and $\boldsymbol{\theta}_1$, according to $\mathcal{D}$. The statement that $\mathbf{x}$ has probability density function (PDF) $p(\mathbf{x}; \mathcal{D})$ is indicated using the distributional equality, $\mathbf{x} \overset{d}{=} p(\mathbf{x}; \mathcal{D})$; the conventional name for $\mathcal{D}$ is explicitly identified, unless it is obvious. I distinguish the true value of a statistical parameter μ of a distribution function from its sample estimate $\hat{\mu}$ with over script hats. The probability that a random variable X exceeds a given threshold η is expressed as $P(X \geq \eta)$. When presenting hypotheses tests, I symbolize a null hypothesis statement as $\mathcal{H}_0$ relative to some alternative hypothesis statement $\mathcal{H}_1$. In general, seismic data are assumed to be realizations of a (wide-sense) stationary random process within a sufficiently short time window.

Concerning geometric quantities, I write the subspace spanned by the columns of matrix $\mathbf{A}$ as $\langle \mathbf{A} \rangle$. I define an inner product $\langle \bullet, \bullet \rangle_{\mathbf{A}}$ on subspace $\langle \mathbf{A} \rangle$ as $\mathbf{u}^{\mathrm{T}}\mathbf{v}$ for $\mathbf{u}, \mathbf{v} \in \langle \mathbf{A} \rangle$ unless I specify otherwise. I will consistently distinguish orthogonal projectors $P_{\mathbf{A}}$ with range $\langle \mathbf{A} \rangle$ from oblique projectors $E_{\mathbf{AB}}$ with range $\langle \mathbf{A} \rangle$ and null space $\langle \mathbf{B} \rangle$. I write more general signal sets (like convex sets) as $\mathcal{C}$ and the projection of $\mathbf{x}$ onto them as $P_{\mathcal{C}}\mathbf{x}$. Vectors with hats like $\hat{\mathbf{u}}$ are normalized. If $\hat{\mathbf{u}}$ is also an estimate for a distribution's parameter, the meaning of the hat will be apparent from it's context.

A.3 Statistical Data Model and Effective Dimension

The initial stage of waveform detection requires formulating appropriate statistical models for the digitized data $\mathbf{x}$. These models conventionally reflect two competing possibilities, $\mathcal{H}_0$ and $\mathcal{H}_1$, regarding the absence or presence of signal at a set of samples k, $(k = 0, 1, \ldots N)$:

$$\begin{aligned} \mathcal{H}_0 : &\quad \mathbf{x}[k] = \mathbf{n}_0[k]; \quad \text{(noise } \mathbf{n}_0 \text{ present)} \\ \mathcal{H}_1 : &\quad \mathbf{x}[k] = \mathbf{n}_1[k] + \mathbf{u}[k] \quad \text{(noise } \mathbf{n}_1 \text{ and signal } \mathbf{u} \text{ present).} \end{aligned} \tag{A.3}$$

Each model depends upon the prevalence of noise sources and any pre-processing operations that introduce correlation between data samples. Narrowband noise adds correlation structure by introducing bias into the dominant frequency of the wavefield. Similarly, processing routines like filtering introduce statistical dependency to the original data by replacing each sample k with a sum of itself and it's neighboring samples (see Figure A.2). Cumulatively, these effects will reduce the time-bandwidth product, or effective dimension, of an N-sample data record to $N_E < N$. This may result in an erroneously hypothesized null distribution for the data, or its statistics, when N_E is misinterpreted to equal N [1]. This uncertainty in N_E constitutes a basic challenge in network processing of seismic data [2]. Consequently, N_E must be estimated as $\hat{N}_E$ from the data $\mathbf{x}$ when it is unknown. The appropriate choice of an estimator for N_E is dependent upon the data statistic being evaluated and the application. Ideally, the desired estimator should be unbiased, have minimum variance, (be statistically "efficient") and therefore achieve the Cramér-Rao lower bound [91]. Analytical procedures for parameter estimation often utilize a maximum likelihood estimator (MLE). In such cases, the associated parameter estimate is that which maximizes the related likelihood, or log-likelihood function [91]. Numerical procedures often use application-specific estimators that require less computation time for large data records, relative to the MLE. I take that approach here, and use the MLE to derive

[1] For similar sample inter-dependency problems in SAR data, see [85, 84].

[2] According to Steven Gibbons of NORSAR in a personal communication: "The number of degrees of freedom in a network signal varies enormously–not just on the time-bandwidth product of a signal, but also on the network configuration. A very large aperture array will usually provide a better correlator than a small aperture array simply because it takes...[more coincidence]...to match each wiggle when the waveforms are so different. The best IMS arrays for correlation detectors are NOA (the NORSAR array) and MJAR: two of the very worst arrays for classical array processing!"

detection statistics when it is analytically convenient, and otherwise numerically compute parameter estimates from moments of empirical PDFs that describe the associated data statistics. Each of these estimators exhibit bias (i.e., the expected estimator value differs from population value), but their effect on the respective value of $\hat{N}_E$ is negligible relative to the effect misinterpreting N as N_E. Further, such estimates for $\hat{N}_E$ are **generally not integer-valued** and are appropriately interpreted as distributional **form factors** rather than sample lengths. I explicitly describe these estimators in Section A.5, Equations A.16, A.19 and A.24.

In summary, while processing and noise may induce an unavoidable reduction in effective data dimension, estimators provide the capability to account for this reduction in the hypothesized data distribution. This suggests that routine detection scenarios should include their implementation.

A.4 The Neyman Pearson Decision Criteria and Ratio Tests

The second stage of waveform detection requires forming the hypothesis test in Equation A.3. In summary, this test involves comparing a data statistic with a chosen threshold value in order to make a decision on the presence of a target waveform. The threshold value of the test determines the success rate of the detector by partitioning the data statistic domain (decision region) into two disjoint "acceptance" and "rejection" regions. Data statistic values that exceed the threshold value form the acceptance region, while those below the threshold value form the rejection region. In practice, this data statistic is constructed from the ratio of two (scalar) maximum likelihood functions. Therefore the data statistic is reducible to a scalar quantity, and each region is one dimensional regardless of waveform dimension. For a prescribed false pick or false alarm rate of a test, P_{FA}, the probability of detection P_D can by maximized by choosing a threshold value and decision region partitioning that satisfies the chosen false alarm constraint. The decision region, threshold, and data statistic then constitute a **Neyman Pearson Detector** [92].

Because I implement these detectors repeatedly, I illustrate their usage explicitly by

considering an arbitrary data statistic s computed from waveform data $\mathbf{x}$. I label the waveform-absent, null hypothesis as $\mathcal{H}_0$ and the alternative, waveform present hypothesis as $\mathcal{H}_1$. The waveform data $\mathbf{x}$ has two competing PDFs under these hypotheses that I respectively denote as $p_0(\mathbf{x}\,;\mathcal{H}_0)$ and $p_1(\mathbf{x}\,;\mathcal{H}_0)$. Equation A.3 is then expressible as:

$$\begin{aligned} \mathcal{H}_0: &\quad \mathbf{x} = \mathbf{n}_0 \stackrel{d}{=} p_0(\mathbf{x}\,;\mathcal{H}_0) \\ \mathcal{H}_1: &\quad \mathbf{x} = \mathbf{n}_1 + \mathbf{u} \stackrel{d}{=} p_1(\mathbf{x}\,;\mathcal{H}_1)\,, \end{aligned} \tag{A.4}$$

where $\stackrel{d}{=}$ is the distributional equality defined in Section A.2. If the signal model includes parameters $\boldsymbol{\theta}$ that are known, the detection statistic s is formed from the quotient of these density functions, as a likelihood ratio [92].

$$s = \frac{p_1(\mathbf{x};\,\mathcal{H}_1)}{p_0(\mathbf{x};\,\mathcal{H}_0)} \tag{A.5}$$

However, the signal and noise models generally have PDFs with parameters $\boldsymbol{\theta}$ that are imprecisely known within geophysical settings. These parameters shape the distribution curves used in hypotheses tests and thereby control the associated distributional overlap and detection performance. In practice, these parameters are estimated using MLEs in parallel with the computation of the detection statistic s as a Generalized Likelihood Ratio (GLR). In its general form, this ratio is:

$$s = \frac{\max_{\boldsymbol{\theta}}\{\, p_1(\mathbf{x};\,\mathcal{H}_1)\,\}}{\max_{\boldsymbol{\theta}}\{\, p_0(\mathbf{x};\,\mathcal{H}_0)\,\}} \tag{A.6}$$

Similarly, the statistic s has associated PDFs under these hypotheses denoted as $p_0(s\,;\mathcal{H}_0)$ and $p_1(s\,;\mathcal{H}_0)$ (Figure A.3, Top). I symbolize the to-be-determined threshold that partitions the decision region as η. This threshold value that satisfies the Neyman-Pearson Lemma is computed by enforcing the false attribution condition and inverting for the threshold η that results in the prescribed P_{FA} over the acceptance region [92]:

$$P_{FA}(s > \eta) = \int_{\eta}^{\infty} p_0(s\,;\mathcal{H}_0)\,ds \tag{A.7}$$

The corresponding probability of detection P_D is computed by integrating the probability distribution function over the acceptance region:

$$P_D(s > \eta) = \int_{\eta}^{\infty} p_1(s\,;\mathcal{H}_1)\,ds \tag{A.8}$$

The inverted value of η, relative to the observed value of s, provides the threshold for evaluating the decision rule that selects either hypothesis. I express this decision rule as:

$$s \underset{\mathcal{H}_0}{\overset{\mathcal{H}_1}{\gtrless}} \eta, \tag{A.9}$$

This expression summarizes the action of the detector: a statistic s is computed from available data, and the presence of a signal ($\mathcal{H}_0$ or $\mathcal{H}_1$) is determined from it's size relative to a value η that is computed from a prescribed false-alarm constraint (Figure A.3, Bottom).

As stated above, test statistics that arise in geophysical experiments generally have unknown parameters shaping their distributions $p_k\left(s\,;\mathcal{H}_k\right)$ $(k=0,1)$ that must be estimated from the data as in Equation A.6. In these realistic cases, the Neyman Pearson maximal-detection criterion is not strictly applicable. However, it will hold for sufficiently long data records (asymptotically), and provides the best discrimination power for the *class* of detectors in this thesis [146].

A.5 The Seismic Energy Detector

Initial discrimination of transient ground (or ice) motion from unspecified seismic sources is often conducted with energy-type detectors. These rely on almost no *a priori* information about the waveform except the expected duration of the signal, or it's bandwidth. In this case, the hypothesis test from Equation A.3 takes the form:

$$\begin{aligned} \mathcal{H}_0: &\quad \mathbf{x}=\mathbf{n}\sim\mathcal{N}\left(\mathbf{0},\sigma^2\mathbf{I}\right), \quad \sigma \text{ unknown} \\ \mathcal{H}_1: &\quad \mathbf{x}=\mathbf{n}+\mathbf{u}\sim\mathcal{N}\left(\mathbf{u},\sigma^2\mathbf{I}\right), \quad \sigma,\,\mathbf{u} \text{ unknown} \end{aligned} \tag{A.10}$$

where $\mathcal{N}\left(\mathbf{u},\sigma^2\mathbf{I}\right)$ describes a multivariate Gaussian random vector with mean $\mathbf{u}$ and covariance matrix $\sigma\mathbf{I}$ characterized by PDF:

$$p_k\left(\mathbf{x};\,\mathcal{H}_1\right)=\frac{1}{\left(2\pi\sigma^2\right)^{\frac{N}{2}}}\exp\left[-\frac{\left(\mathbf{x}-\mathbf{u}\right)^{\mathrm{T}}\left(\mathbf{x}-\mathbf{u}\right)}{2\sigma^2}\right] \tag{A.11}$$

An analogous PDF holds for under $\mathcal{H}_0$ with $\mathbf{u}$ replaced by $\mathbf{0}$. Because each data model contains unknown parameters, the GLR defined by Equation A.6 necessarily includes the MLE of $\mathbf{u}$ and σ. Substituting the general MLEs for the noise vectors $\hat{\mathbf{n}}_k$ (or variances

$\hat{\sigma}_k^2$) under each hypothesis ($k = 0, 1$) into the GLR of Equation A.6 produces the following detection statistic for s [12]:

$$s = \frac{||\hat{\mathbf{n}}_1||^2}{||\hat{\mathbf{n}}_0||^2} = \frac{N_0}{N_1}\frac{\hat{\sigma}_1^2}{\hat{\sigma}_0^2}, \quad \text{where}: \ \hat{\sigma}_k^2 = \frac{||\mathbf{x}||^2}{N_k}. \tag{A.12}$$

The specific energy detector I implement modifies Equation A.12 slightly by using distinct, non-overlapping sample ranges to compute scaled variance values. This (1) improve the variance estimate under the null hypothesis, (2) increases statistical independence between the numerator and denominator, and (3) structures the statistic to have a recognizable PDF. Specifically, this detector computes a short-term and long-term average (STA and LTA) of a digitized signal's energy using an N-sample sequence recorded over $N\Delta t$ sec with entries $x(k\,\Delta t)$, $(k = 0, 1, \ldots, N-1)$, and defines an instantaneous detector value Z_m at each sample m that is a scaled ratio of these averages (STA/LTA):

$$Z_m = \frac{N_0}{N_1} \cdot \frac{\sum_{k=m+1}^{m+1+N_1} x^2(k\,\Delta t)}{\sum_{k=m-1-N_0}^{m-1} x^2(k\,\Delta t)} \quad \text{where:} \quad N = N_1 + N_0, \quad N_0 \geq N_1 \tag{A.13}$$

The scalar Z_m therefore compares a length-N_1 average of signal energy computed after sample m to a length-N_0 average of signal energy preceding sample m (see Figure A.4). A similar energy detector statistic is derived in [92, Chapter 7]. This form is implemented in practice because the window partitioning about sample m enforces statistical independence between the averages when the noise samples are independent and identically distributed (IID). Quotients with the form of Z_m that are composed of sums of squares of IID Gaussian random variables have F-type distributions. This class of distributions has the form:

$$p_k(x;\,\mathcal{H}_k) = e^{-\frac{\lambda}{2}} \sum_{k=0}^{\infty} \frac{1}{k!}\left(\frac{\lambda}{2}\right)^k \frac{\left(\frac{N_1}{N_0}\right)^{\frac{1}{2}\cdot N_1+k} x^{\frac{1}{2}N_1+k-1}}{B\left(\frac{1}{2}\cdot(N_1+2k),\,\frac{1}{2}N_0\right)} \cdot \left(1+\frac{N_1}{N_0}x\right)^{-\frac{1}{2}\cdot(N_1+N_0)-k} \tag{A.14}$$

where $k = 1$ or 2, λ is a noncentrality parameter, N_0 and N_1 are degree-of-freedom of parameters, and $B(\bullet, \bullet)$ is the Beta function. Under the hypothesis $\mathcal{H}_0$ that a waveform is absent, Z_m has a central F-distribution $F_{N_1,N_0}(0)$ with degrees of freedom N_1 and N_0 and a zero noncentrality parameter. Under the hypothesis $\mathcal{H}_1$ that a waveform is present,

Z_m has a non-central F-distribution $F_{N_1,N_0}(\lambda)$ with a non-centrality parameter λ. The functional form of each distribution is documented in [92, Chapter 2] and is included in Matlab's Statistics Toolbox. In the $\mathcal{H}_1$ case, the non-centrality parameter scales with the signal-to-noise ratio (SNR) of the unknown waveform within the short term window:

$$\lambda = \sum_{k=m+1}^{m+1+N_1} \frac{E\{x(k\Delta t)\}^2}{\sigma^2} = (N_1 - 1) \cdot \mathrm{SNR} \tag{A.15}$$

where $E\{\bullet\}$ is the expected value operator. The detection value Z_m increases with λ and is maximized at fixed SNR by waveforms temporally localized between sample indices $m+1$ to $m+1+N_1$. The actual SNR is unknown prior to detection in the general case, but can be computed post-detection using a minimum variance unbiased estimator for λ [99] (see Equation A.24). I consider waveforms with an SNR ≥ 3 energetic enough for seismic event association; the detectable waveform SNR may exceed 3, however, if correlation structure within the noise environment is sufficiently high (see Section A.7 and Figure A.7).

The (Neyman-Pearson) decision rule (Section A.4) that I apply for hypothesis selection requires establishing a false-pick probability under the null hypothesis. However, the presence of structured noise and/or band-limiting operations will introduce correlation between samples and result in a reduction in the assumed degrees of freedom N_1 and N_0 for Z_m. This may lead to an inappropriate parameterization for the PDF of Z_m under $\mathcal{H}_0$ (i.e., Figure A.7). To estimate the effective degrees of freedom $\hat{N}_1$ and $\hat{N}_0$, I compare two empirical estimation methodologies and select the resultant estimates that best fit the observed distribution for Z_m. I select a window of $\sim 1\,\mathrm{hr}$ for each picking routine over which time I consider the data $\mathbf{x}(t)$ to be sufficiently statistically stationary. Using the first estimator, I compute the degrees of freedom of the signal-absent, central F distribution from the moments of the empirical null distribution for Z_m. I approximate this distribution by selecting several thousand non-overlapping windows within each 1 hr detection window to compute Z_m. The true effective parameters N_1 and N_0 are related to the mean and

variance of the ($\sim 1\,\mathrm{hr}$) population through:

$$\begin{aligned} E\{Z_m\} &= \frac{N_0}{N_0 - 2}, \\ \mathrm{var}\{Z_m\} &= \frac{2N_0^2\,(N_1 + N_0 - 2)}{N_1\,(N_0 - 2)^2\,(N_0 - 4)}, \end{aligned} \tag{A.16}$$

but are unknown. I re-emphasize that neither N_1 or N_0 are constrained to be integer valued when interpreted as distributional form factors. To automatically estimate these parameters as $\hat{N}_1$ and $\hat{N}_0$ in the presence of only noise, I adopt a sparsity hypothesis: I assume that very little signal is present in the population so that the empirical PDF parameter estimates can be evaluated by considering the left 99.5% of the empirical distribution's tail. I systematically enforce this by computing the 99.5-percentile cutoff using a $F_{2,L}$ distribution, since this will provide an upper bound on all distribution curves with $N_1 > 2$ and $N_0 < L$ at sufficient distance from the modes of Z_m. Such a distribution arises if the numerator of Z_m is the sum of two identical samples (very correlated), and the denominator is the sum of white noise samples (completely uncorrelated). I concede that this choice of cutoff may include a portion of data containing lower SNR signal, but argue that it provides an unambiguous, consistent upper bound for the cutoff. Once this choice is made, I estimate $\hat{N}_1$ and $\hat{N}_0$ by solving Equation A.16 algebraically using the sample mean and variance. This computation of parameters is considerably faster when compared with MATLAB's `mle.m` and provides a satisfactory fit to the observed distribution in practice.

Using the second estimator, I compute $\hat{N}_1$ and $\hat{N}_0$ from samples of empirically-determined correlation coefficients by adapting a method documented by Wiechecki and others [181, 65]. In this procedure, the variance of the sample correlation between psuedo-independent vectors of background noise is related to the average vector's effective dimension (Figure A.5). In practice, I estimate the sample correlation's distribution by cross correlating several thousand vector pairs $(\mathbf{x}, \mathbf{y})$ of length N_k $(k = 0, 1)$ that are drawn from non-intersecting windows of post-processed, signal sparse data. Signal-sparsity is determined by the 99.5% left tail of the empirical distribution as before. The estimator

$\hat{\rho}$ for the sample correlation is defined by [3]

$$\hat{\rho} = \frac{\mathbf{x}^{\mathrm{T}}\mathbf{y}}{||\mathbf{x}||\,||\mathbf{y}||}. \tag{A.17}$$

where each computed value of in Equation A.17 provides a sample drawn from the distribution function of the signal-absent sample-correlation. The distribution for $\hat{\rho}$ in the signal-absent case when $N \geq 3$ is

$$p(\hat{\rho}) = \frac{1}{B\left(\frac{1}{2},\, \frac{1}{2}N_k - 1\right)} \left(1 - \hat{\rho}^2\right)^{\frac{1}{2}N_k - 2} \tag{A.18}$$

where $B(\bullet, \bullet)$ is again the beta function. The true variance of $\hat{\rho}$ is derived from the 2$^{\text{nd}}$ moment of $p(\hat{\rho})$ and is related to the dimension N_k through $\sigma_{\hat{\rho}}^2 = (N_k - 1)^{-1}$ [181]. I use the sample variance $\hat{\sigma}_{\hat{\rho}}^2$ computed from estimates of $\hat{\rho}$ to approximate $\sigma_{\hat{\rho}}^2$ and solve for $\hat{N}_k$ $(k = 0,\, 1)$:

$$\hat{N}_k = 1 + \frac{1}{\hat{\sigma}_{\hat{\rho}}^2} \leq N_k \quad (k = 0,\, 1) \tag{A.19}$$

The effective dimension for both windows $(k = 0,\, 1)$ is computed in parallel using Equations A.18-A.19. I select the estimates of $\hat{N}_0$ and $\hat{N}_1$ from Equations A.16 and A.19 that provide the best $F_{\hat{N}_1,\hat{N}_0}$ fit to the left 99.5% tail of the observed distribution for Z_m in each detection routine. This improves the applicability of the distribution's parameterization under either hypothesis by making the detection problem more robust to non-stationary noise and/or interference. A formal statement of these robustified, competing hypotheses is given by

$$\begin{aligned} \mathcal{H}_0 :&\quad Z_m \sim F_{\hat{N}_1,\hat{N}_0}(0) \\ \mathcal{H}_1 :&\quad Z_m \sim F_{\hat{N}_1,\hat{N}_0}(\lambda) \end{aligned} \tag{A.20}$$

and the applicable PDFs $p_k(Z_m\,;\mathcal{H}_k)$, $(k = 0, 1)$ defined by Equation A.14 are used to evaluate the Neyman-Pearson decision rule (see Section A.4). This rule requires selecting a fixed false alarm rate P_{FA} to determine the corresponding decision region in each 1hr detection window; it also maximizes the detection probability P_D in the case the distribution parameters are effectively known. By setting $P_{FA} = 10^{-6}$,

$$10^{-6} = P_{FA}(Z_m > \eta) = \int_{\eta}^{\infty} p_0(Z_m\,;\mathcal{H}_0)\, dZ_m \tag{A.21}$$

---

[3] The true correlation $\rho = E\{x(t)\, y(t)\} / (\sigma_x \sigma_y)$ cannot be computed from finite length data records

a hypothetical event per minute generates on the order of one false pick per year on Gaussian noise using pick parameters from Table A.20. The inverted value for η relative to the observed value of Z_m is

$$\eta = 1 \; - \; F^{-1}_{\hat{N}_1,\hat{N}_2}\left(10^{-6}\right) \tag{A.22}$$

and provides the threshold for evaluating the decision rule that selects either hypothesis. This decision rule is then summarized by Equation A.23:

$$Z_m \underset{\mathcal{H}_0}{\overset{\mathcal{H}_1}{\gtrless}} \eta. \tag{A.23}$$

The pick statistic Z_m, decision region, and the threshold η constitute the energy detector. Each depend implicitly upon $\hat{N}_0$ and $\hat{N}_1$. The corresponding probability of detection P_D is computed from the PDF under $\mathcal{H}_1$ and is parameterized by the noncentrality parameter λ, or alternatively by the SNR. I estimate the SNR with the short-term window at each pick time using a minimum variance unbiased estimator for λ [99]:

$$\begin{gathered} \hat{\mathrm{SNR}} = \frac{\hat{\lambda}}{\hat{N}_1 - 1} = \left(\frac{\hat{N}_0 - 2}{\hat{N}_1 - 1}\right)\frac{\hat{N}_1}{\hat{N}_0} Z_m - \frac{\hat{N}_1}{\hat{N}_1 - 1}, \\ \text{where}: \; E\left\{\hat{\mathrm{SNR}}\right\} = \mathrm{SNR}, \quad \text{and} \quad \hat{\lambda} \geq 0. \end{gathered} \tag{A.24}$$

In the presence of correlated noise, this estimate is an effective signal to noise **plus interference** ratio (SINR). I verified that the expected value of this estimator produces the true SINR by using a Monte-Carlo test with prescribed signals in correlated noise (Figure A.8). The probability of detecting a waveform with the computed SNR is obtained by evaluating the signal-present distribution at the noncentrality parameter estimate $\hat{\lambda}$, and integrating over the acceptance region:

$$P_D\left(Z_m > \eta \,|\, \hat{\mathrm{SNR}}\right) = \int_{\eta}^{1} p_1\left(Z_m \,;\mathcal{H}_1\right)\Big|_{\hat{\lambda}} dZ_m \tag{A.25}$$

This is not the conditional probability of detection, given the SNR, which is more complicated; instead, the relationship between P_D calculated from Equation A.25 and $\hat{\lambda}/(\hat{N}_1 - 1)$ provides an empirical measure of the detection performance given the *estimated* SNR. This estimate for P_D is computed in-parallel with the energy detector, for each geophone data stream. In general, the estimates $\hat{N}_1$, $\hat{N}_0$ and $\hat{\lambda}$ are site-dependent and therefore each

geophone energy detector is distinct. If intra-geophone noise is spatially uncorrelated and independent, the detection probability for the whole network P_D^{Net} the product of P_D for each geophone, so that

$$P_D^{\text{Net}} = c \prod_{k}^{M} P_D^{(k)}, \tag{A.26}$$

where c is a normalization constant and $P_D^{(k)}$ refers to the detection probability at geophone k. The detection probability for a sub-network of $M - M'$ receivers is likewise a product of M Bernoulli experiment (detected/missed) probabilities [135]:

$$P_D^{\text{Net}} = c \prod_{k}^{M-M'} P_D^{(k)} \prod_{k'}^{M'} \left(1 - P_D^{(k')}\right), \tag{A.27}$$

To review, this section developed a waveform energy detector using a binary hypothesis test and Neyman Pearson decision rule. This decision rule maximizes detection probabilities when the test statistic parameters are known. The underlying distributions for each test were parameterized by degree-of-freedom estimators to improve the test applicability when data includes correlated noise. In the presence of a seismic waveform, I demonstrated that SNR and detection probability can be computed from efficient estimators. I evaluate the quantities computed from these estimators in Section A.7 and in Chapter 3.

A.6 Seismic Waveform Association

Waveform association is the process of attributing a signal observed on multiple receivers to the same seismic event. It provides a means for relating intra-network detection times and is prerequisite for making seismic interpretations beyond single-station event picking. As with detection, waveform association is generally a statistical problem. Challenges arise if icequake occurrence intervals are comparable to the expected differential transit time of a seismic phase between geophones, as waveforms from different sources can then be mis-associated [6]. This scenario fortunately is improbable with the small networks that I consider in this thesis. Here, transit times are short relative to event frequency, due to relevant aperture width scales (900m - 5km) and range of phase velocities in polar ice ($\geq$ 1.67 km sec^{-1} for surface waves, 3850 km sec^{-1} for p-waves). This gives maximum arrival time differences of $\leq$ 3.5 sec between geophones. This suggests that false association of

waveforms is likely only if distinct, detectable icequakes occur within a few seconds of each other near the network.

To estimate the effect of erroneous association, I examined correlation between single station detections where no association errors *could* occur and whole-network detections in each experiment documented in this thesis. My *posterior* observations indicate that if mis-association occurs, it does not apparently affect detection results. Further, events that may be mis-associated during periods of uncommonly high seismicity are typically rejected by other post-processing methods, such as waveform correlation. Therefore, I assume a negligible probability of false attribution and implement a direct association method: if detection times on distinct geophones match within a time less than the network aperture divided by the slowest expected phase speed, they are assumed to indicate the same icequake.

I implement this associator using detections from every non-singleton combination of geophones after each detection routine and count each event only once. For an N receiver network, this provides $2^N - (N + 1)$ possible combinations of geophone detections that represent seismicity observed from that respective sub-network. This sub-network decomposition is implemented in Chapter 2, Sub-Section 2.6.1 to give spatial resolution to seismicity estimates in the absence of epicentral locations.

A.7 Evaluating the Apparent Diurnality of Seismicity

The adaptive-energy detector developed in this chapter (Section A.5) can be used to assess detection biases of a geophone network exposed to diurnally variable noise. This is of practical concern in glacial environments where noise levels caused by meltwater flow can change over the course of a day and suppress icequake detection rates that are then misinterpreted as a reduction in geophysical activity. I provide a minimal description of a relevant network here since this chapter concerns methodology, and Chapter 3 documents the same network assessment thoroughly in an experimental context.

The geophones illustrated in Figure A.19 were deployed on the Western Greenland

Ice Sheet during an experiment that took place over the 2011 melt season (see Chapter 3). Icequakes were picked using the energy detector with picking parameters documented in Table A.20. I provide the result of this picking procedure as a time series of icequakes-per-hour using a single receiver (FL04) for simplicity (Figure A.10). An apparently diurnal signal dominates this time series following day-of-year 175. To assess if detection biases caused this signal, I compare the observed SNR that is computed from waveforms with the detection capability of the energy detector. The detection capability is defined here as the minimum SNR required to achieve a prescribed detection probability P_D, at a prescribed alarm rate P_{FA}. If this minimum SNR over seismic recording time is highly variable, it suggests that a constant emission rate of icequakes would be incorrectly observed as also variable. I compute the threshold SNR required to achieve a 95 % detection probability at a detection threshold constrained by a fixed $P_{FA} = 10^{-6}$ false alarm rate using Equation A.25. These time series were computed for each hour. The mean SNR over the observation period was binned by hour, and data obtained from windows with null-distribution fit-errors exceeding 20 % were discarded. The observed SNR computed from waveform data exceeds the threshold SNR illustrated in Figure A.11 by 6dB to 10dB in every case. Therefore, it is improbable that detection rates are artificially reduced by elevated or suppressed noise, indicating that the diurnal signal is geophysical in this example.

I implement this energy detector on data acquired from each polar network that concerns this thesis. In each case, pick times are computed within each hour along with updated (hourly) estimates of detection-routine parameters. These parameters include the effective degrees of freedom (DOF) in the data, the fit error for the DOF-parameterized null distribution, and the noise variance that reflects 1-hour average detection conditions. The 1 hour detection windows are used in preference to more computationally efficient, longer detection windows to avoid violating assumed statistical stationarity. These pick times and detection metrics initialize an icequake inventory (catalog) for that respective region. Events are then associated according to their detectability on each station, whereby weak events detected on a single station are ignored. Icequakes with sufficient energy (or SINR) to be observable on each geophone in the network are retained for epicentral

location. Full waveform SNR estimates are computed by time-reversing each detected waveform and re-processing it with the energy detector to compute waveform end-time. The data outside the (original) forward-detected and reverse-detected times were then muted to eliminate noise (Figure A.9). I further discuss geophysical interpretations in terms of icequake detectability in specific experiments (Chapters 2 and 3).

A.8 Rayleigh Wave Detection: The Subspace Detector

Rayleigh waves are a reliable indicator for seismic sources in near-surface ice. In contrast to body waves, Rayleigh waves excite particle motion that is retrograde and elliptically polarized at the free surface and produce displacement amplitudes that decay exponentially with burial depth of the source [4, Chapter 7]. Englacial or basal seismic sources, in contrast, are incapable of exciting Rayleigh waves of detectable amplitudes beyond a certain frequency-dependent depth and instead dominantly produce linearly-polarized particle motion at the free surface [36]. To utilize Rayleigh waves for detecting surficial sources, it is first necessary to develop a statistical method to distinguish Rayleigh waves from body waves. While Rayleigh wave detectors and direction-of-arrival estimators have been employed in test-ban treaty monitoring [24], they have received little attention in glaciology, despite their obvious utility. In this section, I develop a formal statistical hypothesis test to demonstrate that a Rayleigh wave detector can be constructed from the "subspace detector" that has been derived elsewhere [146, 65].

The signal models I consider apply to a single, three-component geophone. Under the first model, or null hypothesis $\mathcal{H}_0$, I consider the wavefield to consist only of Gaussian noise. Under the second model, or alternative hypothesis $\mathcal{H}_1$, I consider the wavefield to consist of a Rayleigh wave and additive Gaussian noise. The characteristic retrograde motion of the Rayleigh wave at the ice surface means that the vertical component of displacement (or velocity) is phase-delayed by 90 degrees relative to any linear combination of the ground-parallel motion. The presence of noise means that the data under both hypotheses are described by probability distribution functions, which have six unknown parameters that must be estimated from the data. Two of these parameters are the

noise variances, σ_0 and σ_1, under the competing hypotheses. The third parameter is the back-azimuth to the seismic source, ϕ, and is only applicable under the Rayleigh-wave present hypothesis, $\mathcal{H}_1$. The remaining two parameters shape the F distribution functions[4] of the subspace detection statistic. I write these competing hypotheses in terms of the vertical channel as follows:

$$\begin{aligned} \mathcal{H}_0: &\quad \tilde{\mathbf{u}}_z = \mathbf{n}_0; \quad \text{(only noise)} \\ \mathcal{H}_1: &\quad \tilde{\mathbf{u}}_z = -\left(\mathbf{n}_1 + [\,\mathbf{u}_e\ \mathbf{u}_n\,] \cdot \boldsymbol{\theta}\right); \quad \text{(Rayleigh wave present)}, \end{aligned} \tag{A.28}$$

where the Hilbert transform $\tilde{\mathbf{u}}_z$ of $\mathbf{u}_z$ is a vectorized time series for the vertical geophone component, $\mathbf{u}_e$ and $\mathbf{u}_n$ are vectorized east and north geophone components, $\mathbf{n}_0$ and $\mathbf{n}_1$ are vectors of Gaussian noise with unknown variance, and $\boldsymbol{\theta}$ is a 2×1 vector of weights. The alternative hypothesis case states that the vertical channel and a weighted combination of horizontal channels are brought in phase when the vertical channel is polarity reversed and Hilbert transformed. A detection statistic for Rayleigh waves is constructed using a generalized maximum likelihood ratio Λ and evaluated using a Neyman Pearson decision rule (see A.4). A full derivation of the surface-wave detector is equivalent to that of a rank-2 subspace detector and I refer to analogous derivations that exist in several places [146, 65, 92]. The final result in Equation A.29

$$\Lambda\left(\tilde{\mathbf{u}}_z\right) = \hat{N}_3 \cdot \frac{\tilde{\mathbf{u}}_z^{\mathrm{T}} P_{\mathbf{A}} \tilde{\mathbf{u}}_z}{\tilde{\mathbf{u}}_z^{\mathrm{T}} P_{\mathbf{A}}^{\perp} \tilde{\mathbf{u}}_z} \underset{\mathcal{H}_0}{\overset{\mathcal{H}_1}{\gtrless}} 1 - F^{-1}_{\hat{N}_1, \hat{N}_2}\left(10^{-6}\right) \tag{A.29}$$

constitutes a Rayleigh wave with a false alarm rate of $P_{FA} = 10^{-6}$. Here, $P_{\mathbf{A}}$ is the orthogonal projector onto the subspace $\langle \mathbf{A} \rangle$ spanned by $\mathbf{A} = -1 \cdot [\,\mathbf{u}_e\ \mathbf{u}_n\,]$, and $P_{\mathbf{A}}^{\perp}$ is it's orthogonal complement. The scalars $\hat{N}_1$ and $\hat{N}_2$ are estimates for degrees-of-freedom of the central F distribution under the null hypothesis and $\hat{N}_3$ is a shape parameter; they are computed numerically by fitting an F-distribution function to histograms of Λ using the method described in Section A.5. The direction of arrival (DOA) of the Rayleigh wave is

[4]The detection statistic in Equation A.29 has an *approximate* F distribution. The true statistic is a sum of sample correlation coefficients, and is therefore impractical to use.

estimated from:

$$\begin{aligned} \phi &= \arctan \frac{\hat{\theta}_2}{\hat{\theta}_1} \\ \hat{\boldsymbol{\theta}} &= \left(\mathbf{A}^{\mathrm{T}}\mathbf{A}\right)^{-1}\mathbf{A}^{\mathrm{T}} \cdot \tilde{\mathbf{u}}_z \end{aligned} \tag{A.30}$$

where $\hat{\boldsymbol{\theta}}$ is the MLE of the coefficient vector that maximizes the coherency of horizontal-plane and vertical motion. Azimuth ϕ is the positive angle between the source-receiver plane (the saggital plane for the Rayleigh wave) and the plane of maximum measured signal variance. In practice, these data are pre-processed by narrow-band filtering the data in 5 Hz bands centered at the dominant frequency in the data, prior to computing $\Lambda\left(\tilde{\mathbf{u}}_z\right)$ and ϕ in Equation A.30. I emphasize that parameters $\hat{N}_k$, $(k = 1, 2, 3)$ must be estimated post-filtering to account for the induced reduction in the data dimension (Section A.3).

The capability of the detector in Equation A.30 is illustrated in Figure A.12. Here, directions-of-arrival are computed from synthetic tests using 500 realizations of a Rayleigh waveform in Gaussian noise (pre-processed data SNR $\approx$ 3). In each case the detector correctly identifies the signal and the source azimuth within $\leq 5^{\circ}$. Detection results using real geophone data collected from the Western Greenland Ice Sheet is illustrated in Figure A.13 (Chapter 3). In this case, Rayleigh waves that were missed using the energy detector, summarized in Section A.5, are identified. A complete discussion of additional detection results from the Greenland Ice Sheet are included in Chapter 3.

A.9 Multiplet Detection and Record Section Correlation

Multiplets are distinct, repeating seismic events that produce nearly identical records of ground motion. Their detection provides an observation of repetitive stress release from the same source region due to similar source mechanisms. These observations are important for attributing the seismicity within a glaciated region to the presence of an reoccurring source [21]. To quantify the similarity between multiplet waveforms, I implement a network-based measure for correlation between events that uses the ground motion recorded by all receivers simultaneously [52, 64]. A vectorial sample of ground velocity $\mathbf{x}(t)$ from an M-receiver network of 3-component geophones is provided by $3M$ associated record sections that are

organized into a column matrix, consistent with Equation A.2:

$$\mathbf{x} = [\,\mathbf{x}_{11},\ \mathbf{x}_{12},\ \mathbf{x}_{13},\ \mathbf{x}_{21},\ \mathbf{x}_{22},\ \mathbf{x}_{23},\ \ldots\ \mathbf{x}_{M3}\,]^{\mathrm{T}} \quad t \in T. \tag{A.31}$$

Vector $\mathbf{x}_{ij}$ in Equation A.31 symbolizes the discretized ground velocity for receiver i in direction j, sampled over time window T and commas separate matrix columns. The explicit dependence of $\mathbf{x}_{ij}$ on sample interval and record length is defined in Section A.2 by Equation A.1. In practice, a network of geophone measurements given by Equation A.31 comprise samples of noise-contaminated ground velocity recorded over T seconds, or equivalently, N samples. Inoperable or absent rows (channels) are down-weighted or deleted from this vector. In certain computational applications, it is convenient to arrange $\mathbf{x}$ as a time-sample multiplexed column vector of length $3MN$ (e.g., [65, 63]). In deriving the detection statistic in this Section (A.9), I will assume the data have been multiplexed into a vector as in Harris [65] so that at sample n $(n = 0, 1, 2, \cdots N)$:

$$\mathbf{x}\big[3Mk + 3(i-1) + j - 1\big] = \mathbf{x}_{ij}[n] \tag{A.32}$$

With this convention, the matrix Frobenius inner product $\langle \mathbf{x}, \bullet \rangle_F$ for $\mathbf{x}$ as defined in Equation A.31 (and implemented in Chapter 2), is equivalent to the vector dot product $\langle \mathbf{x}, \bullet \rangle_2$ for $\mathbf{x}$ as defined in Equation A.32.

The normalized sample correlation between two distinct, T-second record sections $\mathbf{x}$ and $\mathbf{w}$ measured over a network was defined earlier using Equation A.17, and is repeated here:

$$\hat{\rho} \triangleq \frac{\langle \mathbf{x}, \mathbf{w} \rangle}{||\mathbf{x}||\,||\mathbf{w}||} = \frac{\mathbf{x}^{\mathrm{T}}\mathbf{w}}{||\mathbf{x}||\,||\mathbf{w}||} \tag{A.33}$$

Equation A.33 assigns a functional on a product space [156, p. 78], in each time window T. The true correlation coefficient ρ is bounded by ± 1 and is **not** equivalent to the mean channel correlation. Values of $\hat{\rho}$ near $+1$ indicate similar waveforms and source locations, but do not require intra-receiver coherence [21, 52], which is degraded by path and attenuation effects whenever the network aperture is greater than source or path heterogeneity scale (Figure A.14). However, $\hat{\rho}$ maintains a spatial discrimination capability: if two sources are separated in distance but are otherwise identical, the differential arrival

times between the N receivers cause misalignment between the record sections $\mathbf{x}$ and $\mathbf{w}$ so that $|\hat{\rho}| < 1$.

Figure A.16 illustrates two noisy multi-channel record sections with moderate sample correlation ($\hat{\rho}$=0.62) and visually apparent signal overlap. It shows how a low SNR for either $\mathbf{x}$ or $\mathbf{w}$ can additionally reduce record-section correlation even when the underlying waveforms are identical (or nearly so). This degradation in correlation from the infinite-SNR (or zero noise) value (ρ_0) is quantified by relating ρ to the SNR of each waveform through Equation A.34:

$$\rho = \frac{\sqrt{\mathrm{SNR}\,(\mathbf{x}) \cdot \mathrm{SNR}\,(\mathbf{w})}}{\sqrt{(1 + \mathrm{SNR}\,(\mathbf{w})) \cdot (1 + \mathrm{SNR}\,(\mathbf{x}))}} \cdot \rho_0. \tag{A.34}$$

where Equation A.34, is derived assuming the embedding noise and signal are uncorrelated.

The distinction between observed and true (infinite-SNR) correlation become significant in applications where one signal is used as a reference for correlation-based detection. I first consider the case where a reference or "template" record section $\mathbf{w}$ and target waveform $\mathbf{x}$ each have an SNR of 1. Here, their expected correlation is $1/2$. In contrast, a known template has an infinite $\mathrm{SNR}\,(\mathbf{w})$ and produces a correlation with $\mathbf{x}$ of $1/\sqrt{2}$. Therefore, inadequate knowledge of the template record section results in a significant loss in the performance of correlation detectors [53]. Additional loss in correlation between a target record section and template may originate from source or medium changes. Realistic changes include source mechanism evolution (e.g., ice fracture reorientation), and relative motion between the receiver and source medium (e.g., flowing glacial ice). In this case, *a priori* template signal knowledge is even more limited.

A.10 Template Knowledge and Multiplet Identification

Lack of template knowledge has practical consequences for multiplet identification. This is because each constituent record section that represents a multiplet population is unknown prior to its detection. Seismic studies sometimes implement clustering methods in parallel with a correlation metric (see Chapter B) to autonomously identify repeating seismic events

in near real time [60]. The statistics associated with this clustering process generally are not quantified, however. In particular, the expected correlation ρ_0 that controls membership assignment between record sections within a multiplet sequence may change over time with elevated noise levels or medium evolution. Therefore, the minimum correlation threshold required to correctly identify all mutliplet record sections that share a seismic source into a single cluster is unknown. The probability of missing an event that should be attributed to that cluster is also unknown.

I address these uncertainties using an implicit, rather than explicit signal model in the following, semi-self contained section. This model enforces a similarity constraint on the observed multiplet record sections relative to an *unknown* template to define a novel detection statistic. With this detection statistic, the uncertainty in the correct threshold ρ_0 that defines multiplet membership can be determined through a prior distribution function for ρ_0. I show that the corresponding marginal distribution function can also be used to construct a correlation detector. As the case of the Energy and Rayleigh wave detectors, the effective dimension of the data heavily parameterizes the detection statistic, and is considered in several Figures (e.g., Figures A.2 and A.18).

The derivation of the corresponding multiplet detection statistic is a general result which likely will be useful for several geophysical applications in future work.

A.11 Quantitative Development of a Convex Cone Detector [5]

Correlation between *sets* of vectors $\mathbf{x}$ that represent network-observations of ground motion can be stated concisely using the concept of a "convex cone" $\mathcal{C}$ [21, 156]. A cone is a nonlinear analogue to a subspace and may be indexed (conditioned upon) a template waveform $\mathbf{w}$ or other reference vector the same way a linear subspace is. In this thesis, I focus on their application to multiplet detection. The membership criteria for $\mathcal{C}$ that defines a convex cone

[5] This section is intended to be somewhat self-contained, and some definitions are repeated.

has a mathematical representation given by Equation A.35,

$$\mathcal{C} = \left\{ \mathbf{x} : \frac{\langle \mathbf{x}, \mathbf{w} \rangle}{||\mathbf{x}||\,||\mathbf{w}||} \geq \rho_0 \right\}, \tag{A.35}$$

where $\mathbf{x},\ \mathbf{w} \in \mathbb{R}^{3MN \times 1}$ because the network data include $3M$-channels. This cone is visualized with a "vertex" parallel to $\mathbf{w}$ and cone aperture $\arccos(\rho_0)$. The set of all possible multiplet record sections are geometrically represented in $3MN$-dimensional space as occupying the interior or boundary of the cone. The membership condition I have specified with Equation A.35 provides a sufficient constraint to formulate an evaluable hypothesis test: in the signal-absent case, I assume that the data vector $\mathbf{x}$ is composed exclusively of normally distributed noise so that $\mathbf{x} = \mathbf{n} \sim \mathcal{N}\left(\mathbf{0}, \sigma^2\mathbf{I}\right)$ with noise variance σ^2 when $\mathcal{H}_0$ is true. When signal is present and $\mathcal{H}_1$ is true, the multiplet-present data vector $\mathbf{x}$ has a conic representation $\mathbf{x} = \mathbf{u}(t) + \mathbf{n}(t)$ where $\mathbf{u}(t) \in \mathcal{C}$.

Deciding upon the presence or absence of a multiplet signal under these two competing hypotheses is therefore equivalent to testing between the PDFs (distribution functions) in Equation A.36:

$$\begin{aligned} \mathcal{H}_0 :&\quad \mathbf{x}(t) \sim \mathcal{N}\left(\mathbf{0}, \sigma^2\mathbf{I}\right) \\ \mathcal{H}_1 :&\quad \mathbf{x}(t) \sim \mathcal{N}\left(\mathbf{u}, \sigma^2\mathbf{I}\right), \quad \mathbf{u}(t) \in \mathcal{C} \end{aligned} \tag{A.36}$$

Set $\mathcal{C}$ is given by Equation A.35 and is effectively parameterized by the (multiplexed) template waveform $\mathbf{w}$ and correlation ρ_0. The variance of each PDF is effectively unknown and must be estimated from the data as "nuisance parameters"' along with the distributional mean $\mathbf{u}$ under hypothesis $\mathcal{H}_1$ in order to evaluate the test. I assume any template event is (independently) drawn from the same random process as $\mathbf{x}$ and therefore the distribution under $\mathcal{H}_1$ is conditional upon observation of the template event $\mathbf{w}$. To simplify notation, the PDF under $\mathcal{H}_0$ is denoted as $p_0(\mathbf{x}; \mathcal{H}_0)$ and the PDF under $\mathcal{H}_1$ as $p_1(\mathbf{x}; \mathcal{H}_1)$. The competing hypotheses with this notation are as follows:

$$\begin{aligned} \mathcal{H}_0 :&\quad p_0(\mathbf{x}; \mathcal{H}_0) \quad \text{signal absent}, \quad \sigma^2 \quad \text{unknown} \\ \mathcal{H}_1 :&\quad p_1(\mathbf{x}; \mathcal{H}_1) \quad \text{signal present}, \quad \sigma,^2\ \mathbf{u} \quad \text{unknown} \end{aligned} \tag{A.37}$$

To compare these hypotheses, I perform a **generalized likelihood ratio test** (GLRT). This test compares the ratio of the two PDFs, evaluated at the maximum likelihood estimates of their unknown parameter values. These estimates are generally different, and are indexed by their hypothesis. The decision to choose between these two hypotheses (signal absent versus mulitplet present) is then determined by a threshold value η. This threshold partitions the data space into two disjoint decision regions $R_0(\mathbf{x})$ and $R_1(\mathbf{x})$. Therefore, the scalar test:

$$\Lambda(\mathbf{x}) = \frac{\max\limits_{\sigma,\mathbf{u}}\{\, p_1(\mathbf{x};\, \mathcal{H}_1)\,\}}{\max\limits_{\sigma}\{\, p_0(\mathbf{x};\, \mathcal{H}_0)\,\}} \quad \underset{\mathcal{H}_0}{\overset{\mathcal{H}_1}{\gtrless}} \quad \eta, \tag{A.38}$$

constitutes a decision test on the presence of a multiplet waveform. The corresponding decision regions are

$$\begin{aligned} R_1 &= \{\mathbf{x} :\, \text{Decide } \mathcal{H}_1,\ \text{Reject } \mathcal{H}_0\}, \\ R_0 &= \{\mathbf{x} :\, \text{Decide } \mathcal{H}_0,\ \text{Reject } \mathcal{H}_1\}. \end{aligned} \tag{A.39}$$

An application of this test to multiplet detection provides two novel results that require context for proper interpretation. Therefore, I provide a summarized derivation of the test statistic which is preferable to an ambiguous statement of the results. First, I reform the GLRT of Equation A.38 and as an identical logarithmic test in Equation A.40,

$$\ln(\Lambda) = \ln\left[\max_{\sigma,\mathbf{u}}\{\, p_1(\mathbf{x};\, \mathcal{H}_1)\,\}\right] - \ln\left[\max_{\sigma}\{\, p_0(\mathbf{x};\, \mathcal{H}_0)\,\}\right] \tag{A.40}$$

where the maximization and logarithm operations commute due the monotonicity of the log-function. I emphasize that although the *underlying* noise statistics are the same under each hypothesis, the variance σ^2 must be maximized separately as σ_0^2 and σ_1^2 according to the signal model. Because each hypothesis distribution

$$\begin{aligned} p_1(\mathbf{x};\, \mathcal{H}_1) &= \frac{1}{(2\pi\sigma^2)^{\frac{N}{2}}} \exp\left[\frac{(\mathbf{x}-\mathbf{u})^{\mathrm{T}}(\mathbf{x}-\mathbf{u})}{2\sigma^2}\right] \\ p_0(\mathbf{x};\, \mathcal{H}_1) &= \frac{1}{(2\pi\sigma^2)^{\frac{N}{2}}} \exp\left[\frac{\mathbf{x}^{\mathrm{T}}\mathbf{x}}{2\sigma^2}\right] \end{aligned} \tag{A.41}$$

is multivariate normal by assumption, this results in a consider simplification in computing the MLEs for each parameter. Performing the maximizations over the variance under each

hypothesis,

$$\begin{aligned}\hat{\sigma}_1^2 &= \underset{\sigma}{\text{argmax}}\{\ \ln\left[p_1\left(\mathbf{x};\ \mathcal{H}_1\right)\right]\ \} = \frac{\left(\mathbf{x}-\mathbf{u}\right)^{\mathrm{T}}\left(\mathbf{x}-\mathbf{u}\right)}{N} \\ \hat{\sigma}_0^2 &= \underset{\sigma}{\text{argmax}}\{\ \ln\left[p_0\left(\mathbf{x};\ \mathcal{H}_0\right)\right]\ \} = \frac{\mathbf{x}^{\mathrm{T}}\mathbf{x}}{N}\end{aligned} \tag{A.42}$$

results in their (biased) sample estimates [146, 91, 92]. The subscripts on each estimate of the sample variance in Equation A.42 indicate which hypothesis is applicable. I next evaluate $p_1\left(\mathbf{x};\mathcal{H}_1\right)$ at its MLE for σ_1, and perform the required maximization of $\mathbf{u}\in\mathcal{C}$ under $\mathcal{H}_1$,

$$\hat{\mathbf{u}} = \underset{\mathbf{u}\in\mathcal{C}}{\text{argmax}}\{\ \ln\left[p_1\left(\mathbf{x};\ \mathcal{H}_1\right)\right]\ \}|_{\sigma=\hat{\sigma}_1} = \underset{\mathbf{u}\in\mathcal{C}}{\text{argmin}}\left\{\frac{2\left(\mathbf{x}-\mathbf{u}\right)^{\mathrm{T}}\left(\mathbf{x}-\mathbf{u}\right)}{N}\right\}. \tag{A.43}$$

This solution to this equation,

$$\hat{\mathbf{u}} = P_{\mathcal{C}}\left(\mathbf{x}\right), \tag{A.44}$$

must minimize the distance between the observed data, $\mathbf{x}$, and all points that constitute the multiplet set, $\mathcal{C}$. This vector $P_{\mathcal{C}}\left(\mathbf{x}\right)$ is therefore the projection of $\mathbf{x}$ onto convex cone, $\mathcal{C}$. Because I have made no explicit mention of the form of $\mathcal{C}$, this is a general result for any convex set (cones included) when data are normally distributed. When the MLE is combined with the variance MLEs into the log-GLRT, the decision rule

$$\frac{2}{N}\ln\left(\Lambda\right) = -\ln\left[1-\frac{\left|\left|P_{\mathcal{C}}\left(\mathbf{x}\right)\right|\right|^2}{\left|\left|\mathbf{x}\right|\right|^2}\right] \underset{\mathcal{H}_0}{\overset{\mathcal{H}_1}{\gtrless}} \frac{2}{N}\ln\left(\eta\right) \tag{A.45}$$

becomes reducible to an evaluation of the test statistic

$$T\left(\mathbf{x}\right) = \frac{\left|\left|P_{\mathcal{C}}\left(\mathbf{x}\right)\right|\right|^2}{\left|\left|\mathbf{x}\right|\right|^2} \tag{A.46}$$

after routine algebraic manipulation. Equation A.46 demonstrates that $T\left(\mathbf{x}\right)$ compares the projected signal energy to the energy of the original signal. The explicit expression for the projection $P_{\mathcal{C}}\left(\mathbf{x}\right)$ of general $\mathbf{x}$ onto $\mathcal{C}$ has been derived in [156] using the method of Lagrange multipliers. I provide an equivalent form of that expression here:

$$P_{\mathcal{C}}\left(\mathbf{x}\right) = \begin{cases}\mathbf{0} & \dfrac{r}{\sqrt{1-r^2}} \leq -c \\ \mathbf{x} & \dfrac{r}{\sqrt{1-r^2}} > \dfrac{1}{c} \\ \gamma\left(\rho_0\hat{\mathbf{w}} + \sqrt{1+\rho_0^2}\hat{\mathbf{w}}_{\perp}\right) & \text{otherwise}\end{cases} \tag{A.47}$$

The constants and vectors are:

$$\hat{\mathbf{w}}_{\perp} = \frac{\left(\mathbf{I} - \hat{\mathbf{w}}\hat{\mathbf{w}}^{\mathrm{T}}\right)\mathbf{x}}{||\left(\mathbf{I} - \hat{\mathbf{w}}\hat{\mathbf{w}}^{\mathrm{T}}\right)\mathbf{x}||}, \qquad r = \frac{\mathbf{x}^{\mathrm{T}}\hat{\mathbf{w}}}{||\mathbf{x}||},$$

$$c = \sqrt{\frac{1-\rho_0^2}{\rho_0^2}}, \qquad \gamma = \rho_0\left(\mathbf{x}^{\mathrm{T}}\hat{\mathbf{w}}\right) + \sqrt{1-\rho_0^2}\left(\mathbf{x}^{\mathrm{T}}\hat{\mathbf{w}}_{\perp}\right) \tag{A.48}$$

where $\mathbf{w}$ is the template waveform defined in Equation $A.35$ and $\hat{\mathbf{w}} = \mathbf{w}/||\mathbf{w}||$. It is illustrative to contrast this convex cone (conic) projection with the one-dimensional subspace projection onto span$\{\hat{\mathbf{w}}\}$ that is implicitly used in correlation detectors. The convex-cone projection differs in that signals having sufficient negative correlation with $\hat{\mathbf{w}}$ are completely nulled, and differs in that projected signals may contain portions $\perp$ to $\hat{\mathbf{w}}$. Therefore, it is more similar to a higher-dimensional subspace projection, but requires only one template record section to characterize it. However, it's projection depends on the polarity of the waveforms composing the record section relative to the template. In this respect, the conic projection acts as a polarity filter.

Equation A.46 indicates that the generalized likelihood ratio $\Lambda(\mathbf{x})$ in Equation A.38 is reducible into an equivalent sufficient (scalar) test statistic $T(\mathbf{x})$ that maps the higher dimensional decision regions into **scalar regions** and therefore facilitates an equivalent (simpler) decision rule. This scalar test statistic $T(\mathbf{x})$ is also a random variable and consequently, this decision rule can be stated in terms of the pdfs for T, $p_T(t;\mathcal{H}_i)$ ($i = 1, 2$) instead of $\mathbf{x}$. The choice between the decision regions in Equation A.39 can then be optimized via $p_T(t;\mathcal{H}_i)$ such that for a *prescribed* false alarm probability P_{FA} (test size), the detection probability P_D (test power) is asymptotically maximized. This is a result of the Neyman-Pearson Lemma [92] (see also Section A.4).

A.12 The Distribution function for the Convex Cone Detection Statistic

The test statistic $T(\mathbf{x})$ together with the threshold η in Equation A.45 constitute a detector. The threshold η may be found by integrating the PDF of $T(\mathbf{x})$ over the acceptance region $R_1(\mathbf{x})$ under $\mathcal{H}_0$. Alternatively, the PDF for $T(\mathbf{x})$ may be transformed into a

function of the **sample correlation statistic** r and integrated over a transformed region. I implement the transformational approach because the resultant PDF is independent of $\hat{\mathbf{w}}$. I term the transformed, sufficient detection statistic $T'(r)$ and relevant decision rule as the "convex cone", or multiplet detector.

I first note that the projection $P_{\mathcal{C}}(\mathbf{x})$ has three possible values. In the case that $P_{\mathcal{C}}(\mathbf{x}) = \mathbf{x} \in \mathcal{C}$ the hypothesis choice $\mathcal{H}_1$ is mandatory (subject to some false alarm rate); in the case that $P_{\mathcal{C}}(\mathbf{x}) = \mathbf{0}$, $\mathcal{H}_1$ should not be chosen, since this implies that the detector would also decide $\mathcal{H}_1$ when $\mathbf{x} = \mathbf{0}$, because $-c < 0$. Therefore, the partitioning of the decision region should be contained in the set defined by $-c\sqrt{1-r^2} < r < \frac{1}{c}\sqrt{1-r^2}$. In this case, $||P_{\mathcal{C}}(\mathbf{x})|| = \gamma$ within the acceptance region $R_1(\mathbf{x})$ and the decision rule is provided by Equation A.49

$$\frac{\gamma}{||\mathbf{x}||} \underset{\mathcal{H}_0}{\overset{\mathcal{H}_1}{\gtrless}} \eta', \tag{A.49}$$

where η' is the to-be-determined detection threshold.

To consider the PDF over the lower half of the acceptance region, I substitute the identities from A.48 into A.49 and retrieve an equation for the $T'(r)$ that is a function of the sample correlation alone:

$$T'(r) = r + c\sqrt{1-r^2} \underset{\mathcal{H}_0}{\overset{\mathcal{H}_1}{\gtrless}} \eta', \tag{A.50}$$

where I have reused symbol η' as the unknown threshold. The sample correlation statistic r has a well documented PDF that is parameterized by true correlation ρ between the sample vectors, and effective dimension N_E (Figures A.17 and A.18). I denote this PDF as $p_R(r)$, where

$$p_R(r) = \frac{(N_E-2)\left(1-\rho^2\right)^{\frac{1}{2}N_E-\frac{1}{2}}\left(1-r^2\right)^{\frac{1}{2}N_E-2}}{\sqrt{2}\,(N_E-1)\,B\left(\frac{1}{2},N_E-\frac{1}{2}\right)(1-\rho r)^{N_E-\frac{3}{2}}}\,{}_2F_1\left(\frac{1}{2},\frac{1}{2};N_E-\frac{1}{2};\frac{1}{2}(1+\rho r)\right) \tag{A.51}$$

and ${}_2F_1(a,b;c;x)$ is Gauss' Hypergeometric function [181, Equation C.2.5]. It is easily implemented in MATLAB[6]. The multiplet detector PDF is then expressible using $p_R(r)$

[6] A matlab function `corrdist.m` is available from Dr. Xu Cui of Stanford University. I provide a modified, numerically-stabilized version here:

through a change of variables. This variable change requires finding an inverse for $T'(r)$ over the domain $0 \leq r \leq 1$. The function $r + c\sqrt{1-r^2}$ is not directly invertible, but is a two-to-one function over part of it's domain, one-to-one over the remainder of it's domain, and therefore is piecewise-invertible. This domain partitioning is dependent upon the size of the correlation value $\rho_0 \gtrless 1/\sqrt{2}$ that assigns membership to the set $\mathcal{C}$. I first document the PDF for the detector when $\rho_0 > 1/\sqrt{2}$. In this case, $T(r)$ is locally invertible over $\left[0, 2\,\rho_0^2 - 1\right)$ and $\left[2\,\rho_0^2 - 1,\, 1\right]$ with a PDF given by,

$$p_T(t;\mathcal{H}_i) = p_R\left(\rho_0^2\, t - \sqrt{1-\rho_0^2}\,\sqrt{1-(\rho_0\, t)^2}\right) \cdot \left(\rho_0^2 + \frac{\rho_0^2\sqrt{1-\rho_0^2}\, t}{\sqrt{1-(\rho_0\, t)^2}}\right) \tag{A.52}$$

if $0 \leq r < 2\,\rho_0^2 - 1$, $\rho_0 > 1/\sqrt{2}$, and with a PDF given by

$$\begin{aligned} p_T(t;\mathcal{H}_i) = & p_R\left(\rho_0^2\, t - \sqrt{1-\rho_0^2}\,\sqrt{1-(\rho_0\, t)^2}\right) \cdot \left(\rho_0^2 + \frac{\rho_0^2\sqrt{1-\rho_0^2}\, t}{\sqrt{1-(\rho_0\, t)^2}}\right) + \cdots \\ & p_R\left(\rho_0^2\, t + \sqrt{1-\rho_0^2}\,\sqrt{1-(\rho_0\, t)^2}\right) \cdot \left(\rho_0^2 - \frac{\rho_0^2\sqrt{1-\rho_0^2}\, t}{\sqrt{1-(\rho_0\, t)^2}}\right) \end{aligned} \tag{A.53}$$

if $2\,\rho_0^2 - 1 \leq r \leq 1$, $\rho_0 > 1/\sqrt{2}$.

In the lower threshold case, $\rho_0 \leq 1/\sqrt{2}$, and $T'(r)$ is locally invertible over $\left[0, 2\,\rho_0\sqrt{1-\rho_0^2}\right)$ and $\left[2\,\rho_0\sqrt{1-\rho_0^2}, 1\right]$. It has a PDF given by Equation A.54

$$\begin{aligned} p_T(t;\mathcal{H}_i) = & p_R\left(\rho_0^2\, t - \sqrt{1-\rho_0^2}\,\sqrt{1-(\rho_0\, t)^2}\right) \cdot \left(\rho_0^2 + \frac{\rho_0^2\sqrt{1-\rho_0^2}\, t}{\sqrt{1-(\rho_0\, t)^2}}\right) + \cdots \\ & p_R\left(\rho_0^2\, t + \sqrt{1-\rho_0^2}\,\sqrt{1-(\rho_0\, t)^2}\right) \cdot \left(\rho_0^2 - \frac{\rho_0^2\sqrt{1-\rho_0^2}\, t}{\sqrt{1-(\rho_0\, t)^2}}\right) \end{aligned} \tag{A.54}$$

if $0 \leq r < 2\,\rho_0\sqrt{1-\rho_0^2}$, $\rho_0 \leq 1/\sqrt{2}$, and has a PDF given by Equation A.55

$$p_T(t;\mathcal{H}_i) = p_R\left(\rho_0^2\, t + \sqrt{1-\rho_0^2}\,\sqrt{1-(\rho_0\, t)^2}\right) \cdot \left(\rho_0^2 - \frac{\rho_0^2\sqrt{1-\rho_0^2}\, t}{\sqrt{1-(\rho_0\, t)^2}}\right) \tag{A.55}$$

if $2\,\rho_0\sqrt{1-\rho_0^2} \leq r \leq 1$, $\rho_0 \leq 1/\sqrt{2}$.

---

http://earthweb.ess.washington.edu/ joshuadc/matlabscripts.html

I provide three additional comments concerning this PDF to facilitate its interpretation:

First, the template $\hat{\mathbf{w}}$ does not need to be explicitly described because $p_T(t;\mathcal{H}_i)$ depends on the data $\mathbf{x}$ only through sample correlation r. Therefore, the conditioning on $\hat{\mathbf{w}}$ is **effectively removed**. Second, the value of ρ_0 (generally unknown) featured in $p_T(t;\mathcal{H}_i)$ is distinct from both the true (also unknown) correlation ρ and the random variable r. When ρ_0 is a random variable, its corresponding distribution can be multiplied by p_T and integrated (marginalized) out. In this case, $p_T(t;\mathcal{H}_i)$ should instead by thought of as $p_T(t;\mathcal{H}_i|\,\rho_0)$. This is the conditional PDF of t, given correlation ρ_0. Third, the detection probability under $\mathcal{H}_1$ will be parameterized by the true (unknown) correlation ρ. This is also true when a prior distribution for ρ_0 is available. However, the decision rule (Section A.13) requires no knowledge of ρ, since the detection threshold is determined under $\mathcal{H}_0$ where the data has zero expected correlation with the target waveform [181].

A.13 The Correlation Detector

A prior distribution for ρ_0 may be unavailable in many potential applications for the multiplet detector that was introduced in Section A.11. In this case, I use a delta-function prior that is nonzero at $\rho_0 = 1$ to marginalize out ρ_0 and obtain a correlation detector:

$$p_R(t;\mathcal{H}_i) = \int_0^1 p_T(t;\mathcal{H}_i,\rho_0)\,\delta(\rho_0 - 1)\,d\rho_0 \tag{A.56}$$

where

$$\lim_{\rho_0\to+1^{(-)}} p_T(t;\mathcal{H}_i) \;=\; p_R(r;\mathcal{H}_i) \quad \text{since,} \quad \lim_{\rho_0\to1^{(-)}} \frac{\rho_0^2\sqrt{1-\rho_0^2}\,t}{\sqrt{1-(\rho_0\,t)^2}} = 1. \tag{A.57}$$

Here, $1^{(-)}$ indicates the limit from the left of 1. Consequently, **a correlation detector is a limiting case of a convex cone detector**. In this thesis, the detection statistic r and distribution $p_R(r;\mathcal{H}_i)$ will be used instead of t and $p_T(t;\mathcal{H}_i)$.

Finally, to define a decision rule for the correlation detector, I determine the threshold that gives the desired $P_{FA} = 10^{-6}$. Under $\mathcal{H}_0$, the true correlation $\rho = 0$, and Equation

A.58 must be inverted for η',

$$P_{FA} = \int_{\eta'}^{1} p_R\left(r\,;\,\mathcal{H}_0\right) dr \tag{A.58}$$

consistent with the Neyman Pearson Lemma. This inversion is simple to perform in MATLAB after establishing a user-defined distribution for $p_R\left(r;\mathcal{H}_i\right)$. [7] With the inverted value for η', the detection probability under $\mathcal{H}_1$ is:

$$P_D = \int_{\eta'}^{1} p_R\left(r\,;\,\mathcal{H}_1\right) dr \tag{A.59}$$

Figure A.17 illustrates the decision region geometry for the correlation detector.

A.14 Correlation Dependence on Effective Degrees of Freedom

In Sections A.5 and A.8, I described how energy and Rayleigh wave detection statistics Z_m and $\Lambda\left(\tilde{\mathbf{u}}_z\right)$ are parameterized by an effective data dimension N_E. I provided estimators for each effective dimension, and demonstrated that correlated noise degrades the discrimination power of each detector by reducing N_E (Figure A.7). The sample correlation statistic r described in Section A.13 is similarly parameterized by an effective dimension parameter (see Figure A.2) that also influences correlation detector performance. Here, I provide an estimator for N_E through a modification of Equation A.19 from Section A.5. In this case, the noise vector $\mathbf{y}$ in Equation A.17 is replaced with the record section template $\hat{\mathbf{w}}$. This template is then cross-correlated with several thousand windows of signal sparse data to obtain an empirical distribution function for the (true) sample correlation ρ that is approximated by $\hat{\rho}$. The analogous estimate for $\hat{N}_E$,

$$\hat{N}_E = 1 + \frac{1}{\hat{\sigma}^2_{\hat{\rho}}} \leq N_E, \tag{A.60}$$

provides a parameterization for $p_R\left(r\,;\,\mathcal{H}_1\right)$ that greatly improves its representation of the data statistic compared to the generally erroneous parameterization $\hat{N}_E = N$. The explicit functional dependence of p_R on N_E is schematically shown in Figure A.18 (top) (see also Figure 2.6 in [181]).

---

[7] See Section A.12 for a discussion on obtaining an m-file for this function.

The true dimension N_E (and $\hat{N}_E$) also varies substantially with network size. This is because maintaing high coherency with additional geophones, relative to a single channel, requires sustained intra-waveform alignment between the additional record sections that comprise extra columns of the data matrix (Equation A.31). Figure A.18 (bottom) illustrates changes in discrimination power of a correlation detector due to varying N_E at constant detection probability. In one case, a record section template with an effective length of 20 samples provides a 99% detection probability at a 58% false alarm rate; a 100 (effective) sample length template maintains the same detection probability at a reduced false alarm rate of $\sim 10^{-7}$. Hence, a 5-fold increase in sample number provides a $\sim 10^6$ reduction in the false alarm rate.

This network-based correlation detector was implemented in experiments in Antarctica and Greenland to identify repeating seismic events from fracture processes. The network geometry and aperture size from each experiment and is respectively documented in Chapters 2 and 3. In both cases, multiplet populations were identified with the correlation detector to reveal localized, repetitive seismic sources indicative of meltwater triggered fracture. Figure A.16 illustrates the application of a 6-channel detector using two receivers to identify a repeating event on the Greenland Ice Sheet. Figure A.21 illustrates a similar detection exercise using vertical component data. In this special case, a spatially stationary seismic source produced effectively identical waveforms at two distinct times, at almost unit correlation.

In conclusion, this appendix provides a rigorous development of three seismic signal detectors for icequake monitoring. Detection thresholds were objectively set by fixing acceptable false alarm rates as provided by the Neyman-Pearson decision rule. I showed that correlated noise and data processing reduce the discrimination power of these detectors by decreasing the effective data dimension of the underlying detection statistic, and thereby increasing overlap between the competing PDFs, that were erroneously parameterized. In each case, this data reduction was adaptively estimated to correct these

PDFs' parameterization and produce a more robust decision rule.

The resulting detectors each provide contributions to icequake monitoring. The energy detector is capable of accurately assessing the effect of diurnal noise on estimated seismicity. The Rayleigh wave detector is capable of discriminating surficial sources from deeper englacial, or basal sources using three-component data in the absence of a Rayleigh waveform template. The multiplet detector developed here appears new, and becomes a network-based correlation detector in the absence of *prior* information about expected correlation.

I further suggest that the effort I have invested to develop a more complete multiplet detection statistic t relative to r (Section A.11) is valuable in several potential applications. These applications include studies targeting aftershock sequences in which swarms of similar events can be used to construct empirical prior distribution functions for ρ_0 [60], and coda wave interferometry studies where a prior can be derived from principles of waveform scattering [155]. Broader impacts could involve developing a Bayesian icequake detector for network use in both polar regions.

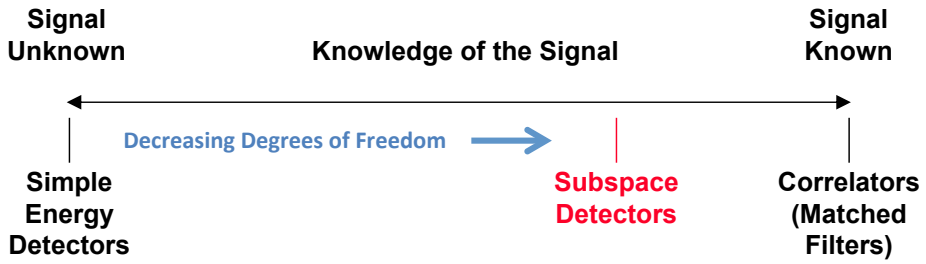

Figure A.1: Diagram of common waveform detectors used in seismology, in order of decreasing signal information. In general, the detection performance (P_D versus P_{FA}) increases with signal specificity at fixed signal dimension. Energy detectors require almost no information about the target waveform, whereas correlation detectors require almost complete information, with only the target waveform amplitude being unspecified. Subspace detectors (including Rayleigh wave detectors) require intermediate information.

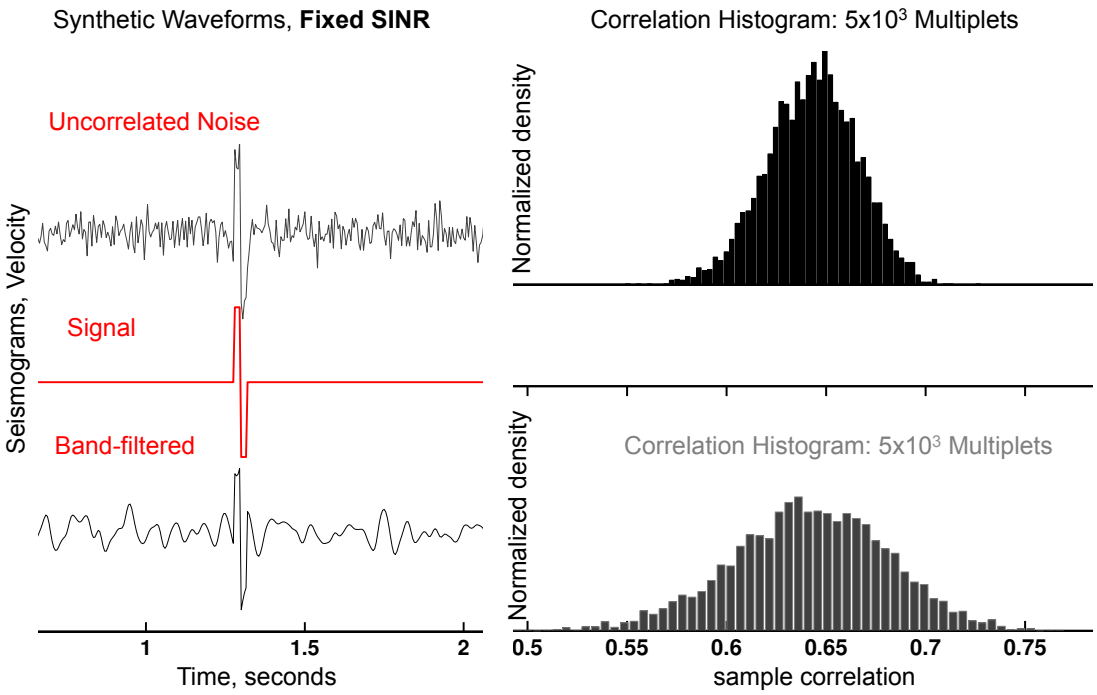

Figure A.2: The effect of correlated noise on sample dependency. Time series with the same signal and 5000 independent realizations white of Gaussian noise (**top-left**), are cross-correlated to produce a histogram showing the relative frequency of obtaining a given sample correlation (**top-right**). Time series of the same signal (**middle-left**) in 5000 independent realizations of band-pass filtered noise (**bottom-left**) are cross-correlated to produce a comparative histogram, again showing the relative frequency of obtaining a given sample correlation (**bottom-right**). The effect of correlated noise clearly broadens the distribution tails and therefore gives the corresponding sample correlation distribution a higher variance.

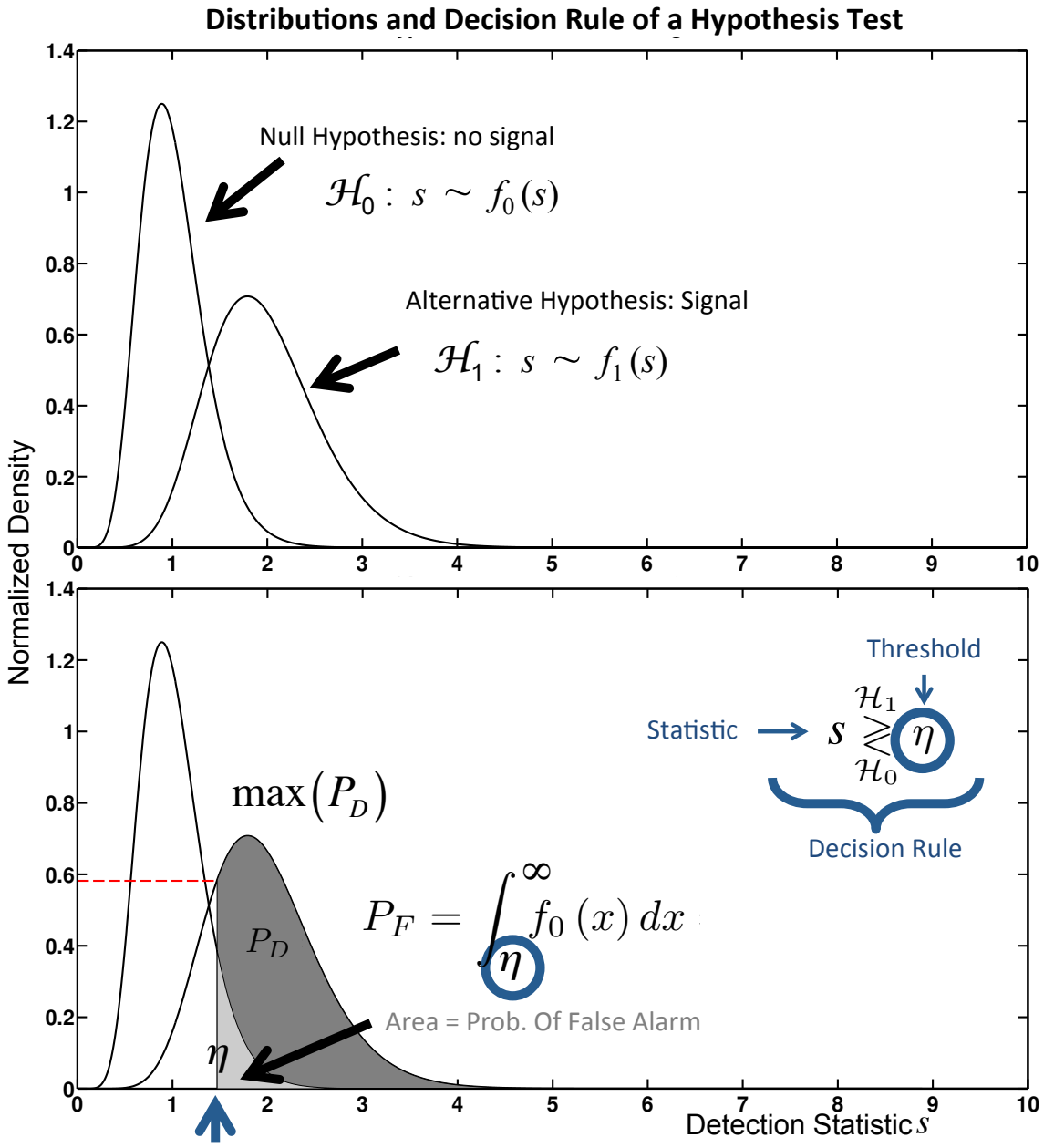
Distributions and Decision Rule of a Hypothesis Test
Null Hypothesis: no signal
$\mathcal{H}_0 : s \sim f_0(s)$
Alternative Hypothesis: Signal
$\mathcal{H}_1 : s \sim f_1(s)$
Normalized Density
Threshold
Statistic
s
$\mathcal{H}_1$
η
$\mathcal{H}_0$
Decision Rule
$\max(P_D)$
$P_F = \int_{\eta}^{\infty} f_0(x)\,dx$
P_D
η
Area = Prob. Of False Alarm
Detection Statistic s

Figure A.3: An illustration of the probability distribution distribution functions (PDFs) for a general detection statistic under two competing hypotheses (discussed in Section A.4). **Top**: Two competing hypothesis formed from an arbitrary scalar detection statistic. The left null distribution corresponds to an absent signal, whereas the right alternative distribution corresponds to a signal present. The considerable overlap between the two distributions implies that a high threshold is needed to avoid false alarms, at the expense of missing detections. **Bottom**: The decision regions for the Neyman Pearson decision rule and partitioning by η. The shaded regions indicate the false alarm probability P_{FA} and the detection probability P_D for this threshold choice.

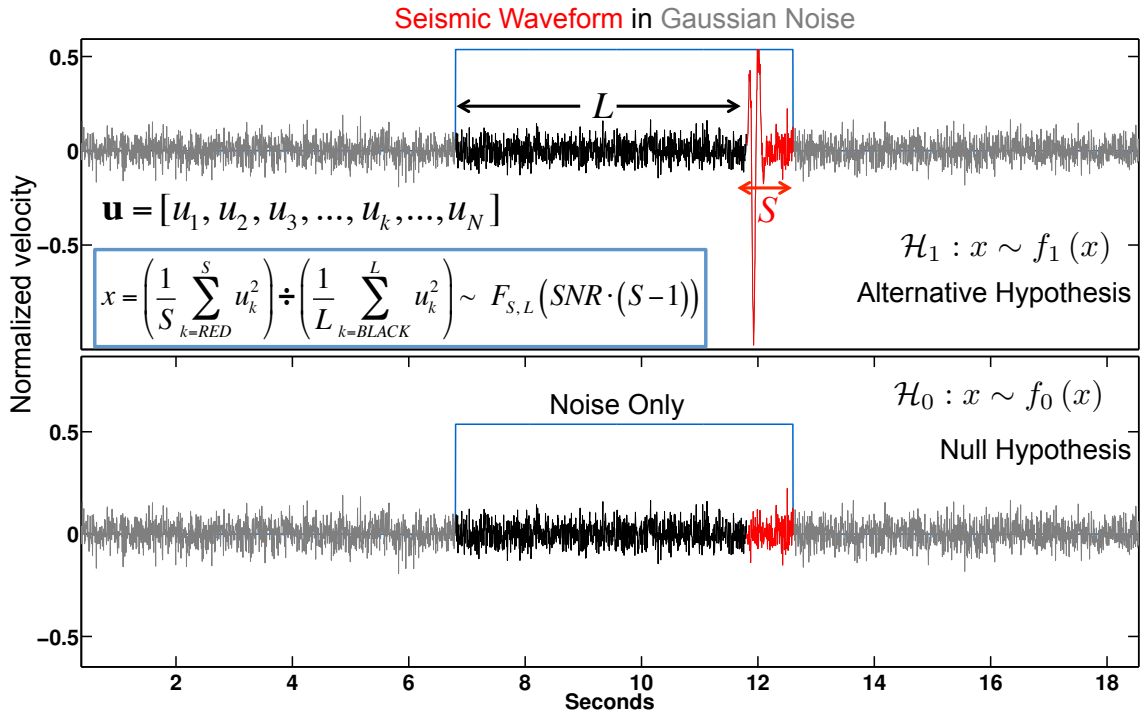

Figure A.4: An illustration of the parameters in the STA/LTA detection statistic discussed in Section A.5. The blue line indicates the sliding detector window, the black data samples indicate the long-term window, and the red samples indicate the short time window. The statistic Z_m is computed from data samples u_k, $k = 1, 2, \ldots, N$ as shown. The detection statistic distribution shape and localization differs according to the presence or absence of seismic signal, indicated by the competing hypotheses.

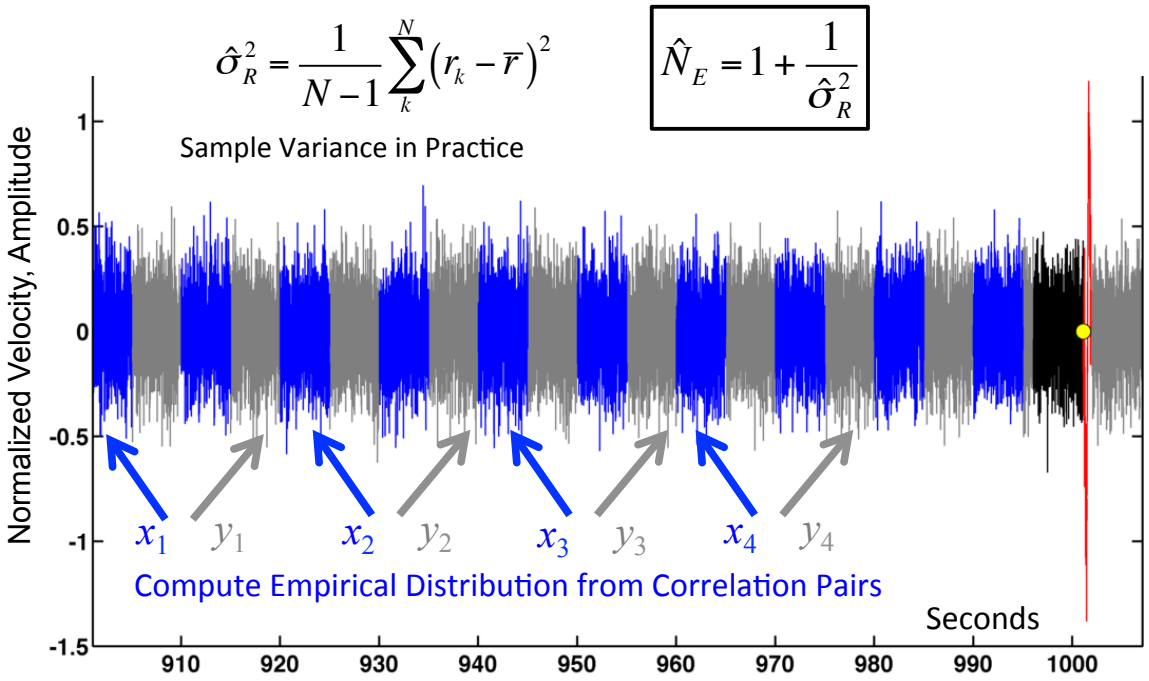

Figure A.5: Implementation of a sample correlation estimator for the effective number of degrees of freedom in the "long" window of the STA/LTA detector. Alternating segments of color-coded data samples indicate non-adjacent windows of data. The normalized sample correlation r is computed between all pairs of such independent windows and these correlation values are binned to form an empirical distribution function (histogram) for r. In the equation, $\bar{r}$ is the (generally zero) sample mean of r, and $\hat{N}_E$ is an estimate of the effective data dimension within a long window.

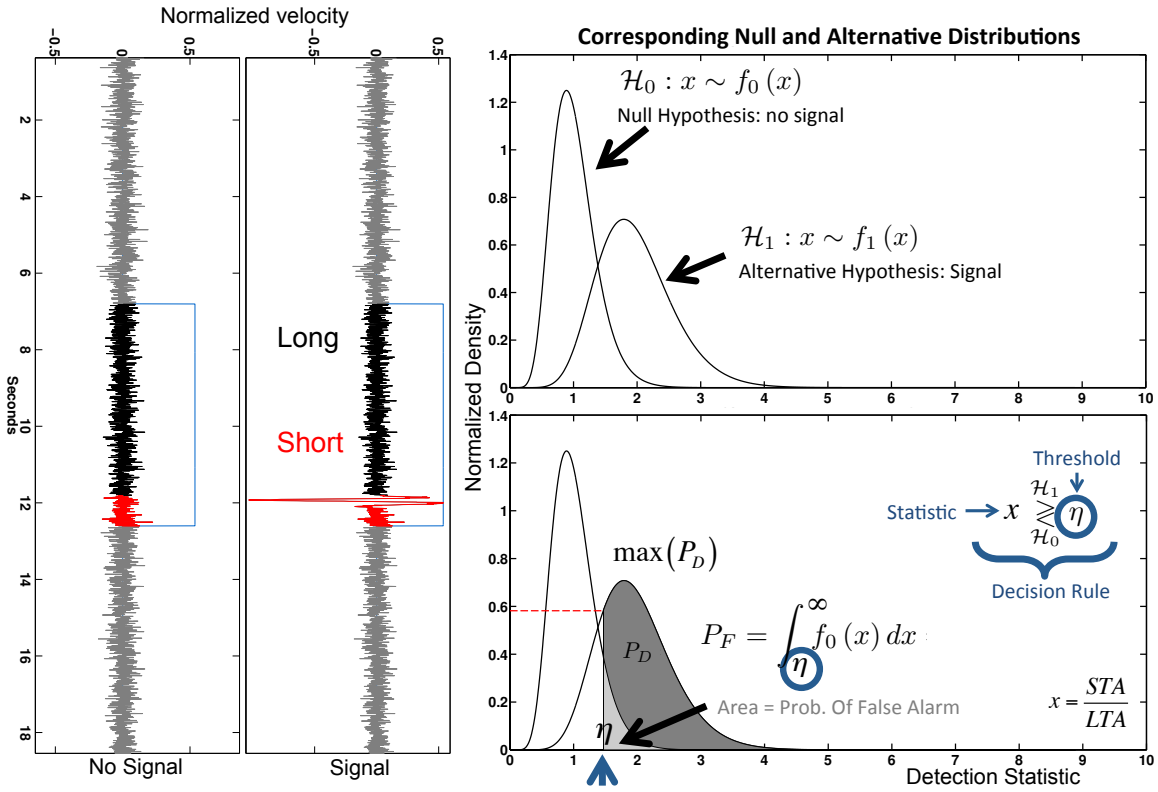

Figure A.6: The time series from Figure A.4 with the corresponding distribution functions and decision region geometry for each hypothesis test. The null and alternative distributions have substantial overlap in this example to illustrate the decision regions. In practice, any overlap is visually unapparent due to very small ($\sim 10^{-6}$) false alarm probabilities.

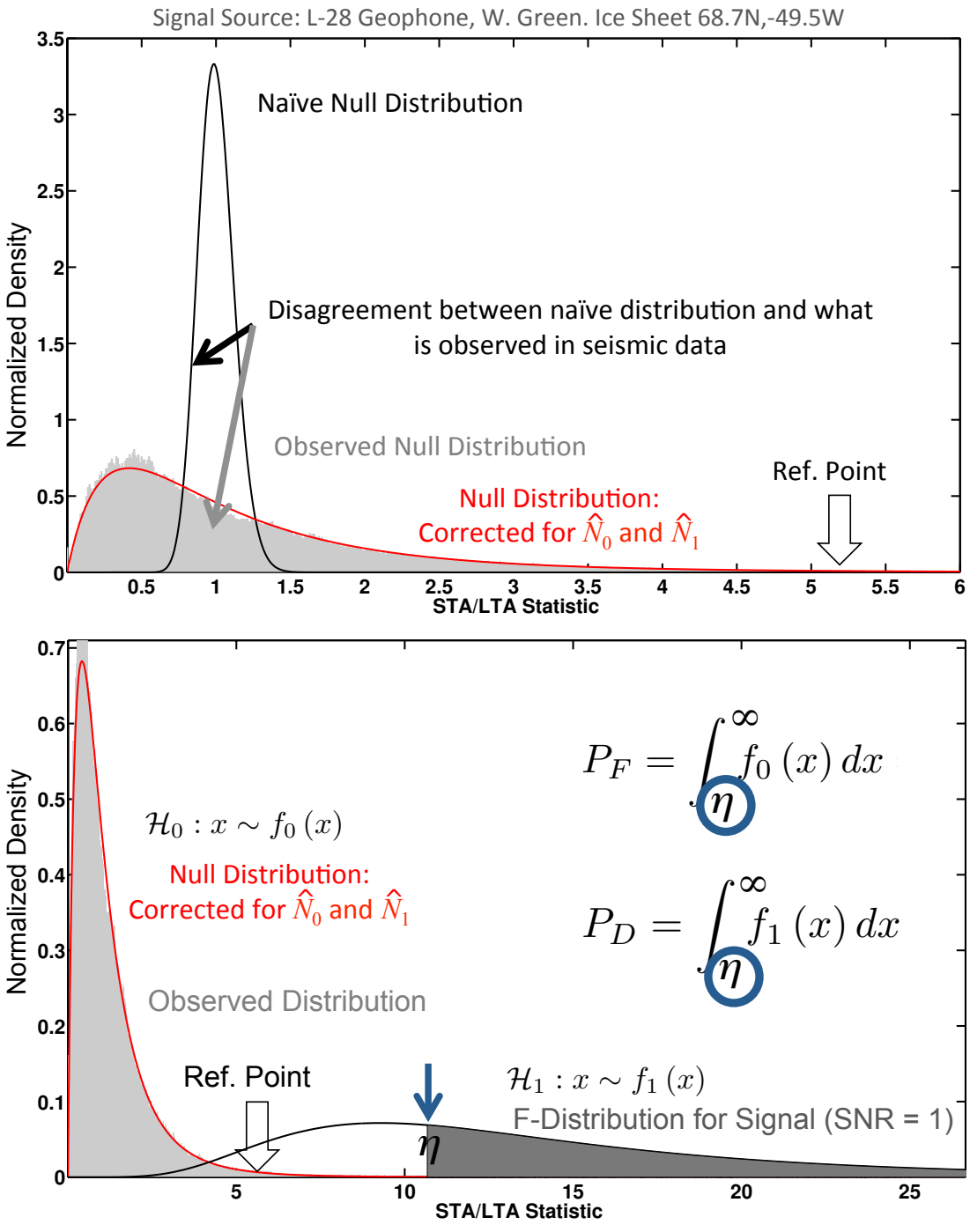
Signal Source: L-28 Geophone, W. Green. Ice Sheet 68.7N,-49.5W
Naïve Null Distribution
Disagreement between naïve distribution and what is observed in seismic data
Observed Null Distribution
Null Distribution: Corrected for $\hat{N}_0$ and $\hat{N}_1$
Ref. Point
Normalized Density
STA/LTA Statistic
$P_F = \int_{\eta}^{\infty} f_0(x)\,dx$
$P_D = \int_{\eta}^{\infty} f_1(x)\,dx$
$\mathcal{H}_0 : x \sim f_0(x)$
$\mathcal{H}_1 : x \sim f_1(x)$
Null Distribution: Corrected for $\hat{N}_0$ and $\hat{N}_1$
Observed Distribution
Ref. Point
η
F-Distribution for Signal (SNR = 1)
Normalized Density
STA/LTA Statistic

Figure A.7: **Top**: The result of picking a null distribution (black) using the conventional (naive) sample-number choice to parameterize the underlying F distribution for the STA/LTA statistic in the energy detector. A histogram of real data (gray) demonstrates the dissimilarity between the naive null distribution and what is observed. The red curves demonstrates the hypothesized null distribution when the effective degrees of freedom are estimated as $\hat{N}_0$ $\hat{N}_1$. The arrow appears as a cross-reference. **Bottom**: The decision rule using the corrected null and alternative distributions for the STA/LTA statistic, in the presence of a low SNR signal. The substantial overlap between the null and alternative distributions is shown here for illustration purposes only, and typical detection SNR values are substantially larger (e.g., Figure A.11).

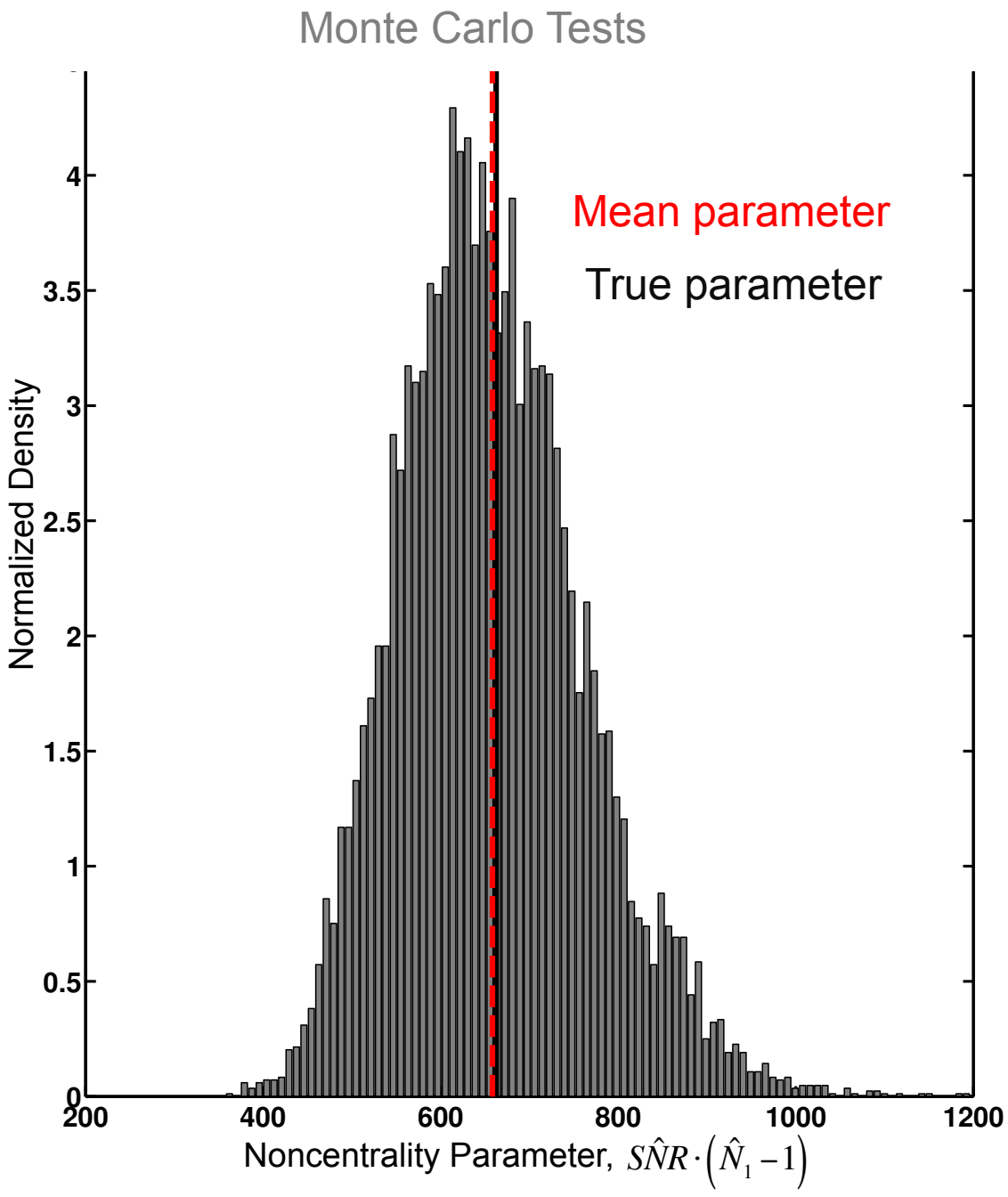

Figure A.8: Monte Carlo testing of the minimum variance, unbiased SNR estimator in Equation A.24 when the true SNR ≈ 4, shown in terms of the non-centrality parameter $SNR \cdot (N_1 - 1)$. The near coincidence between the sample mean and true mean indicates unbiasedness.

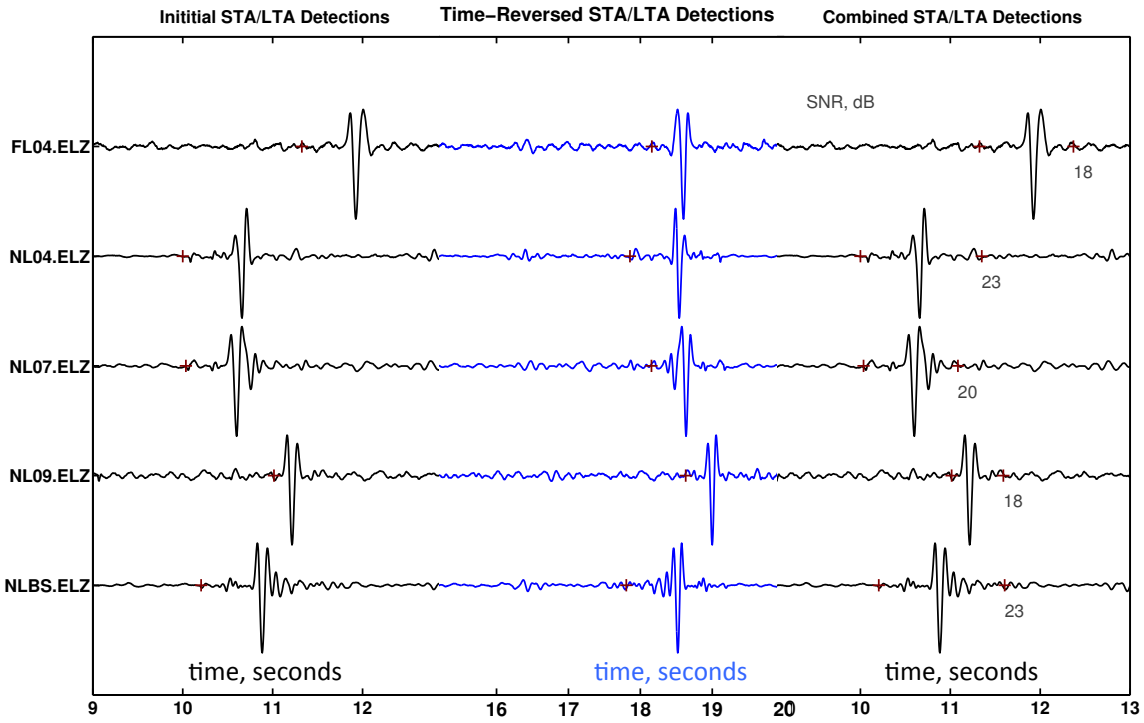
Inititial STA/LTA Detections
Time–Reversed STA/LTA Detections
Combined STA/LTA Detections
SNR, dB
FL04.ELZ
NL04.ELZ
NL07.ELZ
NL09.ELZ
NLBS.ELZ
18
23
20
18
23
time, seconds
time, seconds
time, seconds
9
10
11
12
16
17
18
19
20
10
11
12
13

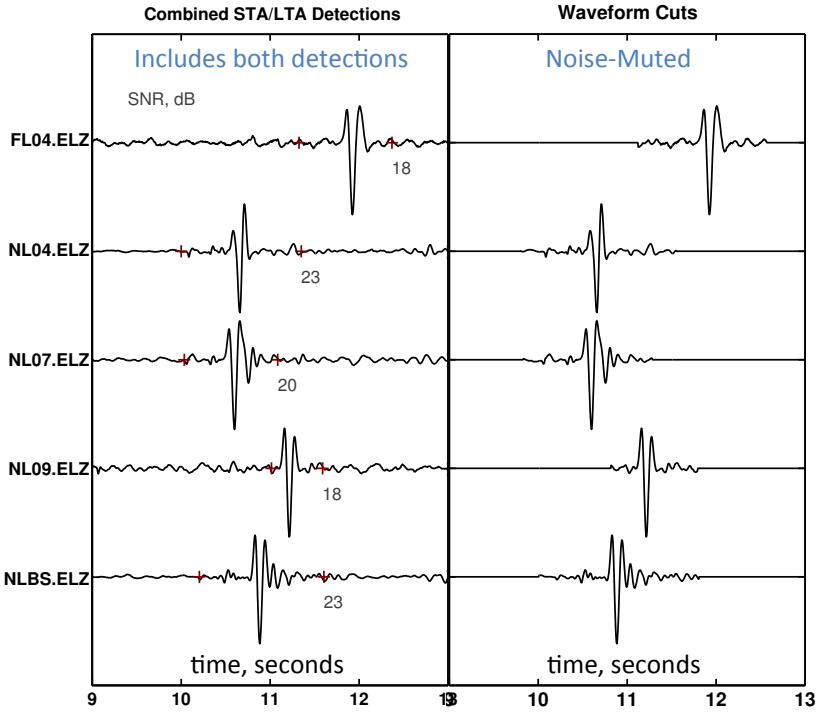
Combined STA/LTA Detections
Waveform Cuts
Includes both detections
Noise-Muted
SNR, dB
FL04.ELZ
NL04.ELZ
NL07.ELZ
NL09.ELZ
NLBS.ELZ
18
23
20
18
23
time, seconds
time, seconds
9
10
11
12
10
11
12
13

Figure A.9: An illustration of how SNR is computed for each waveform comprising an associated icequake event (discussed in Section A.7). From left to right and down, pick times are chosen according the STA/LTA detection statistic used by the energy detector. The waveforms are then time reversed. New pick times for the end of the waveform are computed using the detection statistic parameters computed to obtain the first (original) pick. The data samples between the first and end pick times represent the portion of the signal statistically distinct from noise at a given false alarm probability. Finally, the noise outside the pick-time interval is muted (multiplied by zero), and the SNR is computed according to Equation A.24.

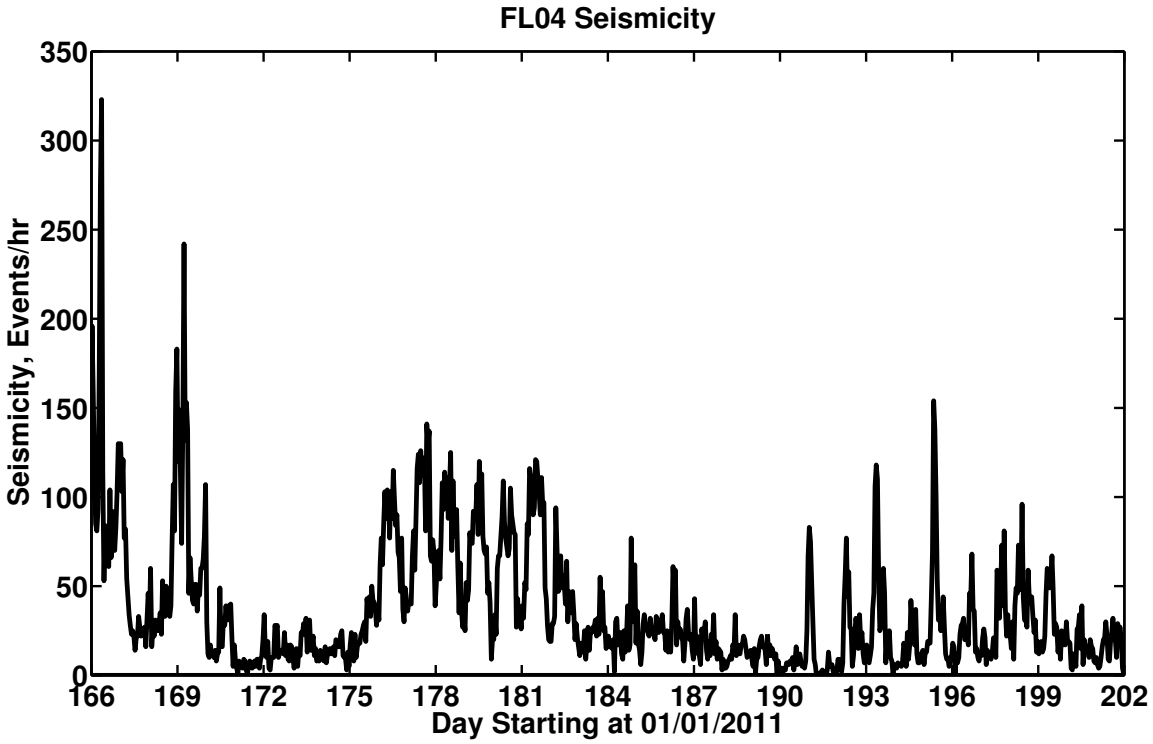

Figure A.10: Seismicity (events/hour) estimated from icequake detections found from the energy detector using a single geophone on the Greenland Ice Sheet in 2011.

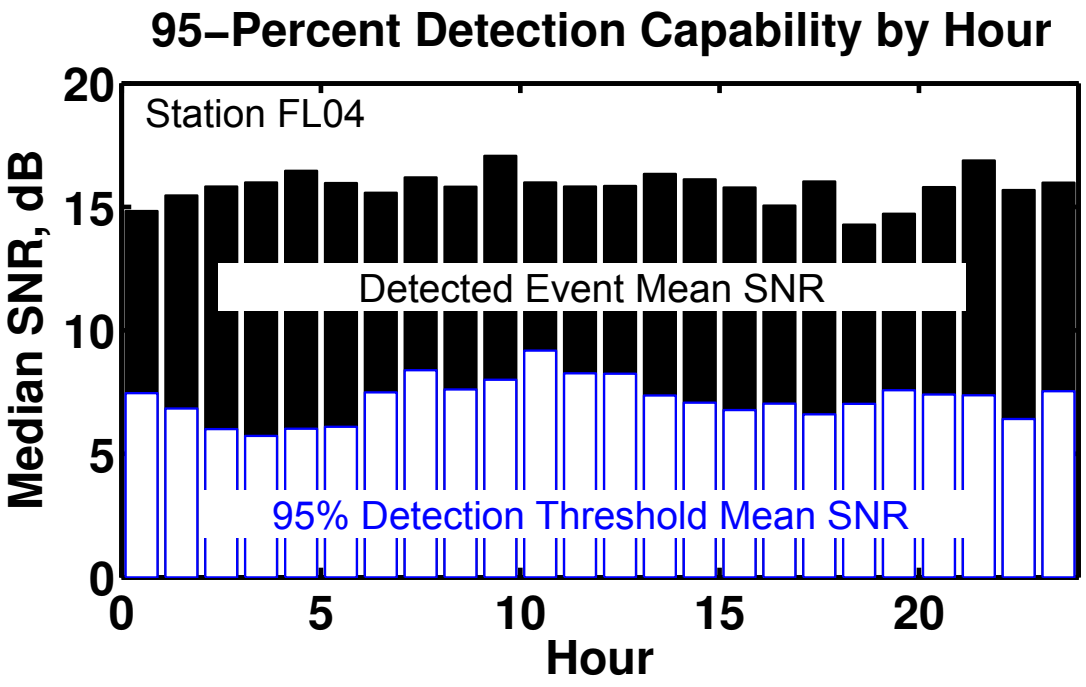

Figure A.11: The average SNR required to obtain an 95% capability for the energy detector by hour (white bars), compared to observed SNR (black bars) from events picked in Figure A.10. The observed mean SNR exceeds the 95% detection capability by several dB every hour of the day.

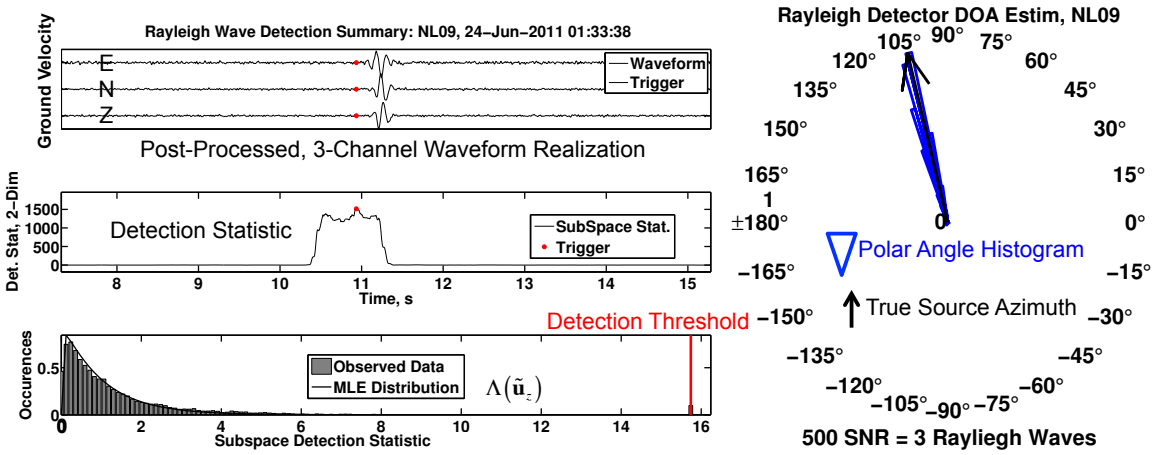

Figure A.12: **Left**: Results from a synthetic Rayleigh wave detection exercise performed using the decision rule summarized by Equation A.29. Three-component data included waveforms with additive Gaussian noise at an SNR = 3, and were pre-processed with 5 Hz width filters at their dominant power-spectral density frequencies (**top**). The middle plot illustrates a point-wise computation of the detection statistic. The null distribution (**bottom**) of the detection statistic is estimated by fitting an F_{N_0,N_1} PDF (black) to the detection statistic histogram (bottom, gray). All vertical axis are normalized. **Right**: A polar histogram of 500 direction-of-arrival estimates using Equation A.30. The true source azimuthal angle is shown by the black arrow.

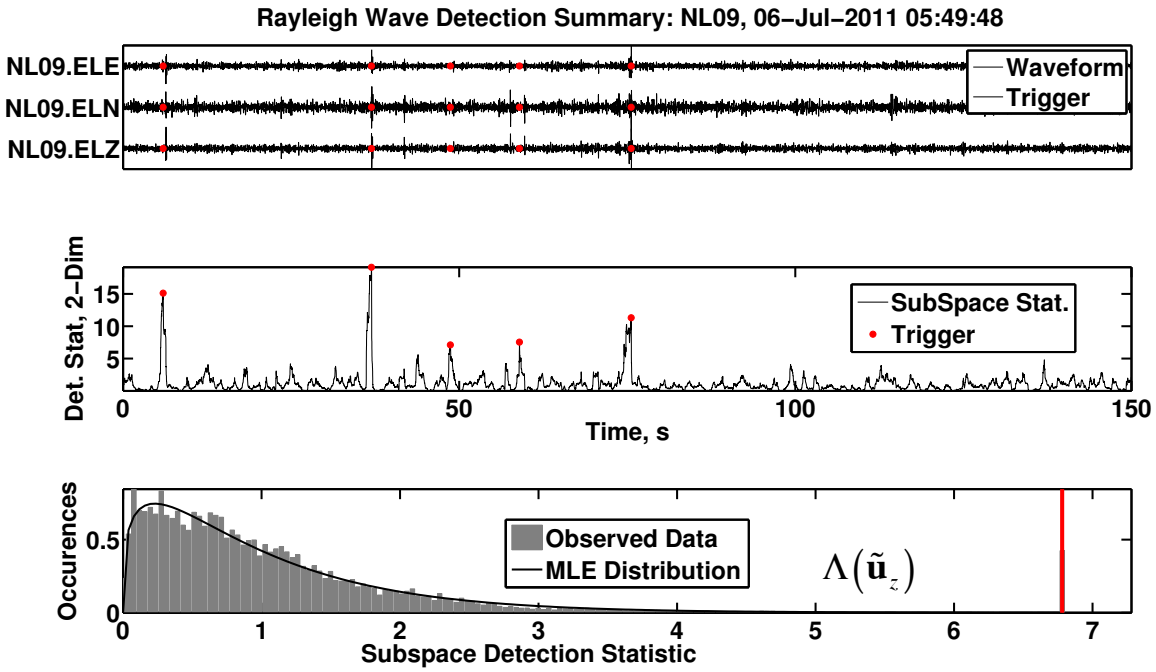

Figure A.13: Rayleigh wave detection results computed from measured data at receiver (NL09) on the Greenland Ice Sheet in 2011; plot is in the same format as presented in Figure A.12. Additional waveforms that were were undetected by the STA/LTA detector register as detections (red dots) in both the waveform plot (top) and the detection statistic plot (Equation A.29).

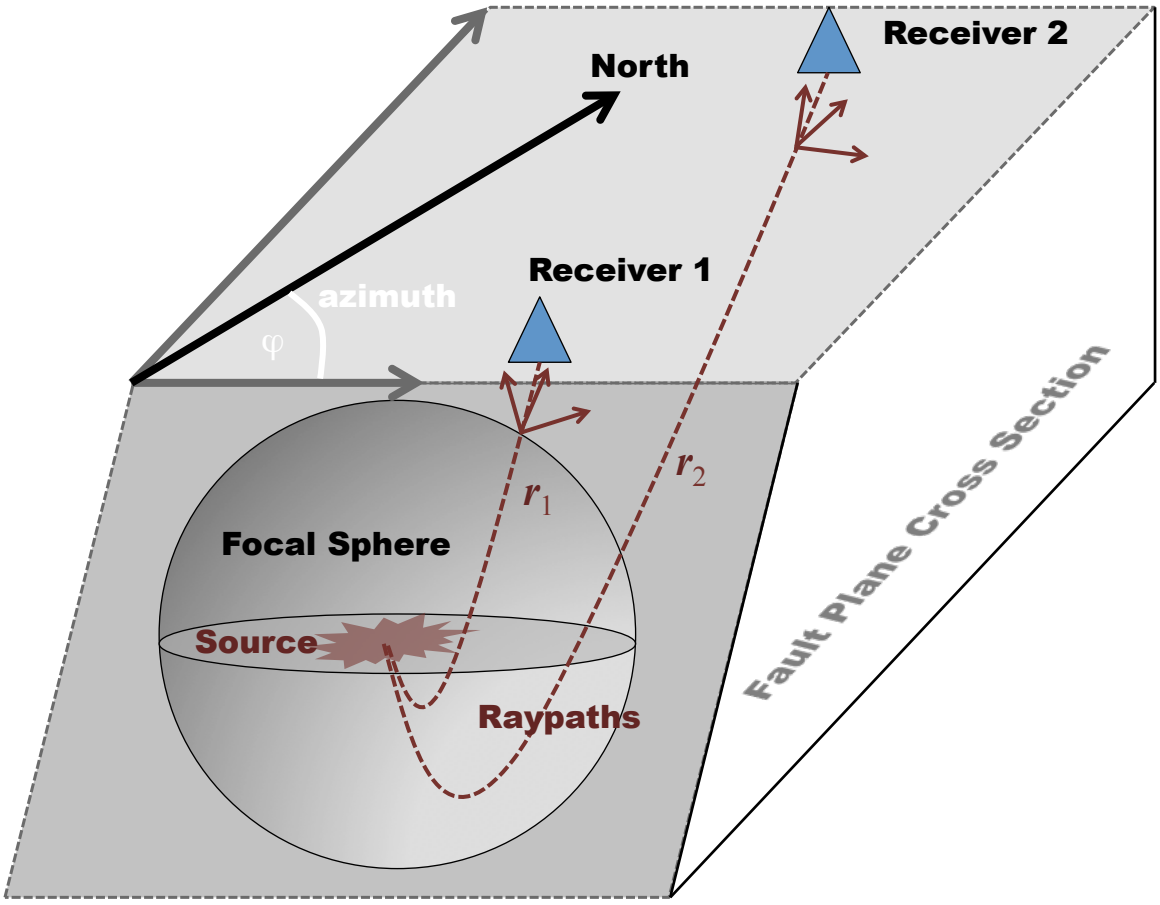

Figure A.14: The vector-wavefield observed at two distinct receivers within a geophone network is generally incoherent. Distinct take-off directions from the focal sphere and raypath sampling can attenuate and/or rotate the waveforms with respect to each other. In this cartoon, a focal sphere centered at a seismic source shows two distinct ray paths and associated seismic displacement vectors. The three components of the displacement vector at a given time sampled along raypaths r_1 and r_2 are rotated with respect to each other. Consequently, the associated three-channel waveforms may exhibit poor intra-receiver correlation.

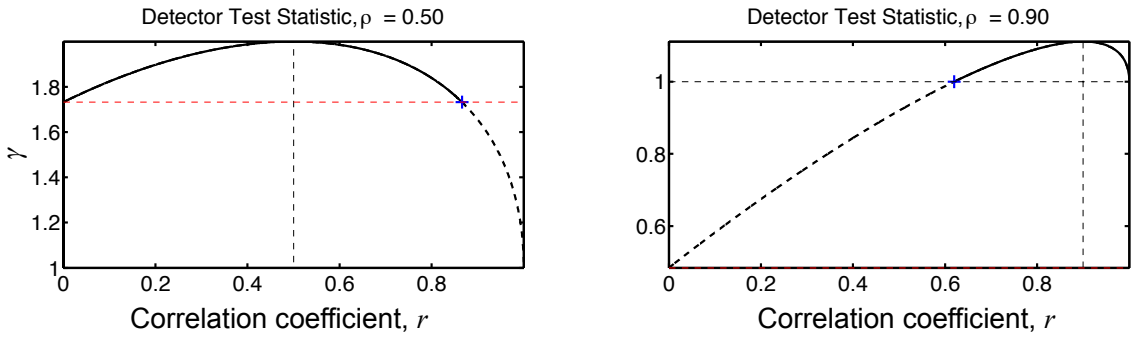

Figure A.15: The multiplet/convex cone detection statistic in Equation A.50 for identifying repeating seismic events, as function of sample correlation. This statistic reduces to the sample correlation in the limit that the template signal is known.

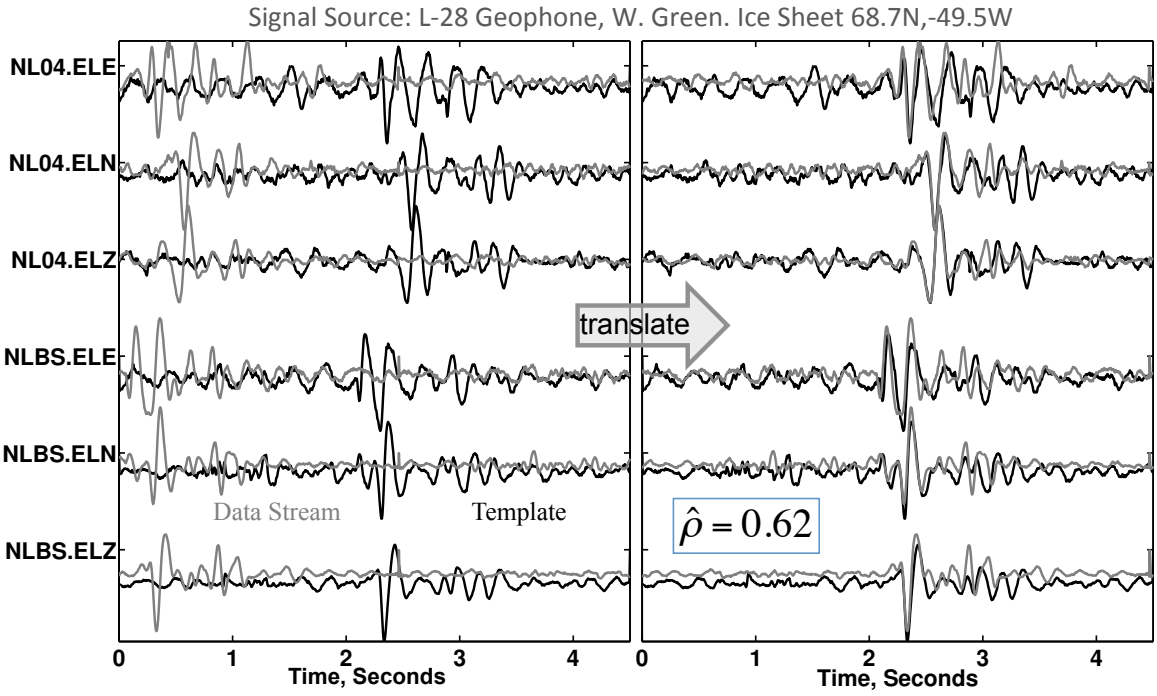

Figure A.16: An example of network-based correlation using six channels, on two receivers to identify a repeating icequake event. From left to right, the template waveform (black) is translated by a data stream (gray), and the normalized sample correlation defined by Equation A.33 is computed in a time window commensurate with the template waveform. A correlation match is found when the data on all channels are sufficiently linearly correlated, as measured by the correlation statistic $\hat{\rho}$ and false alarm rate. High multi-channel correlation requires the waveform in the template and data stream to be generated by the same source location and mechanism. Correlation matches thereby identify repetitive icequakes. In this case, an un-processed correlation of 0.62 was computed.

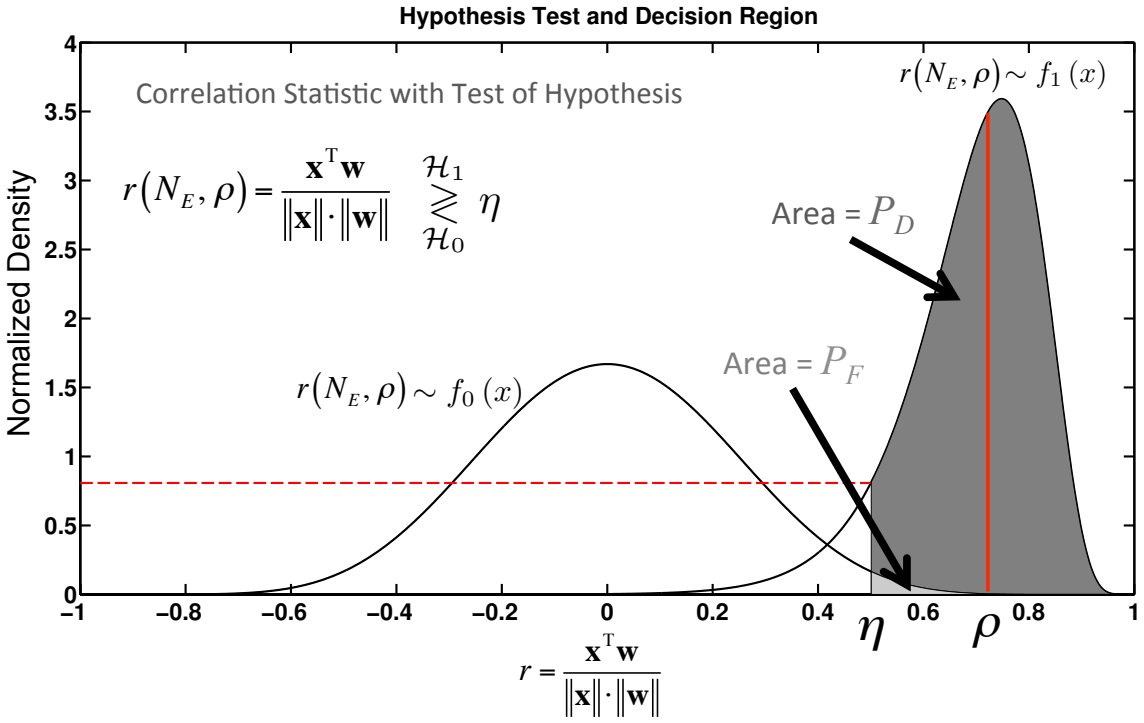

Figure A.17: The decision region geometry and parameters for a correlation detector, using a Neyman Pearson threshold value η. The detection statistic is implicitly parameterized by the true correlation ρ and the effective data dimension, N_E. In this example, the waveform degrees of freedom ($N_E = 50$), are 1/4 of the time-bandwidth product (~ 200). The false alarm probability that is indicated is generally unacceptable, and is inflated to illustration P_{FA} clearly. The true, underlying waveform correlation is $\sim 1/\sqrt{2}$.

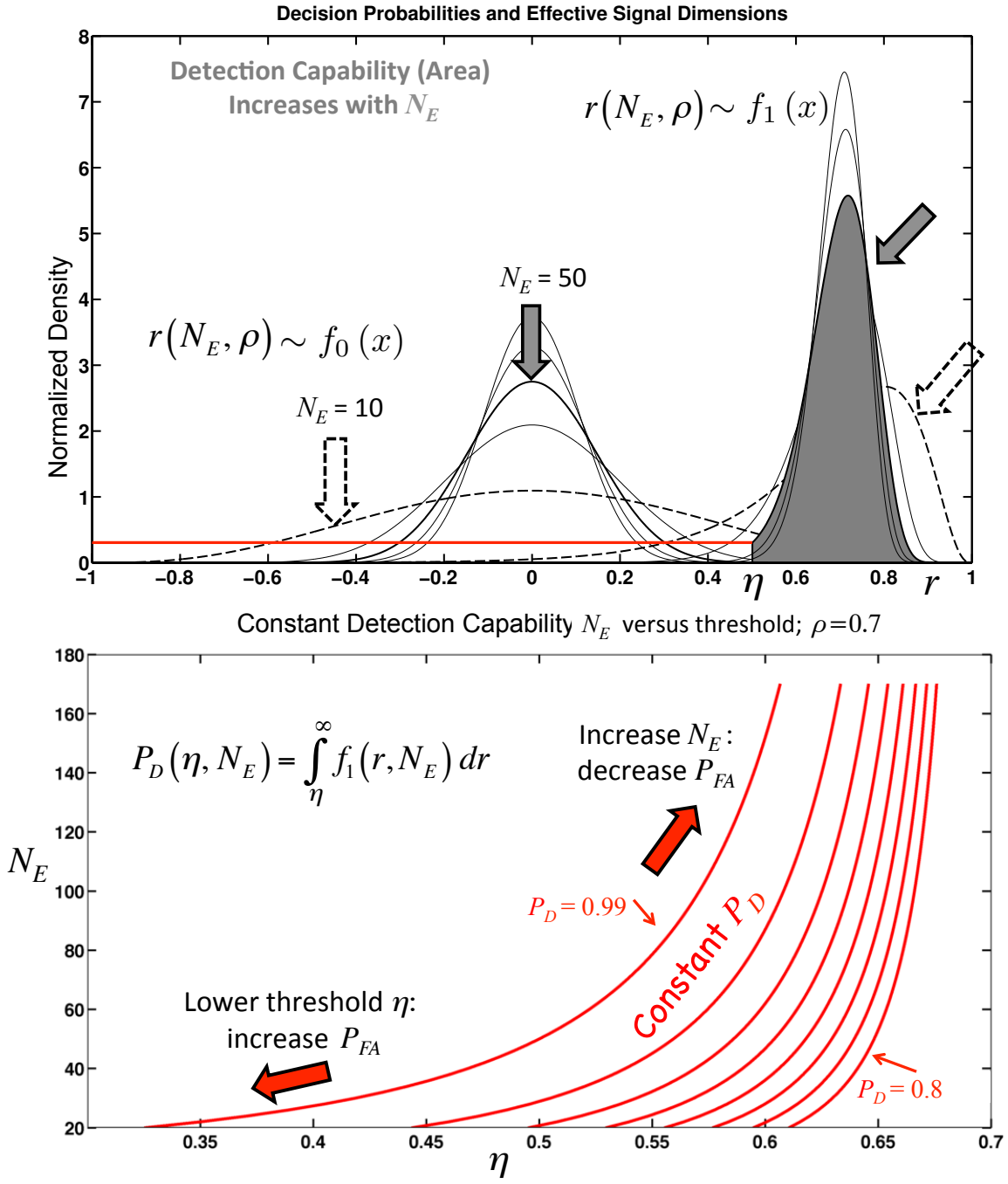
Decision Probabilities and Effective Signal Dimensions
Detection Capability (Area)
Increases with N_E
$r(N_E, \rho) \sim f_1(x)$
$r(N_E, \rho) \sim f_0(x)$
N_E = 50
N_E = 10
Normalized Density
η
r
Constant Detection Capability N_E versus threshold; ρ=0.7
$P_D(\eta, N_E) = \int_{\eta}^{\infty} f_1(r, N_E)\, dr$
Increase N_E:
decrease P_{FA}
P_D = 0.99
Constant P_D
Lower threshold η:
increase P_{FA}
P_D = 0.8
N_E
η

Figure A.18: **Top**: Several null and alternative distribution function-pairs for the correlation detector, with the true-correlation parameter and effective data dimension explicitly shown. Each curve corresponds to a distinct effective data dimension N_E. Distribution overlap decreases with N_E, indicating higher discrimination power. **Bottom**: Contour plots illustrating increased detection performance with higher effective degrees of freedom. Red contours are curves of constant detection capability. These curves are parameterized by the decision rule threshold and effective dimension. In this case, the population correlation is fixed at 0.7. On the left-most curve, each point gives the effective dimension and decision rule threshold pair that are required to constitute a Neyman Pearson detector with a detection capability of 99%. For $N_E = 20$, the decision rule threshold η must be less than 0.35. This low value leads to false alarm rates of 58%. If 100 samples were available, the threshold value for event declaration may be increased to well over 0.55 to still provide a 99% detection capability at a false alarm rate $\sim 10^{-7}$. Moving left to right across each curve decreases false alarm rates, and can be thought of as increasing data length and threshold pairs to maintain detection performance, while simultaneously reducing false alarms.

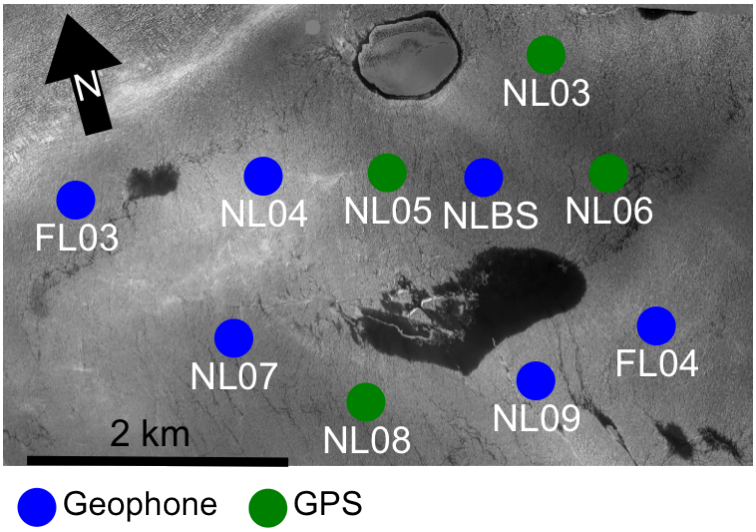

Figure A.19: The geophone network superimposed on a digital elevation model of surface ice on the Western Greenland Ice Sheet, near a draining supraglacial lake (68.73^{o}N, 49.53^{o}W) in the summer of 2011. The dark central region indicates an lake (see Chapter 3). Data from this network are used in the following Figures A.20-A.13.

Detector Parameter	**Value**	**Comments**
Short-term window, N_1	0.8 sec	160 samples at 200Hz
Long-term window, N_0	5 sec	1000 samples at 200Hz
Frequency Band	[2.5, 38] Hz	Minimum Phase Filter
Min Repeat Period, Δt_R	5.8 sec	Prevents redundant triggers on same signal
False Alarm Rate, P_{FA}	10^{-6}	Denoted as FAR
95% Detection Rate SNR $\mathrm{SNR}\left(P_D = 0.95\right)$	1.05	At FAR, in white noise. Larger SNR necessary in correlated noise.

Figure A.20: The parameters in the adaptive STA/LTA (energy) detector developed in Section A.5 for picking icequakes.

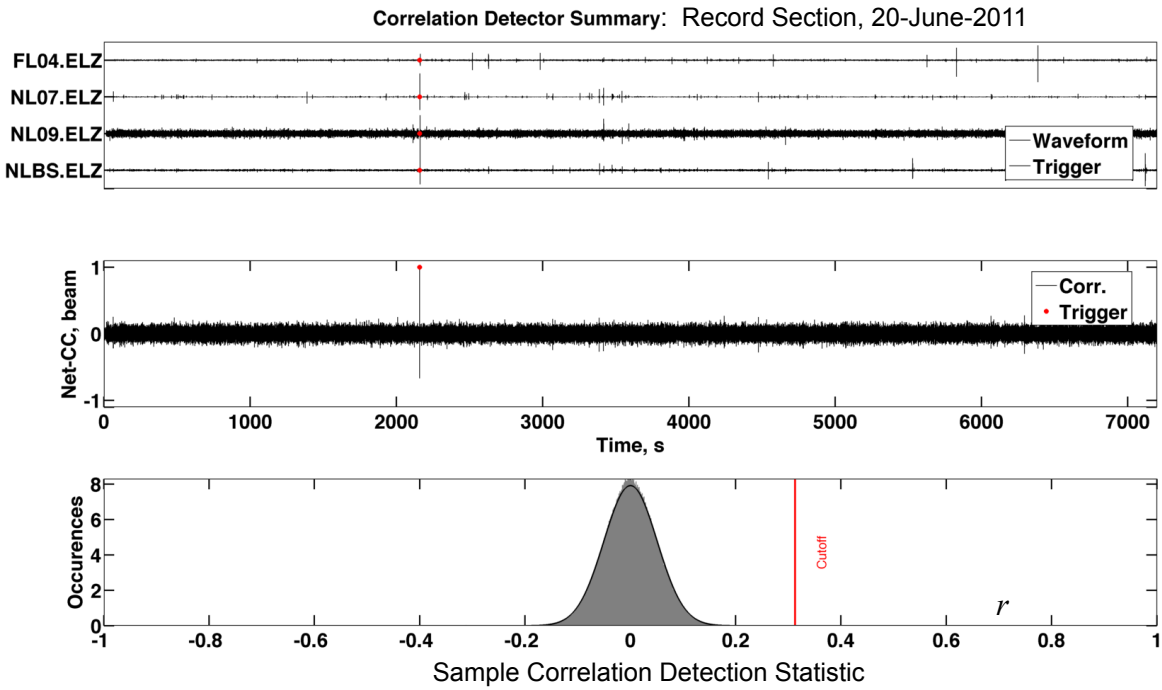

Figure A.21: A summary of a network-based correlation detection exercise using real data from a geophone network deployed on the Greenland Ice Sheet during the summer of 2011; the template signal was ~ 5 seconds long and included correlated noise (see Figure A.20 for network geometry) **Top**: The waveform data from the vertical component of 4 operational geophones in the network. **Middle**: The detection statistic time series giving the network-based correlation coefficient (Equation A.33). **Bottom**: The null distribution from the data (gray) and the hypothesized null distribution (black) that is parameterized by effective degrees of freedom and obtained from a modification of the estimation method show in Figure A.4 (see Section A.14)

Appendix B

NETWORK-BASED CLUSTERING OF SEISMIC DATA

Here we provide criteria for assigning cluster membership for multiplet identification to avoid manual template selection and maintain detection consistency when record section stacks (record section sums) are cluster templates (match filters). Define a Hilbert space $\mathcal{H}$ equipped with an inner product $\langle \bullet, \bullet \rangle$ whose elements are $3N$ channel record sections $\mathbf{v}(t)$. Suppose that $\mathbf{v}_k(t)$, $k = 1, \ldots, n, \ldots, M$, are record sections as defined by Equation A.2 that give samples of ground velocity from M icequakes. Consider a set $S \subset \mathcal{H}$ according to the membership criteria:

$$S = \{\mathbf{v}(t) : \langle \mathbf{v}(t), \hat{\mathbf{w}}_n(t) \rangle \geq \rho_0 \, ||\mathbf{v}(t)||\}, \tag{B.1}$$

Set S in Equation B.1 defines the set of all record sections that belong to a multiplet and represents a higher dimensional convex cone whose vertex is parallel to $\hat{\mathbf{w}}_n(t)$ [156, p. 113]. Seismic clustering methods often implicitly use sets of this form [100]. We address two drawbacks of clustering with this set constraint: first, populating S requires prescribing $\hat{\mathbf{w}}_n(t)$ and second, template matching with stacks depends on detection order.

Consider a multiplet sequence that produces five (normalized) record sections $\{\hat{\mathbf{v}}_1(t), \hat{\mathbf{v}}_2(t), \cdots, \hat{\mathbf{w}}(t)\}$ that satisfy $\langle \hat{\mathbf{v}}_k(t), \hat{\mathbf{w}}(t) \rangle = \rho_0$, where $k = (1, \cdots, 4)$. Each $\hat{\mathbf{v}}_k(t)$ is representable as the sum of its projection onto $\hat{\mathbf{w}}(t)$ and an orthogonal complement (residual). It follows $\langle \hat{\mathbf{v}}_k(t), \hat{\mathbf{v}}_n(t) \rangle = \rho_0^2 + \left(1 - \rho_0^2\right) \cos(\theta_{kn})$ where θ_{kn} represents the angle between the residuals of $\hat{\mathbf{v}}_k(t)$ and $\hat{\mathbf{v}}_n(t)$. Suppose we detect three signals that include $\hat{\mathbf{w}}(t)$ from this sequence and stack them to form a cluster template $\bar{\mathbf{v}}(t)$. Now suppose we then detect an additional signal $\hat{\mathbf{v}}_m(t)$ from this same sequence and test it for cluster membership. We now show that it's membership is conditional upon the detection order using two distinct scenarios. The initial triplets detected in either scenario include a different pair of signals together with $\hat{\mathbf{w}}(t)$, and a different value for m. The correlation of $\hat{\mathbf{v}}_m(t)$ with the stack in

general is:

$$\rho_m = \frac{\langle \hat{\mathbf{v}}_m(t), \bar{\mathbf{v}}(t) \rangle}{||\bar{\mathbf{v}}(t)||} = \frac{2\rho_0^2 + \rho_0 + \left(1 - \rho_0^2\right)\left(\cos\left(\theta_{km}\right) + \cos\left(\theta_{nm}\right)\right)}{\sqrt{3 + 4\rho_0 + 2\rho_0^2 + 2\left(1 - \rho_0^2\right)\cos\left(\theta_{kn}\right)}} \tag{B.2}$$

If the residuals in the initial stack are anti-correlated but the residual of $\hat{\mathbf{v}}_m(t)$ projected onto $\hat{\mathbf{w}}(t)$ is within $\pi/4$ of $\hat{\mathbf{v}}_k(t)$ and $\hat{\mathbf{v}}_n(t)$, $\rho_m = \rho_0$ so $\hat{\mathbf{v}}_m(t)$ is included in the cluster set. However, if the residuals in the initial stack are orthogonal but the residual of $\hat{\mathbf{v}}_m(t)$ projected onto $\hat{\mathbf{w}}(t)$ is within $3\pi/4$ of $\hat{\mathbf{v}}_k(t)$ and $\hat{\mathbf{v}}_n(t)$, $\rho_m < \rho_0$. In particular, if $\rho_0 = 0.65$, $\rho_m = 0.27$, and $\hat{\mathbf{v}}_m(t)$ would be rejected from the cluster set. We avoid this inconsistency in cluster assignment and alternatively define a cluster as a smaller convex set using a more restrictive membership criteria:

$$S_L = \left\{\mathbf{v}(t) : \langle \mathbf{v}(t), \hat{\mathbf{w}}_k(t) \rangle \geq \rho_0 \, ||\mathbf{v}(t)||\right\}, \quad \forall \; k \in [1, 2, \cdots L] \tag{B.3}$$

where $L \leq M$. Elements of S_L correlate above ρ_0 with every record section $\mathbf{w}_k(t)$, $k = 1, \ldots, n, \ldots, L$, so that $S_L \subseteq S$. It also represents record sections produced by a multiplet, but the characteristic ground velocity is provided by L observations, rather than one. Hence, clustering record sections into sets defined by Equation B.3 requires high *mutual* correlation between elements. We implement this requirement as follows. Suppose we detect M icequakes on a given day and record M corresponding record sections. From Equation A.33, we define an upper-triangular matrix $\boldsymbol{\rho}$ whose elements ρ_{ij} provide the $\frac{1}{2}\left(M^2 - M\right)$ normalized correlation coefficients between record sections:

$$\rho_{ij} = \max_{\tau} \frac{\langle \mathbf{v}_i(t), \mathbf{v}_j(t+\tau) \rangle_F}{||\mathbf{v}_i(t)||_F ||\mathbf{v}_j(t)||_F}, \quad i < j \tag{B.4}$$

Suppose now that a subset of $L \leq M$ record sections with indices $\gamma \subseteq \{1, \ldots, L\}$ cross-correlate above ρ_0 with a particular record section $\mathbf{w}_n(t)$, so that $\rho_{n\gamma} \geq \rho_0 \; \forall \; \gamma$. This does not guarantee that $\mathbf{v}_\gamma(t) \in S_L \; \forall \; \gamma$. We therefore test all entries of $\boldsymbol{\rho}$ whose indices are derived from pair-wise combinations of γ as power sets. For example, if $\rho_{1\gamma} \geq \rho_0 \; \forall \; \gamma = \{2, 3, 7\}$, then $\mathbf{v}_\gamma(t) \in S_L \; \forall \; \gamma$ only if ρ_{23}, ρ_{27}, and ρ_{37} each exceed ρ_0 as well. If this condition holds, we define $S_L = \{\mathbf{v}(t) : \langle \mathbf{v}(t), \hat{\mathbf{v}}_k(t) \rangle \geq \rho_0 \, ||\mathbf{v}(t)||\}$, $\forall \; k \in [1, 2, 3, 7]$ as the cluster for a multiplet event.

In general, we identify the clusters from Equation B.4 from a desired catalog, and aggregate them over a record section database by computing $\boldsymbol{\rho}$. To populate the final clusters that are plotted in Figure 2.8 (top), we check mutual correlation between all elements that satisfy $\rho_{ij} \geq \rho_0$ as for catalog record sections. We obtain a representation of a each cluster by coherently aligning the elements to sub-sample precision and linear stacking. Because S_L is convex, any linear combination of record sections with non-negative weights is also contained in S_L. Other weighting schemes for stacking are useful but depend on the performance measure applied to the record section output. A representation model for multiplets from signal subspaces described is elsewhere [63].

Appendix C

PLATFORM OSCILLATIONS AS A SOURCE OF "TREMOR"

The installation of any semi-permanent seismic network on-ice is comparatively difficult relative to a similar land-installation. This complication is partially due to surface ablation that causes instrument melt-out and tilt. To address this challenge, each network geophone was installed using a buried platform-pole assembly intended to both prevent rapid summer melt out and increase ice-instrument coupling from 2009 through 2012. I document that installation procedure here. First, the L-28 geophone was mounted upon small plywood platform that had been drilled with 3 holes so that the L-28 pegs fit firmly into the platform. An additional hole was drilled through the center of the platform to fit a $1.0''$ (3cm) diameter, 1.6m long hollow-core aluminum pole. The total system was then secured together with zip-ties, hose clamps, and duct tape. To bury each geophone mount, a primary $\frac{1}{2}$m-diameter hole was drilled into the ice to a depth of about 2m at each site. A secondary hole roughly 6cm in diameter was then drilled at the bottom of the primary hole to an addition depth of about 2m. The geophone mount was lowered into the primary hole with a rope so that the mount pole was inserted into the secondary, interior hole. This allowed the geophone platform to rest on the bottom of the primary hole. The geophone was then oriented to magnetic north and the platform was tamped down. Once oriented and leveled, the primary hole was filled with ice chips and diagnostics were run upon the cumulative data acquisition system.

This preventative installation process had two distinct consequences on data quality, one positive, one unintended. First, the platform prevented geophone tilting during melt-out so that the horizontal channels were functional throughout the experiment. This improved data integrity relative to previous years in which melt-induced tilt rendered the horizontal components useless. Second, the pole-mount system introduced unintended mechanical oscillations of the pole-platform system as it became exposed during melt-out. This occurred

after the initial 2m of surface ice melted off post-installation, leaving a length L_e of the mount exposed. The power platform (solar panel system) would have also produced vibrational modes during melt out and may explain the more subtle horizontal spectral features in the geophone spectrograms prior to 2009. To determine the effect of melt-out on the oscillatory response of the geophone mount, I model the mount as a point mass m on the end of a cantilevered pole of length L_e, where the end mass acts like an axial load mg (g is gravity) on a structural column. In this model, the instrumented end is free, but the bottom end is fixed. The resonant frequencies of this system are equivalent to the eigenmodes of a slender column given by Equation C.1 [167]:

$$f_n = \frac{1}{2\pi L_e^2}\left[\frac{(2n-1)\,\pi}{2L_e}\right]^2 \sqrt{\frac{EI}{\rho A}} \quad (n = 1, 2, \cdots) \tag{C.1}$$

The quantities E, I, A and ρ respectively represent Young's modulus of the pole, the moment of inertia about the fixed end, the effective cross-sectional area of the system, and the effective density. The product EI is complicated to estimate because the effective stiffness of the system is heavily dependent upon the factors that include the ice content inside the pole core and the quality of the aluminum. I therefore estimate the factor $\sqrt{\frac{EI}{\rho A}}$ from field observations as follows. During a maintenance and recovery mission in June of 2012, the original installation team found that one of the solar panel mounts for a particular site (NL04) had nearly melted out, leaving $\cong$ 3m of the pole exposed (see Figure C.1). This pole had noticeably buckled under the weight of the solar panel assembly, which was roughly known. It therefore behaved like a column buckling under an axial load. The critical buckling weight of column with axial load mg is given by:

$$mg = \frac{\pi EI}{(2L_e)^2} \tag{C.2}$$

where L_e is the length of pole exposed. Because it is likely that the pole buckled at an initially shorter length prior to observation, this likely provides an overestimate for EI. I obtain an estimate the effective product of the density and the pole cross sectional area, ρA, as $2\pi r d\rho$, where r is the pole radius, $d\rho$ is the pole-wall thickness, and $\rho = 2700\frac{\text{kg}}{\text{m}^3}$ is the density of aluminum. By solving Equation C.2 for EI and using the previous estimate of

ρA, I obtain a value of $\sqrt{\frac{EI}{\rho A}}$ for the pole. I emphasize here that this quotient is a material property of the poles used, and is applicable to the seismometer poles as well.

The result of this exercise provides a suite of eigenmode frequencies that are dependent on pole length exposure L_e. To estimate the time dependence for melt-out at each geophone location, I use ablation calculations from a common regional climate model (RACMO) from 2011. I compare the temporal history of the geophone-platform eigenmodes in Figure C.2 with the spectrogram for 2011 at station NLBS. The range of expected eigenmodes effectively matches those in the spectrogram. The disagreement in timing is to be expected, since my estimate of the initial geophone burial depth and location-specific melt rates are inprecise. I propose that the diurnal fluctuation of several Hz in the spectrogram during summer days is due to a melt puddle forming along along the thermally-conductive length of the buried geophone pole. The freeze-thaw cycle of this puddle would effectively lengthen and shorten the pole, thereby coupling and decoupling the pole from the ice surface at diurnal periods.

I suggest that responsibly managed seismic monitoring of the ice sheet ablation zone requires considering the possibility of platform resonance as I have described. Despite the degradation in late summer data quality, the pole and platform did likely prevent each geophone from titling on the ice surface during initial melt out. Early in exposure, when only the upper portion of the geophone had melted out, the system was effectively still rigid. Only after substantial exposure of the pole ($\geq$ 1 m), did it's resonance frequency become problematic. Instead, I suggest a deeper installation depth and thicker (solid core) pole would respectively delay instrument exposure and increase pole stiffness. These and similar counter measures would likely increase the duration over which the expected data quality is high.

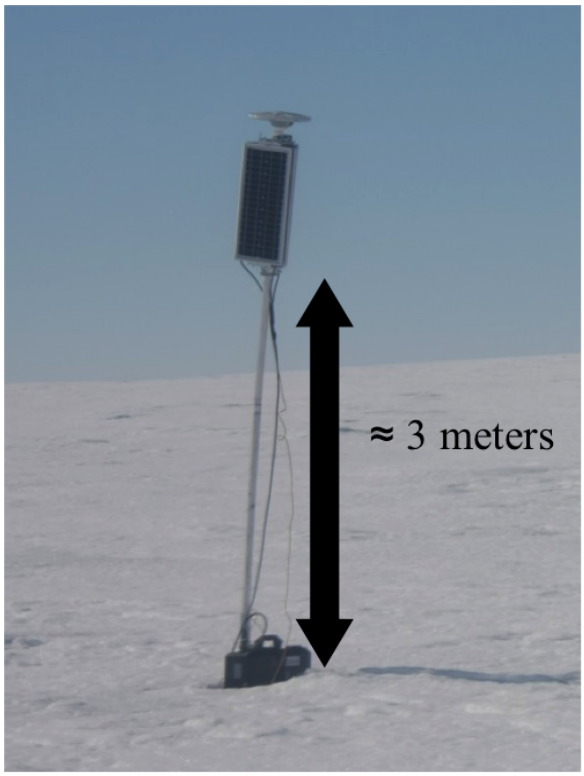

Figure C.1: A crude estimate for the upper bound on pole buckling length was obtained from this image that was taken during an instrument recovery mission in 2012.

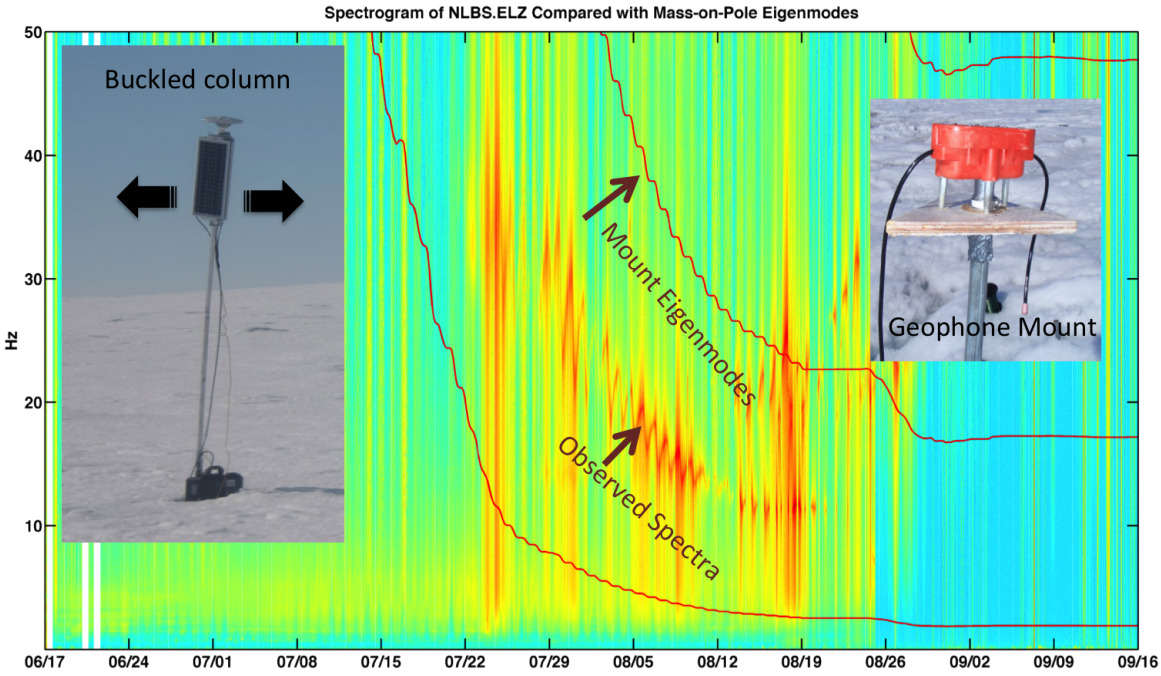

Figure C.2: The spectrogram computed from data collected over 2011 from the vertical channel of geophone NLBS. The lower $[0, 50]$ Hz band is compared with the 3 lowest modeled resonance modes of the geophone platform, displayed here as red curves. The trend in the modeled resonance is parallel with that of the spectral features in the spectrogram, while temporally non-coincident. This difference in timing is probably due to the necessarily crude estimates of install depth and the system moment of inertia. Because resonant frequency change rate (time derivative) matches the observed trend shape, I conclude that the observed spectral features are due to pole-platform oscillations. Diurnal changes in the observed resonance frequency may be due an effective shortening and lengthening of the pole from a melt-puddle forming around the relatively thermally conductive buried portion of the pole during the day, and refreezing at night.